TU/e EINDHOVEN UNIVERSITY OF TECHNOLOGY

Development and understanding of advanced atomic layer deposition processes

Citation for published version (APA):
Vos, M. F. J. (2019). *Development and understanding of advanced atomic layer deposition processes: AlF_3, Co, and Ru*. Technische Universiteit Eindhoven.

Document status and date:
Published: 21/11/2019

Document Version:
Publisher's PDF, also known as Version of Record (includes final page, issue and volume numbers)

Please check the document version of this publication:

• A submitted manuscript is the version of the article upon submission and before peer-review. There can be important differences between the submitted version and the official published version of record. People interested in the research are advised to contact the author for the final version of the publication, or visit the DOI to the publisher's website.
• The final author version and the galley proof are versions of the publication after peer review.
• The final published version features the final layout of the paper including the volume, issue and page numbers.

Link to publication

General rights
Copyright and moral rights for the publications made accessible in the public portal are retained by the authors and/or other copyright owners and it is a condition of accessing publications that users recognise and abide by the legal requirements associated with these rights.

• Users may download and print one copy of any publication from the public portal for the purpose of private study or research.
• You may not further distribute the material or use it for any profit-making activity or commercial gain
• You may freely distribute the URL identifying the publication in the public portal.

If the publication is distributed under the terms of Article 25fa of the Dutch Copyright Act, indicated by the "Taverne" license above, please follow below link for the End User Agreement:

www.tue.nl/taverne

Take down policy
If you believe that this document breaches copyright please contact us at:

openaccess@tue.nl

providing details and we will investigate your claim.

Download date: 27. jan. 2021

Development and Understanding of Advanced Atomic Layer Deposition Processes:

AlF_3, Co, and Ru

PROEFSCHRIFT

ter verkrijging van de graad van doctor aan de Technische Universiteit Eindhoven, op gezag van de rector magnificus prof.dr.ir. F.P.T. Baaijens, voor een commissie aangewezen door het College voor Promoties, in het openbaar te verdedigen op donderdag 21 november 2019 om 13:30 uur

door

Martinus Franciscus Johannes Vos

geboren te Eindhoven

Dit proefschrift is goedgekeurd door de promotoren en de samenstelling van de promotiecommissie is als volgt:

voorzitter:	prof.dr.ir. G.M.W. Kroesen
1e promotor:	prof.dr.ir. W.M.M. Kessels
copromotor:	dr.ir. A.J.M. Mackus
leden:	prof.dr. J.T. Zuilhof (WUR)
	prof.dr.ir. W. Vandervorst (KU Leuven)
	prof.dr. K.A. Williams
	prof.dr. R. Chen (Huazhong University of Science and Technology)
adviseur:	dr. L.B.F. Juurlink (UL)

Het onderzoek dat in dit proefschrift wordt beschreven is uitgevoerd in overeenstemming met de TU/e Gedragscode Wetenschapsbeoefening.

Funding information

This research is supported by the Netherlands Organisation for Scientific Research (NWO), in the framework of the *Zwaartekracht* program 'Research Centre for Integrated Nanophotonics'.

Front cover design by Martijn Vos & Maria Antonietta Mione, showing AlF_3-coated GaP nanowires imaged using a Zeiss Sigma scanning electron microscope.

This dissertation is typeset in LaTeX.

Printed and bound by: Ipskamp Printing

A catalogue record is available from the Eindhoven University of Technology Library
ISBN: 978-90-386-4900-9

Contents

1 General Introduction **1**

2 Atomic Layer Deposition **17**

3 Advanced ALD cycles **37**

4 Atomic Layer Deposition of Aluminum Fluoride using $Al(CH_3)_3$ and SF_6 plasma **61**

5 Reaction Mechanisms during Atomic Layer Deposition of AlF_3 using $Al(CH_3)_3$ and SF_6 plasma **81**

6 Atomic Layer Deposition of Cobalt Using H_2-, N_2-, and NH_3-Based Plasmas: On the Role of the Co-reactant 109

7 Area-Selective Deposition of Ruthenium by Combining Atomic Layer Deposition and Selective Etching 143

8 Atomic Layer Deposition and Etching of Ruthenium for Area-Selective Deposition: Temperature and Supercycle Optimization 161

9 Conclusions and outlook 191

Summary 197

Contributions of the author 199

Publications 201

Acknowledgments 203

Curriculum Vitae 207

1 General Introduction

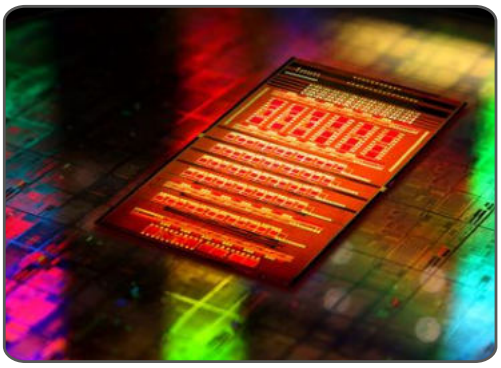

The last few decades can be characterized by a range of technological breakthroughs in information and communications technology, which have drastically changed our society. Many of these breakthroughs were enabled by advancements in the field of electronic integrated circuits (ICs) using Si as semiconducting material, which among other things relied on developments in thin film technology.[1] Thin films are currently widely used for the fabrication of functional components in semiconductor nanoelectronics, but also in photovoltaics, displays and batteries.[2] Moreover, thin film technologies are continuously under development, which is to a large extent motivated by the downscaling of semiconductor devices.[3] Notably, this downscaling led to the doubling of the number of transistors on an IC every two years, as is described by Moore's law.[4] The semiconductor industry has grown to a market with a revenue of nearly $500 billion in 2018.[5] Upcoming technologies including the next-generation mobile communication infrastructure (5G), self-driving cars, and artificial intelligence will keep driving advancement in thin film technology and its application in the semiconductor industry.[6] Moreover, the transition to a data-based society requires the coupling of existing electronic technologies with integrated photonics. Relying on transport of photons rather than electrons, photonics can allow for faster data transfer at a lower power consumption.[7,8] Ongoing trends in the fields of semiconductor nanoelectronics, integrated photonics, and thin film processing are identified in this chapter, in order to provide the context for the research addressed later in this thesis.

Figure above after Ref. 9

1.1 Introduction of new materials

Until approximately the year 2000, the semiconductor industry made use of a small set of materials (mainly $Si/SiO_2/SiN_x$, W and Al) for the fabrication of electronic devices. Advances in the semiconductor industry were mostly made by geometric scaling of device architectures, meaning that all features on ICs were shrinking simultaneously through continuous improvements in optical lithography.[10,11] However, dictated by the miniaturization and increasing functionality of devices, the number of employed materials has grown drastically in recent years, and continues to grow.[10,12]

Figure 1.1 shows examples of materials which have been introduced recently, or are being considered for future transistor fabrication. For instance, materials such as Cu, strained Si, SiGe, as well as low-k and high-k dielectrics have facilitated scaling in the last two decades.[10,13] To allow further miniaturization of semiconductor devices, researchers are considering the integration of various novel thin film materials.[5,13,14] A significant, current example which illustrates this point is the replacement of Cu by Co and Ru in small-dimension interconnects. Metal interconnects are structures which serve to electrically connect the features of an IC with each other, and were originally made from Al until they were replaced by Cu in the late 90s.[12] As metal interconnects in the back-end-of-line of semiconductor devices are further decreasing in size, the resistance of the Cu line is rising significantly due to electron scattering at external surfaces and grain boundaries.[15,16] This increase in resistance results in a substantial RC (Resistance-Capacitance) delay, which hinders the performance of ICs.[12,17] At small dimensions, the wire resistance of Co and Ru can be lower than that of Cu, and the industry is therefore investigating, and starting with, the replacement of Cu by Co or Ru.[18–20]

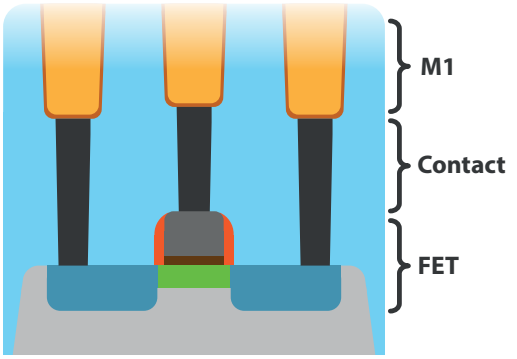

	Past	Present	Future
Channel	Si	Strained Si, SiGe	Ge, GaAs, InGaAs, 1D/2D materials
Gate	Poly-Si	Metal	Advanced metal stacks
Gate oxide	SiO_2	HfO_2	Rare earth oxides, perovskites
Dielectric	SiO_2	Porous SiO_2 & SiOCH	Air gaps
Contact	W	W	Co
Interconnect	Al	Cu	Ru, Co

Figure 1.1 Simplified representation of a field-effect transistor ('FET'), and the first layer metal interconnects ('M1'). Materials which were used in the past, and materials which are currently being used for transistor fabrication are listed, in addition to materials which might be introduced in the near or far future. The list illustrates an increase in the number of employed materials. Examples of 1D and 2D materials being investigated for application as channel in FETs are nanowires, carbon nanotubes, graphene and 2D-transition metal dichalcogenides such as MoS_2 and WS_2. Ferroelectric materials considered for integration in the gate stack include $Pb(Zr_xTi_{1-x})O_3$ and $BaTiO_3$, while potential perovskite high-k gate insulators are doped-HfO_2, $BaHfO_3$ and $SrTiO_3$.[21,22] Gate oxide materials typically have a high dielectric constant ('high-k'), whereas dielectric insulators between contacts and interconnects are 'low-k'.[23,24] Note that the timeline by which future materials might be introduced varies (e.g. air gaps are already being introduced, while 2D materials might be expected in >10 years). This image was inspired by review articles of King *et al.* and Salahuddin *et al.*[10,13] The selection of materials being considered for future FETs was based on a collection of literature reports and serves an illustrative purpose rather than being a comprehensive overview.[18,21–30]

1.2 Transition to bottom-up fabrication

Conventional semiconductor device fabrication relies on subtractive, top-down fabrication schemes using a sequence of deposition, lithography and etch steps, as illustrated in Figure 1.2a.[31] By repeating these processing steps, a multi-layered device structure (i.e. an IC) is build up. The downscaling of device dimensions results however in issues regarding the alignment of features on top of each other, quantified by the 'edge placement error' (EPE).[32,33] The EPE is the mismatch between the intended and actual feature position (see Figure 1.2a), and can lead to decreased device performance or even device failure. For this reason, the semiconductor industry is currently looking for processing technologies that mitigate these issues by employing self-aligned fabrication schemes.[14,34,35] Self-aligned schemes result in features exactly on the desired location, and thereby reduce alignment issues. A relevant example of such self-aligned schemes is area-selective deposition, which allows for bottom-up fabrication by depositing material only on specific areas. Since the deposition is limited to areas where it is required, some of the lithography and etch steps can be eliminated (see Figure 1.2b).[36,37] Area-selective deposition is thus an additive process, rather than subtractive.[38] Since semiconductor devices are approaching the 5-nm scale, area-selective deposition is currently receiving significant interest from the industry.[38,39]

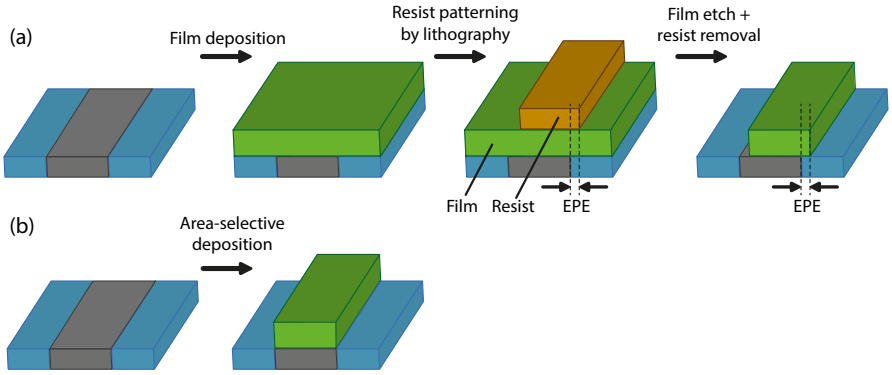

Figure 1.2 Schematics illustrating (a) top-down fabrication using deposition, lithography and etching, and (b) bottom-up fabrication based on area-selective deposition. Misalignment during the lithography step in (a) results in an edge placement error ('EPE'). During area-selective deposition the film preferentially grows on one area of the substrate ('growth area'), while no material is deposited on the other area ('non-growth area'). Note that area-selective deposition is used for specific layers of a device structure, and that other layers are formed by employing the conventional top-down fabrication steps. The structure serving as the starting point for area-selective deposition (here consisting of the two different materials in blue and grey) is thus typically obtained using top-down processing.

1.3 Integration of electronics and photonics

Although developments in integrated electronics have enabled great technological breakthroughs in recent decades, it is believed that the introduction of integrated photonics is required to allow for the growth of data traffic in the 21st century.[7,40] Photonic devices rely on transport of photons instead of electrons and generally demonstrate a higher speed and lower power consumption as compared to electronics.[41] Photonic integrated circuits (PICs) are expected to become an integral part of information and communication technologies.[42–45] In addition, photonics has applications in various other fields, for instance in sensors used in health care and aerospace. In 2009 the European Commission announced photonics as one of its six *Key Enabling Technologies*, meaning it is recognized to be of key value to the society and economy.[46] However, as compared to electronics, the production of integrated photonics is still in its infancy. Nevertheless, the photonics industry is expected to grow significantly in the coming decades, and significant investments are being made for projects ranging from fundamental research to the scale-up of production.[46] Research on photonics has focused in recent years on the integration of multiple photonic devices on a PIC, and on the integration with electronics.[47,48] Figure 1.3 shows a recent example were photonic and electronic components are combined on one single Si microchip.[48]

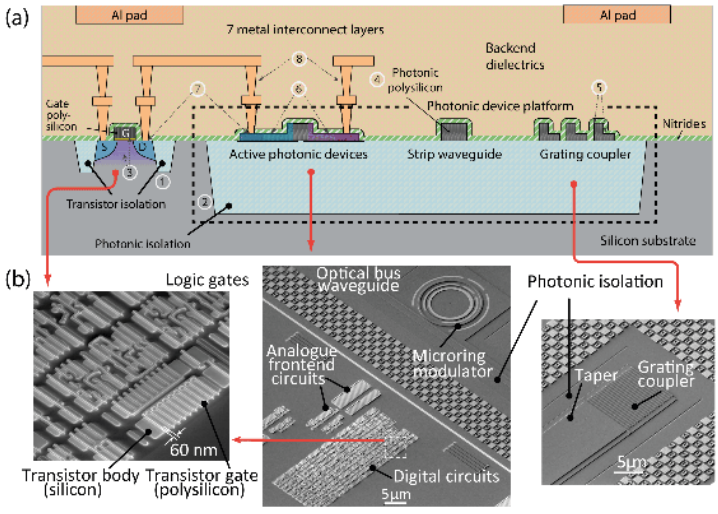

Figure 1.3 (a) Schematic example of electronic and photonic components integrated on a single chip. (b) Scanning electron microscopy images of photonic (i.e. a modulator, a grating coupler and waveguides) and electronic components (i.e. 65-nm node transistors). Polycrystalline Si (polysilicon) serves as the active material in the photonic components and as the gate material in the electronic transistors, while SiO_2 (in blue) was used for isolation. Adapted from Atabaki *et al.*[48]

It can be expected that similar developments will occur in the photonics industry as previously have been observed in the semiconductor industry. For instance, the complexity of PICs will increase significantly, and a transition to high-volume manufacturing will lead to a cost-reduction. Although the scaling of photonic devices is limited by the wavelength of light, a Moore's law for photonics has been proposed in terms of the number of components integrated on a single PIC, which has been increasing steadily in recent years.[49,50] Bringing the field of integrated photonics closer to widespread industrial application will be accompanied by developments in thin film technologies and the use of novel thin film materials.[51]

1.4 Atomic Layer Deposition

Overall, an increasing complexity in terms of thin film materials and processing techniques can be observed within a wide range of application fields, including electronics and photonics. Atomic layer deposition (ALD) is a thin film deposition technique which is playing a significant and expanding role in those trends. This vapor-phase deposition technique relies on the cyclic dosing of precursor (in sub-cycle 'A') and co-reactant chemicals (in sub-cycle 'B'), as is illustrated in Figure 1.4a.[52] These doses are separated by purge steps and result in self-limiting surface reactions. As will be further elaborated in Chapter 2, the precursor generally delivers the main desired element (typically a metal), while the co-reactant results in removal of the precursor ligands, and, if needed, the incorporation of additional elements (e.g. O, N, S, F, ...).[53] By dosing sufficient precursor and co-reactant species to the surface, saturation of the surface reactions is achieved. This self-limiting behavior allows for deposition of uniform and conformal films on large-area and 3D-structured substrates. The technique is characterized by very precise thickness control, with typically less than 0.2 nm of material being deposited per ALD cycle. By combining precursors with different co-reactant chemicals, different additional elements can be incorporated, which enables the deposition of a wide variety of materials, including metals, oxides, nitrides, sulfides, and fluorides.[54] Because ALD results in uniform and pinhole-free films, the technique was introduced in the semiconductor industry around the year 2000 and since then evolved into a key technique in device fabrication.[55] Furthermore, it can be expected that ALD will play an even more significant role in the coming decades, driven by decreasing device dimensions. Notably, the increased use of ALD in the industry will be accompanied by further development of the deposition technique.

1.4.1 Advanced ALD cycles

While the conventional ALD cycle consist of a combination of a precursor and a co-reactant dose in an AB-type ALD cycle (see Figure 1.4a), other variations of ALD cycles are possible. Such *advanced* ALD cycles go beyond standard AB-type cycles and typically rely on the use of more than two chemicals (see Figure 1.4). Advanced ALD cycles are generally more sophisticated and challenging than traditional ALD processes, and offer unique opportunities to extend the possibilities of ALD. For instance, combination of more than two precursor and/or co-reactant chemicals in one ALD cycle (i.e. an ABC-type cycle), or combination of multiple ALD cycles (i.e. a supercycle, see Figure 1.4c) enables the growth of doped, ternary and quaternary materials, with control over the composition.[56] As will be discussed in Chapter 3, advanced ALD cycles can also allow for extension of process parameters such as deposition temperature, and can be used to achieve area-selective deposition. Driven by the increasing requirements of thin film materials, and the introduction of new materials, researchers are more and more investigating advanced ALD cycles.

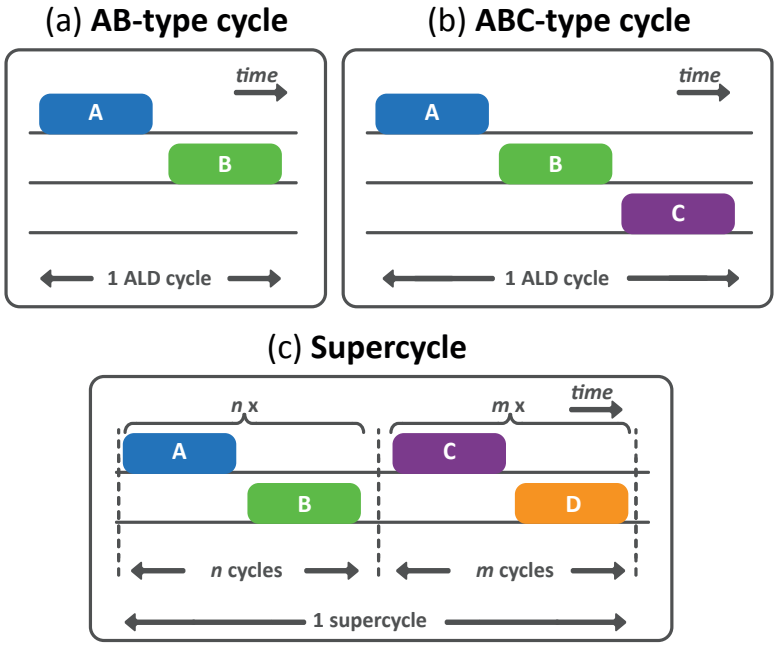

Figure 1.4 (a) Conventional AB-type ALD cycle, relying on sequential dosing of a precursor ('A') and a co-reactant ('B'). (b) ABC-type cycle, where three different chemicals are used. (c) Supercycle consisting of two different ALD cycles. The ABC-type cycle and the supercycle are examples of *advanced* ALD cycles.

1.4.2 ALD: from nanoelectronics to photonics

Thus far, the main driver for ALD has been the semiconductor industry, and ALD is now a critical technology for numerous steps in the fabrication of micro- and nanoelectronics.[55–58] Examples of ALD-deposited films include the high-k metal gate oxide (HfO_2) and the metal electrode (TiN) for fin field-effect transistors (finFETs), the spacer material (e.g. SiO_2) for self-aligned double or multiple patterning, and the word line (W) for 3D NAND flash memory.[54,58] ALD has also proven its potential for a variety of related technologies outside of the IC industry, including displays and Si-photovoltaics.[57,59,60] For instance, Si solar cells can be passivated using ALD of Al_2O_3, resulting in a very low surface recombination.[61,62]

A relatively new application of ALD can be found in the field of photonics, where researchers have investigated ALD for a variety of photonic structures and devices, including waveguides, resonators and modulators, as well as photonic crystals.[63,64] ALD typically results in the reduction of scattering losses due to a decrease in surface roughness, as well as lower surface absorption losses as a consequence of passivation of dangling (i.e. unoccupied) bonds at the surface.[65–68] The reduction of surface roughness was among others reported for Si and Si_3N_4 waveguides.[65,66] The Si and Si_3N_4 were coated with TiO_2 (40 nm) and Al_2O_3 (50 nm) by ALD, respectively, achieving a significant reduction in propagation loss of approximately 90 % in both cases.[65,66] Furthermore, ALD-grown TiO_2 and HfO_2 were employed to tune the dispersion (i.e. the dependence of the refractive index on the wavelength) of Si and Si_3N_4 based waveguides.[67,68] Various other photonic components have also been modified or fabricated using ALD. Recently, ALD was used for the surface passivation of InP nanowires, yielding an improvement of the photoluminescence efficiency by 20%.[69] Guha *et al.* demonstrated a very high quality (Q) factor of 6×10^6 for GaAs disk resonators by depositing 5 nm of Al_2O_3 on top.[70] Furthermore, a grating coupler was created by sandwiching ALD-grown HfO_2, Al_2O_3 or AlN as low index slot material between amorphous Si layers.[71]

Interestingly, ALD supercycles (see Figure 1.4c) have been used to deposit doped materials, multilayers and laminates for photonic waveguides. Karvonen *et al.* fabricated a slot waveguide (i.e. a waveguide were the light is confined in a narrow slot between two high-refractive-index strips) by coating Si strips with a stack of Al_2O_3 and TiO_2.[72] In addition, the deposition of a conformal Ta_2O_5/polyimide multilayer was demonstrated on Si strips, where the nanolaminate is a metamaterial that serves as a slot waveguide.[73] The number of Ta_2O_5 or polyimide ALD cycles in the supercycle can be varied in order to change the thickness of the individual layers and thereby tune the effective refractive index.[73] More recently, a slot waveguide was fabricated by coating Si_3N_4 with Er-doped Al_2O_3 using an ALD

supercycle.[74] In this case, the Er-doped Al_2O_3 acts as an active gain material, of which the Er concentration can be varied by changing the supercycle ratio (i.e. the ratio between Er_2O_3 and Al_2O_3 ALD cycles).[75] Roussey *et al.* fabricated a new type of waveguide called 'strip-loaded horizontal waveguide' by depositing a $TiO_2/SiO_2/TiO_2$ trilayer by ALD and placing a polymer strip on top.[76] In this design, the optical mode is contained in the SiO_2 film, which means that the device benefits from low losses at the interfaces enabled by the high uniformity of ALD.[76]

In addition to an extensive exploration of ALD coating of waveguides, ALD has been performed on top of photonic crystals.[63] 1D Si nanocavities have for example been coated with Al_2O_3, which resulted in an increase in the Q factor of 38 %.[77] The tuning of the optical response of 2D photonic crystals has been reported using TiO_2, HfO_2 and Al_2O_3.[78–81] ALD has also been performed on top of 3D photonic crystals, for instance to cover them with TiO_2, VO_2, Mn-doped ZnS and WS_2, thereby changing their optical characteristics.[82–85] Except for modification of the properties of the photonic crystals, ALD was also carried out in order to replicate their shape, using the crystal as a template. Fabrication of such inverse photonic crystals by infiltrating a template using ALD, followed by removal of the template (e.g. by annealing or etching), has been reported for a variety of ALD materials, including TiO_2, ZnO and the Al_2O_3/SiO_2 alloy mullite.[86–88]

ALD-grown Al_2O_3 thin films have also been used for wafer bonding, which is a technique that can be used to integrate active III-V photonic devices on passive Si-based substrates. InP chips have for instance been bonded onto a Si wafer, by first coating the chips and the wafer with a thin Al_2O_3 adhesion layer (5 nm - 20 nm).[89] Ikku *et al.* formed a low-loss InGaAsP waveguide on a SiO_2/Si wafer after bonding an InGaAsP/InP wafer to the SiO_2/Si wafer using 6 nm Al_2O_3 as adhesion layer on both wafers.[90]

The examples above demonstrate that ALD is a valuable technique for both the modification and the fabrication of photonic structures and devices. Especially the characteristics of low-temperature deposition, reduced surface roughness and good conformality are often mentioned as benefits for the use of ALD.[63,64] Although mostly ALD of binary metal oxides has been explored thus far, other types of materials have also been investigated, including metal sulfides, doped materials and multilayer films, and the use of other material categories (e.g. fluorides as low-index material or metals for connections to electronic devices) can be expected for the future. Finally, to enable further use of ALD for specific applications within the field of photonics, it will be required to extend the toolbox of ALD in terms of materials than can be deposited, as well as the required processing conditions.

1.5 Setting, aim and outline of this thesis

The research described in this thesis was carried out within the *Zwaartekracht* program 'Research Centre for Integrated Nanophotonics', which is funded by the Netherlands Organization for Scientific Research (NWO). The research program is a long-term collaboration between six groups of the Applied Physics and Electrical Engineering departments at the Eindhoven University of Technology, and is aimed at the development of the next-generation photonic integrated circuits and systems, and the corresponding material technologies. The role of the *Plasma and Materials Processing* (PMP) group is to explore and develop nanolayers for application in integrated photonic devices and circuits (PICs) fabricated by the other research groups in the project. These nanolayers are typically deposited by ALD, although other deposition techniques such as chemical vapor deposition (CVD) are also available. The set of available materials is extended by developing novel ALD processes for materials which are potentially relevant for photonic applications.

The broader goal of this thesis is to extend the ALD toolbox, aiming at the application of nanolayers in both integrated photonics and integrated electronics. To this end, ALD processes were developed that allow the growth of new materials by ALD, or enable area-selective ALD and innovative applications of ALD. The investigated ALD processes were based on novel co-reactants and *advanced* ALD cycles. In addition to characterizing the growth behavior and material properties, the aim was to obtain a fundamental understanding of the reaction mechanisms of film growth, such that these insights can be translated to other material systems, and ALD in general.

More specifically, the research focused on three different material systems: aluminum fluoride (AlF_3), cobalt (Co) and ruthenium (Ru). Metal fluorides are important for optical and photonic applications due to their interesting optical properties (i.e. they are highly transparent and have a low refractive index in the range of 1.3 to 1.6), while Co and Ru are currently considered for use as metal interconnect material in electronic circuits (because of superior conductivities as compared to Cu at small dimensions). Firstly, the goal was to investigate whether SF_6 plasma is a suitable co-reactant for ALD. To enable the use of SF_6 plasma for ALD of other metal fluorides, the growth mechanisms of AlF_3 using $Al(CH_3)_3$ and SF_6 plasma were determined. ALD of Co was performed using H_2- and N_2-based plasmas, elucidating the role of the various plasma species. Finally, it was

studied how ALD can be combined with etching in order to achieve area-selective deposition, using Ru as a model system. Here, the objective was to identify design rules and guidelines for an area-selective deposition process which is based on a supercycle of ALD and etch cycles.

This thesis is structured as follows. In Chapter 2, the principles of ALD are explained, followed by a description of the ALD reactor, and the procedure for the development of an ALD process. The three sections of Chapter 2 can be read independently and serve to provide the general background on ALD. Chapter 3 then describes the fundamental roles of the precursor and co-reactant during film growth, and discusses how advanced ALD cycles can be used to fulfill those. In addition, opportunities offered by advanced ALD cycles are discussed, including growth of multiconstituent materials and area-selective ALD. This chapter addresses the extension of the ALD toolbox using advanced ALD cycles on a general level, based on a selection of examples from the literature. Chapter 4 deals with the development of an ALD process for deposition of AlF_3, using SF_6 plasma as a novel co-reactant. In order to help the development of ALD processes for other metal fluorides using SF_6 plasma, the reaction mechanisms of the AlF_3 ALD process are described in Chapter 5. In Chapter 6 the growth of Co by ALD using H_2- and N_2-based plasmas is discussed, and insight into the influence of different co-reactants on the growth and film properties is obtained. Chapter 7 demonstrates that a cycle for Ru ALD can be combined with an etch cycle in a supercycle recipe to obtain area-selective ALD. This advanced ALD cycle allows for achieving area-selective ALD with high selectivity, which is currently one of the main challenges for area-selective deposition. In Chapter 8, the Ru ALD-etch process is investigated further by varying the etch duration and frequency, to provide insights into how an ALD-etch supercycle can be optimized in terms of selectivity and net growth rate. Finally, the main conclusions of this work are summarized in Chapter 9, together with recommendations for further research.

References

[1] Ohring, M., in *Mater. Sci. Thin Film.*, pp. xiii–xv, Academic Press, second edition, ISBN 9780080491783, **2002**.

[2] Wasa, K., Kitabatake, M., and Adachi, H., in *Thin Film Mater. Technol.*, chapter 1, pp. 1–16, William Andrew, New York, **2008**.

[3] Seshan, K., in *Handb. Thin Film Depos. Tech. Process. Technol.*, pp. 19–40, Elsevier Inc., third edition, ISBN 9781437778748, **2012**.

[4] Moore, G., *Electronics* **1965**, 38(8), 114–117.

[5] Antonelli, G. A., Herr, D., and King, S. W., *APL Mater.* **2018**, 6(5), 058001.

[6] IRDS, International Roadmap for Devices and Systems 2017, *Technical report*, **2018**.

[7] Mashanovich, G. Z., *Nature* **2018**, 556(7701), 316–317.

[8] Thylén, L. and Wosinski, L., *Photonics Res.* **2014**, 2(2), 75–81.

[9] IBM Research Zurich, Silicon photonics takes the next step toward a high-bandwidth future, https://www.zurich.ibm.com/news/15/photonics.html, **2015**, [Accessed online: 17-Okt-2019].

[10] Salahuddin, S., Ni, K., and Datta, S., *Nat. Electron.* **2018**, 1(8), 442–450.

[11] Brown, G. A., Zeitzoff, P. M., Bersuker, G., and Huff, H. R., *Mater. Today* **2004**, 7(1), 20–25.

[12] Baklanov, M. R., Adelmann, C., Zhao, L., and De Gendt, S., *ECS J. Solid State Sci. Technol.* **2014**, 4(1), Y1–Y4.

[13] King, S. W., Simka, H., Herr, D., Akinaga, H., and Garner, M., *APL Mater.* **2013**, 1(4), 040701.

[14] Clark, R., Tapily, K., Yu, K. H., Hakamata, T., Consiglio, S., O'Meara, D., *et al.*, *APL Mater.* **2018**, 6(5), 058203.

[15] Tokei, Z., Ciofi, I., Roussel, P., Debacker, P., Raghavan, P., Van Der Veen, M. H., *et al.*, *2016 IEEE Symp. VLSI Technol.* **2016**, pp. 1–2.

[16] Gall, D., *J. Appl. Phys.* **2016**, 119(8), 085101.

[17] Schuegraf, K., Abraham, M. C., Brand, A., Naik, M., and Thakur, R., *IEEE J. Electron Devices Soc.* **2013**, 1(3), 66–75.

[18] Nogami, T., Zhang, X., Kelly, J., Briggs, B., You, H., Patlolla, R., *et al.*, in *Dig. Tech. Pap. - Symp. VLSI Technol.*, **2017** pp. 6–7.

[19] Auth, C., Aliyarukunju, A., Asoro, M., Bergstrom, D., Bhagwat, V., Birdsall, J., *et al.*, in *2017 IEEE Int. Electron Devices Meet.*, **2017** pp. 673–676.

[20] Wen, L. G., Roussel, P., Pedreira, O. V., Briggs, B., Groven, B., Dutta, S., *et al.*, *ACS Appl. Mater. Interfaces* **2016**, 8(39), 26119–26125.

[21] Tu, L., Wang, X., Wang, J., Meng, X., and Chu, J., *Adv. Electron. Mater.* **2018**, 4(11), 1–17.

[22] Kim, Y. M., Park, C., Ha, T., Kim, U., Kim, N., Shin, J., *et al.*, *APL Mater.* **2017**, 5(1), 016104.

[23] Robertson, J. and Wallace, R. M., *Mater. Sci. Eng. R Reports* **2015**, 88, 1–41.
[24] Shamiryan, D., Abell, T., Iacopi, F., and Maex, K., *Mater. Today* **2004**, 7(1), 34–39.
[25] Heyns, M. and Tsai, W., *MRS Bull.* **2011**, 34(07), 485–492.
[26] Wang, F. F., Hu, X. Y., Niu, X. X., Xie, J. Y., Chu, S. S., and Gong, Q. H., *J. Mater. Chem. C* **2018**, 6(5), 924–941.
[27] Robinson, J. A., *APL Mater.* **2018**, 6(5), 058202.
[28] Rakhi, M. and Subodh, G., *Ceram. Int.* **2016**, 42(9), 10886–10891.
[29] Engström, O., Raeissi, B., Hall, S., Buiu, O., Lemme, M. C., Gottlob, H. D., *et al.*, *Solid. State. Electron.* **2007**, 51(4 SPEC. ISS.), 622–626.
[30] Koike, J., Hosseini, M., Hai, H. T., Ando, D., and Sutou, Y., in *IEEE Int. Electron Devices Meet.*, **2017** pp. 725–728.
[31] May, G. S. and Spanos, C. J., in *Fundam. Semicond. Manuf. Process Control*, pp. 1–24, John Wiley & Sons, **2006**.
[32] Mulkens, J., Hanna, M., Wei, H., Vaenkatesan, V., Megens, H., and Slotboom, D., *Proc. SPIE 9422, Extrem. Ultrav. Lithogr. VI* **2015**, 9422(March 2015), 94221Q.
[33] Mulkens, J., Hanna, M., Slachter, B., Tel, W., Kubis, M., Maslow, M., *et al.*, *Proc. SPIE 10145, Metrol. Insp. Process Control Microlithogr. XXXI* **2017**, 10145(March 2017), 1014505.
[34] Juncker, A., Clark, W., Vincent, B., Franke, J.-H., Halder, S., Lazzarino, F., *et al.*, in *Proc. SPIE*, March, **2018** p. 10583.
[35] Mohanty, N., Smith, J., Farrell, R., Huli, L., Pereira, C., Hetzer, D., *et al.*, *SPIE Newsroom* **2017**, pp. 2–4.
[36] Gladfelter, W. L., *Chem. Mater.* **1993**, 5(10), 1372–1388.
[37] Lu, W. and Lieber, C. M., *Nat. Mater.* **2007**, 6(11), 841–850.
[38] Mackus, A. J. M., Merkx, M. J. M., and Kessels, W. M. M., *Chem. Mater.* **2019**, 31(1), 2–12.
[39] Fang, M. and Ho, J. C., *ACS Nano* **2015**, 9(9), 8651–8654.
[40] Sun, C., Wade, M. T., Lee, Y., Orcutt, J. S., Alloatti, L., Georgas, M. S., *et al.*, *Nature* **2015**, 528(7583), 534–538.
[41] Girtan, M., *Mater. Today* **2014**, 17(3), 100–101.
[42] Kish, F. A., in *Device Res. Conf. - Conf. Dig. DRC*, volume August, IEEE, ISBN 9781467381345, **2015** pp. 23–24.
[43] Miller, D. A., *Proc. IEEE* **2009**, 97(7), 1166–1185.
[44] Mohammadhosseini, H. and Heck, M. J., in *MWP 2017 - Int. Top. Meet. Microw. Photonics*, **2017** pp. 1–4.
[45] Matera, F., *Fiber Integr. Opt.* **2017**, 36(1-2), 1–2.
[46] European Technology Platform Photonics21, Jobs and Growth in Europe - Realizing the Potential of Photonics, *Technical Report 643995*, **2017**.

[47] Yamada, K., *Front. Mater.* **2015**, 2(65), 5–6.
[48] Atabaki, A. H., Moazeni, S., Pavanello, F., Gevorgyan, H., Notaros, J., Alloatti, L., *et al.*, *Nature* **2018**, 560(7716), E4.
[49] Thylén, L., He, S., Wosinski, L., and Dai, D., *J. Zhejiang Univ. A* **2006**, 7(12), 1961–1967.
[50] Smit, M., van der Tol, J., and Hill, M., *Laser Photonics Rev.* **2012**, 6(1), 1–13.
[51] Vitiello, M. S. and Razeghi, M., *APL Mater.* **2017**, 5(3), 1–2.
[52] George, S. M., *Chem. Rev.* **2010**, 110(1), 111–131.
[53] Zaera, F., *J. Phys. Chem. Lett.* **2012**, 3(10), 1301–1309.
[54] Knoops, H. C. M., Faraz, T., Arts, K., and Kessels, W. M. M., *J. Vac. Sci. Technol. A* **2019**, 37(3), 030902.
[55] Raaijmakers, I. J., *ECS Trans.* **2011**, 41(2), 3–17.
[56] Mackus, A. J. M., Schneider, J. R., MacIsaac, C., Baker, J. G., and Bent, S. F., *Chem. Mater.* **2019**, 31(4), 1142–1183.
[57] Johnson, R. W., Hultqvist, A., and Bent, S. F., *Mater. Today* **2014**, 17(5), 236–246.
[58] Ritala, M. and Niinistö, J., *ECS Trans.* **2009**, 25(8), 641–652.
[59] van Delft, J., Garcia-Alonso, D., and Kessels, W., *Semicond. Sci. Technol.* **2012**, 27(7), 074002.
[60] Leskelä, M., Mattinen, M., and Ritala, M., *J. Vac. Sci. Technol. B* **2019**, 37(3), 030801.
[61] Hoex, B., Heil, S. B. S., Langereis, E., Van De Banden, M. C. M., and Kessels, W. M. M., *Appl. Phys. Lett.* **2006**, 89(4), 3–6.
[62] Dingemans, G., Seguin, R., Engelhart, P., van den Sanden, M. C. M., and Kessels, W. M. M., *Phys. Status Solidi RRL* **2010**, 4(1), 10–12.
[63] Saleem, M. R., Ali, R., Khan, M. B., Honkanen, S., and Turunen, J., *Front. Mater.* **2014**, 1(18), 1–15.
[64] Im, H., Wittenberg, N. J., Lindquist, N. C., and Oh, S. H., *J. Mater. Res.* **2012**, 27(4), 663–671.
[65] Alasaarela, T., Korn, D., Alloatti, L., Säynätjoki, A., Tervonen, A., Palmer, R., *et al.*, *Opt. Express* **2011**, 19(12), 11529–11538.
[66] Khanna, A., Subramanian, A. Z., Häyrinen, M., Selvaraja, S., Verheyen, P., Van Thourhout, D., *et al.*, *Opt. Express* **2014**, 22(5), 5684–5692.
[67] Erdmanis, M., Karvonen, L., Saleem, M. R., Ruoho, M., Pale, V., Tervonen, A., *et al.*, *J. Light. Technol.* **2012**, 30(15), 2488–2493.
[68] Riemensberger, J., Hartinger, K., Herr, T., Brasch, V., Holzwarth, R., and Kippenberg, T. J., *Opt. Express* **2012**, 20(25), 27661.
[69] Black, L. E., Cavalli, A., Verheijen, M. A., Haverkort, J. E., Bakkers, E. P., and Kessels, W. M., *Nano Lett.* **2017**, 17(10), 6287–6294.
[70] Guha, B., Marsault, F., Cadiz, F., Morgenroth, L., Ulin, V., Berkovitz, V., *et al.*,

Optica **2017**, 4(2), 218.
[71] Naiini, M. M., Henkel, C., Malm, G. B., and Östling, M., *Solid. State. Electron.* **2012**, 74, 58–63.
[72] Karvonen, L., Saynatjoki, A., Chen, Y., Tu, X., Liow, T. Y., Hiltunen, J., *et al.*, *IEEE Photonics Technol. Lett.* **2012**, 24(22), 2074–2076.
[73] Autere, A., Karvonen, L., Säynätjoki, A., Roussey, M., Färm, E., Kemell, M., *et al.*, *Opt. Express* **2015**, 23(21), 26940–26951.
[74] Rönn, J., Zhang, W., Autere, A., Leroux, X., Pakarinen, L., Alonso-Ramos, C., *et al.*, *Nat. Commun.* **2019**, 10(1), 1–9.
[75] Rönn, J., Karvonen, L., Kauppinen, C., Perros, A. P., Peyghambarian, N., Lipsanen, H., *et al.*, *ACS Photonics* **2016**, 3(11), 2040–2048.
[76] Roussey, M., Ahmadi, L., Pélisset, S., Häyrinen, M., Bera, A., Kontturi, V., *et al.*, *Opt. Lett.* **2017**, 42(2), 211–214.
[77] Gehl, M., Gibson, R., Hendrickson, J., Homyk, A., Säynätjoki, A., Alasaarela, T., *et al.*, *J. Opt. Soc. Am. B* **2012**, 29(2), 55–59.
[78] Stenberg, P., Roussey, M., Ryczkowski, P., Genty, G., Honkanen, S., and Kuittinen, M., *Opt. Express* **2013**, 21(20), 24154–24162.
[79] Graugnard, E., Gaillot, D. P., Dunham, S. N., Neff, C. W., Yamashita, T., and Summers, C. J., *Appl. Phys. Lett.* **2006**, 89, 181108.
[80] Yang, X., Chen, C. J., Husko, C. A., and Wong, C. W., *Appl. Phys. Lett.* **2007**, 91, 161114.
[81] Kiravittaya, S., Lee, H. S., Balet, L., Li, L. H., Francardi, M., Gerardino, A., *et al.*, *J. Appl. Phys.* **2011**, 109, 053115.
[82] King, J. S., Heineman, D., Graugnard, E., and Summers, C. J., *Appl. Surf. Sci.* **2005**, 244(1-4), 511–516.
[83] Sechrist, Z. A., Schwartz, B. T., Lee, J. H., McCormick, J. A., Piestun, R., Park, W., *et al.*, *Chem. Mater.* **2006**, 18(15), 3562–3570.
[84] Povey, I. M., Bardosova, M., Chalvet, F., Pemble, M. E., and Yates, H. M., *Surf. Coatings Technol.* **2007**, 201(22), 9345–9348.
[85] Chen, C. T., Pedrini, J., Gaulding, E. A., Kastl, C., Calafiore, G., Dhuey, S., *et al.*, *Sci. Rep.* **2019**, 9(1), 1–9.
[86] King, J. S., Graugnard, E., Roche, O. M., Sharp, D. N., Scrimgeour, J., Denning, R. G., *et al.*, *Adv. Mater.* **2006**, 18(12), 1561–1565.
[87] Scharrer, M., Wu, X., Yamilov, A., Cao, H., and Chang, R. P., *Appl. Phys. Lett.* **2005**, 86(15), 1–3.
[88] Furlan, K. P., Larsson, E., Diaz, A., Holler, M., Krekeler, T., Ritter, M., *et al.*, *Appl. Mater. Today* **2018**, 13, 359–369.
[89] Anantha, P. and Tan, C. S., *ECS J. Solid State Sci. Technol.* **2014**, 3(4), 43–47.
[90] Ikku, Y., Yokoyama, M., Iida, R., Sugiyama, M., Nakano, Y., Takenaka, M., *et al.*, *Conf. Proc. - Int. Conf. Indium Phosphide Relat. Mater.* **2011**, pp. 1–4.

2 Atomic Layer Deposition

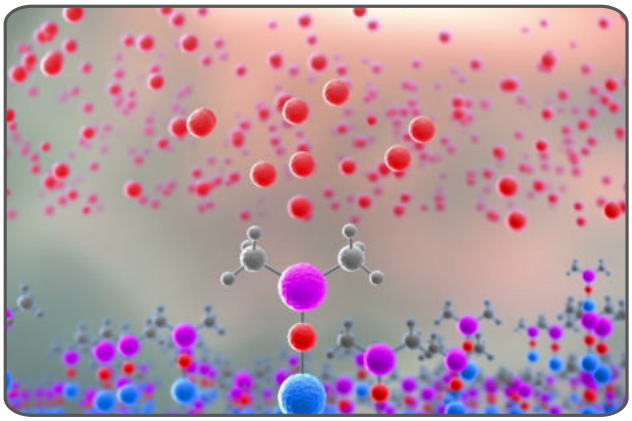

This chapter is devoted to atomic layer deposition (ALD), and serves to familiarize the reader with the basics of ALD. First, the working principles and characteristics of ALD are discussed. The experimental reactor that was used for the majority of the experiments is then described, together with typical experimental conditions. Finally, a procedure for developing and characterizing an ALD process is discussed. This procedure is comprised of ten steps, serving as a guideline when setting up a novel ALD process.

2.1 Principles of ALD

Atomic layer deposition is a surface-controlled thin film deposition technique that can enable ultimate control over the film thickness, uniformity on large-area substrates and conformality on 3D (nano)structures.[1–5] A standard ALD cycle consists at least two sub-cycles, containing a precursor dose step and a co-reactant exposure step, separated by purge or pump steps (see Figure 2.1). In principle, the same amount of material is deposited in each cycle, due to the self-limiting nature of the surface reactions (see below). By carrying out a certain number of ALD cycles, the targeted film thickness can be obtained. As will be discussed in Chapter 3, ALD cycles can be more complex and can rely on the use of more than just two chemicals.

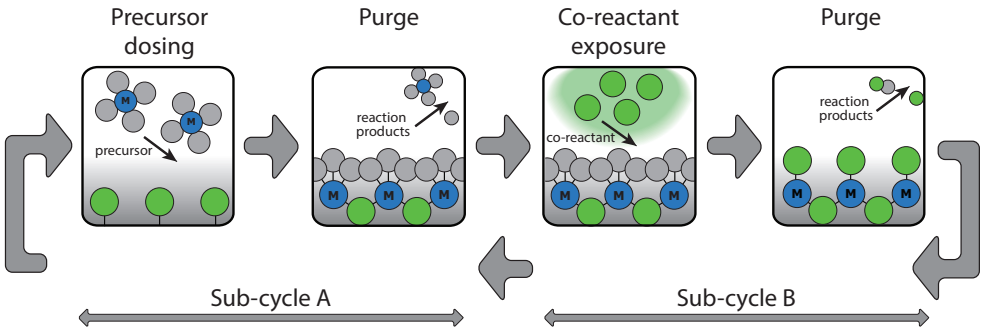

Figure 2.1 Schematic illustration of a typical AB-type ALD cycle consisting of two sub-cycles for the growth of a binary material. Sequential precursor ('A') and co-reactant ('B') doses are separated by purge or pump steps, leading to self-limiting surface reactions. Precursor ligands are colored grey and are first partly eliminated in the reaction with the surface, before the remainder is removed by the co-reactant. 'M' indicates the metal atom (in blue), which can for instance be bound to oxygen or nitrogen atoms (in green), to form a metal oxide or metal nitride, respectively. The formed reaction products are evacuated from the reactor chamber in purge steps.

An ALD cycle generally starts with dosing a precursor which contains the main element to be incorporated in the film. During this dosing step, the precursor reacts with the surface groups (e.g. OH), typically leading to elimination of a part of the precursor ligands, while the remainder of the ligands (or fragments thereof) stays on the surface. The formed reaction products contain (fragments of) the precursor ligands and are pumped away. After dosing sufficient precursor, all reactive surface groups are consumed. This means that all available surface sites are occupied, and the surface is terminated with ligands that are unreactive towards the precursor. Dosing more precursor therefore does not lead to addi-

tional precursor adsorption, hence the reaction is self-limiting. After saturation has been reached, the remaining reaction products are evacuated from the reaction chamber by performing a purge and/or pump step. In the following sub-cycle, the co-reactant interacts with the precursor ligands left after the precursor dosing, resulting in their removal. The formed reaction products are again pumped away. If a binary material (e.g. metal oxide or nitride) is desired, the co-reactant typically also results in the incorporation of an additional element. After exposing the surface sufficiently long to the co-reactant, all precursor ligands are removed, and the formed surface groups are not reactive towards the co-reactant. Similar to during the precursor sub-cycle, the reactions in the co-reactant sub-cycle are self-limiting. It is noted that in some literature different terminology is used for the precursor and co-reactant (e.g. 'metal precursor' and 'non-metal precursor', 'precursor' and 'reagent', or 'reactant A' and 'reactant B').[6]

A distinction can be made between 'thermal ALD' and 'plasma ALD' (also called 'plasma-assisted ALD', or 'plasma-enhanced ALD'. In a thermal process, a co-reactant chemical is dosed as a gas, while a plasma is used as co-reactant for plasma ALD. For instance, Al_2O_3 can be grown using H_2O or O_3 in thermal processes, or using O_2 plasma. As compared to thermal ALD, plasma ALD can offer the benefit of a higher growth rate at low temperatures and lower impurity incorporation, due to the additional reactivity of the plasma species.[7,8] Furthermore, tuning of the plasma properties such as pressure and power can allow for tuning of the obtained material properties.

2.1.1 Merits of ALD

Due to the self-limiting nature of the surface reactions during ALD, a fixed amount of material (typically less than 0.2 nm) is deposited per cycle. The technique therefore gives a very precise control over the film thickness. Moreover, by ensuring that saturation occurs everywhere on the sample, ALD allows for deposition of films with high uniformity on large-area substrates and conformality on 3D-structures. These three key characteristics are illustrated in Figure 2.2, and make ALD a technique which is highly attractive for application in the fabrication of semiconductor devices, where complex 3D structures require coatings with films of thicknesses in the nanometer regime.[9] Furthermore, in other technologies the application of ALD has also proven to be highly relevant, for instance in photovoltaics, in high-surface-area catalysts, and in 3D structured batteries.[10]

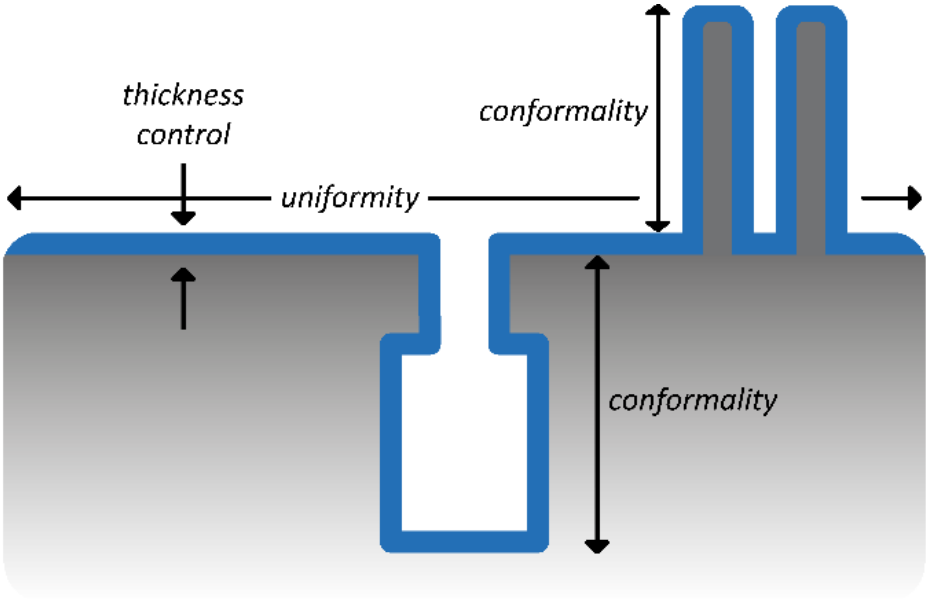

Figure 2.2 The key merits of ALD: thickness control, uniformity and conformality. The precise thickness control of ALD is obtained by tuning the number of ALD cycles, since the same amount of material (typically less than 0.2 nm) is deposited each cycle. High uniformity means that there is little variation in thickness across the sample, while conformality is the ability to coat 3D structures with material of the same thickness along the structure.

Another benefit of ALD is that a wide variety of materials can be deposited using ALD, ranging from metals, oxides, and nitrides to sulfides and fluorides. In addition to elemental and binary films, ALD can also be used to deposit ternary or quaternary materials, as will be addressed in Chapter 3. By combining a specific precursor with different co-reactants, various types of materials can be grown, as is illustrated in Figure 2.3. For instance, trimethylaluminum (TMA, $Al(CH_3)_3$) can be used to deposit an oxide, a nitride, or a fluoride, by combining it with H_2O, NH_3, or HF as co-reactant, respectively.[2,11–13] Several review articles published in the literature and book chapters provide extensive overviews of the materials that have been grown by ALD.[2,4,6,8,14]

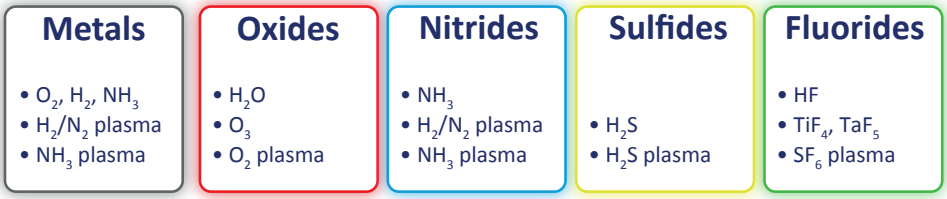

Figure 2.3 Categories of materials commonly deposited by ALD and corresponding co-reactants that are frequently used.[14] In addition to the materials listed, ALD is employed to grow other types of materials, including carbides, phosphides, phosphates, and tellurides, although they are reported less often in the literature.[15–19]

2.1.2 Precursors and co-reactants

The development of an ALD process starts with the selection of the precursor and the co-reactant. The selected chemicals need to meet certain requirements to be suitable for the use in an ALD process. Most importantly, they should demonstrate a high volatility and reactivity (see also Section 2.3).[14,20] Some examples of precursors and co-reactants employed for ALD are discussed below, together with considerations for use.

Precursors

As mentioned before, the precursor molecule serves to deliver the main element to the surface. In most cases the main element is a metal, such as Al or Pt, but it can also be a semimetal or metalloid (e.g. Si or B). ALD precursors are generally coordination complexes consisting of a central metal, surrounded by organic or inorganic ligands. The chemical properties of a precursor molecule such as volatility and thermal stability are largely determined by the ligands. A wide variety of precursor ligands exists, and common ligands are based on halides (Cl, F), alkyls (CH_3, C_2H_5), carbonyl (CO), alkoxides (OC_xH_y) and cyclopentadienyl (Cp, C_5H_5) groups.[2,14] Figure 2.4 shows an example of each of these categories.

Halide-based (Cl, F) precursors are traditionally used in the industry, since they are low-cost and stable, although organometallic or metal-organic compounds are also becoming more employed.[14] For organometallic precursors, the stability is largely determined by the strength of the metal-carbon (M-C) bond. For instance, metal alkyls and metal carbonyls generally have relatively low bond energies, while the Cp ligand results in a stronger M-C bond. Metal-organic precursors (lacking a direct M-C bond) such as alkoxides and alkylamides (e.g. with $N(CH_3)_2$ ligands, not shown in Figure 2.4) are typically more stable than alkyls and carbonyls.

Finally it is noted that homoleptic, symmetric precursors (i.e. with only one type of ligand) generally demonstrate a low volatility, while heteroleptic precursors are more volatile.[14]

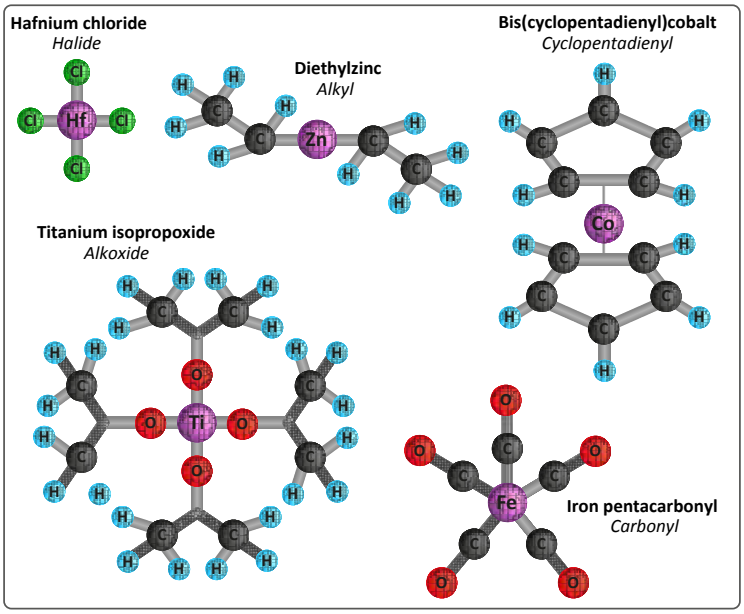

Figure 2.4 Examples of precursors based on ligands commonly used for ALD. Bis(cyclopentadienyl)cobalt is also known as cobaltocene and abbreviated as $CoCp_2$, while diethylzinc and titanium isopropoxide are usually abbreviated as DEZ and TTIP, respectively. The text in italic indicates the type of ligand. Note that the molecules are not drawn to scale. Based on Ref. 14

.

Co-reactants

Although the development and selection of precursors generally receives most attention in the ALD literature, the choice of co-reactant is equally important. Not only does the co-reactant to a large extent determine the composition of the deposited film, together with the precursor it also influences the conditions (e.g. deposition temperature) that can be used for the process. A wide variety of co-reactants has been reported for ALD. In Figure 2.5 some examples of typical co-reactants are shown. ALD researchers are increasingly investigating novel co-reactants, and the list of employed co-reactants keeps increasing. Examples of less-common co-reactant chemicals include hydrazine, disilane, formic acid, 1-propanol, propanethiol, and sulphur hexafluoride (see Figure 2.5).[15,21–24]

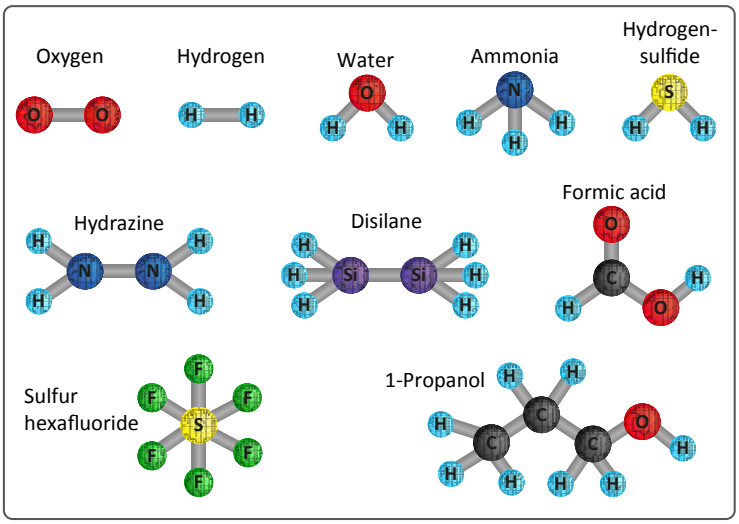

Figure 2.5 Different examples of co-reactants used for ALD. O_2, H_2, H_2O, NH_3 and H_2S have historically been widely used for ALD. Note that the molecules are not drawn to scale.

Selection of an appropriate co-reactant can be difficult for ALD of challenging materials such as fluorides and metals. The use of an alternative co-reactant can enable deposition of a new material by ALD, or can allow for the widening of process parameters such as deposition temperature. For instance, Golrokhi *et al.* demonstrated that the use of tertiary butyl hydrazine (TBH, $C_4H_{12}N_2$) as co-reactant for Ag ALD allowed for a significantly larger temperature window than for a earlier reported Ag ALD process using 1-propanol as co-reactant (using the same precursor).[25,26] The ALD process for AlF_3 using SF_6 plasma (Chapters 4 and 5) provides another example of a novel co-reactant. Thus far ALD of metal fluorides was less straightforward due to limited availability of suitable co-reactants.[27]

2.2 ALD Reactor

The majority of the experiments discussed in this dissertation were performed in a home-built ALD reactor. The studies on Co and Ru ALD were done using this reactor, while the AlF_3 depositions were performed in a commercial tool from Oxford Instruments, the FlexAL.[28] Both reactors are similar in design and working principles, and are equipped with a similar pump system and the same type of plasma source. A significant difference is nevertheless that the FlexAL reactor is equipped with a loadlock to position samples on the substrate table automatically, whereas the home-built reactor is not. Since apart from this aspect the reactors are very similar, only the home-built reactor will be described here.

A photograph and a schematic of the home-built reactor are shown in Figure 2.6. The reactor consists of a vacuum vessel connected to a rotary vane prepump and a turbomolecular pump, allowing for a base pressure of $\sim 10^{-6}$ Torr. The reactor is an open-load system, meaning that it is vented to atmospheric pressure each time a sample is loaded. The pressure in the reactor chamber is monitored with pressure gauges. The reactor wall is heated using heating wires wrapped around the vacuum vessel, allowing for wall temperatures up to ~120 °C.

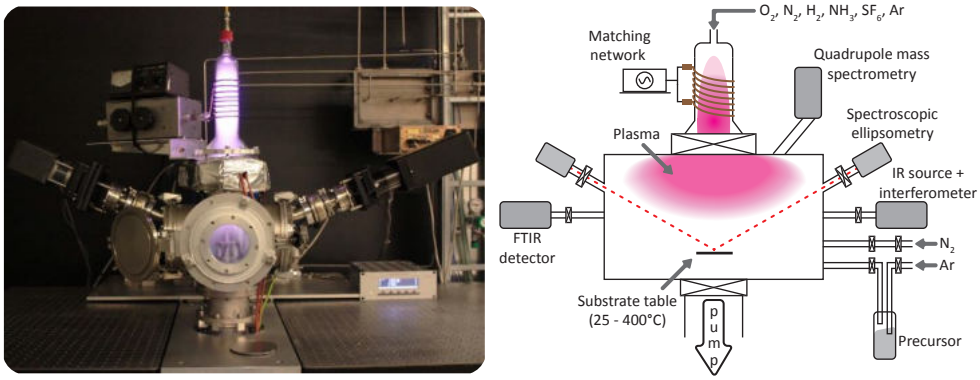

Figure 2.6 Home-built ALD reactor used for the majority of the experiments. The reactor consists of a vacuum chamber connected to a prepump and a turbomolecular pump (not shown here). The precursors are contained in a stainless steel canisters, and Ar can be used as carrier or purge gas. An inductively coupled plasma source is installed above the substrate table, through which several gases can be dosed in both thermal and plasma ALD processes. A matching box is connected to the coil around the plasma tube for impedance matching. Furthermore, several *in situ* diagnostics are mounted on the reactor chamber, i.e. quadrupole mass spectrometry (QMS), spectroscopic ellipsometry (SE), and Fourier transform infrared spectroscopy (FTIR).

Precursor chemicals are stored in stainless steel canisters, which can be heated (up to 120 °C) to increase the vapor pressure if necessary. Precursors are dosed to the reactor through a small inlet (~4 mm diameter), using open-close gas valves. Two types of valves are installed on the reactor, a fast 'ALD' valve, with an accuracy up to ~10 ms, which is used for precursor doses up to 100 ms, and a 'normal' dose valve, used for longer doses. Depending on the vapor pressure of the precursor, it can be delivered to the reactor chamber by different methods: vapor drawn; by flowing an inert carrier gas such as Ar or N_2 over the precursor ('carrier gas assisted'); or by flowing a carrier gas through the precursor ('bubbling'). The precursor delivery lines are typically heated (between 30 °C and 120 °C) in order to prevent condensation of precursor and blockage of the line.

An inductively coupled plasma (ICP) source is installed on top of the reactor chamber, which is used for the co-reactant exposures during plasma ALD (Chapters 4 to 6), O_2 plasma etch steps for area-selective ALD of Ru (Chapters 7 and 8), as well as pretreatments of the samples prior to deposition. The ICP source consists of a dielectric quartz tube, surrounded by a copper coil. Through electromagnetic induction the electrons in the plasma gas are heated using the coil in order to generate and sustain a plasma. Furthermore, a matching box is installed, to match the impedance of the power source to the impedance of the plasma. The plasma source is operated at a radiofrequency (rf) of 13.56 MHz (13.553 - 13.567 MHz range), which is one of the frequency bands available for industrial, scientific and medical purposes ('ISM band').[29] The required plasma power typically scales with the surface area of the substrate table. A power of 100 W is normally used on the home-built reactor (which has a table with a 4 inch diameter), although in general, powers vary between 0 W and 600 W when employing ICP plasmas for ALD.[7,30] Co-reactant gases are delivered to the reactor chamber through the plasma source and the gas flow is controlled with the use of needles valves. Typical pressures during co-reactant exposures are in the order of 10 mTorr. Source gases which can be dosed through the plasma source are O_2, N_2, H_2, NH_3, SF_6, Ar, and mixtures thereof. H_2O is dosed from a stainless steel canister if needed for a thermal metal oxide ALD process, similar to dosing a precursor. All source gases fed through the top of the plasma source can also be used for thermal processes. To protect the plasma source from deposition inside the tube, a gate valve is installed between the chamber and the source, which is usually closed during precursor dosing.

The substrate can be heated between room temperature and 450 °C. Two different types of table heating were used. The Co work was carried out with a heating coil mounted underneath the table. A thermocouple was fed through the back flange of the reactor and installed in the side of the table. This heating mechanism is affected by changes in reactor pressure, since both the thermocouple and the heating coil are in vacuum when the reactor is pumped down. At low pressure, the thermal contact between the heating coil and the table, and between the table and the thermocouple is reduced as compared to atmospheric pressure. This reduced thermal contact can cause temperature fluctuations which need time to stabilize. For this reason, the Ru work was performed using a substrate table containing heating rods (instead of coils) and two thermocouples, installed inside the substrate table, which are left at atmospheric pressure at all time. The two thermocouples are installed at the center and the edge of the table, such that the temperature homogeneity can be monitored and controlled.

Before starting a set of experiments, the reactor walls are typically coated ('conditioned'). This is done by first carrying out a number of ALD cycles (500 - 1000) for Al_2O_3, followed by a number of ALD cycles for the material of interest. Furthermore, material deposited on the reactor walls is removed regularly (approximately once a year) by means of sand blasting, since flaking of the material on the walls occurs after performing many depositions.

To allow for the use of *in situ* diagnostics, several ports and valves are installed on the side of the reactor chamber (see Figure 2.6). Spectroscopic ellipsometry (SE) is used to monitor the development of the film thickness and optical properties as a function of ALD cycles. The light with wavelengths of 245 nm - 1000 nm is directed through quartz windows, which are protected by gate valves during film deposition. To allow for an SE measurements, the recipe is interrupted for a short period of time (typically 40 s), and the gate valves are opened. SE serves as a powerful tool during the development of an ALD process, and was used for the work described in Chapters 4 to 8. The light source and detector for SE are installed at an angle of $\sim$70 $^\circ$ with respect to the substrate normal, which is close to the Brewster angle of Si. Optical emission spectroscopy can be performed by mounting a optical fiber horizontally to the side of the transparent quartz tube of the plasma source. This technique allows for identification of excited species in the plasma, and was employed to study the SF_6 plasma and the H_2- and N_2-based plasmas used for AlF_3 (Chapters 4 and 5) and Co ALD (Chapter 6), respectively. In addition, an infrared light source, Fourier transform infrared (FTIR) interferometer and detector can be connected to the reactor for identification of gas-phase reaction products or surface species (see Figure 2.6). The IR light travels parallel to the substrate table, through KBr windows also protected by gate valves. A manipulator can be used to mount the sample and align it to the light source. Surface IR spectroscopy was employed for studying the reaction mechanism of AlF_3 ALD, as is described in Chapter 5. Finally, a quadrupole mass spectrometer (QMS) detector is mounted vertically to the side of the reactor chamber to identify gas phase reaction products, such as done in Chapters 5 and 6.

2.3 ALD Process Development*

Although the principle of ALD appears to be relatively simple, developing an ALD process is not necessarily a trivial task and it requires careful attention.[6] Here, steps are suggested and described to successfully set up an ALD process. Although the steps are roughly ordered chronologically, the preferred order will depend on the process, while repetition of some steps might also be needed at a later stage.

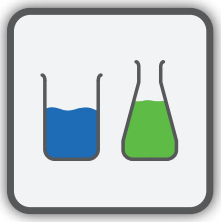

1. Precursor and co-reactant selection

Before setting up an ALD process, a suitable combination of precursor and co-reactant has to be decided on. Most importantly, the precursor and co-reactant molecules should consist of the appropriate elements, to obtain a material of the desired composition. In addition, they need to be reactive towards the surface groups present after the preceding sub-cycle, and in turn result in reactive surface groups after dosing.[14] Moreover, volatility, thermal stability and reactivity need to be sufficiently high.[20] Other requirements include availability and safety of the chemicals. Furthermore, reactor constraints and the application of the ALD film have to be considered, since they can limit the choice of possible chemicals. In addition to selecting the precursor it has to be determined how the precursor will be delivered to the chamber: vapor drawn, carrier gas assisted (i.e. carrier gas flowing over the precursor), bubbling (i.e. carrier gas flowing through the precursor), etc.

2. Chemical composition

Soon after deposition of the first ALD film, it is valuable to check if the grown material consists of the intended elements. Common ways to investigate the chemical composition are X-ray photoelectron spectroscopy (XPS) and Rutherford backscattering spectroscopy (RBS), although XPS is typically more readily available. In case the material should be conductive, a simple four-point probe conductivity measurement can tell if the material is of high purity. Furthermore, a quick assessment of the refractive index can also indicate whether the desired material is obtained. If the deposited material is very different from the expectation, it might be good to reconsider Step 1, since proceeding can be a waste of time. However, in many cases, optimization of the deposition temperature or dosing and purge times can lead to improvement of the material composition. It is important to realize that the chemical composition will determine the final material properties.

* This section appeared online as a blog post on AtomicLimits.com.

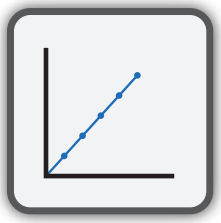

3. Thickness control

An important characteristic of ALD is the deposition of the same amount of material in each cycle, allowing for ultimate thickness control.[31] To confirm this, the thickness or material increase is to be determined per cycle, which is called the growth per cycle (GPC). Determining the GPC can be done both in situ, by following the material increase during deposition, as well as ex situ, by depositing multiple samples with varying number of cycles. Typically, the film thickness is measured (e.g. by spectroscopic ellipsometry), although alternative ways to check for linear growth are by determining the number of deposited atoms (e.g. by Rutherford backscattering spectroscopy) or deposited mass (e.g. by a quartz-crystal microbalance). Figure 2.7 shows a typical example of the film thickness increasing linearly with the number of ALD cycles. Note that the initial growth on the substrate might occur differently than at a later stage, as will be discussed in Step 9. For this reason the focus should lie on relatively thick films, with thicknesses over ~10 nm.

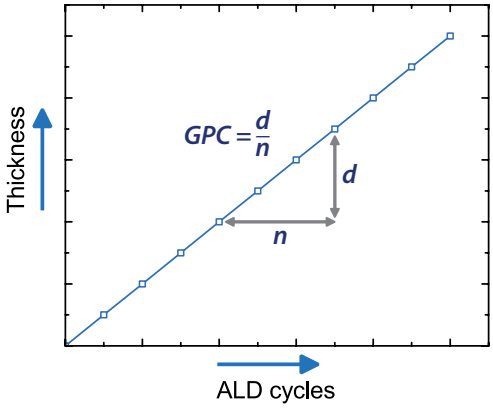

Figure 2.7 Typical example showing the film thickness as a function of number of ALD cycles, illustrating the linear growth behavior which is typical for ALD. The growth per cycle (GPC) can be defined as the slope of the thickness as a function of cycles. In case the number of deposited atoms or the mass is measured as function of cycles, the GPC is given in terms of atoms per unit area or grams per unit area deposited per cycle.

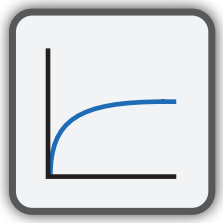

4. Saturation

To confirm self-limiting growth, one of the key characteristics of ALD, the growth per cycle (GPC) has to be determined as a function of dosing and purge times. In the case of a standard AB-type (i.e. two-step) process, the precursor dosing time, precursor purge time, the co-reactant exposure time and co-reactant purge time need to be optimized. This is done by choosing a relatively long time for three of the four times and keeping those constant, while varying the fourth. This needs to be done for every step and, logically, the first step would be to confirm saturation of the precursor dosing time (see Figure 2.8a). After this the saturation of the other dosing times can be investigated, and perhaps the whole procedure has to be reiterated with slightly different dosing and purge times based on the findings.

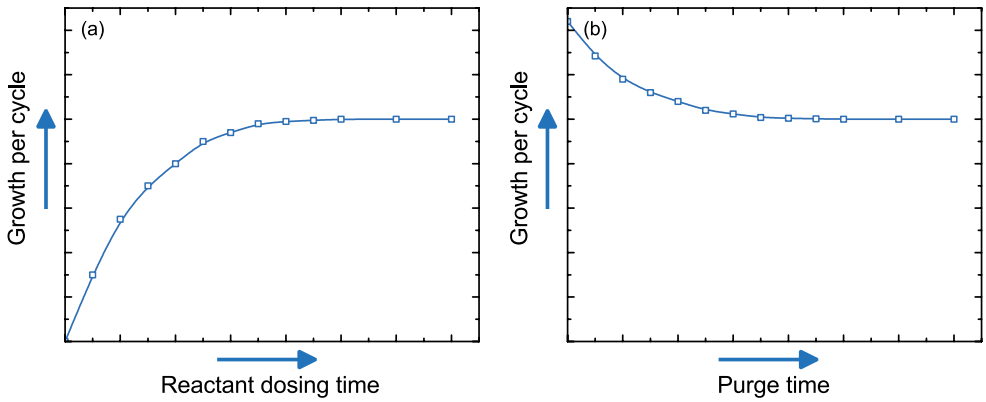

Figure 2.8 Idealized growth per cycle (GPC) as a function of (a) reactant (precursor or co-reactant) dosing time and (b) purge time, illustrating the self-limiting ALD behavior. After saturation is reached, dosing additional reactant, or prolonging the purge time does not lead to a change in GPC. Note that it is important to include a measurement for the data point corresponding to 0 s precursor (or co-reactant) dosing time. When purge times are too short, parasitic CVD can occur, leading to a higher GPC.

Ideally, a clear plateau is observed when investigating saturation, meaning that the GPC does not increase or decrease when more precursor/co-reactant is dosed, or the purge time is extended.[31] Certain phenomena can however cause deviation, such as precursor condensation and precursor decomposition in the case of the precursor saturation curve. In addition, too short co-reactant dosing times can cause impurity incorporation, while too short purge times (see Figure 2.8b) can lead to a parasitic CVD component (i.e. reaction of the precursor and co-reactant

molecules in the gas phase or at the surface), which can impact conformal and uniform deposition. Too long dosing and purge times, on the other hand, can significantly slow down the experiment, or in the case of industrial application, fabrication time. It can also be insightful to perform experiments where only the precursor or co-reactant is dosed, to see if this leads to film deposition or modification of the substrate. Furthermore, saturation should also be confirmed at other process conditions, such as different table temperatures, as will be addressed later.

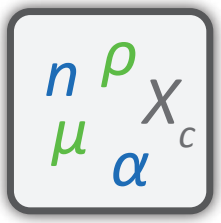

5. Material properties

Apart from the desired chemical composition, several other material properties are highly important. Depending on the application of the ALD films, it can be of interest to check the following: optical properties (refractive index n, absorption coefficient α), electrical properties (resistivity ρ, carrier density N_e and mobility μ), film and surface morphology (roughness, crystallinity X_c), et cetera. Note that the material properties are strongly linked to the chemical composition of the film, which should be investigated in detail first, and that tuning of the chemical composition can enable different material properties.

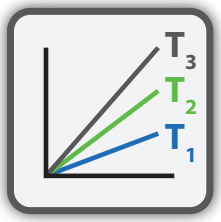

6. Temperature dependence

Varying the deposition temperature can have a significant effect on both the growth behavior and the material properties. For this reason, it is advised to deposit films over a range of substrate temperatures, for example between 50 °C and 350 °C. ALD researchers often speak about an ALD window, i.e. a region where the GPC is (nearly) constant, allowing for reliable and repeatable results despite slight temperature variations (see Figure 2.9).[32] However, this constant GPC is not a necessity for an ALD process, and it is mostly important that saturation behavior is found for all temperatures. Effects such as precursor condensation (at low temperature) and precursor decomposition (at high temperature) can namely become visible by verifying saturation at various temperatures. While a constant GPC is a desirable feature, numerous reports actually exist of ALD processes that demonstrate a temperature dependent GPC, but do show saturating ALD behavior over a wide temperature range (e.g. Al_2O_3 and AlF_3 using $Al(CH_3)_3$ and H_2O or HF).[2,13]

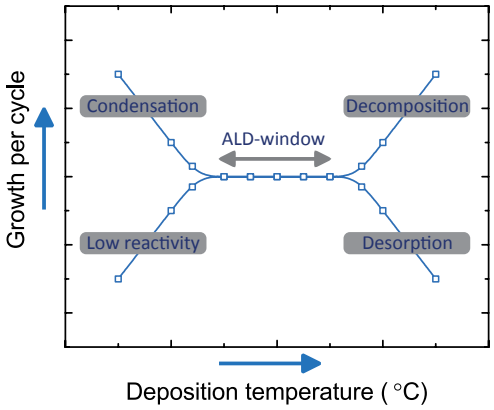

Figure 2.9 Growth per cycle (GPC) as a function of deposition temperature, showing the idealized ALD window. In addition, precursor related phenomena which can occur at high or low temperature are indicated.

It should be noted that the actual temperature of the sample can be significantly lower than the set temperature of the substrate table, especially when working with a warm (instead of hot) wall reactor at high vacuum. This difference in temperature can be due to the reduced thermal contact between the table and the sample, which is pressure dependent.

7. Uniformity

Another important merit of ALD is the uniformity of the film over large area substrates.[33] Often, saturation is verified using coupon samples at the center of the substrate table, which does not mean that precursor or co-reactant dosing is sufficient everywhere. Moreover, non-uniformity is generally a clearer signal of a CVD component than obtained through saturation curves. Hence, a good uniformity is evidence that the process is a well-behaving ALD process. Therefore, it is a recommended that a film is deposited on the largest substrate that fits in the ALD reactor. Most importantly, the thickness variation can easily be determined, either manually, or using an automated mapping stage. However, certain material properties such as composition and resistivity can also be important with respect to uniformity. It might for example be that the thickness uniformity of the deposited film is good, while the resistivity of the film varies significantly over the substrate.

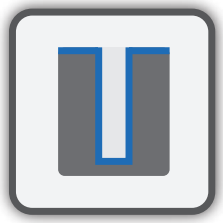

8. Conformality

Although often disregarded during ALD process development, the conformality of the ALD film should be taken into account. Conformality is the ability to conformally deposit a film on 3D structures, i.e. with (ideally) no variation in thickness along the structure.[34] Instead of the conventional planar coupons, specific samples are required to assess the conformality, which contain trenches or vias. A way to quantify the conformality is to deposit in a vertical trench or via with a certain aspect ratio (AR), and, after preparation of a cross-section, calculate the ratio between the thickness at different locations (see Figure 2.10). Another approach is to use a specifically designed structure with a lateral via, such as Pillar Hall, allowing for assessment of the thickness profile without the need of a cross-section.[35,36] In addition to conformality in terms of film thickness, variations in material properties along the 3D structure can also be significant.

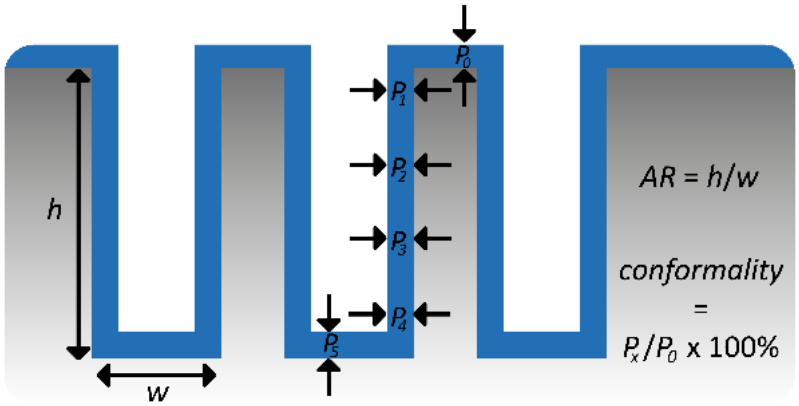

Figure 2.10 Schematic explaining conformality, which can be defined as the film thicknesses at different positions in the trench relative to the thickness at the top of the trench. The trench has an aspect ratio (AR), defined as the height of the trench divided by the width.

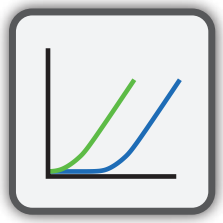

9. Nucleation behavior

The film growth during an ALD process might initially show a different behavior than at a later stage of the deposition (see Figure 2.11). The reason for this is that reactions of the precursor with the material and the chemical groups present on the substrate will probably occur differently than reactions with surface groups on the deposited film. As is

shown in Figure 2.11, it is generally possible to distinguish three cases that can manifest themselves during the initial cycles: linear growth, accelerated or enhanced growth, and delayed growth.[37] The nucleation behavior can affect material properties, such as defect or pinhole density, crystalline structure, surface roughness and film resistivity. Moreover, sometimes differences between nucleation on various substrates can be observed, which can be the starting point for an area-selective ALD process. This means that a delayed growth can be beneficial in certain cases, although usually fast nucleation is desired for regular applications.

The nucleation behavior is strongly dependent on the growth mode of the ALD material. ALD of a metal on a metal oxide often starts with island growth, also known as Volmer-Weber-type growth, before a closed films is obtained, while certain other materials growth in a layer-by-layer fashion or Frank-Van Der Merwe mode.[38] Note that the growth mode depends on the difference in surface energy between the substrate and the deposited film. After investigating the nucleation behavior, it is important to realize that specific thickness effects may start playing a role in the growth behavior after the initial nucleation phase. For instance, crystallization of the film after a certain film thickness is reached might lead to an increase of the GPC.

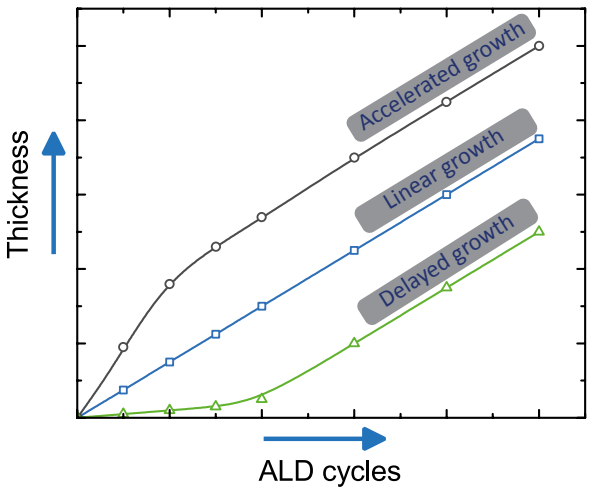

Figure 2.11 Example of the thickness as a function of number of ALD cycles, illustrating the difference between accelerated, linear, and delayed growth during the initial ALD cycles.

10. Other important aspects

Several other aspects are also important during ALD process development, although they are not necessarily specific to ALD.

- Safety: Apart from considering the safety of the used chemicals, it is wise to inform yourself whether any poisonous or potentially harmful reaction products are produced during the ALD reactions, or upon contact with the environment. Moreover, it should be checked if the film material itself is not creating any safety risk.
- Film stability: The stability of the deposited films over time and their sensitivity to the environment (e.g. the ambient) need to be taken into account. Especially in case the film is intended for use in a certain environment, it should be confirmed if it can withstand these conditions (e.g temperature, humidity, etc.).
- Reproducibility: It should be confirmed that the same film thickness and film properties can be obtained by repeating the same deposition recipe. Conditioning of the reactor wall can play a role in this context, although variations in substrate temperature or reactor pressure can also be responsible for unwanted effects.
- Precursor consumption: Efficient use of the precursor becomes more significant for expensive precursors and can for instance be achieved by minimizing the size of the reactor chamber and by avoiding overdosing. Note that the required precursor dosing typically depends on the total surface area of the substrate, which is larger when working on 3D substrates.
- Precursor stability: Prolonged heating of the precursor, which is usually needed to obtain a certain vapor pressure, can sometimes cause degradation of the precursor. For this reason it might be needed to turn off the precursor heating during periods that no deposition runs are being performed.
- Literature comparison: It is advised to verify whether the obtained results are in agreement with previous reports on the same (or very similar) ALD process, especially in terms of chemical composition and growth behavior. If this is not the case, an explanation for the distinctions should be found.
- Device performance: The real test for the developed process will be the application in a working device, such as a transistor or solar cell. Certain phenomena, for instance the presence of defect states or film pinholes and the incorporation of particles, might not be detected by basic characterization techniques and might only become visible when testing the film in a device.

References

[1] Leskelä, M. and Ritala, M., *Thin Solid Films* **2002**, 409(1), 138–146.
[2] Puurunen, R. L., *J. Appl. Phys.* **2005**, 97(12), 121301.
[3] George, S. M., *Chem. Rev.* **2010**, 110(1), 111–131.
[4] Miikkulainen, V., Leskelä, M., Ritala, M., and Puurunen, R. L., *J. Appl. Phys.* **2013**, 113(2), 021301.
[5] Johnson, R. W., Hultqvist, A., and Bent, S. F., *Mater. Today* **2014**, 17(5), 236–246.
[6] Ritala, M. and Leskela, M., in *Handb. Thin Film Mater. Vol. 1 Depos. Process. Thin Film.*, volume 1, chapter 2, pp. 103–159, ISBN 0-12-512909-2, **2002**.
[7] Profijt, H. B., Potts, S. E., van de Sanden, M. C. M., and Kessels, W. M. M., *J. Vac. Sci. Technol. A Vacuum, Surfaces, Film.* **2011**, 29(5), 050801.
[8] Knoops, H. C. M., Faraz, T., Arts, K., and Kessels, W. M. M., *J. Vac. Sci. Technol. A* **2019**, 37(3), 030902.
[9] Raaijmakers, I. J., *ECS Trans.* **2011**, 41(2), 3–17.
[10] Ritala, M. and Niinistö, J., *ECS Trans.* **2009**, 25(8), 641–652.
[11] Mayer, T. M., Michalske, T. A., and Rogers, J. W., *Chem. Mater.* **1991**, 3(4), 641–646.
[12] Feng, J., Chen, Y., Blair, J., Kurt, H., Hao, R., Citrin, D. S., *et al.*, *J. Vac. Sci. Technol. B Microelectron. Nanom. Struct.* **2009**, 27(2), 568.
[13] Lee, Y., DuMont, J. W., Cavanagh, A. S., and George, S. M., *J. Phys. Chem. C* **2015**, 119(25), 14185.
[14] Knoops, H. C. M., Potts, S. E., Bol, A. A., and Kessels, W. M. M., in *Handb. Cryst. Growth Thin Film. Ep.*, pp. 1101–1134, Elsevier B.V., second edition, ISBN 9780444633057, **2014**.
[15] Sarr, M., Bahlawane, N., Arl, D., Dossot, M., McRae, E., and Lenoble, D., *J. Phys. Chem. C* **2014**, 118(40), 23385–23392.
[16] Sarr, M., Bahlawane, N., Arl, D., Dossot, M., McRae, E., and Lenoble, D., *Appl. Surf. Sci.* **2016**, 379, 523–529.
[17] Dobbelaere, T., Roy, A. K., Vereecken, P., and Detavernier, C., *Chem. Mater.* **2014**, 26(23), 6863–6871.
[18] Hämäläinen, J., Holopainen, J., Munnik, F., Heikkilä, M., Ritala, M., and Leskelä, M., *J. Phys. Chem. C* **2012**, 116(9), 5920–5925.
[19] Pore, V., Hatanpaeae, T., Ritala, M., and Leskelae, M., *ChemInform* **2009**, 40(22), 3478–3480.
[20] Koponen, S. E., Gordon, P. G., and Barry, S. T., *Polyhedron* **2016**, 108, 59–66.
[21] Burton, B. B., Lavoie, A. R., and George, S. M., *J. Electrochem. Soc.* **2008**, 155(7), D508.
[22] Grubbs, R. K., Steinmetz, N. J., and George, S. M., *J. Vac. Sci. Technol. B*

Microelectron. Nanom. Struct. **2004**, 22(4), 1811.
[23] Klesko, J. P., Kerrigan, M. M., and Winter, C. H., *Chem. Mater.* **2016**, 28(3), 700–703.
[24] Kalanyan, B., Beams, R., Katz, M. B., Davydov, A. V., Maslar, J. E., and Kanjolia, R. K., *J. Vac. Sci. Technol. A* **2018**, 37(1), 010901.
[25] Golrokhi, Z., Chalker, S., Sutcliffe, C. J., and Potter, R. J., *Appl. Surf. Sci.* **2016**, 364, 789–797.
[26] Golrokhi, Z., Marshall, P. A., Romani, S., Rushworth, S., Chalker, P. R., and Potter, R. J., *Appl. Surf. Sci.* **2017**, 399, 123–131.
[27] Vos, M. F. J., Knoops, H. C. M., Synowicki, R. A., Kessels, W. M. M., and Mackus, A. J. M., *Appl. Phys. Lett.* **2017**, 111(11), 113105.
[28] Heil, S. B. S., van Hemmen, J. L., Hodson, C. J., Singh, N., Klootwijk, J. H., Roozeboom, F., *et al.*, *J. Vac. Sci. Technol. A Vacuum, Surfaces, Film.* **2007**, 25(5), 1357.
[29] International Telecommunication Union (ITU), Radio Regulations, *Technical report*, **2016**.
[30] Profijt, H. B., Kudlacek, P., van de Sanden, M. C. M., and Kessels, W. M. M., *J. Electrochem. Soc.* **2011**, 158(4), G88.
[31] Puurunen, R. L., *Chem. Vap. Depos.* **2003**, 9(6), 327–332.
[32] Leskelä, M., Niinistö, J., and Ritala, M., in *Compr. Mater. Process.*, ISBN 978-0-08-096533-8, **2014**.
[33] Elers, K. E., Blomberg, T., Peussa, M., Aitchison, B., Haukka, S., and Marcus, S., *Chem. Vap. Depos.* **2006**, 12(1), 13–24.
[34] Dendooven, J. and Detavernier, C., in *At. Layer Depos. Energy Convers. Appl.*, ISBN 9783527339129, **2017**.
[35] Gao, F., Arpiainen, S., and Puurunen, R. L., *J. Vac. Sci. Technol. A Vacuum, Surfaces, Film.* **2015**, 33(1), 010601.
[36] Ylilammi, M., Ylivaara, O. M., and Puurunen, R. L., *J. Appl. Phys.* **2018**, 123(20), 205301.
[37] Puurunen, R. L. and Vandervorst, W., *J. Appl. Phys.* **2004**, 96(12), 7686.
[38] Puurunen, R. L., *Chem. Vap. Depos.* **2004**, 10(3), 159–170.

3 Advanced ALD cycles

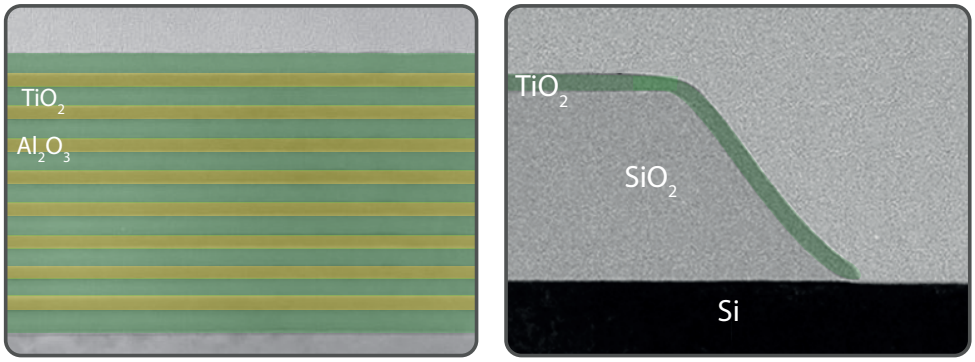

Advanced ALD cycles rely on the use of more than two chemicals serving as precursor and co-reactant, and offer unique opportunities to extend the possibilities of ALD. They can for instance be used to grow materials that cannot be obtained using a standard AB-type ALD cycle. Furthermore, advanced ALD cycles allow for deposition of multiconstituent or multilayer materials, as well as area-selective deposition (see figure above). However, the development of an ALD process based on an advanced cycle is typically more challenging than the development of a standard AB-type cycle. In this chapter, categories of advanced ALD cycles are discussed, as well as considerations that need to be taken into account. Furthermore, examples of advanced ALD cycles from the literature are given, in order to obtain a general understanding of the challenges and opportunities offered by advanced ALD cycles.

Figures above after Refs. 1 and 2.

3.1 Introduction

Atomic layer deposition (ALD) relies on the cyclic dosing of precursor and co-reactant chemicals. The standard two-step ('AB-type') ALD cycle consists of one precursor dose ('A') and one co-reactant dose ('B'), separated from each other by purge steps, whereas *advanced* ALD cycles are more complex. To be able to understand how advanced cycles can be used to extend the possibilities of ALD, it is relevant to discuss the distinctive roles that the precursor and co-reactant have to fulfill in a proper ALD process. Note that the general case of common reaction mechanisms is described below, and that processes exist which deviate from this. From a fundamental point of view, the main role of the precursor is the deposition of the (semi) metal atom, as is illustrated in Figure 3.1.[3] As was discussed in Chapter 2, there are several characteristics for a chemical to be suitable as an ALD precursor.[4,5] Identifying or developing a chemical with all of these characteristics is not trivial, and synthesis of precursor chemicals can be a challenging endeavor. For example, the precursor should be sufficiently volatile and demonstrate thermal stability.[5,6] Moreover, a precursor molecule should react with the surface groups in a self-limiting manner, and result in surface groups reactive towards the co-reactant.[6,7] To assess the volatility and thermal stability of a molecule, synthetic chemists typically rely on thermogravimetric analysis, which is a technique where a sample of the precursor is gradually heated to determine at which temperatures the molecule starts to volatize and to decompose.[6,7] In addition, density functional theory (DFT) calculations can be carried out to predict the reactivity of a precursor with a specific surface, by evaluating the pathways for precursor adsorption and the corresponding reaction energies.[8,9]

Although the precursor has only one main role contributing to the ALD growth (i.e. incorporation of the metal atom), the co-reactant generally has to fulfill three distinctive roles to obtain ALD growth (see Figure 3.1). First, the co-reactant dosing should lead to elimination of the precursor ligands, or fragments thereof.[3] This role is referred to as '*Role I: Ligand-elimination*'. Although precursor ligands often partly leave during the precursor dose, ligands or ligand fragments typically remain after the precursor has reacted with the surface. These remaining ligands therefore have to be removed during the subsequent co-reactant sub-cycle. Second, a change of the oxidation state of the metal atom can be required, since the metal atom is often in a different oxidation state in the precursor as in the film.[3] This role is termed '*Role II: Redox reaction*'. For instance, during ALD of metallic TaN_x using $Ta(NMe_2)_5$, the oxidation state of the Ta atom should change from 5+ to 3+.[10] Examples exist of ALD processes where the change in oxidation state (partly) takes place during precursor adsorption, although it is more com-

mon that the co-reactant is responsible for the redox reaction. Third, in case of non-elemental deposition, the co-reactant is generally needed for incorporation of a second (or sometimes third), element, e.g. O or N.[3] This role is referred to as '*Role III: Element-incorporation*'. Examples exist where the second element is provided by the precursor (e.g. TiN from tetrakis(dimethylamido)titanium (TDMAT) or NiC_x from bis(N,N'-di-*tert*-butylacetamidinato)nickel), but these are exceptions.[11,12] Note that all of the abovementioned reactions should be self-limiting. This means that the surface groups formed in a sub-cycle should not be reactive towards the reactant (precursor or co-reactant) being dosed during that sub-cycle.

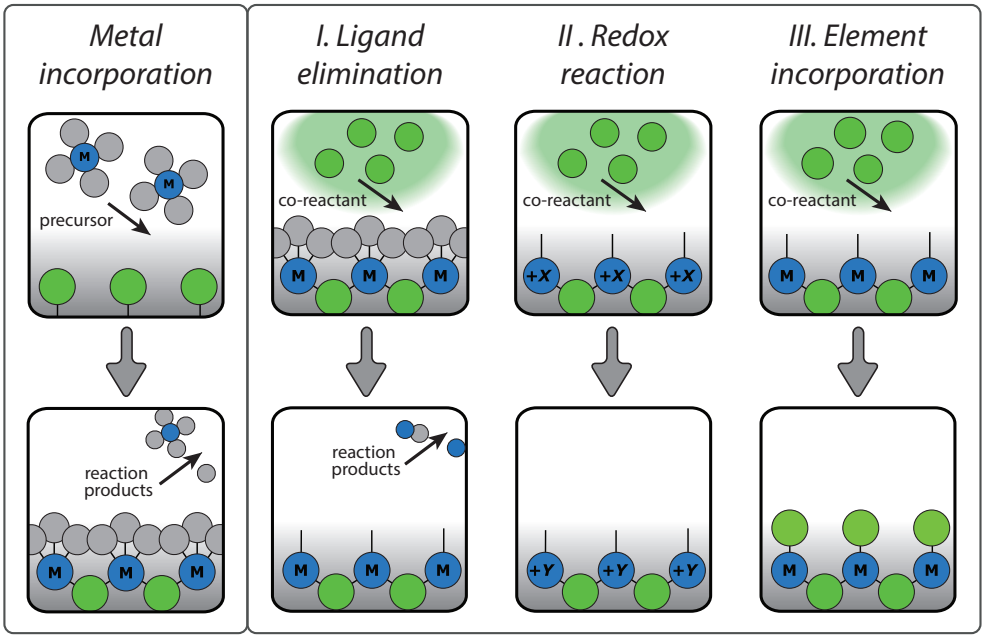

Figure 3.1 Fundamental roles that the precursor and co-reactant typically have to fulfill to enable ALD growth. The precursor should result in the incorporation of the (semi) metal atom. Role I of the co-reactant is the removal of precursor ligands or fragments. Role II is the promotion of the redox reaction, resulting in a change in oxidation state from $+X$ to $+Y$. Role III concerns the incorporation of a second element, which generally needs to occur during the co-reactant sub-cycle when a binary material is desired. Note that all reactions should be self-limiting.

Ideally, all of the roles described above are fulfilled by the combination of one precursor and one co-reactant in an AB-type ALD cycle. However, sometimes the two selected chemicals are not sufficient for the reactions essential for ALD growth to occur, and sometimes additional roles or functionalities are desired. At first sight, the solution would be to identify, or design, alternative precursor or

co-reactant chemicals, such that all required roles are fulfilled. However, instead of trying to solve the puzzle using just two chemicals, it can be beneficial or more straightforward to employ an *advanced* ALD cycle.

Advanced ALD cycles go beyond the standard AB-type cycle and rely on the use of more than just two chemicals. In such cycles the employed chemicals serve different purposes, in order to fulfill all the fundamental roles as described above. Furthermore, the toolbox of advanced ALD cycles offers other opportunities. The use of an advanced ALD cycle can namely be motivated by special requirements which can hold for an ALD process. For instance, advanced cycles are widely used for growth of multiconstituent (i.e. doped, ternary, or quaternary) materials. Another use of advanced cycles can be found the field of area-selective ALD, and recently several different advanced ALD cycles have been investigated for this purpose.[13] Since advanced ALD cycles offer a wide range of opportunities, ALD processes based on advanced cycles are increasingly being reported in the literature. However, the development of such advanced ALD processes is typically less trivial than for a conventional AB-type process, and several pitfalls can occur, as will be illustrated in this chapter.

This chapter is structured as follows. In Section 3.2, different categories of advanced cycles are described on a general level, and the opportunities as well as the non-trivialities that need to be considered when employing these cycles are addressed. Illustrative examples of advanced ALD processes are discussed in Section 3.3. In Section 3.3.1 advanced ALD cycles to fulfill the fundamental roles are addressed. Other opportunities offered by advanced ALD cycles are discussed in Section 3.3.2. This section focuses on multiconstituent materials and area-selective deposition, although more additional uses of advanced cycles can exist. Some generalizations on the basis of the discussed examples and the main conclusions are summarized in Section 3.4.

3.2 Categories of advanced ALD cycles

Generally, three different types of advanced ALD cycles can be identified (see Figure 3.2):

- **The co-dosing cycle**, where either two precursor or two co-reactant chemicals are dosed simultaneously.
- **The ABC-type cycle**, where an additional C-step is included in the ALD cycle.
- **The supercycle**, which can consist of two (or more) ALD cycles, or the combination of an ALD process with a surface treatment (e.g. a plasma exposure).

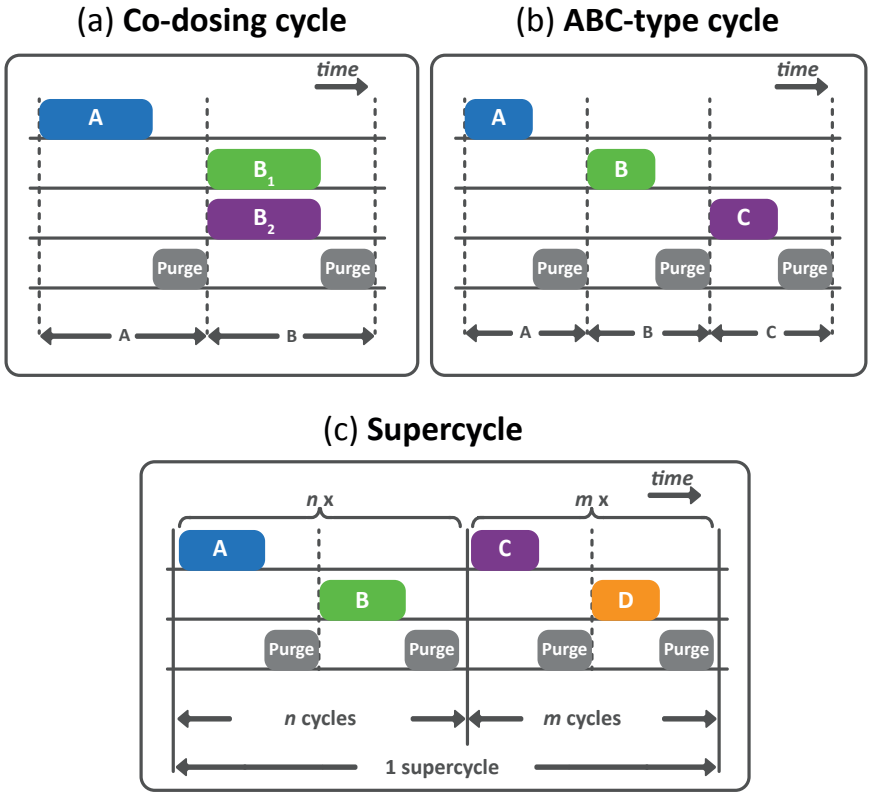

Figure 3.2 Schematic illustrations of different categories of advanced ALD cycles: (a) co-dosing cycle using co-reactants B_1 and B_2, (b) an ABC-type cycle where a C-step is added, and (c) a supercycle comprised of two different AB-type cycles. In one supercycle, first n cycles of one process are performed, followed by m cycles of the other process. Their ratio (i.e. 'supercycle ratio') is typically defined as $n/(n+m)$.

In case either the precursor or the co-reactant cannot fulfill all the required roles, a relatively simple solution is to add a third chemical during one of the reactant (i.e. precursor or co-reactant) doses.[5] As will be discussed later, such a co-dosing cycle is mostly employed for ALD of doped or ternary materials. The mixing ratio of the two chemicals can influence the growth behavior as well as the material properties, and a co-dosing cycle therefore typically requires additional optimization as compared to a standard AB-type ALD cycle. Another important aspect is the possibility of competitive adsorption of the two chemicals, which can result in the loss of control over the film composition, in addition to loss of self-limiting behavior.[14]

In some cases, it is not sufficient to combine two reactant chemicals in a co-dosing cycle to fulfill all roles and requirements. Moreover, in a co-dosing cycle the interaction of chemicals with each other can be undesirable. At high working pressures, the combination of O_2 and H_2 can for instance pose explosion hazards. In such cases, an additional C-step can be included in the ALD cycle, resulting in an ABC-type cycle. This additional step is often a second co-reactant exposure, which is contributing to film growth. It can however also have another purpose, e.g. growth inhibition to enable area-selective ALD, as will be discussed in Section 3.3.2.[15] When using ABC-type cycles certain aspects should be considered. Firstly, the order of the different dosing steps is to be determined. For certain processes, the order can be switched, but typically one reaction step needs to take place before the other one. Moreover, the inclusion of the C-step can change the saturation behavior of the other sub-cycles, and additional experiments are therefore required to confirm saturation of all dosing steps.

The cyclic nature of ALD makes that the same reaction steps occur during every (AB- or ABC-type) ALD cycle. Although this allows for precise thickness control (i.e. the same amount of material is deposited every cycle), it can be a drawback that all of the steps are performed every cycle. For this reason, it is sometimes decided to carry out one or more steps after several ALD cycles, in a supercycle manner. Such a supercycle where an ALD cycle is combined with either another ALD cycle, or with a surface treatment, can further extend the possibilities of ALD. For example, supercycles of two ALD cycles have extensively been employed to enable growth of doped or ternary materials.[14] Recently, also other variations have been reported, where an ALD cycle is combined with a treatment, such as for example a plasma exposure.[16,17] Several nontrivialities can play a role for supercycle processes. Nucleation effects after switching between the two processes can lead to an overall growth rate which deviates from what is expected. In addition, it is worth noting that both the cycle ratio and number of cycles per supercycle need to be optimized.

3.3 Illustrative examples of advanced ALD cycles

To illustrate how the different advanced ALD cycles can be employed to meet the requirements as described above, several examples of advanced ALD cycles are discussed in this section. First, ALD cycles are described where the fundamental roles are fulfilled by using more than two reactants. Subsequently, two additional uses of advanced ALD cycles are discussed: ALD of doped and ternary materials, and area-selective deposition.

3.3.1 Fulfilling the fundamental roles

Co-dosing two co-reactants during In_2O_3 ALD

The ALD process for H-doped In_2O_3 (In_2O_3:H) using InCp as precursor and H_2O and O_2 as co-reactants provides a successful example of a co-dosing cycle (see Figure 3.3a).[18,19] In this ALD process, H_2O and O_2 both serve a separate role, and the ALD reaction does not proceed when using only one of them. In the work by Libera *et al.* it was shown that H_2O is needed for the removal of the Cp ligand (see Figure 3.3b), which corresponds to Role I ('*ligand elimination*', see Figure 3.2). Apart from elimination of the Cp, H_2O also results in the formation of hydroxyl surface groups, needed for precursor chemisorption in the next ALD cycle. Meanwhile, the O_2 leads to a change of the oxidation state of the In atom from 1+ to 3+ and additional O incorporation, connecting to Role II ('*redox reaction*') and III ('*element incorporation*').

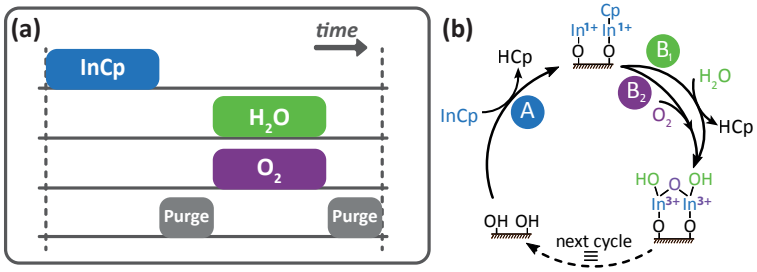

Figure 3.3 (a) Schematics of the co-dosing cycle and (b) the reaction mechanism for ALD growth of In_2O_3:H using co-dosing of O_2 and H_2O. Ligand elimination by H_2O results in OH surface groups and the release of HCp as reaction product ('B_1'), while O_2 leads to a change in oxidation state of the In atom ('B_2'). The modifications by H_2O and by O_2 are indicated in green and purple, respectively. After Ref. 19.

In addition, to the co-dosing cycle, Libera *et al.* investigated two different variations of an ABC-type cycle, with the O_2 and H_2O dosed after one another. It was demonstrated that the order has an effect on the growth characteristics and the material properties. Co-dosing however resulted in the best results in terms of growth per cycle (GPC) and carrier mobility. Furthermore, subsequent dosing in an ABC-type cycle results in a longer cycle-time. Finally, it is noted that the InCp precursor can also be combined with O_2 plasma as co-reactant to grow In_2O_3.

H_2/N_2 plasmas for ALD of nitrides and metals

Co-dosing of H_2 and N_2 has widely been used for plasma ALD of both nitrides and metals.[20–26] As will also be discussed in Chapter 6, a relevant aspect for these types of plasmas is the presence of NH_3 and NH_x, $x \leq 3$ species in the plasma. When

using a mixed H_2/N_2 plasma, NH_3 can be formed at the reactor walls through recombination reactions of incoming H and N radicals, while subsequent dissociation of NH_3 results in $NH_{x,\ x\leq 3}$ species.[27,28] These species can play a role in the ALD growth mechanism, as will be illustrated below.

An example of an ALD cycle based on a mixed H_2/N_2 plasma is the co-dosing cycle for conductive TaN films using $TaCl_5$ as precursor shown in Figure 3.4. TaN_x can exist in the conductive TaN phase, or in the resistive Ta_3N_5 phase, and precise control of the stoichiometry is therefore essential. In the co-dosing cycle for TaN, N species in the plasma are responsible for the formation of a metal nitride film, which is Role III as described above. H species, on the other hand, are needed to fulfill Roles I and II, i.e. to reduce the Ta atom from 5+ in $TaCl_5$ to 3+ in TaN and to eliminate the Cl ligands. As can be seen in Figure 3.4b, the N/Ta ratio of the deposited films depends on the N_2/H_2 mixing ratio of the plasma source gas, which allows for tuning of the composition and material properties. It is noted that growth of TaN films has also been reported by thermal ALD using ABC-type cycles employing $TaCl_5$ and NH_3 as precursor and co-reactant, together with elemental Zn or $Al(CH_3)_3$ in an additional C-step to reduce the film from Ta_3N_5 to TaN.[29,30] These approaches however resulted in a higher film resistivity than obtained using the H_2/N_2 plasma process, which can be explained by a different stoichiometry (N/Ta ratio) or a higher impurity content.

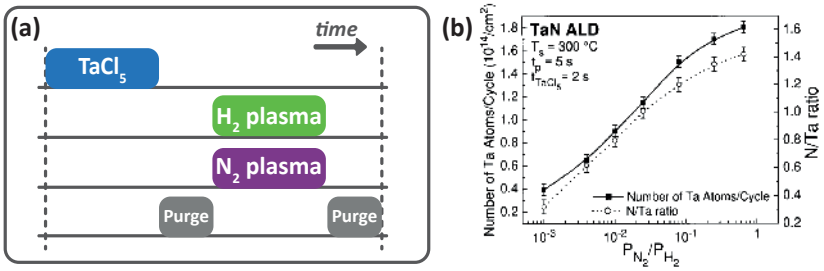

Figure 3.4 (a) Co-dosing cycle using $TaCl_5$ and a mixed H_2/N_2 plasma for deposition of conductive TaN. (b) Number of Ta atoms deposited per cycle and N/Ta ratio as a function of N_2/H_2 mixing ratio of the plasma source gas. After Ref. 20.

Apart from ALD of metal nitrides, H_2/N_2 plasmas can be used for ALD of metals. In this type of process, N or H should not be incorporated in the film, but the $NH_{x,\ x\leq 3}$ species in the plasma can be required for removal of the precursor ligands (Role I). For ALD of Pt-group metals O_2 is a typical co-reactant, but during certain fabrication processes, as well as for ALD of metals such as Co, Ni and Cu, it is often not possible to use oxidizing agents. Figure 3.5 shows a cycle employing an H_2/N_2 plasma for ALD of Ru. Interestingly, the Ru

atom is already in the zero oxidation state in the employed precursor (isopropylmethylbenzene)(cyclohexadiene)Ru(0)), meaning that Role II ('*redox reaction*') does not need to be fulfilled. In the work of Hong *et al.*, the $N_2/(N_2+H_2)$ mixing ratio was varied, and it was found that the resistivity of the films increased for higher N_2 fractions due to N-contamination (see Figure 3.5b).[26] This finding illustrates that for these types of plasmas, optimization of the mixing ratio is required, as will be further discussed in Chapter 6, where H_2/N_2 plasmas are employed for Co ALD, and the role of the various plasma species is investigated.

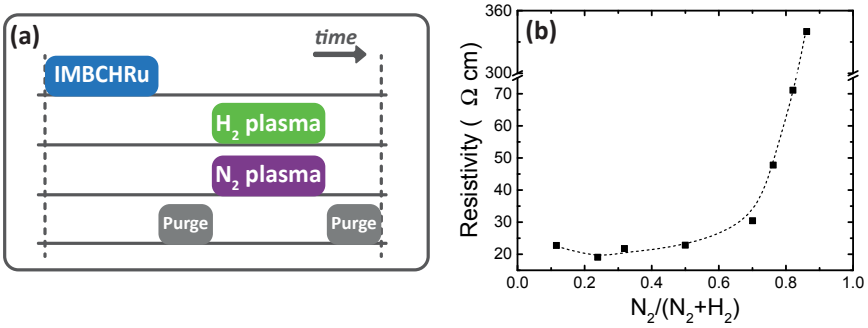

Figure 3.5 (a) Co-dosing cycle for ALD of Ru employing isopropylmethylbenzene)(cyclohexadiene)Ru(0) (IMBCHRu) and an H_2/N_2 plasma. (b) Film resistivity as function of the $N_2/(N_2+H_2)$ mixing ratio. The lowest resistivity was obtained for an N_2 fraction of ~0.25, while the resistivity increased up to ~340 μΩ cm for higher N_2 fractions due to N-incorporation. After Ref. 26.

ALD of Pt-group metals using ABC-type cycles

The ALD growth of Pt-group metals using a combination of an oxidizing agent (O_2 gas or plasma, or O_3) and a reducing agent (H_2 gas or plasma) is another example of an ALD process using two different co-reactants. In this case the oxidizing and reducing agents are dosed consecutively in an ABC-type cycle. Such a cycle is typically used for depositing Pt-group metals at low temperature. Examples of metals grown using these ABC-type cycles include Ir, Rh, Ru, Pt and Pd.[31–36] Low deposition temperatures (<150 °C) can be required to avoid damage or intermixing of materials during device fabrication. However, the use of O_2 gas as co-reactant in an AB-type cycle at low temperatures (<150 °C) typically does not lead to film growth.[31,36,37] On the other hand, for Ir, Rh, Pt and Pd it is reported that using the stronger oxidizing agents O_3 or O_2 plasma typically leads to deposition of a metal oxide instead of a metallic film below deposition temperatures of ~200 °C. The deposition of a metal oxide occurs because the oxidizing agent results in the combustion of the precursor ligands, as well as O-incorporation at these temperatures.[31,37] This means that Role I of ligand removal is met, whereas Role

II of the redox reaction is not. The addition of the reducing H_2 (gas or plasma) dose is therefore needed to also fulfill Role II.

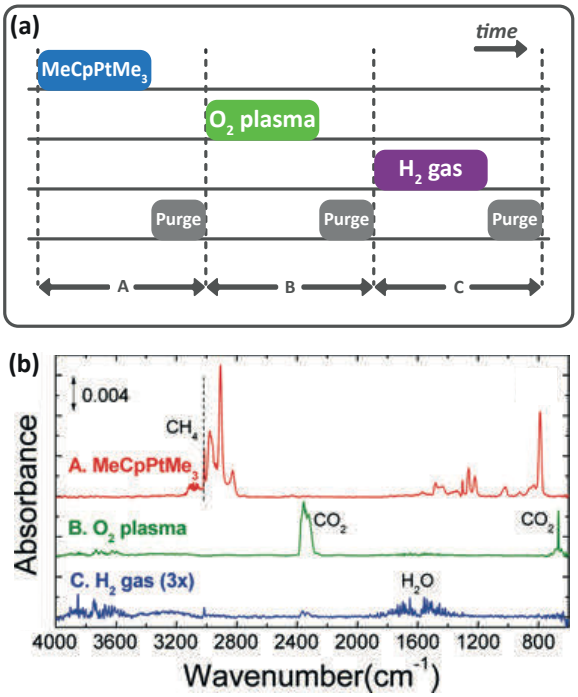

Figure 3.6 (a) ABC-type cycle for growth of Pt at $\geq$ 100 °C, using subsequent O_2 plasma and H_2 gas exposures. For deposition at room temperature the H_2 gas dose should be replaced by an H_2 plasma exposure. (b) Gas-phase Fourier-transform infrared spectroscopy (FTIR) spectra for the $MeCpPtMe_3$, O_2 plasma, and H_2 gas exposures at 100 °C, showing the formation of CO_2 and H_2O as main reaction products during the co-reactant steps. These reaction products indicate the ligand elimination and the reduction of PtO_x to Pt. After Ref. 35.

Mackus *et al.* demonstrated low-temperature ALD of Pt using trimethyl(methylcyclopentadienyl)platinum ($MeCpPtMe_3$) as precursor, and subsequent O_2 plasma and H_2 gas exposures as co-reactants (see Figure 3.6a).[35] To investigate the reaction mechanism of this ABC-type ALD cycle, Fourier-transform infrared spectroscopy (FTIR) was employed (see Figure 3.6b). It was found that combustion-reactions during the O_2 plasma exposure result in elimination of the ligand fragments and in CO_2 formation, meaning that Role I is fulfilled. Reduction of the surface oxide corresponds to Role II ('*redox reaction*') and results in release of H_2O. Whereas for Pt ALD the oxidizing agent was dosed first, Weber deposited Pd using $Pd(hfac)_2$ ($Pd(C_5HF_6O_2)_2$, hfac = hexafluoroacetylacetonate) by performing the H_2 plasma before the O_2 plasma.[36] It was found that performing the

O_2 plasma before the H_2 plasma results in almost no growth and significant C and F contamination. This observation was explained by the presence of F in the hfac precursor ligand, which has been reported to lead to metal fluoride surface species and other by-products during the O_2 plasma exposure.[36,38] F-containing ligands or surface species are more efficiently removed by first dosing the H_2 plasma. Depending on the precursor, either O_2 or H_2 should thus be dosed first. An ABC-type cycle using subsequent oxidation and reduction steps is employed for ALD of Ru at <150 °C in Chapter 7 and Chapter 8.

Stoichiometry control of VO_x using ABC-type cycles

ABC-type cycles have also been employed to control the stoichiometry of VO_x films. VO_x can exist in different oxidation states, including V_2O_3, VO_2, and V_2O_5.[39] The oxidation state greatly affects the material properties and obtaining the correct stoichiometry is therefore essential. Interestingly, V_2O_3 and VO_2 can both demonstrate a phase-change from semiconductor to metal. Weimer *et al.* demonstrated an ABC-type cycle using consecutive H_2O and O_2 dosing steps to grow V_2O_5, with V in the 5+ state (see Figure 3.7a). Vanadium-tris(N,N'-diisopropylacetamidinate) ($V(amd)_3$) was used as the precursor, which contains V in the 3+ oxidation state. H_2O is believed to be responsible for the ligand exchange reaction, donating OH to the surface and accepting an one *amd*-precursor ligand. H_2O thus fulfills Role I (*ligand-elimination*), and partly Role III (*element-incorporation*). O_2, on the other hand, causes the oxidation reaction to occur (Role II: *redox reaction* and Role III: *element-incorporation* combined), and leads to the change of V^{3+} to V^{5+}. The use of only H_2O or only O_2 does not lead to sustainable film growth and stops after ∼6 nm. However, the use of O_3 as co-reactant in an AB-type cycle does result in deposition of V_2O_5 (see Figure 3.7c), since O_3 is a stronger oxidizing agent than H_2O and O_2.

In the quest to find a method to deposit VO_2 (instead of V_2O_5), an ABC-type cycle using H_2O_2 (hydrogen peroxide) and H_2 was developed (see Figure 3.7b). In VO_2, the V atom is in the 4+ state. The H_2O_2 dosing step of this ABC-type cycle leads to removal of the precursor ligands (Role I) and the incorporation of O as the second element (Role III), while the H_2 step serves to obtain the correct oxidation state (Role II). Notably, the V atom is fully oxidized (V^{5+}) after the H_2O_2 exposure, before it is reduced to an intermediate oxidation state (V^{4+}) during the H_2 dose.

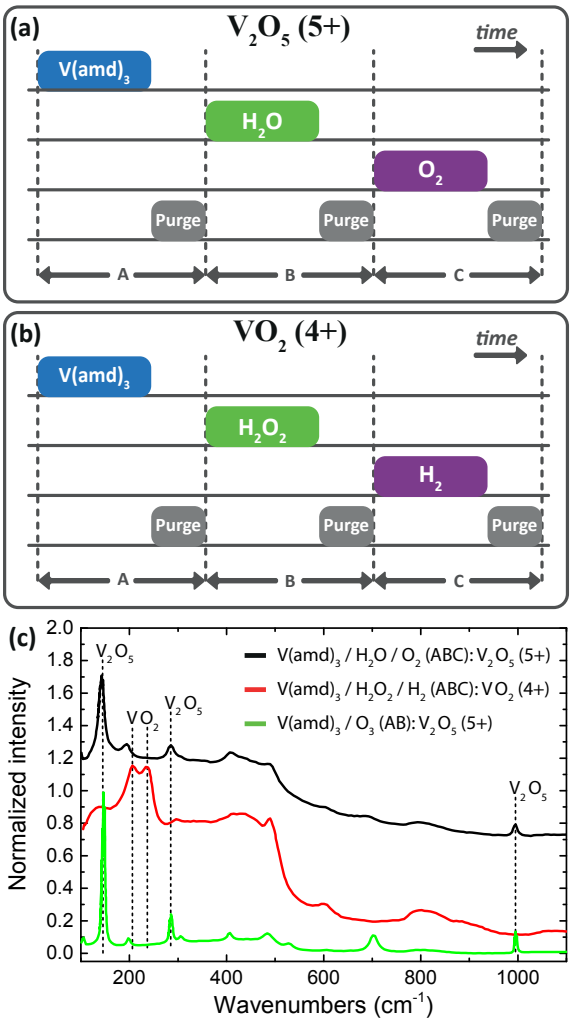

Figure 3.7 (a,b) ABC-type cycles using H_2O-O_2 and H_2O_2-H_2 as co-reactant pairs for ALD of V_2O_5 and VO_2, respectively. Both processes use vanadium-tris(N,N'-diisopropylacetamidinate) ($V(amd)_3$) as precursor. (c) Raman spectroscopy was employed to determine the oxidation states of the films deposited using different ALD cycles. The presence of characteristic Raman peaks indicates whether the film corresponds to either V_2O_5 or VO_2. After Ref. 39.

ABC-type ALD cycle for WS_2

Other cases exist where the change of oxidation state (Role II) and the incorporation of the second element (Role III) were achieved by using multiple co-reactants. For the growth of WS_2 using tungsten hexafluoride (WF_6) as precursor, it was shown that an ABC-type cycle with H_2 plasma followed by H_2S gas exposure can be used (see Figure 3.8).[40,41]

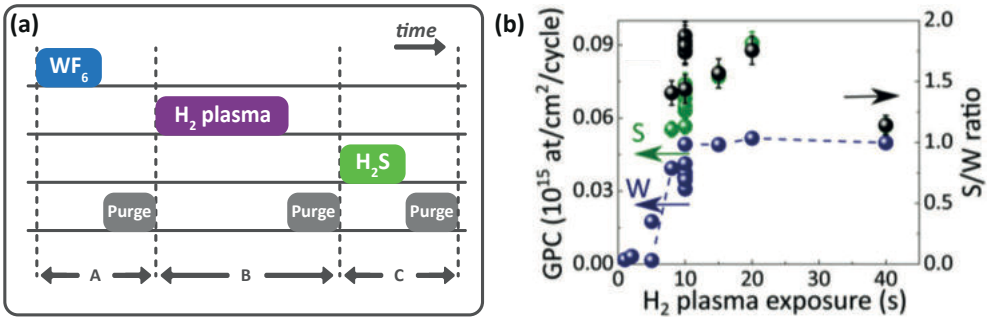

Figure 3.8 (a) ABC-type cycle for growth of WS_2, using WF_6 (tungsten hexafluoride) as precursor and H_2 plasma and H_2S as consecutive co-reactants. (b) Growth per cycle (GPC) in terms of W and S atoms deposited per cm^2 and S/W ratio as a function of H_2 plasma exposure time. After Ref. 41.

In this ABC-type cycle, the H_2 plasma is responsible for the reduction of the W atom from +6 in WF_6 to +4 in WS_2 (Role II: *redox reaction*), while the H_2S results in the incorporation of S (Role III: *element-incorporation*). Moreover, during the H_2 plasma exposure, the F ligands are eliminated (Role I: *ligand-elimination*), accompanied by the release of volatile HF. Interestingly, the AB-type cycle using H_2 plasma results in a W film, while growth is not achieved using only H_2S gas. As can be seen in Figure 3.8a, precise optimization of the H_2 plasma duration is needed to obtain material with the desired stoichiometry (S/W = 2). Furthermore, the S/W ratio was found to decrease with increasing H_2 plasma power. This dependence on the H_2 plasma duration and power is explained by the reduction of the WS_x film during the plasma exposure, which leads to removal of S from the film. This ABC-type cycle does therefore not demonstrate ideal self-limiting behavior.

3.3.2 Opportunities provided by advanced ALD cycles

In the previous section it was described how advanced ALD cycles have been used to fulfill the fundamental roles required for ALD growth. The insights from these advanced ALD processes offer opportunities for the development of other processes. As mentioned before, special requirements can hold for an ALD process, which can potentially be met by employing an advanced ALD cycle. In this section, two additional uses of advanced ALD cycles will be discussed, starting with the growth of multiconstituent materials, followed by area-selective deposition.

Multiconstituent materials

Most current industrial applications of ALD make use of binary metal oxides, such as SiO_2, Al_2O_3 and HfO_2. However, as discussed in the introduction, the deposition of a doped, ternary (AB_xC_y), or quaternary ($AB_xC_yD_z$) material is sometimes desired. Multiconstituent materials are currently receiving increased interest, as they can possess material properties different from simple binary materials.[14] Moreover, variation of the film composition of doped, ternary or quaternary materials allows for more accurate tuning of the material properties. For deposition of a multiconstituent material an extra requirement is the incorporation of one or two additional elements. This incorporation can be achieved in different ways, namely by co-dosing two precursors, by co-dosing two co-reactants, or by combining two ALD cycles in a supercycle. In this section examples of all three options are discussed, together with some points of attention.

An example where two precursors have been co-dosed is the process for $AlZn_xO_y$ using trimethylaluminum (TMA), diethylzinc (DEZ) and H_2O (see Figure 3.9a).[42] When using two precursors X and Y in a co-dosing cycle, the composition of the material can typically be controlled by varying the relative partial pressure $p_X/(p_X+p_Y)$.[42,43] However, the growth can be influenced by competitive adsorption of the two precursors, which can lead to loss of self-limiting behavior. Due to the dependence on the partial pressure of the two precursors, this loss of self-limiting behavior can manifest itself in uniformity issues, and poor conformality in trenches and other 3D structures. For $AlZn_xO_y$, the Al/(Zn+Al) ratio was found that to depend on the precursor (TMA and DEZ combined) exposure time (see Figure 3.9b), meaning that control over the film composition is lost. Furthermore, the Al concentration could also be varied by varying the TMA flow. These findings indicate that competitive adsorption occurs, meaning that Zn species on the surface are etched by TMA.

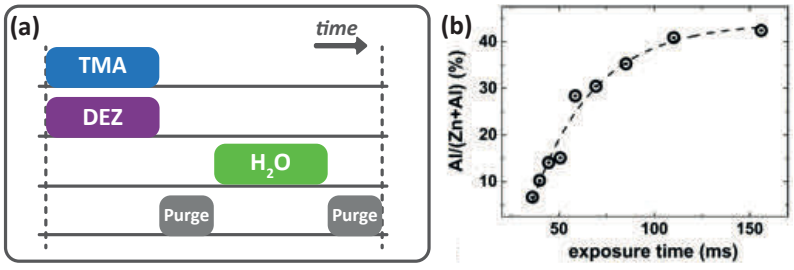

Figure 3.9 (a) Co-dosing cycle using $Al(CH_3)_3$ (TMA) and $(C_2H_5)_2Zn$ (DEZ) as precursors for growth of $AlZn_xO_y$. H_2O is used as the co-reactant. (b) Al/(Zn+Al) ratio as a function of precursor (TMA and DEZ together) exposure time. The Al-content increases with exposure time due to etching of Zn species by TMA. After Ref. 42.

While the co-dosing of two metal-based precursors can be employed when a metal is desired as third element, the co-dosing of two co-reactants allows for additional incorporation of a non-metal. An example where two co-reactant molecules are dosed simultaneously to achieve a ternary material is the ALD process for ZnOS using H_2O and H_2S as co-reactants (see Figure 3.10a).[44,45]

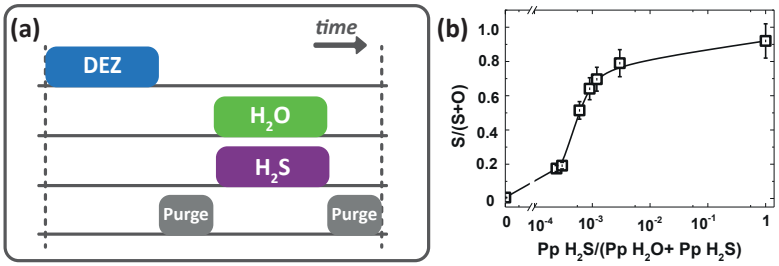

Figure 3.10 (a) Co-dosing cycle for ZnOS using H_2O and H_2S as co-reactants. (b) S/(S+O) ratio as a function of the relative partial pressure (P_p) of H_2S in the H_2O/H_2S gas mixture ($p_{H_2S}/(p_{H_2S}+p_{H_2O})$). After Ref. 44.

To tune the stoichiometry of the ZnOS films (i.e. the S/(S+O) ratio), the mixing ratio between H_2O and H_2S was varied (see Figure 3.10b). This allowed for tuning of the material properties such as the refractive index (1.9 - 2.3) and bandgap (2.6 - 3.4 eV). Alternatively, the deposition temperature could be varied to change the S/(S+O) ratio. The GPC of the process was found be strongly correlated to the mixing ratio between H_2O and H_2S (and therefore the stoichiometry), which was explained by a change from crystalline to amorphous material. Similar to the process for $Al_xZn_{1-x}O$ discussed above, the co-dosing of H_2O and H_2S leads to a dependence on the co-reactant exposure time. Longer exposures result in a higher S-content, which is due to the gradual replacement of surface O by S (from H_2S), and a release of H_2O as well.

A different method to achieve a material composed of three or four elements it to use a supercycle of two ALD cycles, for instance cycles for Al_2O_3 and ZnO ALD such as illustrated in Figure 3.11a.[46,47] Doped, ternary (AB_xC_y) or quaternary materials ($AB_xC_yD_z$), as well as multilayer films, after often grown with such a supercycle. The majority of ternary materials deposited by ALD are metal oxides (e.g. $AlZn_xO_y$, $TaZr_xO_y$ and $SrTi_xO_y$).[14,46,48,49] However, other examples of materials deposited using supercycles include oxysulfides (e.g. ZnOS), metal nitrides (e.g. InGaN), sulfides (e.g. $CuInS_2$), and fluorides (e.g. $LiAlF_4$).[50–53]

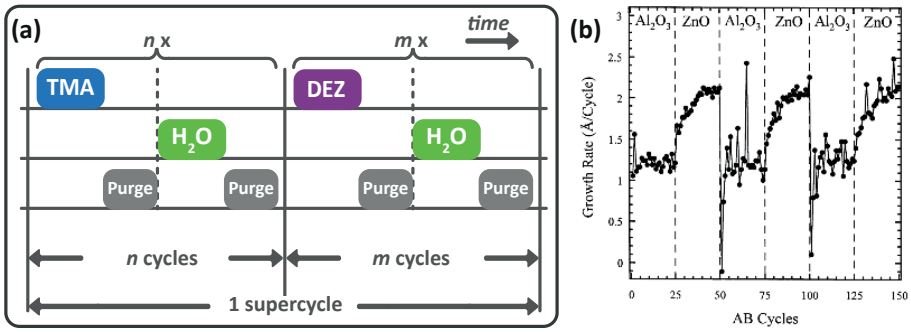

Figure 3.11 (a) Supercycle composed of ALD cycles for Al_2O_3 and ZnO which can be used to grow Al_2O_3/ZnO multilayer films, Al-doped ZnO films, or the ternary material $AlZn_xO_y$. Note that the supercycle ratio $n/(n+m)$ determines which of these three types of materials is deposited. (b) Growth rate as a function of ALD cycles. The growth of ZnO on Al_2O_3, and the growth of Al_2O_3 on ZnO demonstrate a nucleation period of approximately 3 and 12 ALD cycles, respectively, before a constant growth rate is achieved. After Ref. 46.

The composition of the ternary films can to a certain extent be controlled by varying the number of n and m cycles in one supercycle, and their ratio $n/(n+m)$. However, nucleation effects often occur when switching from one material to the other, which can affect the obtained film composition and can lead to an undesired distribution of material in the matrix.[14,47,54] For instance, the growth of Al_2O_3 on ZnO demonstrates a short nucleation period, due to the removal of ZnO species by TMA.[47,55,56] Similarly, ZnO shows a nucleation delay on an Al_2O_3 surface (see Figure 3.11b).[46,47] One explanation for this nucleation delay has been the formation of $ZnOH^{2+}$•••AlO^- complexes as a result of proton transfer between ZnOH and AlOH when dosing DEZ onto Al_2O_3.[47,55,56] The formation of these complexes would cause a loss of surface OH-groups, and since this is the reactive site to which DEZ binds, less precursor would adsorb to the surface. This results in a nucleation period which lasts until the OH-density is restored. A second explanation can be found in precursor ligands remaining after co-reactant dosing (i.e. 'persisting ligands' which are not built into the film but eliminated during subsequent ALD cycles).[14] For ALD of ZnO, it was reported that ~16% of the ligands persisted at 150 °C, while ~50% of the ligands was found to remain for Al_2O_3 ALD.[14,57] A higher amount of CH_3 ligands remaining on the surface can result in a reduced amount of DEZ precursor when switching from Al_2O_3 ALD to ZnO ALD.[14] Together these effects make that the supercycle should carefully be optimized to achieve the desired thickness and material composition.

Finally, an interesting example of an ALD supercycle to achieve a ternary material is the process for H-doped ZnO reported by Macco *et al.*[17] In this case the ALD cycle was not combined with another ALD cycle, but with an H_2 plasma treatment instead (carried out after every n ZnO ALD cycles as illustrated in Figure 3.12a). This plasma exposure results in H incorporation in the film, but has the side-effect that the ZnO film is slightly etched. This means that there is a competition between deposition and etching and that the supercycle ratio affects the obtained net deposition. Interestingly, there is no net deposition for $n \leq 2$ (see Figure 3.12b), due to the etching of all ZnO by the H_2 plasma. For 3 ZnO ALD cycles or more, net deposition is obtained, but the length of the nucleation delay depends on the number of ALD cycles. The observation that the nucleation delay and net deposition depends on the number of ZnO cycles corroborates that the cycle ratio should be optimized when employing supercycle recipes.

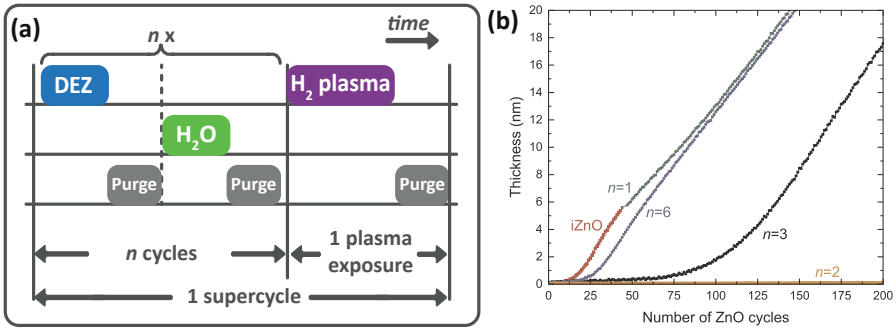

Figure 3.12 (a) Supercycle for H-doped ZnO consisting of ZnO ALD cycles combined with an interleaved H_2 plasma exposure. (b) Thickness as a function of ALD cycles for different number (n) of ZnO ALD cycles in one supercycle. Due to etching of the ZnO film by the H_2 plasma, $n \leq 2$ results in no overall film deposition. However, when a thin starting layer is deposited using ALD only (iZnO), the deposition can be continued using a supercycle with $n = 1$. After Ref. 17.

Area-selective ALD

Advanced ALD cycles also offer opportunities for area-selective ALD. Due to the growing challenges with respect to alignment of device features, area-selective ALD is especially being considered for fabrication of nanoelectronics. The field of area-selective ALD is however in an early stages of development, and large scale application requires more specialized processes. In principle, precursor molecules can in some cases be designed such that they selectively adsorb to a surface, by carefully selecting the precursor ligands. However, this can be a challenging task, and in practice the chance of success is higher when the different substrate areas

are modified such that precursor adsorption is hindered. This so-called selective functionalization is typically done prior to starting the ALD recipe, often by applying self-assembled monolayers (SAMs) using wet-chemistry based processes.[58] However, the selectivity obtained by this pretreatment is usually lost after a certain number of ALD cycles, and the used processes are typically time-consuming.[58] It can therefore be beneficial to repeat a functionalization or correction step during the ALD recipe using vapor-phase chemistry. One way to achieve this is to dose an inhibitor molecule in an additional step, resulting in an ABC-type cycle. An acetylacetone (Hacac) dose was for instance added to an ALD cycle for SiO_2, as shown in Figure 3.13.[15] When using this process, Hacac only adsorbs to specific surfaces, including for instance Al_2O_3 and TiO_2, leading to blocking of the growth on these surfaces, and eventually to area-selective deposition on areas that are not covered by Hacac (e.g. GeO_2 and SiN_x).

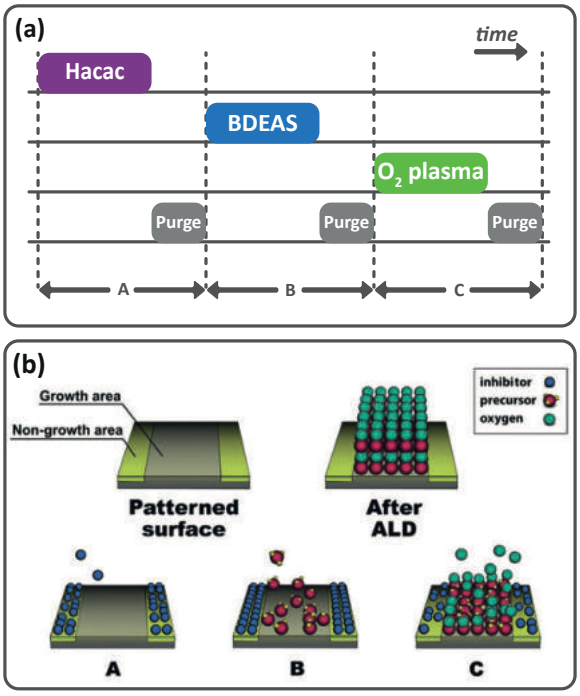

Figure 3.13 (a) ABC-type cycle consisting of acetylacetone (Hacac) dosing, bis-(diethylamino)silane (BDEAS) dosing, and O_2 plasma exposure, which is used for area- selective ALD of SiO_2. (b) Schematic illustrating the concept of area-selective ALD by using inhibitor molecules which selectively adsorb to the non-growth area. After Ref. 15.

In practice, the selectivity of area-selective ALD processes (including the one described above) is typically limited to a certain number of cycles due to modification of the substrate by the ALD precursor and/or co-reactant. This modification means that defects can be formed on which the growth can start, after an initial nucleation delay. A method to improve the selectivity of an area-selective ALD process, is to integrate correcting etch steps in a supercycle recipe of ALD and etching. In this case, the precursor can to some extent adsorb to the non-growth area and (minimal) nucleation is initially acceptable. The undesired growth on the non-growth area is removed by performing an etch step or cycle after a certain number of cycles. This concept is illustrated in Figure 3.14. For such an ALD-etch supercycle, the number of the ALD cycles in the supercycle, as well as etch frequency (i.e. the cycle ratio) have to be optimized. Note that the ABC-type cycle using inhibitors mentioned above can potentially be combined with etching cycles in a supercycle, to improve the selectivity further.5

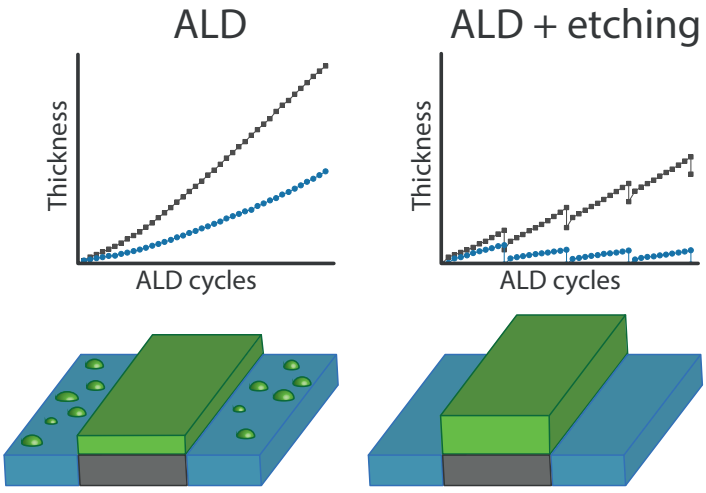

Figure 3.14 Schematic illustrating how ALD can be combined with etch steps to obtain area-selective deposition. The etch steps result in removal of material from both the growth and the non-growth area. However, since the growth rate on the growth area is significantly higher than on the non-growth area, the ALD-etch supercycle results in net deposition on the growth area. The development and optimization of an ALD-etch supercycle for area-selective ALD is described in Chapters 7 and 8.

Vallat *et al.* recently demonstrated area-selective ALD of Ta_2O_5 and TiO_2 on TiN employing intermediate etch steps. The etch step was done using a mixed O_2/NF_3 plasma (i.e. co-dosing), in order to remove deposited Ta_2O_5 or TiO_2 from the Si and SiO_2 non-growth areas.[16,59] The supercycle employed for TiO_2 and a SEM image demonstrating selectivity are shown in Figure 3.15.

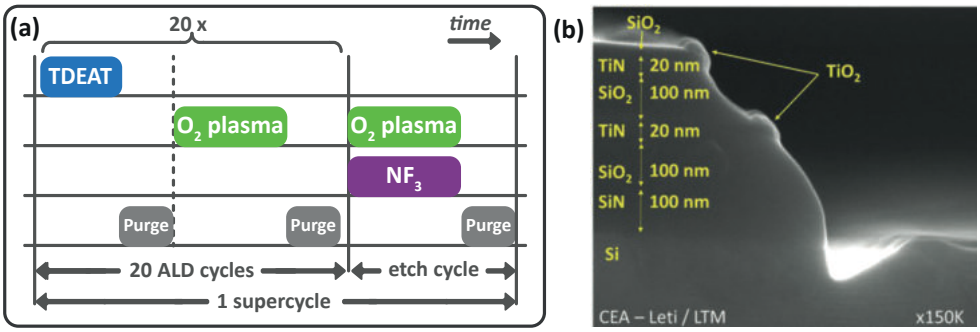

Figure 3.15 (a) Supercycle recipe where an ALD process for TiO_2 is combined with an etch cycle to achieve area-selective ALD.[59] An O_2 plasma is used as co-reactant during the ALD cycle, while the etching of TiO_2 is done with a mixed O_2/NF_3 plasma. A similar supercycle using TBTDET (tertiary-butylimidotrisdiethyl-amino tantalum) as precursor instead of TDEAT (tetrakis(diethylamido) titanium) was employed for area-selective ALD of Ta_2O_5.[16] (b) Scanning electron microscopy (SEM) image of a 3D pattern structure with TiO_2 selectively deposited on top of TiN, demonstrating that no deposition is present on the SiO_2 and SiN regions. After Ref. 59.

Recently, Song *et al.* used a similar approach as Vallat *et al.* for area-selective deposition of TiO_2.[2] In this case, an atomic layer etching (ALE, "inverse ALD") process was employed to remove TiO_2 nuclei from the H-terminated Si non-growth area, enabling area-selective deposition on SiO_2. Chapters 7 and 8 of this dissertation address the development of ALD-etch cycle for Ru, which allows for growth of Ru on Pt with negligible deposition on SiO_2. In this case the employed etch cycle consists of an O_2 etching step, followed by a reducing H_2 step, which results in quasi self-limiting etch behavior.

3.4 Conclusions

Generally, the fundamental roles to obtain ALD growth are fulfilled by just two chemicals: one precursor and one co-reactant chemical. During the precusorsor sub-cycle, the precursor serves to deliver the main elemental to the surface (a metal or semimetal). The co-reactant should subsequently result in the removal of precursor ligands, promote the redox reaction such that the correct oxidation state is obtained (if necessary), and in case of non-elemental films the incorporation of an additional element.

In this chapter it was shown that standard AB-type ALD cycles are sometimes not sufficient to fulfill all of these fundamental roles, and that advanced ALD cycles can offer a solution to this. The examples discussed above demonstrate that advanced ALD cycles can be a powerful tool to extend the capabilities of ALD, and that they can be employed for a variety of reasons and applications. For instance, the roles of ligand elimination and element incorporation sometimes have to be fulfilled by two separate co-reactants in either a co-dosing or ABC-type cycle. Obtaining the right oxidation state is often an important aspect in the reaction mechanism, and the addressed literature reports demonstrate various methods to modify the oxidation state of the main element. Furthermore, advanced ALD cycles can be used for low-temperature deposition of Pt-group metals, growth of multiconstituent materials, and area-selective ALD deposition.

Despite demonstrating the opportunities of advanced ALD cycles, the examples also showed that designing an advanced cycle is not trivial, and that several aspects have to been considered. More specifically, when employing a co-dosing cycle, competitive adsorption or etching effects can influence the material composition. In an ABC-type recipe, the order of the dosing steps can be of significance. Furthermore, the addition of a C-step to an existing AB-type cycle requires the re-establishment of saturation, and in some cases leads to loss of self-limiting behavior. When employing a supercycle, the most significant point of attention is the optimization of the cycle ratio and the number of cycles of the individual processes in the cycle. Furthermore, nucleation effects can play a role when switching from one type of cycle to the other. Similar as for co-dosing cycles, etching of surface species by either the precursor or the co-reactant has been reported for supercycle recipes. Finally, the opportunities offered by advanced ALD cycles such as low-temperature deposition, growth of multiconstituent materials and area-selective deposition are highly relevant for the extension of the ALD toolbox, and for the broadening of the application possibilities of ALD.

References

[1] Kim, Y. S. and Jin Yun, S., *J. Cryst. Growth* **2005**, 274(3), 585–593.

[2] Song, S. K., Saare, H., and Parsons, G. N., *Chem. Mater.* **2019**, 31(13), 4793–4804.

[3] Zaera, F., *J. Phys. Chem. Lett.* **2012**, 3(10), 1301–1309.

[4] Bernal Ramos, K., Saly, M. J., and Chabal, Y. J., *Coord. Chem. Rev.* **2013**, 257(23), 3271–3281.

[5] Knoops, H. C. M., Potts, S. E., Bol, A. A., and Kessels, W. M. M., in *Handb. Cryst. Growth Thin Film. Ep.*, pp. 1101–1134, Elsevier B.V., second edition, ISBN 9780444633057, **2014**.

[6] Koponen, S. E., Gordon, P. G., and Barry, S. T., *Polyhedron* **2016**, 108, 59–66.

[7] Hatanpää, T., Ritala, M., and Leskelä, M., *Coord. Chem. Rev.* **2013**, 257(23-24), 3297–3322.

[8] Dey, G., Wrench, J. S., Hagen, D. J., Keeney, L., and Elliott, S. D., *Dalt. Trans.* **2015**, 44(22), 10188–10199.

[9] Filatova, E. A., Hausmann, D., and Elliott, S. D., *J. Vac. Sci. Technol. A Vacuum, Surfaces, Film.* **2017**, 35(1), 01B103.

[10] Knoops, H. C. M., Langereis, E., van de Sanden, M. C. M., and Kessels, W. M. M., *J. Vac. Sci. Technol. A Vacuum, Surfaces, Film.* **2012**, 30(1), 01A101.

[11] Faraz, T., Knoops, H. C. M., Verheijen, M. A., Van Helvoirt, C. A. A., Karwal, S., Sharma, A., *et al.*, *ACS Appl. Mater. Interfaces* **2018**, 10(15), 13158–13180.

[12] Guo, Q., Guo, Z., Shi, J., Xiong, W., Zhang, H., Chen, Q., *et al.*, *ACS Appl. Mater. Interfaces* **2018**, 10(9), 8384–8390.

[13] Mackus, A. J. M., Merkx, M. J. M., and Kessels, W. M. M., *Chem. Mater.* **2019**, 31(1), 2–12.

[14] Mackus, A. J. M., Schneider, J. R., MacIsaac, C., Baker, J. G., and Bent, S. F., *Chem. Mater.* **2019**, 31(4), 1142–1183.

[15] Mameli, A., Merkx, M. J. M., Karasulu, B., Roozeboom, F., Kessels, W. M. M., and Mackus, A. J. M., *ACS Nano* **2017**, 11(9), 9303–9311.

[16] Vallat, R., Gassilloud, R., Eychenne, B., and Vallée, C., *J. Vac. Sci. Technol. A* **2017**, 35(1), 01B104.

[17] Macco, B., Knoops, H. C. M., Verheijen, M. A., Beyer, W., Creatore, M., and Kessels, W. M. M., *Sol. Energy Mater. Sol. Cells* **2017**, 173, 111–119.

[18] Libera, J. A., Hryn, J. N., and Elam, J. W., *Chem. Mater.* **2011**, 23(8), 2150–2158.

[19] Wu, Y., Macco, B., Vanhemel, D., Kölling, S., Verheijen, M. A., Koenraad, P. M., *et al.*, *ACS Appl. Mater. Interfaces* **2017**, 9(1), 592–601.

[20] Kim, H., Kellock, A. J., and Rossnagel, S. M., *J. Appl. Phys.* **2002**, 92(12), 7080–7085.

[21] Kim, H., Detavenier, C., Van Der Straten, O., Rossnagel, S. M., Kellock, A. J., and Park, D. G., *J. Appl. Phys.* **2005**, 98(1), 014308.
[22] Kim, J. Y., Seo, S., Kim, D. Y., Jeon, H., and Kim, Y., *J. Vac. Sci. Technol. A Vacuum, Surfaces, Film.* **2004**, 22(1), 8–12.
[23] Alevli, M., Ozgit, C., Donmez, I., and Biyikli, N., *J. Cryst. Growth* **2011**, 335(1), 51–57.
[24] Chung, H.-S., Kwon, J.-D., and Kang, S.-W., *J. Electrochem. Soc.* **2006**, 153(11), C751.
[25] Yoon, J., Lee, H.-B.-R., Kim, D., Cheon, T., Kim, S.-H., and Kim, H., *J. Electrochem. Soc.* **2011**, 158(11), H1179.
[26] Hong, T. E., Mun, K.-y., Choi, S.-k., Park, J.-y., Kim, S.-H., Cheon, T., *et al.*, *Thin Solid Films* **2012**, 520(19), 6100–6105.
[27] Van Helden, J. H., Van Den Oever, P. J., Kessels, W. M. M., Van De Sanden, M. C. M., Schram, D. C., and Engeln, R., *J. Phys. Chem. A* **2007**, 111(45), 11460–11472.
[28] Van Helden, J. H., Wagemans, W., Yagci, G., Zijlmans, R. A. B., Schram, D. C., Engeln, R., *et al.*, *J. Appl. Phys.* **2007**, 101(4), 043305.
[29] Ritala, M., Kalsi, P., Riihelä, D., Kukli, K., Leskelä, M., and Jokinen, J., *Chem. Mater.* **1999**, 11(7), 1712–1718.
[30] Alén, P., Juppo, M., Ritala, M., Sajavaara, T., Keinonen, J., and Leskelä, M., *J. Electrochem. Soc.* **2002**, 148(10), G566.
[31] Hämäläinen, J., Ritala, M., and Leskelä, M., *Chem. Mater.* **2014**, 26(1), 786–801.
[32] Hämäläinen, J., Puukilainen, E., Sajavaara, T., Ritala, M., and Leskelä, M., *Thin Solid Films* **2013**, 531, 243–250.
[33] Hämäläinen, J., Puukilainen, E., Kemell, M., Costelle, L., Ritala, M., and Leskelä, M., *Chem. Mater.* **2009**, 21(20), 4868–4872.
[34] Lu, J. and Elam, J. W., *Chem. Mater.* **2015**, 27(14), 4950–4956.
[35] Mackus, A. J. M., Garcia-Alonso, D., Knoops, H. C. M., Bol, A. A., and Kessels, W. M. M., *Chem. Mater.* **2013**, 25(9), 1769–1774.
[36] Weber, M. J., Mackus, A. J. M., Verheijen, M. A., Longo, V., Bol, A. A., and Kessels, W. M. M., *J. Phys. Chem. C* **2014**, 118(16), 8702.
[37] Knoops, H. C. M., Mackus, A. J. M., Donders, M. E., van de Sanden, M. C. M., Notten, P. H. L., and Kessels, W. M. M., *Electrochem. Solid-State Lett.* **2009**, 12(7), G34.
[38] Putkonen, M., Szeghalmi, A., Pippel, E., and Knez, M., *J. Mater. Chem.* **2011**, 21(38), 14461–14465.
[39] Weimer, M. S., Kim, I. S., Guo, P., Schaller, R. D., Martinson, A. B., and Hock, A. S., *Chem. Mater.* **2017**, 29(15), 6238–6244.
[40] Delabie, A., Caymax, M., Groven, B., Heyne, M., Haesevoets, K., Meersschaut,

J., *et al.*, *Chem. Commun.* **2015**, 51(86), 15692–15695.
[41] Groven, B., Heyne, M., Nalin Mehta, A., Bender, H., Nuytten, T., Meersschaut, J., *et al.*, *Chem. Mater.* **2017**, 29(7), 2927–2938.
[42] Illiberi, A., Scherpenborg, R., Wu, Y., Roozeboom, F., and Poodt, P., *ACS Appl. Mater. Interfaces* **2013**, 5(24), 13124–13128.
[43] Pan, X., Wang, X., Xiao, H., Wang, C., Yang, C., Li, W., *et al.*, *Appl. Surf. Sci.* **2011**, 257(20), 8718–8721.
[44] Frijters, C. H., Poodt, P., and Illiberi, A., *Sol. Energy Mater. Sol. Cells* **2016**, 155, 356–361.
[45] Illiberi, A., Frijters, C., Ruth, M., Bremaud, D., Poodt, P., Roozeboom, F., *et al.*, *J. Vac. Sci. Technol. A* **2018**, 36(5), 051511.
[46] Elam, J. W., Sechrist, Z. A., and George, S. M., *Thin Solid Films* **2002**, 414(1), 43–55.
[47] Elam, J. W. and George, S. M., *Chem. Mater.* **2003**, 15(4), 1020–1028.
[48] Kukli, K., Kemell, M., Vehkamäki, M., Heikkilä, M. J., Mizohata, K., Kalam, K., *et al.*, *AIP Adv.* **2017**, 7(2), 025001.
[49] Riedel, S., Neidhardt, J., Jansen, S., Wilde, L., Sundqvist, J., Erben, E., *et al.*, *J. Appl. Phys.* **2011**, 109(9), 094101.
[50] Lancaster, D. K., Sun, H., and George, S. M., *J. Phys. Chem. C* **2017**, 121(34), 18643–18652.
[51] Boutros, K. S., McIntosh, F. G., Roberts, J. C., Bedair, S. M., Piner, E. L., and ElâMasry, N. A., *Appl. Phys. Lett.* **1995**, 67(13), 1856–1858.
[52] Schneider, N., Bouttemy, M., Genevée, P., Lincot, D., and Donsanti, F., *Nanotechnology* **2015**, 26(5), 054001.
[53] Xie, J., Sendek, A. D., Cubuk, E. D., Zhang, X., Lu, Z., Gong, Y., *et al.*, *ACS Nano* **2017**, 11(7), 7019–7027.
[54] Wiegand, C. W., Faust, R., Meinhardt, A., Blick, R. H., Zierold, R., and Nielsch, K., *Chem. Mater.* **2018**, 30(6), 1971–1979.
[55] Na, J. S., Scarel, G., and Parsons, G. N., *J. Phys. Chem. C* **2010**, 114(1), 383–388.
[56] Wu, Y., Potts, S. E., Hermkens, P. M., Knoops, H. C. M., Roozeboom, F., and Kessels, W. M. M., *Chem. Mater.* **2013**, 25(22), 4619–4622.
[57] Vandalon, V. and Kessels, W. M. M., *Appl. Phys. Lett.* **2016**, 108(1), 1–5.
[58] Hashemi, F. M. S., Prasittichai, C., and Bent, S. F., *ACS Nano* **2015**, 9(9), 8710–8717.
[59] Vallat, R., Gassilloud, R., Salicio, O., El Hajjam, K., Molas, G., Pelissier, B., *et al.*, *J. Vac. Sci. Technol. A* **2019**, 37(2), 020918.

Atomic Layer Deposition of Aluminum Fluoride using $Al(CH_3)_3$ and SF_6 plasma

4

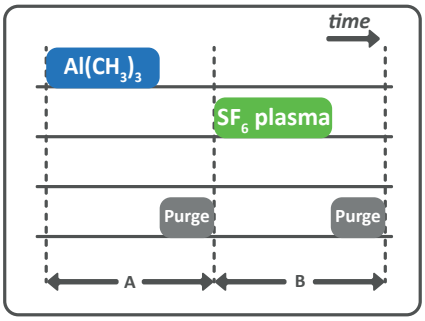

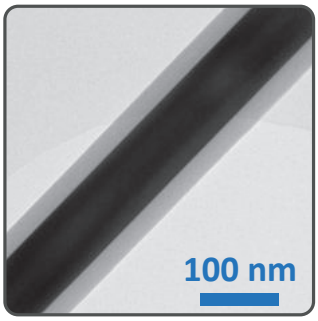

Metal fluorides typically have a low refractive index and a very high transparency and find many applications in optical and optoelectronic devices. Nearly stoichiometric, high-purity AlF_3 films were deposited by atomic layer deposition (ALD) using trimethylaluminum (TMA, $Al(CH_3)_3$) and SF_6 plasma. Self-limiting growth was confirmed and the growth per cycle (GPC) was determined to range from 1.50 Å to 0.55 Å for deposition temperatures between 50 °C to 300 °C. In addition, the film density of $\sim$2.8 g·cm^{-3} was found to be relatively close to the bulk value of 3.1 g·cm^{-3}. Spectroscopic ellipsometry (SE) measurements over the wavelength range of 140 - 2275 nm showed a refractive index n of 1.35 at 633 nm, and an extinction coefficient k of $<10^{-4}$ above 300 nm, for all deposition temperatures. Optical emission spectroscopy (OES) during the SF_6 plasma exposure step of the ALD cycle revealed the consumption of F radicals and the formation of C_2H_2 and CF_2 species, resulting from the interaction of the plasma with the surface after $Al(CH_3)_3$ exposure. On the basis of these results and insights from the literature a reaction mechanism is proposed in which F radicals from the SF_6 plasma participate in the surface reactions. Overall this work demonstrates that SF_6 plasma is a promising co-reactant for ALD of metal fluorides, providing an alternative to co-reactants such as metal fluorides, HF or HF-pyridine.

Published as: M.F.J. Vos, H.C.M. Knoops, R.A. Synowicki, W.M.M. Kessels and A.J.M. Mackus, *Appl. Phys. Lett* **111**, 113105 (2017).

4.1 Introduction

Metal fluorides such as AlF_3, MgF_2 and CaF_2 generally have a wide bandgap (>10 eV) and low refractive index (1.3-1.6).[1–4] Due to these properties they find use in many optical devices, including waveguides, Bragg reflectors, optical filters, and mirrors.[5–9] Moreover, metal fluorides have been used as electron-selective contacts in photovoltaics and protective layers in Li-ion batteries.[10–12] Thin metal fluoride films have been deposited using a variety of techniques such as sputtering, evaporation, and more recently atomic layer deposition (ALD).

ALD is a chemical vapor deposition technique that is based on alternating precursor and co-reactant exposures. Compared to other deposition techniques, ALD offers the benefits of precise thickness control and the ability to deposit uniform and conformal films on large-area substrates.[13] These merits can facilitate applications of metal fluorides such as 3D-nanostructured optical devices and batteries. Mostly metal oxides have been explored by ALD, often using H_2O, O_3, or O_2 plasma as the co-reactant.[14] Metal nitrides have also been studied extensively, in this case mainly with NH_3 gas or H_2, N_2, and NH_3-based plasmas. The choice of co-reactant is not only important for determining the type of material that is deposited (oxide, nitride, etc.) but also since it often affects the deposition conditions (such as deposition temperature) and the threshold for industrial implementation. In this respect, ALD of metal fluorides is more challenging, due to limited choice of suitable co-reactants. Previously, ALD of fluorides has been demonstrated using TiF_4 and TaF_5 as the F-source for the deposition of AlF_3, MgF_2, CaF_2, LiF, and LaF_3, which can be accompanied by Ti or Ta incorporation.[15–19] More recently, AlF_3, ZrF_4, MnF_2, HfF_2, MgF_2 and ZnF_2 have been deposited by HF either using pure HF or a HF-pyridine solution.[9,20–22] Lee *et al.* gave insight into the reaction mechanisms during ALD using HF as the co-reactant and postulated that HF adsorbed on the surface serves as the reactive sites for the precursor molecules to bind.[21,22] Moreover, DumMnt and George found that the temperature dependence of the growth per cycle (GPC) can be explained by the amount of HF adsorbed on AlF_3, which decreases with temperature.[23]

In this work, SF_6 plasma was explored as the co-reactant for ALD of metal fluorides. Using trimethylaluminum (TMA, $Al(CH_3)_3$) as precursor and SF_6 plasma as F-source, high-purity AlF_3 films were deposited in an Oxford Instruments FlexAL ALD reactor. It is demonstrated that this approach is a promising alternative to HF or HF-pyridine as co-reactant. As compared to thermal ALD, the use of a plasma as co-reactant generally allows for an increased GPC at lower temperatures, reduction of the purge times and additional control over the material properties.[24] SF_6 is a stable, non-toxic gas that is relatively easy to handle and therefore commonly

applied. The dominant neutral species in an inductively-coupled SF_6 plasma are known to be SF_6, F, F_2 and SF_4, while the dominant ions are SF_5^+ and F^-.[25–27] The concentration of S and S^+ is typically a factor $\sim 10^3$ lower than the concentration of F and F^-.[25] SF_6 plasmas, as well as other F-containing plasmas such as CF_4 and NF_3 are extensively used for etching (Si, SiO_2, Si_3N_4, ...) and chamber cleaning, meaning that the existing knowledge can be utilized for ALD process development. Moreover, F-based plasmas are widely available both in research and manufacturing, which can facilitate the implementation and scale-up of plasma ALD of metal fluorides.[28]

4.2 Results and discussion

To confirm ALD behavior, the GPC was determined using *in situ* spectroscopic ellipsometry (SE) as a function of TMA dosing time, plasma exposure time and purge times at a deposition temperature of 200 °C.[29] The saturation curve for the plasma exposure time in Figure 4.1 clearly indicates saturation around 5-10 seconds. 20 cycles of Al_2O_3 ALD were performed prior to AlF_3 deposition to prevent etching of the Si (100) substrate. See the Supporting Information ()S.I.) for additional experimental details. The GPC as a function of precursor dosing time was found to saturate after 40 ms, and self-limiting behavior was also confirmed as a function of both purge times and for a deposition temperature of 50 °C (Figure S4.1, S.I.). Based on the saturation curves, a TMA dose of 80 ms, followed by a purge step of 6 s, a plasma exposure of 10 s and a final purge step of 4 s were used for the remainder of the experiments.

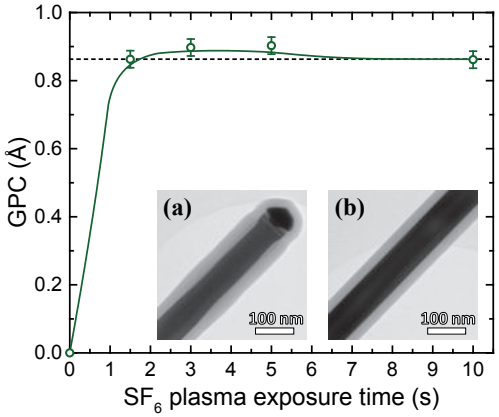

Figure 4.1 Growth per cycle (GPC) as a function of plasma exposure time for a precursor dosing time of 40 ms and a deposition temperature of 200 °C. The line serves as a guide to the eye. Inset: TEM images of (a) the top and (b) the middle of a GaP nanowire ($\sim$7 µm in length) after deposition of a $\sim$20 nm AlF_3 film at 200 °C, illustrating the conformality of the ALD process.

The uniformity and conformality were investigated (without additional optimization) to further demonstrate the ALD behavior of the process. Using SE-mapping of a film deposited on a 200 mm wafer, the thickness and refractive index non-uniformity (standard deviation, 1 sigma) were determined to be 3.9 % and 0.3 %, respectively, which indicates good uniformity (see Figure 4.2). The conformality was studied by depositing AlF_3 on a GaP nanowire array and analyzing separated nanowires using transmission electron microscopy (TEM). The ∼7 µm long nanowires were randomly located on the substrate, spaced at 0 nm - 500 nm (meaning that the ratio between the length and spacing is 14 or higher). The TEM pictures in the inset of Figure 4.1 clearly show a conformal, ∼20 nm thick film along the full length of a nanowire (see also Figure S4.2, S.I.). The ratio between the thickness at the bottom and the top of the nanowire was determined to be >0.9, indicating a SF_6 plasma can enable conformal deposition on 3D structures.

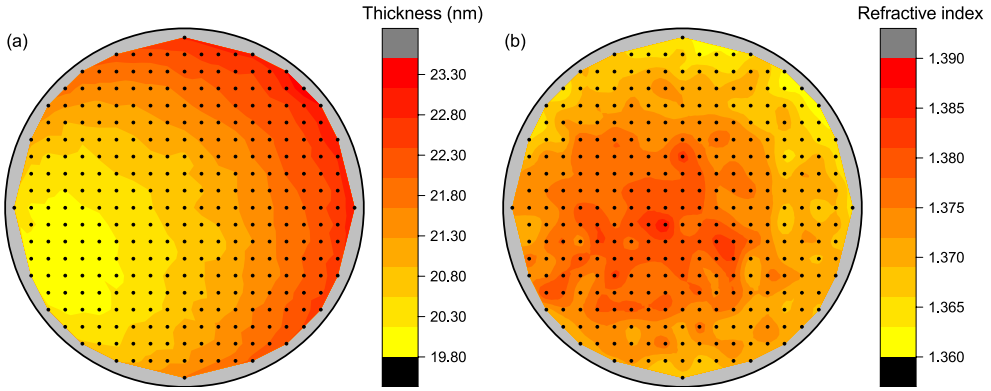

Figure 4.2 Contour maps of (a) the AlF_3 thickness and (b) the refractive index *n* across a 200 mm wafer as determined from SE-mapping. 300 ALD cycles were performed at a table temperature of 200 °C. The grey circle indicates the dimensions of the wafer and an edge-exclusion of 5 mm was used. The thickness and refractive index non-uniformity (standard deviation, 1 sigma) were determined from these maps to be 3.9 % and 0.3 %, respectively. The TMA inlet is located at the top-right of the wafer and the thickness gradient towards the bottom-left seems to correlate with the flux of TMA.

The effect of the table temperature on the growth of the AlF_3 films was investigated by depositing films at temperatures of 50 °C, 100 °C, 200 °C and 300 °C. The thickness as a function of ALD cycles in the inset of Figure 4.3 shows a linear behavior for all temperatures as is expected for ALD. The GPC in terms of thickness as determined from SE in Figure 4.3 is strongly dependent on the table temperature and decreases from 1.50 Å for a temperature of 50 °C to 0.55 Å for 300 °C. The GPC in terms of Al atoms deposited per nm^{-2} as determined from Rutherford backscattering spectroscopy (RBS) follows a similar trend. This

indicates the decrease in GPC is not caused by an increased atomic density at higher temperatures, but rather by reduced precursor adsorption. The decrease in GPC with temperature is similar to the observations by Lee *et al.* and Hennessy *et al.* for thermal ALD of AlF_3 using HF as co-reactant.[9,21] This trend is likely related to a reduced amount of HF adsorbed on the surface at higher temperatures, leading to decreased TMA adsorption in the precursor sub-cycle, which is analogous to dehydroxylation for metal oxide ALD.[23] A transition from AlF_3 ALD to Al_2O_3 atomic layer etching (ALE) as found by Lee *et al.* above 250 °C was however not observed. This difference can be explained by the fact that our actual sample temperature is lower than the set table temperature due to reduced thermal contact in vacuum (see also the Supporting Information, S.I.).

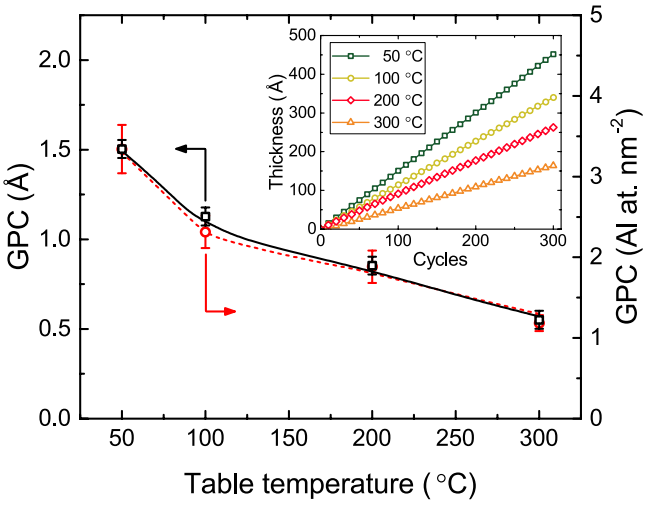

Figure 4.3 Growth per cycle (GPC) as a function of substrate table temperature in terms of thickness as determined from SE (left axis) and deposited Al atoms per nm^2 as measured by RBS (right axis). The lines serve as guides to the eye. Inset: Thickness as a function of ALD cycles for deposition temperatures between 50 °C and 300 °C.

Table 4.1 summarizes the properties of the AlF_3 films as determined by a combination of SE, RBS and elastic recoil detection (ERD) measurements. No significant impurity levels of S, O and C were detected in the AlF_3 films using RBS, even for low deposition temperatures. The S-content was found to be 0.5 at.% for a deposition temperature of 50 °C and decreased to below the detection limit for 300 °C. The minimal amount of S incorporation can be explained by the difference in reactivity of F and S. From a comparison of the electronegativity and electron

affinity of F and S it becomes evident that it is much more likely to incorporate F.[30] Furthermore, RBS measurements showed a F/Al ratio of 2.9-3.1 and an O content of around 0.5-1 at.%. From ERD, the H content of the AlF_3 films was determined to be between 3.2 at.% and 1.3 at.%. These results are in agreement with XPS measurements (see Figure S4.3, S.I.). Using the RBS, ERD and SE data, the density of the films was calculated to be between 2.7 g·cm^{-3} and 2.9 g·cm^{-3}, which is relatively close to the AlF_3 bulk value of 3.1 g·cm^{-3}. Moreover, atomic force microscopy (AFM) measurements indicated very smooth films with root mean square (RMS) roughness values $\leq$0.2 nm (see Figure S4.4, S.I.). Grazing-incidence X-ray diffraction (XRD) measurements revealed that the films were amorphous for all deposition temperatures (see Figure S4.5, S.I.), which is in line with the low surface roughness. Note that the obtained properties are very similar to the results reported for AlF_3 ALD using HF as co-reactant.[21]

Table 4.1 Properties of AlF_3 films for deposition temperatures (T) between 50 °C - 300 °C. The growth per cycle (GPC) in terms of Al atoms nm^{-2} cycle^{-1} and the chemical composition were determined from RBS and ERD, the refractive index from SE, and the mass density by combining the RBS and SE results. Typical errors are indicated in the top row, unless the error varies with temperature.

T (°C)	GPC (Å)	GPC (Al at. nm^{-2})	F/Al	[S] (at. %)	[H] (at. %)	Mass density (g cm^{-3})	Refractive index
50	1.50 ± 0.05	3.3 ± 0.3	3.1 ± 0.5	0.5 ± 0.1	3.2 ± 0.8	2.8 ± 0.3	1.35 ± 0.01
100	1.13	2.3 ± 0.2	3.1	0.3	2.3 ± 0.5	2.7	1.34
200	0.85	1.9 ± 0.2	2.9	0.2	1.7 ± 0.3	2.9	1.35
300	0.55	1.2 ± 0.1	2.9	0.0	1.3 ± 0.2	2.7	1.35

Figure 4.4 shows the optical properties as obtained from VUV/VIS/NIR (vacuum ultraviolet/visible/near-infrared, 140 - 2275 nm) SE measurements for an AlF_3 film deposited at 200 °C.[31] The refractive index n is ~1.35 at 633 nm (1.96 eV) and the film shows a relatively low dispersion (i.e. a weak dependence of n on wavelength). The refractive index values for the other deposition temperatures are similar with values between 1.34 and 1.36 at 633 nm (see Figure S4.6a, S.I.). The extinction coefficient k is $<10^{-6}$ over the wavelength range of 300 - 2275 nm for a deposition temperature of 200 °C (Figure 4.4). Moreover, the inset of Figure 4.4 shows low absorption for all other deposition temperatures, i.e. $<10^{-4}$ below photon energies of 4.1 eV (wavelengths >300 nm). The extinction

coefficient for 50 °C is higher than for 100 °C and 200 °C, which might be related to a higher S content at 50 °C. The reason for the increased absorption for 300 °C is currently not understood and requires additional investigation. To obtain a good fit to the data, a Tauc-Lorentz and two Gaussian oscillators were needed to describe the dielectric function. The two Gaussian oscillators used to fit the absorption below the band gap are visible at photon energies around 6.4 eV and 7.8 eV (inset Figure 4.4). The presence of an absorption band around 6.4 eV was previously observed by Barriere *et al.*[1] Note that the band gap (>10 eV) cannot be determined from the VUV/VIS/NIR-SE data since it lies above the maximum photon energy of 8.8 eV. The refractive index values of ∼1.35 are in agreement with AlF_3 films prepared by ALD using HF and TiF_4 as the co-reactants.[16,21] Moreover, the obtained *n* and *k* values are close to what can be expected for AlF_3 and indicate that SF_6 plasma enables ALD of high-quality metal fluoride films.[1–3]

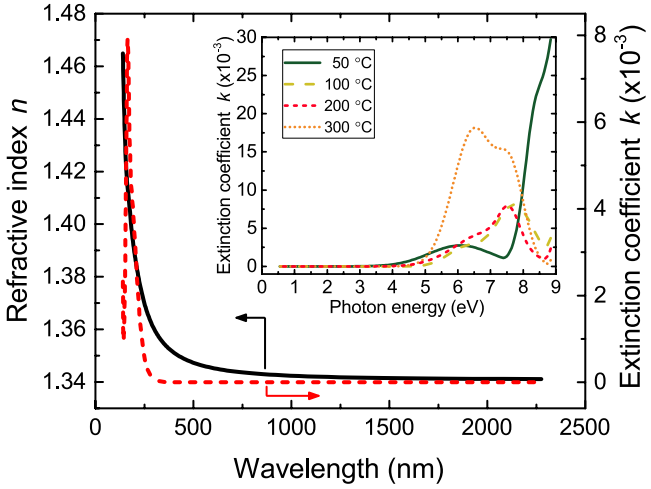

Figure 4.4 Refractive index n and extinction coefficient k as a function of wavelength as determined from VUV/VIS/NIR-SE for a ∼35 nm thick film deposited at a temperature of 200 °C. Inset: Extinction coefficient *k* as a function of photon energy for deposition temperatures between 50 °C and 300 °C.

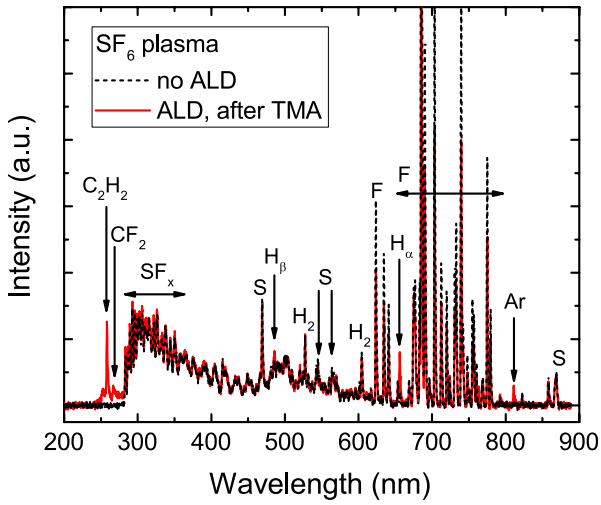

Figure 4.5 Optical emission spectra of an SF_6 plasma ('no ALD') and an SF_6 plasma during an AlF_3 ALD cycle ('ALD, after TMA'). In the latter case, in addition to lines related to the SF_6 plasma and reaction products, an Ar line is visible at 811.5 nm, which is due to Ar residing in the chamber after the preceding purge step. The SF_6 gas flow was set to 50 sccm (instead of 100 sccm) to increase the residence time of the species in the plasma.

To get more insight into the SF_6 plasma as co-reactant for ALD, Figure 4.5 shows optical emission spectrometry (OES) data collected during a steady-state SF_6 plasma (no ALD, i.e. without preceding TMA dosing) and during the plasma exposure step of an AlF_3 ALD cycle (i.e. after TMA dosing).[32] Comparison of the two spectra gives insight in the consumption and formation of species during the plasma exposure step of the ALD cycle. The spectrum for the normal SF_6 plasma is dominated by characteristic lines for F at 685.6 nm, 703.7 nm and 739.9 nm.33 In addition, the SF_x band starting at 289.3 nm and the S-lines at 469.4 nm, 545.4 nm and 564.0 nm can be identified.[33,34] Furthermore, H-lines at 486.1 nm and 656.3 nm are present, which can be attributed to residual background species (e.g. H_2O) in the plasma.[33] In the OES spectrum collected during an ALD cycle (after TMA dosing) additional lines are visible around 250 nm - 300 nm, indicating the formation of C_2H_2 and CF_2 as reaction products.[35–39] Moreover, this spectrum shows a decreased intensity for the F-lines, implying consumption of F, and an increased intensity for the H-lines, related to excitation of hydrogen from the methyl groups (see Figure S4.7, S.I. for a zoom of the region between 650 nm and 800 nm). These observations indicate that F radicals react with methyl surface groups during the SF_6 plasma exposure step, which leads to formation of hydrofluorocarbons (CH_yF_{4-y}), both in surface and plasma reactions. The

presence of C_2H_2 can be explained by the reaction of hydrofluorocarbons in the plasma (see below).[39] Based on these findings, and on the work of Lee *et al.*[21], the following reaction equations can be proposed for the two sub-cycles:

$$HF_{\ (ads)} + Al(CH_3)_{3\ (g)} \rightarrow AlF(CH_3)_{2\ (ads)} + CH_{4\ (g)}, \tag{4.1}$$

$$AlF(CH_3)_{2\ (ads)} + F_{\ (g)} \rightarrow AlF_{3\ (s)} + HF_{\ (ads,g)} + CH_yF_{4-y\ (g)}. \tag{4.2}$$

For simplicity, these equations are written unbalanced and it is assumed that the hydrofluorocarbon species (CH_yF_{4-y}) contain only one C atom with $0 \leq y \leq 3$. In the first sub-cycle (Equation 4.1), the TMA molecule reacts with HF adsorbed on the surface, releasing CH_4 as product.[21] In this way, the density of HF on the surface determines the amount of TMA precursor adsorption. The temperature dependence of the HF surface density can thus explain the decrease of GPC with temperature.[23] Note that Equation 4.1 states that one methyl group is eliminated upon precursor adsorption, although removal of two or three methyl groups may also be possible. In the plasma sub-cycle (Equation 4.2), the adsorbed $AlF(CH_3)_2$ reacts with F radicals from the plasma, forming HF, which partly remains on the surface, and CH_yF_{4-y} species, which are released from the surface and end up in the plasma where they can be dissociated and form other species. The reaction mechanism for thermal ALD with HF is different, as only CH_4 is produced in both sub-cycles.[21] Note that the release of CH_4 ($y = 4$) as a reaction product in the SF_6 plasma sub-cycle requires a source of H, such as HF. However HF is formed according to Equation 4.2 and can enable a secondary, thermal reaction pathway, resulting in the release of CH_4. This CH_4 can subsequently react in the plasma to form C_2H_2.[39] It is noted the presence of HF, CH_4, C_2H_2 and CH_yF_{4-y} species was corroborated using quadrupole mass spectrometry (see Figure S4.8, S.I.), as will be discussed in more detail in Chapter 5.

4.3 Conclusion

In conclusion, it was demonstrated that the ALD process using TMA and SF_6 plasma yields high-purity, nearly stoichiometric AlF_3 films. Self-limiting behavior was confirmed for all process steps and the GPC was found to decrease with temperature. In addition, material properties such as density and refractive index were found to be in line with literature reports on AlF_3. A reaction mechanism was proposed where F radicals remove the CH_3-ligands and bind to Al to form AlF_3. CH_4 is released as reaction product in the precursor sub-cycle, whereas HF and hydrofluorocarbons are released during the plasma exposure. Considering the high reactivity of SF_6 plasma and the low amount of S incorporation in the films, SF_6 plasma can likely be used as the co-reactant for ALD of other metal fluorides

such as MgF_2, LiF and CaF_2. Moreover it can be expected that NF_3 can be used similarly. The wide availability and the ease of handling of these gases make plasma ALD of metal fluorides feasible on a wide scale.

Acknowledgements

This work was financially supported by the Zwaartekracht program of the Netherlands Organisation for Scientific Research (NWO). The authors gratefully acknowledge C.A.A. van Helvoirt and J. van Gerwen for technical assistance and A. Kurek from Oxford Instruments Plasma Technology for performing the SE-mapping measurements. The authors would also like to thank Dr. S. Assali and L. Gagliano for providing the GaP nanowires and Dr. M. A. Verheijen for the TEM analysis. Solliance and the Dutch province of Noord-Brabant are acknowledged for funding the TEM facility.

4.4 Supporting Information

Additional experimental details

All depositions were done in an Oxford Instruments FlexAL reactor, which reaches a base pressure of $\sim 10^{-6}$ Torr. An activated carbon filter is installed on the reactor, and no special calcium oxide filter was used to neutralize the HF that is produced during the ALD process. The reactor is however situated inside a cleanroom and all exhaust gasses go through a gas scrubber before being released into the environment. The FlexAL reactor is equipped with an inductively coupled plasma (ICP) source, operated at a radiofrequency of 13.56 MHz and typically a power of 300 W. The TMA precursor (Sigma Aldrich, $>$99.9999%) was contained in a stainless steel bubbler, kept at a temperature of 30 °C. The precursor line was heated to 60 °C to avoid condensation of the precursor. The chamber pressure was set to 15 mTorr and 50 mTorr during the TMA dose and SF_6 plasma exposure, respectively. During the ALD cycle 100 sccm SF_6 gas was continuously injected from the top of the ICP source. It was confirmed that no growth occurs without igniting the plasma, indicating TMA does not react with SF_6 gas. Depositions were performed on Si (100) with native oxide (Siegert Wafer, 10-20 Ohm cm). Prior to any film deposition the samples were cleaned with an O_2 plasma for 30 s. To avoid etching of the Si, 20 Al_2O_3 ALD cycles were performed using TMA and O_2 plasma, prior to deposition of the AlF_3, at the same deposition temperature as the subsequent AlF_3 deposition.

The characterization of the ALD process was done on small pieces of wafer, which were placed on a 200 mm carrier wafer. Depositions were performed at a table temperature between 50 °C and 300 °C. The FlexAL is a warm wall reactor, and for depositions at a table temperature of 100 °C and higher the wall temperature was set to 120 °C. For deposition at a table temperature of 50 °C the wall was set to 50 °C. Note that the actual temperature of the samples is lower than the table temperature due to reduced thermal contact in vacuum.[40] Since the pressure during the ALD process is 15 - 50 mTorr, the difference between the table temperature and actual sample temperature is quite significant. This temperature deviation can explain why we do not observe etching at temperatures above 250 °C in contrast to the work of Lee *et al.* (performed at $\sim$1 Torr in a hot wall reactor).

The growth of the AlF_3 films was monitored *in situ* by spectroscopic ellipsometry (SE) using a J.A. Woollam Co., Inc. M2000U ellipsometer. In order to obtain the optical properties of the AlF_3 films over the wavelength range of 140 nm - 2275 nm *ex situ* SE measurements were performed using a vacuum ultraviolet ellipsometer (VUV/VIS/NIR range) at J.A. Woollam Co., Inc. For the *in situ* SE and the SE-mapping measurements (both 245 nm - 1000 nm) the dielectric function of the films was parameterized using a Cauchy model, since the films are transparent over this full wavelength range. For the *ex situ* VUV/VIS/NIR-SE measurements (140 nm - 2275 nm) the model consisted of a combination of a Tauc-Lorentz and two Gaussian oscillators.

Optical emission spectroscopy (OES) was performed using a USB4000 spectrometer from OceanOptics. Rutherford backscattering spectroscopy (RBS) and elastic recoil detection (ERD) were performed by Detect99 (Eindhoven, The Netherlands) using a Singletron with a 3 MeV He^+ beam to determine the chemical composition of the films. X-ray photoelectron spectroscopy (XPS) was done with a Thermo Scientific KA1066 spectrometer, using monochromatic Al Kα X-rays with an energy of 1486.6 eV. An Ar ion source was employed for depth profiling using an energy of 500 eV. A PANalytical X'Pert Pro MRD system was used for gracing-incidence X-ray diffraction (XRD) measurements, with Cu Kα X-rays (λ = 1.54 Å).

Self-limiting ALD growth

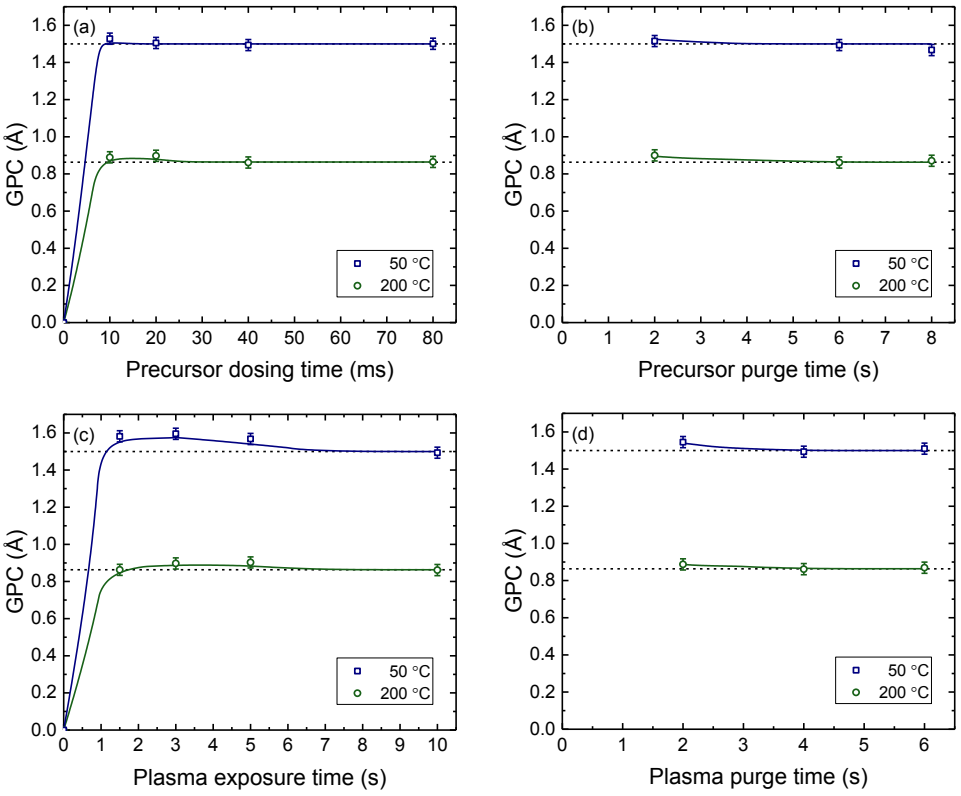

Figure S4.1 Growth per cycle (GPC) as a function of (a) precursor dosing time, (b) precursor purge time, (c) plasma exposure time and (d) plasma purge time for deposition at 50 °C and 200 °C. As can be seen, all saturation curves show self-limiting behavior. The fact that the precursor purge time also shows saturation for 50 °C confirms that the higher GPC at low temperature is not a consequence of precursor condensation. Based on these saturation curves, a TMA dose of 80 ms, followed by a purge step of 6 s, a plasma exposure of 10 s and a final purge step of 4 s where chosen as standard recipe. The lines serve as guides to the eye.

Conformality

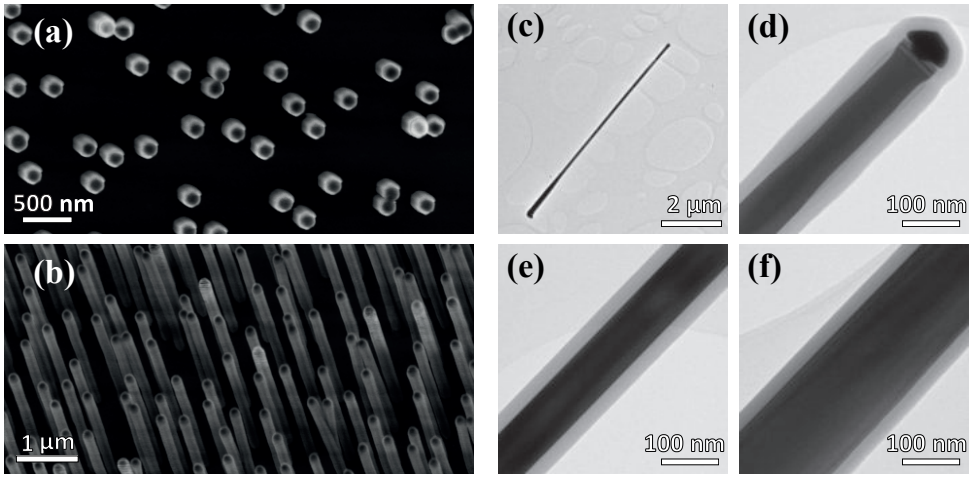

Figure S4.2 (a) Top-view and (b) tilt-view SEM images of the nanowire array after 300 cycles at a deposition temperature of 200 °C. The nanowires are randomly located on the substrate and the spacing is typically 0-500 nm. Note that figure (b) does not show the full length of the nanowires (∼7 µm). (c-f) TEM images of a GaP nanowire with a ∼20 nm AlF_3 film, originating from the array as shown in (a) and (b). Figure (c) indicates that the nanowires are ∼7 µm long. Figure (d), (e) and (f) show the top, middle and bottom of the nanowire, respectively. Prior to AlF_3 deposition the nanowire array was treated with 30 s O_2 plasma and 20 cycles Al_2O_3 ALD, which probably lead to slight oxidation of the top of the nanowire (figure (d)). The thickness of the nanowire increases to the bottom of the nanowire, while the AlF_3 thickness (∼20 nm) remains almost constant along the full length of the nanowire. The nanowire was part of the nanowire array during ALD.

Chemical composition from XPS

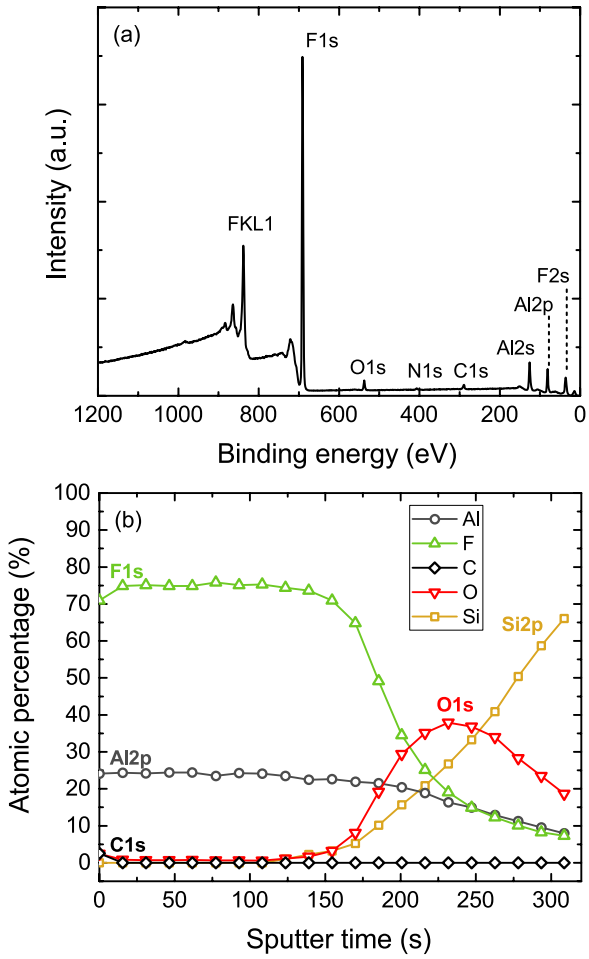

Figure S4.3 (a) XPS survey spectrum and (b) depth profile for an AlF_3 sample of ∼35 nm thick. 300 cycles were performed at a deposition temperature of 200 °C using the standard recipe. The survey spectrum was collected prior to Ar sputtering. No S and C were detected in the bulk of the film, and the amount of O incorporation is minimal (∼1 at.%). Moreover, the depth profile in (b) shows an F/Al ratio very close to 3. The presence of O at the Si interface is related to both the Al_2O_3 protection layer and a SiO_2 interlayer. Note that the XPS results are in line with the composition as determined from RBS/ERD measurements.

Atomic force microscopy

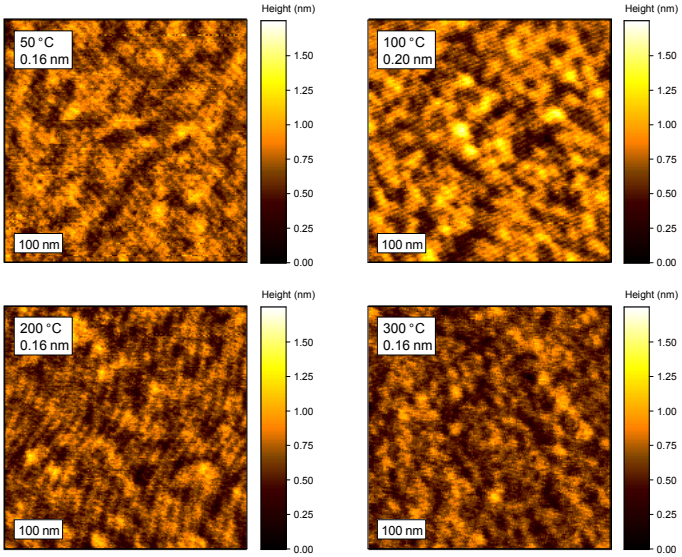

Figure S4.4 Atomic force microscopy (AFM) scans (0.5 µm x 0.5 µm) of AlF_3 films deposited at temperatures of 50 °C, 100 °C, 200 °C and 300 °C using the standard recipe. All films were between 25 nm and 35 nm thick and were smooth with a root mean square (RMS) roughness of $\leq$0.2 nm, as indicated in the top left of the figures.

Crystallinity from X-ray diffraction

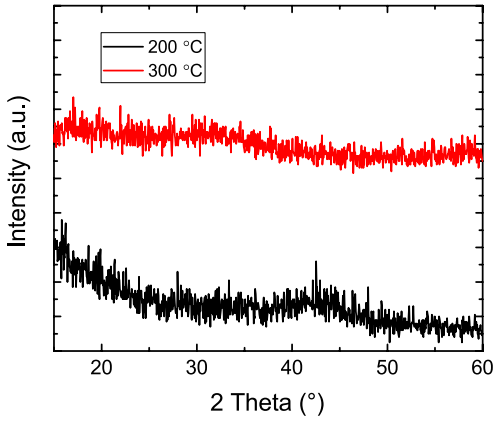

Figure S4.5 X-ray diffractograms for AlF_3 films deposited at 200 °C and 300 °C. The two diffractograms do not show any clear peaks, certainly not at the positions corresponding to AlF_3, indicating the films are predominantly amorphous in nature. This is in line with the literature on AlF_3 films prepared by ALD at these temperatures. Note that crystalline peaks for AlF_3 have been reported to be located at 25 °, 45 ° and 53 °.

Optical properties from SE

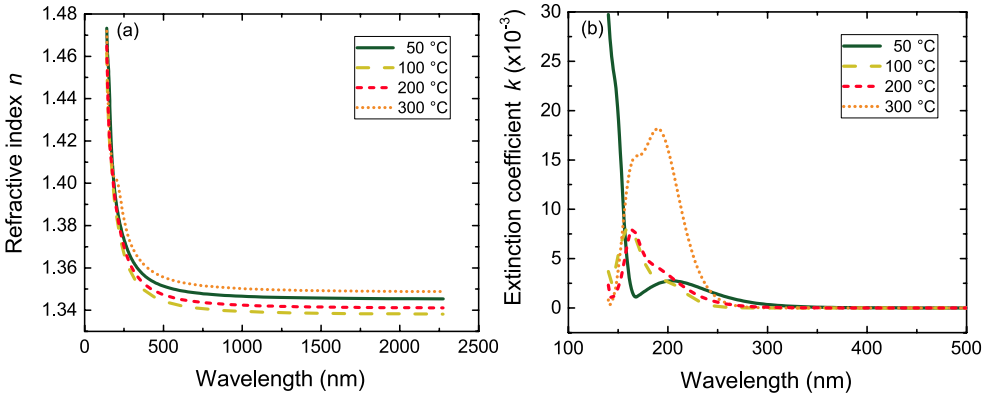

Figure S4.6 (a) Refractive index n over the wavelength range of 140-2275 nm for deposition temperatures between 50 °C and 300 °C. All n values are between 1.34 and 1.36 at 633 nm, which is in agreement with AlF_3 films prepared by ALD using HF and TiF_4 as the co-reactants. (b) Extinction coefficient k over the wavelength range of 140 - 500 nm for deposition temperatures between 50 °C and 300 °C. The extinction coefficient is nearly zero above 300 nm. For absorption below the band gap two Gaussian oscillators were used, as was discussed in the main text. By comparing the n and k values for all temperatures it can be concluded that the optical properties of the films deposited at 100 °C and 200 °C are closest to ideal AlF_3, i.e. low refractive index (∼1.34) and low absorption.

Optical emission spectroscopy

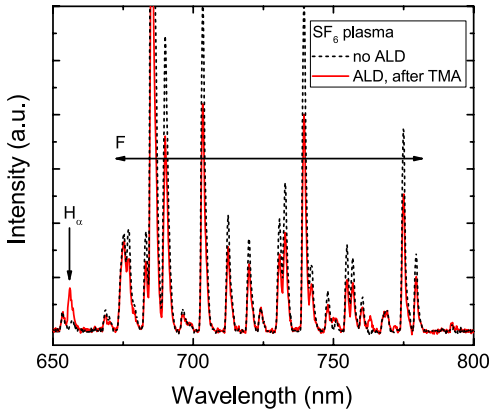

Figure S4.7 Optical emission spectra of an SF_6 plasma ('no ALD') and an SF_6 plasma during an AlF_3 ALD cycle ('ALD, after TMA'), over the wavelength range of 650 nm - 800 nm (zoom of Figure 4.5). The intensity of the characteristic F-lines (685.6 nm, 703.7 nm and 739.9 nm, among others) is lower in the spectrum collected during the ALD cycle as compared to the normal SF_6 spectrum ('no ALD'), indicating the consumption of F.

Quadrupole mass spectrometry

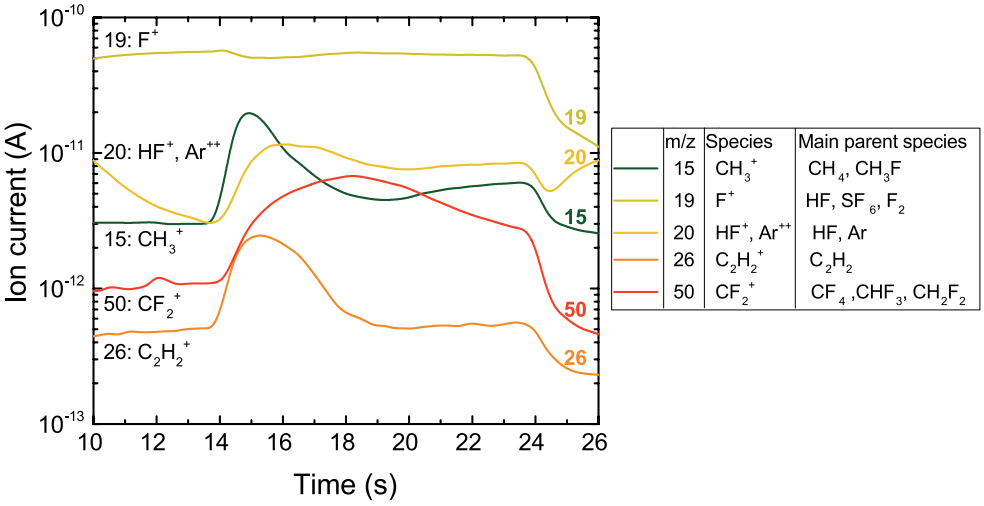

Figure S4.8 Time resolved QMS signals for selected m/z ratios (m/z = 15, 19, 20, 26, 50), collected during the plasma sub-cycle. The plasma is ignited at approximately 14 s and lasts 10 s. After the plasma starts HF (20), CH_4 (15), C_2H_2 (26) and CF_2 (50) are released, while F (19) is slightly consumed. Data over five ALD cycles were averaged to improve the signal to noise ratio.

References

[1] Barrière, A. and Lachter, A., *Appl. Opt.* **1977**, 16(11), 2865–2871.

[2] Sun, J., Li, X., Zhang, W., Yi, K., and Shao, J., *Appl. Opt.* **2012**, 51(35), 8481–8489.

[3] Liao, B.-H., Liu, M.-C., and Lee, C.-C., *Appl. Opt.* **2008**, 47(13), C41–5.

[4] Traylor Kruschwitz, J. D. and Pawlewicz, W. T., *Appl. Opt.* **1997**, 36(10), 2157.

[5] Zhang, L., Zhao, J.-h., Liu, P., Liu, T., Zhou, Y.-f., Yu, X.-f., *et al.*, *J. Light. Technol.* **2015**, 33(11), 2228–2232.

[6] Muallem, M., Palatnik, A., Nessim, G. D., and Tischler, Y. R., *ACS Appl. Mater. Interfaces* **2015**, 7(1), 474–481.

[7] Kedawat, G., Srivastava, S., Jain, V. K., Kumar, P., Kataria, V., Agrawal, Y., *et al.*, *ACS Appl. Mater. Interfaces* **2013**, 5(11), 4872–4877.

[8] Hennessy, J., Balasubramanian, K., Moore, C. S., Jewell, A. D., Nikzad, S., France, K., *et al.*, *J. Astron. Telesc. Instruments, Syst.* **2016**, 2(4), 041206.

[9] Hennessy, J., Jewell, A. D., Balasubramanian, K., and Nikzad, S., *J. Vac. Sci. Technol. A Vacuum, Surfaces, Film.* **2016**, 34(1), 01A120.

[10] Wan, Y., Samundsett, C., Bullock, J., Allen, T., Hettick, M., Yan, D., *et al.*, *ACS Appl. Mater. Interfaces* **2016**, 8(23), 14671–14677.

[11] Sun, Y. K., Lee, M. J., Yoon, C. S., Hassoun, J., Amine, K., and Scrosati, B., *Adv. Mater.* **2012**, 24(9), 1192–1196.

[12] Ding, F., Xu, W., Choi, D., Wang, W., Li, X., Engelhard, M. H., *et al.*, *J. Mater. Chem.* **2012**, 22(25), 12745.

[13] George, S. M., *Chem. Rev.* **2010**, 110(1), 111–131.

[14] Johnson, R. W., Hultqvist, A., and Bent, S. F., *Mater. Today* **2014**, 17(5), 236–246.

[15] Mäntymäki, M., Hämäläinen, J., Puukilainen, E., Munnik, F., Ritala, M., and Leskelä, M., *Chem. Vap. Depos.* **2013**, 19(4), 111–116.

[16] Mäntymäki, M., Heikkilä, M. J., Puukilainen, E., Mizohata, K., Marchand, B., Räisänen, J., *et al.*, *Chem. Mater.* **2015**, 27(2), 604–611.

[17] Pilvi, T., Hatanpää, T., Puukilainen, E., Arstila, K., Bischoff, M., Kaiser, U., *et al.*, *J. Mater. Chem.* **2007**, 17(48), 5077.

[18] Pilvi, T., Ritala, M., Leskelä, M., Bischoff, M., Kaiser, U., and Kaiser, N., *Appl. Opt.* **2008**, 47(13), C271.

[19] Pilvi, T., Puukilainen, E., Arstila, K., Leskelä, M., and Ritala, M., *Chem. Vap. Depos.* **2008**, 14(3-4), 85–91.

[20] Hennessy, J., Jewell, A. D., Greer, F., Lee, M. C., and Nikzad, S., *J. Vac. Sci. Technol. A Vacuum, Surfaces, Film.* **2015**, 33(1), 01A125.

[21] Lee, Y., DuMont, J. W., Cavanagh, A. S., and George, S. M., *J. Phys. Chem.*

C **2015**, 119(25), 14185.
[22] Lee, Y., Sun, H., Young, M. J., and George, S. M., *Chem. Mater.* **2016**, 28(7), 2022–2032.
[23] DuMont, J. W. and George, S. M., *J. Chem. Phys.* **2017**, 146(5), 1–10.
[24] Profijt, H. B., Potts, S. E., van de Sanden, M. C. M., and Kessels, W. M. M., *J. Vac. Sci. Technol. A Vacuum, Surfaces, Film.* **2011**, 29(5), 050801.
[25] Kokkoris, G., Panagiotopoulos, A., Goodyear, A., Cooke, M., and Gogolides, E., *J. Phys. D. Appl. Phys.* **2009**, 42(5), 055209.
[26] Mao, M., Wang, Y., and Bogaerts, A., *J. Phys. D. Appl. Phys.* **2011**, 44(43), 435202.
[27] Oh, S.-j., Lee, H.-c., Chung, C.-w., Oh, S.-j., Lee, H.-c., and Chung, C.-w., *Phys. Plasmas* **2017**, 24(1), 013512.
[28] D'Agostino, R. and Flamm, D. L., *J. Appl. Phys.* **1981**, 52(1), 162–167.
[29] Langereis, E., Heil, S. B. S., Knoops, H. C. M., Keuning, W., van de Sanden, M. C. M., and Kessels, W. M. M., *J. Phys. D. Appl. Phys.* **2009**, 42(7), 073001.
[30] Luo, Y.-R., *Comprehensive Handbook of Chemical Bond Energies*, CRC-Press, Boca Raton, FL, **2007**, ISBN 9780849373664.
[31] Hilfiker, J. N., Bungay, C. L., Synowicki, R. A., Tiwald, T. E., Herzinger, C. M., Johs, B., *et al.*, *J. Vac. Sci. Technol. A Vacuum, Surfaces, Film.* **2003**, 21(4), 1103–1108.
[32] Mackus, A. J. M., Heil, S. B. S., Langereis, E., Knoops, H. C. M., van de Sanden, M. C. M., and Kessels, W. M. M., *J. Vac. Sci. Technol. A Vacuum, Surfaces, Film.* **2010**, 28(1), 77–87.
[33] Sansonetti, J. E. and Martin, W. C., *J. Phys. Chem. Ref. Data* **2005**, 34(4), 1559–2259.
[34] Petrović, Z. L., Tochikubo, F., Kakuta, S., and Makabe, T., *J. Appl. Phys.* **1993**, 73(5), 2163–2172.
[35] Gaydon, R. and Pearse, A., *The Identification of Molecular Spectra*, Chapman & Hall, London, **1950**.
[36] Labelle, C. B. and Gleason, K. K., *J. Appl. Polym. Sci.* **2001**, 80(11), 2084–2092.
[37] Durrant, S. F., Mota, R. P., and Bica De Moraes, M. A., *J. Appl. Phys.* **1992**, 71(1), 448–455.
[38] Proshina, O. V., Rakhimova, T. V., Lopaev, D. V., Šamara, V., Baklanov, M. R., and de Marneffe, J.-F., *Plasma Sources Sci. Technol.* **2015**, 24(5), 055006.
[39] Majumdar, A., Behnke, F., Hippler, R., Matyash, K., and Schneider, R., *J. Phys. Chem. A* **2005**, 109(41), 9371–9377.
[40] Knoops, H. C. M., Braeken, E. M. J., de Peuter, K., Potts, S. E., Haukka, S., Pore, V., *et al.*, *ACS Appl. Mater. Interfaces* **2015**, 7(35), 19857–19862.

Reaction Mechanisms during Atomic Layer Deposition of AlF_3 using $Al(CH_3)_3$ and SF_6 plasma

5

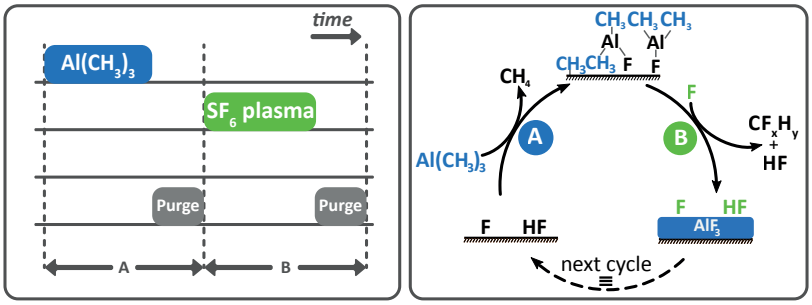

Metal fluorides generally demonstrate a wide band gap and a low refractive index and they are commonly employed in optics and optoelectronics. Recently, an SF_6 plasma was introduced as a novel co-reactant for atomic layer deposition (ALD) of metal fluorides. In this work, the reaction mechanisms underlying the ALD growth of aluminum fluoride (AlF_3) from $Al(CH_3)_3$ and an SF_6 plasma are investigated. Surface infrared spectroscopy studies suggested that $Al(CH_3)_3$ reacts with the surface in a ligand-exchange reaction by accepting F from the AlF_3 film, and forming CH_3 surface groups. It was found that at low deposition temperatures $Al(CH_3)_3$ also reacts with HF surface species. These HF species are formed during the SF_6 plasma exposure, and were detected both at the surface and in the gas-phase using infrared spectroscopy and mass spectrometry, respectively. Furthermore, mass spectrometry and optical emission spectroscopy measurements showed that CH_4 and CH_yF_{4-y} ($y \leq 3$) species are the main reaction products during the SF_6 plasma exposure. The CH_4 release is explained by the reaction of CH_3 ligands with HF, while CH_yF_{4-y} species originate from the interaction of the SF_6 plasma with CH_3 ligands. The obtained insights indicate a reaction pathway where F radicals from the SF_6 plasma eliminate the CH_3 ligands remaining after precursor dosing, and where F radicals are simultaneously responsible for the fluorination reaction. The understanding of the reaction mechanisms during AlF_3 growth can help in developing ALD processes for other metal fluorides (such as LiF, MnF_2, ZnF_2 and MgF_2) using SF_6 plasma as the co-reactant.

M.F.J. Vos, H.C.M. Knoops, W.M.M. Kessels and A.J.M. Mackus, in preparation for submission to *J. Phys. Chem. C*.

5.1 Introduction

Metal fluorides typically have a low refractive index (1.3-1.6) and a wide band gap (10 eV) and due to these properties they are widely used in optical devices.[1–6] For example, AlF_3 has been applied as protective coating for Al mirrors, while MgF_2/ZnS and CaF_2/ZnS multilayer films have been used for dielectric optical filters or Bragg reflectors, respectively.[5–8] Recently, metal fluorides, AlF_3 and LiF in particular, have also received considerable attention for application in Li-ion batteries, either as protective layer on electrodes or as active electrode material.[9–15] Furthermore, metal fluorides have been employed in photovoltaics, e.g. as electron-selective contact.[16–23] A variety of methods has been employed for deposition of metal fluorides, including evaporation,[1,24,25] sputtering,[26–28] ion-assisted deposition,[29–31] as well as atomic layer deposition (ALD).[7,8,32–38] Since ALD is a chemical vapor deposition technique that relies on sequential and self-limiting surface reactions, it typically results in ultrathin films which are highly uniform and conformal. These characteristics are often relevant for the aforementioned applications of metal fluorides.[39,40] ALD of metal fluorides has been reported using various co-reactants, such as NH_4F, the volatile metal fluorides TaF_5 and TiF_4, and HF.[7,8,32–38] Moreover, Lee *et al.* demonstrated ALD of AlF_3, ZrF_4, MnF_2, HfF_4, MgF_2 and ZnF_2 using HF from a HF-pyridine solution.[41,42] For thermal ALD of AlF_3 using HF, it was proposed that the reaction occurs according to the following two reaction equations:[41]

$$x\ HF_{\ (ads)} + Al(CH_3)_{3\ (g)} \ \rightarrow\ AlF_x(CH_3)_{3\text{-}x\ (ads)} + x\ CH_{4\ (g)}, \tag{5.1}$$

$$AlF_x(CH_3)_{3\text{-}x\ (ads)} + 3\ HF_{\ (g)} \ \rightarrow\ AlF_{3\ (s)} + x\ HF_{\ (ads)} + (3\text{-}x)\ CH_{4\ (g)}. \tag{5.2}$$

In the precursor sub-cycle (Equation 5.1), the $Al(CH_3)_3$ precursor reacts with HF that remained adsorbed to the surface after the preceding co-reactant sub-cycle. Upon this reaction with HF, one or more CH_4 molecules are released, resulting in $AlF_x(CH_3)_{3\text{-}x}$ ($x = 1, 2$) surface species. Based on quartz crystal microbalance (QCM) measurements, it was found that mainly $AlF(CH_3)_2$ is formed.[41] In the following co-reactant dose (Equation 5.2), the remaining CH_3 ligands combine with H (from HF) and are eliminated as CH_4, accompanied by the fluorination of the surface to AlF_3. The amount of $AlF_x(CH_3)_{3\text{-}x}$ species adsorbed to the surface was found to decrease with temperature, explaining why this ALD process is strongly dependent on the deposition temperature.[41,43] Interestingly, the temperature-dependent desorption of $AlF_x(CH_3)_{3\text{-}x}$ species makes that TMA and HF can also be used for atomic layer etching (ALE) of Al_2O_3 at temperatures $>$ $\sim$250 °C.[41,43,44]

The main reactions that govern this ALE process are given by:[44]

$$Al_2O_{3\ (s)} + 6\ HF_{\ (g)} \rightarrow 2\ AlF_{3\ (s)} + 3\ H_2O_{\ (g)}, \tag{5.3}$$

$$2\ AlF_{3\ (s)} + 4\ Al(CH_3)_{3\ (g)} \rightarrow 6\ AlF(CH_3)_{2\ (g)}\ \ (T > \sim 250°C). \tag{5.4}$$

In Equation 5.3, HF is responsible for the self-limiting fluorination of the Al_2O_3 surface. Subsequently, the formed AlF_3 surface layer can be removed by dosing $Al(CH_3)_3$, leading to the formation of volatile $AlF(CH_3)_2$, as described by Equation 5.4. The reaction in Equation 5.4 can be considered a ligand-exchange transmetalation reaction, where TMA accepts F, and donates CH_3 to the surface.[43,45] As mentioned, the volatility of $AlF_x(CH_3)_{3-x}$ species is dependent on the temperature, and desorption of these species at high temperatures enables ALE. In addition to the reaction of Equation 5.4, $Al(CH_3)_3$ can react with Al_2O_3 after the AlF_3 layer is etched, resulting in $AlCH_3$ species on the surface, which are responsible for the self-limiting behavior of the surface reactions.

Recently, we presented an ALD process for AlF_3 using SF_6 plasma as alternative, easy-to-handle and readily-available co-reactant.[46] SF_6 is a stable and non-toxic gas, which is widely used in the industry. Notably, F-containing plasmas such as SF_6, NF_3, CF_4 and C_2F_6 are employed for etching of Si-based materials (Si, SiO_2, Si_3N_4, ...).[47] Since an SF_6 plasma etches Si or SiO_2 substrates, ALD-grown Al_2O_3 was used as a protective coating in our previous work.[48] An SF_6 plasma is characterized by high concentrations of F radicals and F^- ions, which are known to be $\sim 10^3$ times higher than the concentrations of S and S^+.[49] SF_6 gas can form electronegative plasmas where significant concentrations of positive ions (mainly SF_5^+ and SF_4^+) are balanced by negative ions (mainly F^- and SF_6^-) and electrons.[49–51] In an inductively-coupled SF_6 plasma, the dominant neutral species are reported to be F_2, SF_6, and SF_4.[49–51] It is noted that F is very reactive due to a very high electronegativity and electron affinity. The high concentration of reactive F radicals makes SF_6 plasma a suitable co-reactant for ALD of metal fluorides.[52]

The ALD process using SF_6 plasma as co-reactant yields high-purity films, with material properties such as refractive index and mass density (see Table 4.1) similar to those reported in the literature for AlF_3 films deposited using various other methods, including thermal evaporation, sputtering and thermal ALD.[1,8,53,54] Furthermore, a decrease in the growth per cycle (GPC) was found from 1.50 Å at a deposition temperature of 50 °C to 0.55 Å at 300 °C, similar to previous findings for the thermal ALD process using TMA and HF.[8,41,46] This decrease of the GPC was believed to be related to a lower density of HF surface species at high tem-

peratures (see Equation 5.1). To extend the use of SF_6 plasma as co-reactant to ALD of other metal fluorides, understanding of the chemistry behind the process is required. Moreover, it is valuable to investigate whether an SF_6 plasma can also be used for ALE of metal oxides. For these reasons, this article provides insight into the reaction mechanisms taking place during TMA - SF_6 plasma cycles.

This article is structured as follows. First the experimental conditions are described in Section 5.2. In Section 5.3.1, surface infrared spectroscopy results are discussed, revealing the surface reactions during $Al(CH_3)_3$ - SF_6 plasma cycles and a transition to etching of Al_2O_3 at higher temperatures. This is followed by an identification of the plasma species and gas-phase reaction products in Section 5.3.2. Based on the insights obtained from these experiments, a detailed description of the reactions mechanisms of AlF_3 ALD is given in Section 5.4.

5.2 Experimental Details

5.2.1 ALD reactor and conditions

The quadrupole mass spectrometry (QMS) and optical emission spectroscopy (OES) experiments were performed using an Oxford Instruments FlexAL reactor.[55] For the surface infrared (IR) studies a home-built ALD tool was used, which has a very similar pumping system and plasma source as the FlexAL reactor.[56] Both reactors reach a base pressure of $\sim 10^{-6}$ Torr and are equipped with an inductively coupled plasma (ICP) source, operated at a radio-frequency of 13.56 MHz. The conditions for the AlF_3 ALD process in the FlexAL reactor have been reported elsewhere.[46] Briefly, a TMA dose of 80 ms, followed by a purge step of 6 s, an SF_6 plasma exposure of 10 s (300 W power), and a final purge step of 4 s were used. The TMA precursor (Sigma Aldrich, 99.9999%) was contained in a stainless steel canister, kept at a temperature of 30 °C. The chamber pressure was set to 15 mTorr and 50 mTorr during the TMA dose and SF_6 plasma exposure, respectively. The substrate table and reactor walls were kept at temperatures of 200 °C and 120 °C, respectively. Since the surface area of the reactor wall is significantly larger than of the substrate table, a large part of the QMS signal originates from reactions occurring on the wall at a temperature of 120 °C.

For the *in situ* infrared (IR) spectroscopy studies in the home-built reactor, an SF_6 plasma pressure of 15 mTorr and a plasma power of 100 W were used. Measurements were performed on Aerosil OX50 SiO_2 powders, pressed on a tungsten grid. As will be discussed in Sections 5.3.1 and 5.4, a transition from AlF_3 ALD to Al_2O_3 ALE was observed in the infrared spectroscopy experiments, whereas

this was not observed for the temperatures studied in the FlexAL reactor.[46] This difference can likely be attributed to the higher temperature of the SiO_2 powder as compared to the Si wafer coupons. For depositions on the SiO_2 powder, the tungsten grid was heated directly by resistive heating using DC current, and the temperature was monitored using a thermocouple. This method of heating is significantly different from the heating employed for deposition on blanket wafers in the FlexAL reactor, where wafer coupons are placed on a carrier wafer, which is loaded onto a heated substrate table. Due to reduced thermal contact at low working pressure between the wafer coupons, the carrier wafer, and the table heater, the actual sample temperature is significantly lower than the substrate table.[57] For instance, the sample temperature is estimated to be 200 - 220 °C for a table temperature of 300 °C. This is in contrast to the depositions on SiO_2 powder where the actual temperature of the powder surface is expected to be in agreement with the set temperature. Moreover, it was found that the SF_6 plasma exposure resulted in slight heating ($\sim$20 - 30 °C) of the tungsten grid, while this effect is expected to be less pronounced on wafer coupons.

5.2.2 Studies on the reaction mechanism

The *in situ* surface spectroscopy studies were done with a Bruker Tensor Fourier transform IR spectrometer, as described in previous work.[58] Prior to AlF_3 ALD, the SiO_2 powder was coated with Al_2O_3 using 50 thermal (TMA + H_2O) ALD cycles at $\sim$275 °C. Sets of five AlF_3 ALD cycles were performed at temperatures between 100 °C and 250 °C, while collecting an IR spectrum after each sub-cycle. After each set of AlF_3 ALD cycles, 10 Al_2O_3 ALD cycles were repeated at 275 °C to obtain the same starting surface. The TMA dose and SF_6 plasma exposure time for these experiments were 1.1 s and 30 s, respectively, which was confirmed to be sufficient to reach saturation of the ALD reactions on the Al_2O_3-coated SiO_2 powder. To correct for changes in surface area of the powder due to film growth, the absorbance spectra were normalized based on the signal for $Al(CH_3)_3$ adsorption on Al_2O_3. For this correction, the normalized integrated IR absorbance corresponding to CH_3 stretching vibrations in the range of 3060 - 2800 cm^{-1} was used. This absorbance peak serves as a measure for the quantity of adsorbed $Al(CH_3)_3$, and was determined by calculating the difference spectrum using measurements before and after dosing $Al(CH_3)_3$ on the Al_2O_3-coated powder.

Quadrupole mass spectrometry (QMS) measurements were performed using a Pfeiffer Vacuum Prisma QME-200 (mass-to-charge ratio m/z = 1 - 200), connected to a flange on the side of the reactor chamber. The selection of measured m/z ratios was based on initial screening and mostly corresponds to SF_x and

CH_xF_y. The procedure for time-resolved QMS measurements was similar to a method described previously.[59] In short, six m/z ratios were measured simultaneously, of which one was always $m/z = 40$. This m/z value corresponds to Ar^+ and is used as reference. For each type of recipe, five cycles were performed and averaged. OES was done using a four-channel AvaSpec ULS2048 spectrometer from Avantes (200 nm - 1100 nm), as a line-of-sight measurement perpendicular to the substrate table (i.e. the fiber is installed vertically at the top of the plasma source). For the OES measurements, an SF_6 gas flow of 50 sccm was used instead of the standard 100 sccm, to increase the residence time of plasma species.

5.3 Results

5.3.1 Surface reactions

In situ surface infrared spectroscopy was performed to investigate the surface reactions taking place during the sub-cycles. Figure 5.1 shows absorbance spectra in the range of 4250 cm^{-1} to 2500 cm^{-1} for the TMA sub-cycle and the SF_6 plasma sub-cycle, performed at temperatures between 100 °C and 250 °C. For all temperatures, an absorbance gain is observed in the spectrum for the TMA sub-cycle in the region of 3060 - 2800 cm^{-1}, which corresponds to the formation of CH_3 stretching vibrations.[60–62] The presence of CH_3 can be explained by $AlF(CH_3)_2$, $AlF_2(CH_3)_2$ or $AlCH_3$ species formed upon reaction of TMA with the surface.[43] With increasing temperature, the absorbance gain decreases, indicating less $Al(CH_3)_3$ adsorption at high temperatures, which is in line with the decrease of the GPC as a function of temperature.[46] This temperature dependence of the CH_3 stretching vibrations is similar to what was observed by DuMont and George for thermal ALD/ALE using HF.[43] Furthermore, an absorbance loss can be seen in the range of 3700 - 3060 cm^{-1} in the spectra for 100 °C and 150 °C, which is attributed to the consumption of HF species on the AlF_3 surface.[43,63] These HF species are formed during the SF_6 plasma exposure, as evidenced by the positive absorbance peaks in the spectra for the plasma sub-cycle at 100 °C and 150 °C. Note that HF was also detected as a gas-phase reaction product during the SF_6 plasma exposure using QMS, as will be addressed in Section 5.3.2. At temperatures of 200 °C and 250 °C, negligible peaks corresponding to HF are observed, which reveals that no significant amount of HF is consumed or adsorbed during the TMA or SF_6 plasma sub-cycle, respectively. Although the removal of HF surface species is only observed at 100 °C and 150 °C, the spectra for the TMA sub-cycle indicate the formation of CH_3 groups at all investigated temperatures. This implies that at higher temperatures, the $Al(CH_3)_3$ reacts directly with the AlF_3 film, likely by accepting F from the surface and forming CH_3 surface groups.[44]

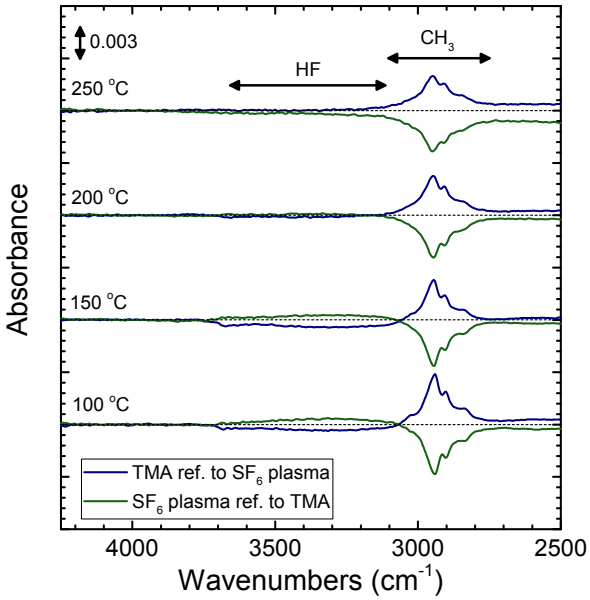

Figure 5.1 Difference spectra of the IR absorbance for the TMA sub-cycle and for the SF_6 plasma sub-cycle, for deposition temperatures between 100 °C and 250 °C. Spectra were collected after TMA dosing or SF_6 plasma exposure, and were referenced to the spectrum for the preceding sub-cycle. The pairs of spectra were given an offset on the vertical axis for clarity.

Multiple cycles were performed, and the collected spectra for each cycle were referenced to the first cycle to gain insight into the progression of the film with the number of cycles. From these measurements, the data collected after two and after five cycles are displayed in Figure 5.2 for temperatures between 100 °C and 250 °C. The spectra for 100 °C and 150 °C show a small positive absorbance peak starting around 775 cm^{-1} which can be attributed to the Al-F stretching vibrations in AlF_3.[64] Unfortunately, the end of the detector range lies at ∼700 cm^{-1}, meaning that only a part of the peak corresponding to Al-F stretching vibrations could accurately be measured. However, the positive absorbance between ∼775 - 750 cm^{-1} increases when additional cycles are performed, in line with the growth of the AlF_3 film. Interestingly, an absorbance loss can be observed in the region below 950 cm^{-1} for temperatures of 200 °C and 250 °C. The region around ∼1030 - 550 cm^{-1} corresponds to the Al-O stretching vibrations in amorphous Al_2O_3, and the absorbance loss therefore suggests the removal of Al_2O_3. For a temperature of 250 °C, the absorbance loss is larger than for 200 °C, indicating that more Al_2O_3 is etched, in agreement with what can be expected based on of the literature.[41,43] The data in Figure 5.2 thus show that a transition from AlF_3 ALD to Al_2O_3 ALE occurs at higher temperatures.

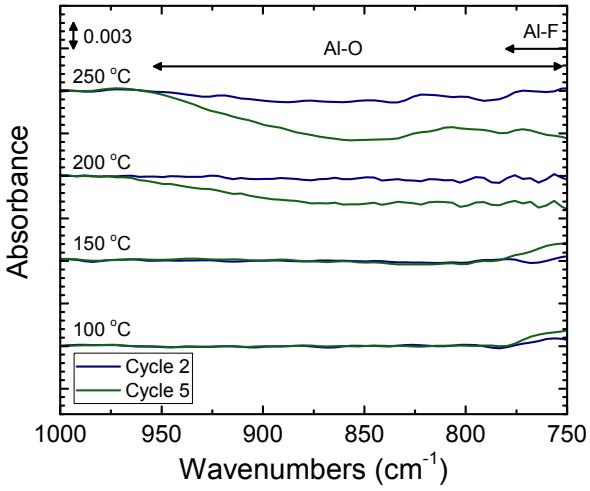

Figure 5.2 Absorbance spectra collected after performing two and five TMA - SF_6 plasma cycles, both referenced to the spectrum collected after performing one TMA - SF_6 plasma cycle on Al_2O_3-coated SiO_2 at the corresponding temperature. The pairs of spectra were given an offset on the vertical axis for clarity.

To corroborate the observed transition from AlF_3 ALD to Al_2O_3 ALE, it was confirmed that an SF_6 plasma can be used for fluorination of Al_2O_3 similarly as HF is used for thermal ALE. ~10 nm thick Al_2O_3 films were exposed to SF_6 plasma and subsequently analyzed by spectroscopic ellipsometry (SE, see Figure S5.1, in the Supporting Information, S.I.). It was found that exposing Al_2O_3 to SF_6 plasma leads to a small increase in thickness and a decrease in refractive index, due to self-limiting fluorination of the top surface. Furthermore, XPS results in Figures S5.2 and S5.3 (S.I.) demonstrate that most of the F is located in the top layer of the Al_2O_3, and that Al_xF_y bonds are present in addition to Al_2O_3. Similar self-limiting behavior can be expected for fluorination of MgO, HfO_2 and ZnO films, since their fluorides are non-volatile and have been deposited by ALD using HF.[42] These findings thus suggest that SF_6 plasma can be used for ALE of metal oxides, as will be discussed in Section 5.4.

5.3.2 Gas phase reaction products

QMS was employed to study the formation of gas phase reaction products during AlF_3 ALD. Figure 5.3 shows time-resolved QMS data for selected mass-to-charge (m/z) ratios 15, 16, 19 and 89, which correspond to CH_4 and key plasma species (F and SF_x). In addition, Table 5.1 lists the most relevant m/z ratios and the assignment of these m/z ratios to corresponding parent species. The increase in signals for $m/z = 15$ (CH_3^+) and 16 (CH_4^+) upon TMA dosing (at $t = 0$ s) in Figure 5.3 can be explained by the release of CH_4 as a reaction product, as well as by dissociation of the precursor in the QMS detector. The small increase in ion current for $m/z = 89$ (SF_3^+) is likely due to an increase in chamber pressure after TMA dosing. Subsequently, at the start of the SF_6 gas flow around $t = 6$ s, the chamber pressure increases from 15 mTorr to 50 mTorr, leading to an increase in ion current for all m/z ratios. After ignition of the SF_6 plasma (at $t \approx 12.5$ s), the ion currents for F^+ ($m/z = 19$) and SF_3^+ ($m/z = 89$) decrease slightly, attributed to consumption and dissociation of F radicals and SF_6, respectively. Meanwhile, the signals for $m/z = 15$ (CH_3^+) and 16 (CH_4^+) go up, indicating the formation of CH_4 as reaction product. After the initial increase, ion currents for $m/z = 15$ and 16 decrease quickly, which suggests that CH_4 is being evacuated from the reactor or dissociated in the plasma.

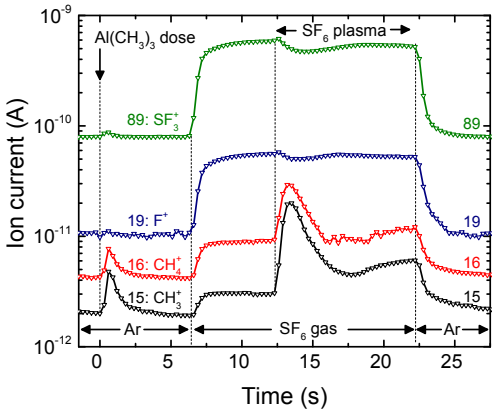

Figure 5.3 Time-resolved QMS signals for selected m/z ratios 15, 16, 19, and 89. Five AlF_3 ALD cycles were averaged to improve the signal-to-noise ratio. The pressure in the reactor increases from 15 mTorr to 50 mTorr when the SF_6 gas flow is started (at $t \approx 6$ s), leading to an increase in ion currents.

Table 5.1 Relevant m/z ratios, their assigned ions and their (main) assigned parent molecules. Most m/z ratios are corresponding to SF_6 or CH_yF_{4-y} species ($y \leq 4$). The assignments for CH_yF_{4-y} species are based on cracking patterns taken from the NIST database.[65]

m/z	Assigned ion(s)	Assigned parent species
15	CH_3^+	CH_3F, CH_4, $Al(CH_3)_3$
16	CH_4^+	CH_4
19	F^+	HF, SF_6, F_2, CH_yF_{4-y}
20	HF^+, Ar^{++}	HF, Ar
26	$C_2H_2^+$	C_2H_2, C_2H_4, C_2H_6
31	CF^+	CH_3F, CH_2F_2, CHF_3, CF_4
32	S^+, CHF^+	SF_6, CH_3F, CH_2F_2, CHF_3
33	CH_2F^+	CH_2F_2, CHF_3
40	Ar^+	Ar
50	CF_2^+	CH_2F_2, CHF_3, CF_4
51	SF^+, CHF_2^+	SF_6, CH_2F_2, CHF_3
69	CF_3^+	CHF_3, CF_4
70	SF_2^+, CHF_3^+	SF_6, CHF_3
89	SF_3^+	SF_6

Figure 5.4 shows time-resolved QMS data for additional m/z ratios collected during the co-reactant sub-cycle. At the start of the SF_6 plasma exposure, the signals for m/z ratios 16, 31, 33, 50 and 69 increase, all of which are corresponding to CH_yF_{4-y} (hydrofluorocarbon) species. See Figure S5.4 for the cracking patterns of CH_yF_{4-y} species. In addition, the signal for $m/z = 26$ indicates the production of C_2H_2 (or possibly C_2H_4, or C_2H_6), which can be explained by reactions of for instance CH_4 ($m/z = 16$) in the plasma (in the literature it is reported that C_2H_2 forms in CH_4 plasmas).[66] Several other m/z ratios (18, 28, 32, 34, 35, 48 and 52) were also investigated, but their ion currents were found not to be affected by TMA dosing. Upon closer inspection of Figure 5.4, it can be seen that the temporal behavior is not the same for all of the investigated species. Signals related to CH_4 and C_2H_2 in Figure 5.4a show the highest ion currents at the beginning of the plasma exposure ($t \approx 14$ s) and a rapid decrease, while others (especially in Figure 5.4b) show the highest intensity later on. More specifically, the higher the concentration of F atoms in the species, the later the maximum intensity occurs. This suggests that the F-concentration of surface species increases due to interaction with F radicals from the plasma before they are released from the surface, or that CH_4 and CH_yF_{4-y} plasma species react with F in the plasma. The

signal for $m/z = 20$ is also displayed in Figure 5.4a and corresponds to Ar (Ar^{++} in this case), as well as HF. Between $t \approx 8$ s and 12 s, the ion current for $m/z = 20$ decreases, which can be attributed to Ar being evacuated from the chamber (Ar is used as background gas during the TMA dose). At the start of the SF_6 plasma ($t \approx 12$ s), the ion current quickly rises, indicating the formation of HF, after which the ion current stabilizes (at $t \approx 17$ s). The formation of HF can be explained by recombination of H and F radicals (likely at the surface), and can lead to an additional thermal component in the reaction mechanism (see Equation 5.2). This reaction between HF and CH_3 surface groups is likely responsible for the release of CH_4 groups, as will be addressed in Section 5.4.

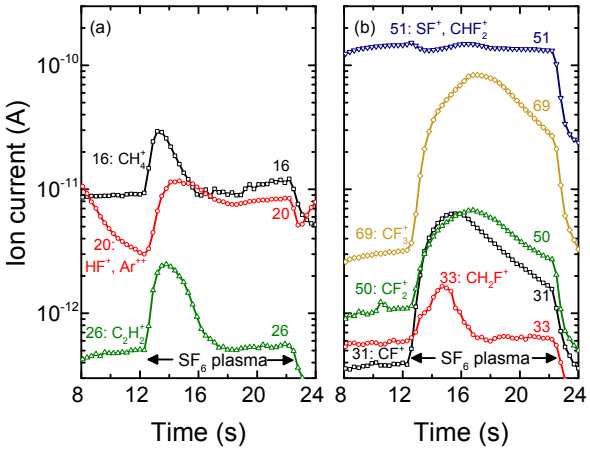

Figure 5.4 Time-resolved QMS signals collected during the plasma subcycle corresponding to (a) CH_4, HF, and C_2H_2 ($m/z = 16$, 20, 26), and (b) hydrofluorocarbons ($m/z = 31$, 33, 50, 51, 69). Note that time for which the species reach the maximum intensity correlates to the F-content and that signals corresponding to species with a higher F-content in (b) ($m/z = 31$, 50 and 69) reach the maximum later than H-rich species in (a). The data for $m/z = 16$ is also shown in Figure 5.3.

To confirm that the detected species are corresponding to reaction products instead of SF_6 plasma species, the ion currents for selected masses were measured during an SF_6 plasma exposure of an ALD cycle and during an SF_6 plasma exposure (without preceding TMA). Signals of key reaction products ($m/z = 15$, 16, 20, 25, 26, 30, 33, 50 and 69) in Figure 5.5 are significantly higher for the ALD cycle as compared to the signals for only SF_6 plasma. The higher ion currents prove that all these species are formed due to interaction of the SF_6 plasma with the precursor ligands remaining after the precursor dose, or due to interaction of the SF_6 plasma with formed reaction products. For instance, CH_4 species can be formed in a surface reaction, and subsequently undergo dissociation reactions in

the plasma. Certain signals (e.g. m/z = 32, 51 and 70) simultaneously correspond to hydrofluorocarbons and SF_x, and do not show a higher current for the ALD cycle than for the SF_6 plasma without TMA dosing. Probably the production of CH_yF_{4-y} species does not affect the currents for those m/z ratios due to the high background signal from SF_6. It is noted that the ion currents for m/z = 15-16 (CH_3^+, CH_4^+), m/z = 25-29 ($C_2H_x^+$, x =1 - 5) and m/z = 31, 50, 69 (CF_x^+) also increased slightly during the SF_6 plasma exposure without preceding TMA dosing, which indicates that some C-containing species were present on the reactor wall due to previously performed ALD cycles.

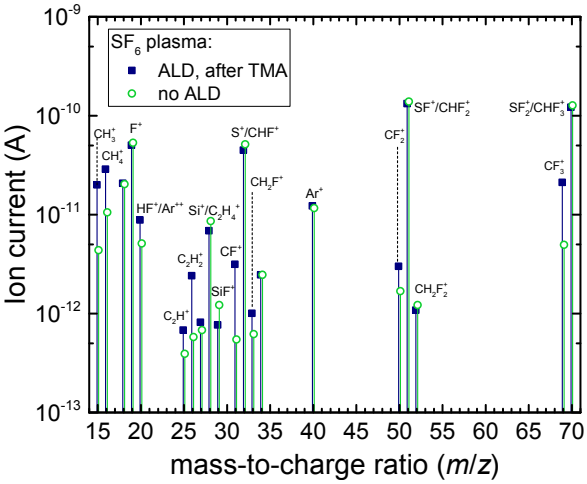

Figure 5.5 QMS mass spectra showing selected masses during the SF_6 plasma exposure of an ALD cycle and during an SF_6 plasma exposure (without TMA dosing). The spectra were collected at $t \approx 13.5$ s, which is approximately 1.5 s after igniting the plasma.

The excited species present in the plasma were analyzed using OES to corroborate the findings from the QMS measurements. Figure 5.6a shows optical emission spectra for an SF_6 plasma during an ALD cycle (after TMA dosing) and an SF_6 plasma (without preceding TMA dosing). Various key excited species can be identified in both spectra, including F, S, H, and H_2.[67,68] Emission related to F and S can be attributed to dissociation of SF_6 in the plasma, whereas H and H_2 are likely related to residual background species (e.g. H_2O). For the plasma during an ALD cycle, additional emission peaks corresponding to C_2H_2 and CF_2 are detected at wavelengths of 247.8 nm, 257.7 nm and 259.2 nm (see inset Figure 5.6a).[69–72] The OES spectrum for the ALD cycle thus corroborates the presence of CH_yF_{4-y} species as reaction products.

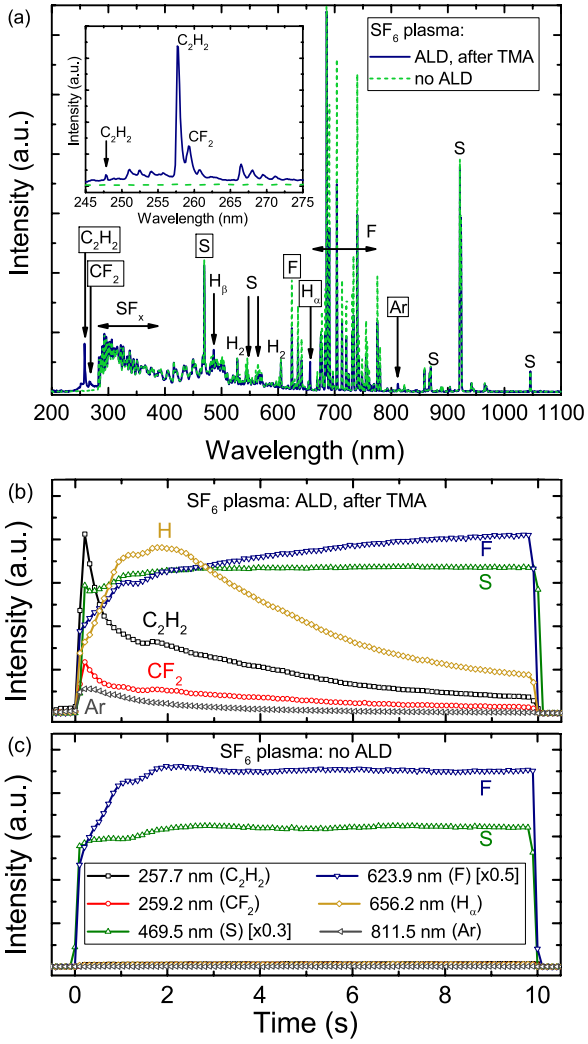

Figure 5.6 (a) Optical emission spectra of an SF_6 plasma during an AlF_3 ALD cycle ('ALD, after TMA'), and an SF_6 plasma ('no ALD'), which serves as reference. Signals corresponding to highlighted species (i.e. C_2H_2, CF_2, S, F, H_α, and Ar) are plotted as a function of time in (b) and (c). Inset: zoom of the range between 245 nm and 275 nm, indicating emission peaks corresponding to C_2H_2 and CF_2. (b, c) Time resolved OES signals for selected wavelengths during (b) the SF_6 plasma exposure in an ALD cycle, after TMA dosing, and (c) an SF_6 plasma ('no ALD'). For clarity the signals related to S (467.5 nm) and F (685.2 nm) have been scaled. Note that the SF_6 gas flow was decreased from the standard value of 100 sccm to 50 sccm in order to increase the residence time of the species in the plasma.

Intensities corresponding to relevant species were followed as function of time during an SF_6 plasma exposure of an ALD cycle (Figure 5.6b) and during the SF_6 plasma exposure without TMA, (Figure 5.6c). Figure 5.6b shows that the signal corresponding to F radicals (623.9 nm) increases gradually after the plasma is started. As compared to the reference signals (Figure 5.6c), there is initially less emission related to excited F species, indicating that F is consumed in the surface reactions. At the end of the plasma exposure, the emission signal at 623.9 nm approaches the same intensity as in an SF_6 plasma (Figure 5.6c), which can be explained by the saturation of the surface reactions between CH_3 ligands and F radicals. Emission peaks at other wavelengths related to F (e.g. 712.8 nm, 720.2 nm, and 733.1 nm) were found to show a similar behavior as function time, corroborating saturation. When comparing Figure 5.6b and Figure 5.6c, it becomes clear that signals assigned to reaction products (257.7 nm, 259.2 nm and 656.2 nm), demonstrate a quick rise and subsequent decrease during the ALD cycle, while they are not observed for the reference measurement of the SF_6 plasma (without TMA dosing). The additional emission in Figure 5.6b can be explained by the formation of reaction products (i.e. CH_yF_{4-y} and HF species) due to the reaction of plasma species, most likely F radicals, with the surface groups. The gradual decrease in emission from these reaction products indicates the elimination of precursor ligands by F radicals and their removal from the reactor chamber. Note that a small amount of excited Ar is observed for the ALD cycle, which is apparently still present in the reactor after the precursor purge step, but decreases soon after plasma ignition. Overall, the OES results are in line with the QMS data, indicating the consumption of F radicals, and the formation of CH_yF_{4-y} species as reaction products.

5.4 Discussion

The insights obtained from the IR, QMS and OES data of Section 5.3 help to understand the reaction mechanism of AlF_3 growth using $Al(CH_3)_3$ and SF_6 plasma. Before discussing the reaction mechanisms, the main results can be summarized as follows:

i. $Al(CH_3)_3$ dosing in the precursor sub-cycle results in CH_3 groups on the surface, which are removed in the co-reactant sub-cycle.

ii. Surface IR spectroscopy revealed that at low temperatures ($\leq$ 150 °C) adsorbed HF is consumed during the TMA dose and formed during the SF_6 plasma exposure, while it does not play a role in the surface reactions at

higher temperatures. The presence of HF in the gas phase was observed during the SF_6 plasma exposure by QMS (at a temperature of 120 °C).

iii. CH_4 and CH_yF_{4-y} gas-phase species are formed during the SF_6 plasma exposure, indicating reactions of CH_3 groups with plasma species and HF.

iv. During the SF_6 plasma step, F radicals are consumed in surface reactions with CH_3 groups (and possibly other surface species), and lead to the fluorination of the surface.

The role of HF in the reactions mechanism requires some more discussion before the complete mechanism can be postulated. QMS measurements revealed that HF is produced as a reaction product during the SF_6 plasma, which can adsorb to the AlF_3 surface. The surface infrared spectroscopy data presented in Figure 5.1 show the adsorption of HF surface species during the SF_6 plasma exposure sub-cycle, and the consumption of HF in the TMA sub-cycle (for 100 °C and 150 °C). Since the GPC for the plasma process is similar to the GPC for thermal process, it is possible to compare the relative absorbance values for the two processes. For the thermal ALD process, DuMont and George also reported the consumption of HF, as indicated by a negative absorbance peak in the range of $\sim$ 3700 - 3000 cm^{-1} (corresponding to HF) which was similar in intensity as the absorbance peak in the region $\sim$ 3000 - 2800 cm^{-1} corresponding to $AlCH_3$ species.[43] However, when comparing the data shown in Figure 5.1 with the data reported by DuMont and George, it becomes clear that the relative absorbance corresponding to adsorbed HF is much smaller for the SF_6 plasma process than for the thermal process using HF as co-reactant. Although some HF is produced during the SF_6 plasma of the co-reactant sub-cycle, the HF exposure and resulting surface coverage is likely much lower than when dosing HF directly as co-reactant. The smaller relative absorbance corresponding to HF therefore indicates that $Al(CH_3)_3$ likely also reacts directly with the AlF_3 in a ligand-exchange reaction during the plasma process (forming $AlF(CH_3)_2$, see discussion Equation 5.4).

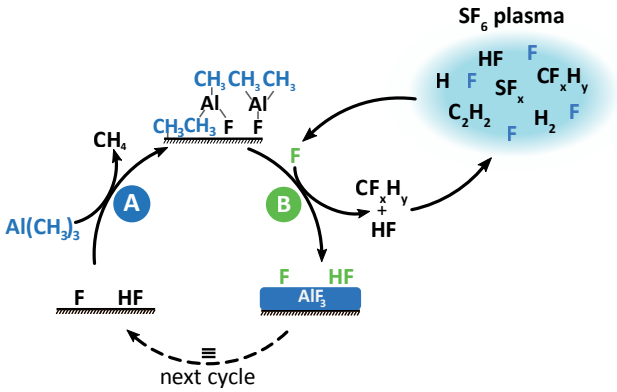

Figure 5.7 Schematic diagram of the proposed reaction mechanism for AlF_3 ALD when using $Al(CH_3)_3$ and SF_6 plasma. The orange and blue colors indicate elements introduced during the precursor or co-reactant sub-cycle, respectively. In the precursor sub-cycle ('A'), $Al(CH_3)_3$ reacts with HF and AlF_3, resulting in $AlF(CH_3)_2$ surface species. During the plasma sub-cycle ('B'), F radicals from the plasma remove the CH_3 ligands, and fluorinate the film to AlF_3. HF which is formed during the SF_6 plasma exposure can adsorb to the surface, serving as an additional reactive site at low deposition temperatures. The formed reaction products can undergo dissociation and recombination reactions in the SF_6 plasma and at the reactor wall. Note that the reaction between AlF_3 and $Al(CH_3)_3$ results in three $AlF_x(CH_3)_{3-x}$ groups, although only two are displayed. For simplicity only $AlF(CH_3)_2$ species are drawn after TMA dosing, whereas $AlF_2(CH_3)$ can also be present.

Based on the results, it can be concluded that during AlF_3 ALD using $Al(CH_3)_3$ and SF_6 plasma, $Al(CH_3)_3$ reacts with AlF_3 as well as with HF adsorbed on the surface, and that part of the CH_3 ligands is released as CH_4. This is illustrated in Figure 5.7 and described by Equations 5.5 and 5.6. $Al(CH_3)_3$ reacts with the AlF_3 film in a ligand-exchange reaction, forming $AlF_2(CH_3)$ or $AlF(CH_3)_2$ (Equation 5.5). In addition, at low temperatures ($\leq$ 150 °C) adsorbed HF serves as a reactive site for $Al(CH_3)_3$ to bind (Equation 5.6). HF is formed during the preceding co-reactant sub-cycle, and partly remains adsorbed on the surface. Saturation of the reactions between $Al(CH_3)_3$ and the surface likely occurs due to steric hindrance effects between CH_3 groups. It is noted that based on QCM measurements for thermal ALD using HF it was found that mainly $AlF(CH_3)_2$ is formed upon dosing $Al(CH_3)_3$.[41] Equation 5.5 and Equation 5.6 therefore describe formation of $AlF(CH_3)_2$, although $AlF_2(CH_3)$ surface species might probably also be present.[41]

$$AlF_{3\,(s)} + 2\ Al(CH_3)_{3\,(g)} \rightarrow 3\ AlF(CH_3)_{2\,(ads)}, \tag{5.5}$$

$$HF_{\,(ads)} + Al(CH_3)_{3\,(g)} \rightarrow AlF_x(CH_3)_{2\,(ads)} + CH_{4\,(g)}\ (T \leq 150\ ^\circ C). \tag{5.6}$$

The CH_3 ligands remaining after the precursor sub-cycle are eliminated by F radicals during the following SF_6 plasma exposure, resulting in the formation of CH_yF_{4-y} species (see Equation 5.7 and Figure 5.7). These CH_yF_{4-y} species can be formed either in surface reactions, or in the plasma. Furthermore, HF is produced as a reaction product in Equation 5.7, leading to an additional thermal component, which results in production of CH_4, and which is described by Equation 5.8. It is was found that at low temperatures ($\leq$ 150 °C) a small part of the formed HF remains adsorbed on the surface after the SF_6 plasma, providing reactive sites for the next TMA dose (Equation 5.6).

$$\begin{aligned} &AlF(CH_3)_{2\ (ads)} + 4(4\text{-}y)\ F_{\ (g)} \rightarrow \\ &\quad AlF_{3\ (s)} + 2\ CH_yF_{4-y\ (g)} + 2(3\text{-}y)\ HF_{(ads,\ g)} \quad (y \leq 3), \end{aligned} \tag{5.7}$$

$$AlF(CH_3)_{2\ (ads)} + 2\ HF_{\ (ads,\ g)} \rightarrow\ AlF_{3\ (s)} + 2\ CH_{4\ (g)} \quad (T \leq 150\ °C). \tag{5.8}$$

Combining the reactions described by Equations 5.5 to 5.8 results in the following overall reaction equation for the complete AlF_3 ALD cycle:

$$Al(CH_3)_{3\ (g)} + 4(4\text{-}y)\ F_{(g)} \rightarrow AlF_{3\ (s)} + 2\ CH_yF_{4-y\ (g)} + 2(3\text{-}y)\ HF_{\ (ads,\ g)}. \tag{5.9}$$

In the mechanism described by Equations 5.5 to 5.8 and Figure 5.7, $Al(CH_3)_3$ reacts with both AlF_3 and HF species, while F radicals play the dominant role in the ligand removal and the fluorination reaction. These mechanisms differ from the thermal ALD process on two aspects. During the thermal ALD process, $Al(CH_3)_3$ is believed to only react with HF, resulting in the formation of CH_4.[41] For the plasma-based process, the main pathway is likely the ligand-exchange reaction between $Al(CH_3)_3$ and AlF_3, due to the lower coverage of adsorbed HF. The second difference between the two processes is which products are formed in the co-reactant sub-cycle. Whereas only CH_4 is released in the thermal process, the SF_6 plasma process is characterized by formation of CH_yF_{4-y} species due to the interaction of F radicals from the SF_6 plasma with CH_3 surface groups. Furthermore, the reaction products released from the surface can undergo a wide range of reactions in the plasma.

Note that some analogies can be identified between the reaction mechanism described by Equation 5.9 and plasma ALD of Al_2O_3 using $Al(CH_3)_3$, where the formation of H_2O, CH_4 and C_2H_2 species is reported.[73] During plasma ALD of Al_2O_3, H_2O is formed due to interaction of O radicals with CH_3 surface groups, which triggers a thermal component in the reaction mechanism, resulting in for-

mation of CH_4. The formed CH_4 can subsequently be dissociated in the plasma, and lead to formation of C_2H_2 species. Furthermore, the OH group serves as the reactive surface site, which can be seen in analogy with adsorbed HF during AlF_3 ALD. However, during AlF_3 ALD, $Al(CH_3)_3$ is also believed to react with the AlF_3 in a ligand-exchange reaction (forming $AlF(CH_3)_2$), while such a pathway is not reported for Al_2O_3 ALD.

Based on the reaction mechanisms that were found, it can be speculated that SF_6 plasma as co-reactant can be combined with metal organic precursors containing carbohydrate-based ligands (i.e. metal alkyls) for growth of metal fluorides. Similar to AlF_3 ALD this would lead to the release of C_xH_y species in the precursor sub-cycle. The reaction with F radicals during the plasma exposure would result in elimination of the remaining ligands and formation of CH_yF_{4-y} species. Note that Lee *et al.* demonstrated ALD of MnF_2, MgF_2, ZnF_2 and AlF_3 using metal organic compounds with carbohydrate containing ligands as precursors and HF as co-reactant.[42] In addition, they employed precursors containing alkylamide and alkoxide groups, suggesting that also these types of precursors might be combined with SF_6 plasma.

Interestingly, the chemistry based on fluorination and TMA dosing can also be used for ALE of Al_2O_3 at higher substrate temperatures.[44] The transition between AlF_3 ALD and Al_2O_3 ALE is governed by the substrate temperature, and is believed to depend on the desorption temperature of $AlF_x(CH_3)_{3-x}$ species.[43] At low sample temperatures $AlF_x(CH_3)_{3-x}$ species remain adsorbed to the surface, leading to growth, while at higher temperatures they desorb from the surface, hence etching is observed. As described by Equations 5.3 and 5.4, two steps are essential for the ALE mechanism. The top surface of Al_2O_3 should be fluorinated, followed by the formation of volatile $AlF_x(CH_3)_{3-x}$ species upon TMA dosing. The data on fluorination of Al_2O_3 using SF_6 plasma in Figures S5.1 to S5.3 (S.I.) showed that an SF_6 plasma converts the top surface to AlO_xF_y in a self-limiting manner, similar to when HF is used as F-source for ALE. Furthermore, the results in Figure 5.2 showed negative absorbance peaks in the region below $\sim$950 cm^{-1} at temperatures $\geq$ 200 °C, indicating the removal of Al_2O_3. As discussed in the experimental details section, the actual sample temperature during experiments on wafer coupons deviates from the sample temperature during infrared spectroscopy experiments. This difference in sample temperature can explain why etching was observed in the infrared spectroscopy experiments, while it was not observed for deposition in the FlexAL reactor for table temperatures up to 300 °C. Notably, DuMont and George also observed a lower transition temperature for experiments on SiO_2 powder than on blanket samples. The lower transition temperature was

attributed to additional heating of the Al_2O_3-coated SiO_2 powder due to the fluorination reaction, which is very exothermic.[43] Initial experiments on the ALE process using SF_6 plasma and TMA revealed that TMA doses as long as 1 s are needed to reach saturation during the precursor step. Although additional research is required to fully understand the ALE process, the insights suggests that SF_6 plasma can be employed for ALE.

5.5 Conclusion

Following up previous work where the use of an SF_6 plasma was demonstrated, the reaction mechanisms during AlF_3 ALD using TMA and SF_6 plasma were studied. Based on the infrared spectroscopy results and the information on gas-phase reaction products from QMS and OES, a pathway for AlF_3 ALD was proposed where $Al(CH_3)_3$ reacts with AlF_3 and HF surface species during the precursor sub-cycle. During the subsequent SF_6 plasma exposure, F species fluorinate the surface, and eliminate the CH_3 surface groups, resulting in CH_yF_{4-y} species as well as HF. The infrared spectroscopy data showed growth of AlF_3 at low temperatures ($\leq$ 150 °C), and etching of Al_2O_3 at high temperatures ($\geq$ 200 °C), which is explained by the desorption of $AlF_x(CH_3)_{3-x}$ species at high temperatures. It was discussed that the postulated reaction mechanisms can be generalized to plasma ALD of metal fluorides using metal alkyl compounds as precursor. It can be speculated that C_xH_y species are released upon adsorption of such precursors on the metal fluoride surface, and that F radicals from the SF_6 plasma exposure result in elimination of the remaining ligands and formation of CH_yF_{4-y} species. Furthermore, it is also expected that an SF_6 plasma can be employed for self-limiting fluorination of a variety of metal oxides. The understanding provided in this work can thus help to develop ALD processes for other metal fluorides, as well as ALE processes for metal oxides using SF_6 plasma as the F-source.

Acknowledgments

The authors gratefully acknowledge J.J.A. Zeebregts, C.A.A. van Helvoirt, C. van Bommel, J.J.L.M. Meulendijks and J. van Gerwen for technical support. M.J.M. Merkx and N.F.W. Thissen area acknowledged for assistance with the FTIR experiments and fruitful discussions on the ALE process, respectively. This work was financially supported by the Netherlands Organization for Scientific Research (NWO) through the Zwaartekracht program 'Research Centre for Integrated Nanophotonics'.

5.6 Supporting Information

Fluorination of Al_2O_3 by SF_6 plasma

As mentioned in the main text, thermal ALE of Al_2O_3 and other metal oxides can occur through subsequent fluorination and ligand-exchange reactions, for example using HF for the fluorination of Al_2O_3.[44] It is thus valuable to investigate whether an SF_6 plasma can alternatively be used for the self-limiting fluorination of metal oxides such as Al_2O_3.[74] Furthermore, for possible applications it is relevant to understand whether an interfacial layer is formed between the metal oxide film and the metal fluoride during the initial ALD growth of a fluoride on an oxide. Notably, a $\sim$1 nm thick Al_2O_3 was previously used as a protective layer for AlF_3 ALD, since SF_6 plasmas typically result in etching of Si-based materials.[46] Although it is known that Al_2O_3 is not etched by an SF_6 plasma, it can be expected that SF_6 plasma exposure results in F incorporation.[75,76] For these reasons, the influence of the SF_6 plasma of film thickness and F-content was studied by exposing Al_2O_3 films to SF_6 plasma for various times between 5 s and 60 s, followed by analysis using spectroscopic ellipsometry (SE).

100 Al_2O_3 ALD cycles using TMA and O_2 plasma were performed at 300 °C, resulting in a film of approximately 10 nm. Coupons of this Al_2O_3 film were subsequently exposed to SF_6 plasma (100 W) at a table temperature of 300 °C. The Al_2O_3 films were analyzed by SE and X-ray photoelectron spectroscopy (XPS) to determine the changes in film properties upon SF_6 plasma exposure. The thickness and optical constants were determined from SE measurements using an *ex situ*, variable-angle J.A. Woollam Co., Inc. M2000D ellipsometer, with a wavelength range of 193 - 1000 nm. All Al_2O_3 samples were measured prior and post SF_6 plasma exposure, and the data was fitted according to the Cauchy equation for both the as-deposited and the fluorinated Al_2O_3 films.[77] This means that the fluorinated top surface and the Al_2O_3 were modeled as one homogenous layer, although there likely is a gradient in the F-content. The chemical composition, and the F-content in particular, were assessed with a Thermo Scientific KA1066 XPS spectrometer, using monochromatic Al Kα X-rays (1486.6eV). Sputtering during the XPS analysis was performed using Ar^+ ions with an energy of 500 eV.

Figure S5.1a shows an abrupt change in thickness and refractive index upon SF_6 plasma exposure. After this initial change, self-limiting behavior is observed (on the time-scales studied in this work). The film increased about 0.35 nm in thickness, and the refractive index decreased from approximately 1.67 to 1.64. Note that the refractive indices reported for ALD-grown Al_2O_3 and AlF_3 are approximately 1.66 and 1.35, respectively.[46,78] Furthermore, the XPS results in Fig-

ure S5.1b indicate that the F-content of the top surface was around 25 at.%. The F-content does not increase significantly with longer plasma exposure, which demonstrates the self-limiting fluorination of the Al_2O_3 film. As can be seen in Figure S5.1b, the F-content decreased to 5 at.% after a short Ar^+ sputter step of 30 s, indicating that most F is located at top surface. Furthermore, the XPS depth profiles in Figure S5.2 show a quick decrease of the F-content as a function of sputter time, further corroborating that the F is not diffused into the complete Al_2O_3 layer, irrespective of the duration of the plasma exposure time. In addition, the Al2p XPS peak is displayed in Figure S5.3, which suggests that AlO_xF_y bonds are present in addition to Al_2O_3. Similarly, Cano *et al.* also reported the presence of a contribution from AlO_xF_y in the XPS data, when using HF for fluorination of Al_2O_3.[74]

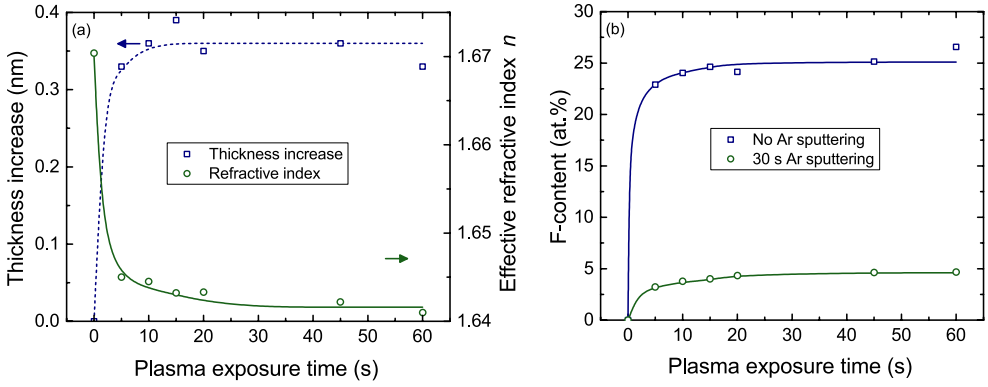

Figure S5.1 (a) Thickness increase and refractive index at 633 nm and (b) F-content of fluorinated Al_2O_3 films as a function of SF_6 plasma exposure time. The preparation of the Al_2O_3 layers and the subsequent plasma treatments were done at a table temperature of 300 °C. 100 Al_2O_3 ALD cycles were performed, resulting in an as-prepared Al_2O_3 film of approximately 10 nm thick. The SF_6 pressure and plasma power during fluorination were 50 mTorr and 300 W, respectively. Based on the results, in can be concluded that exposing Al_2O_3 to SF_6 plasma leads to a small increase in thickness and a decrease in refractive index, due to self-limiting fluorination of the top surface. This finding also suggests that the SF_6 plasma can be used for atomic layer etching (ALE).

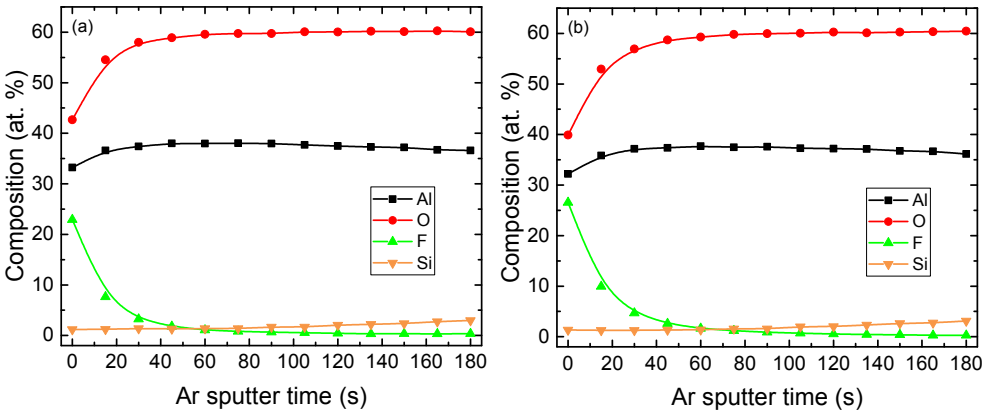

Figure S5.2 XPS depth profiles for ~10 nm thick Al_2O_3 films exposed to (a) 5 s and (b) 60 s SF_6 plasma. It was sound that most of the F is located in the top layer of the Al_2O_3, since the Al_2O_3 films were approximately 10 nm thick, and an Ar^+ sputter time of more than 90 s was required before the underlying Si started to become visible (See Figure S5.3). This finding is similar to the observations by Cano *et al.* who studied the fluorination of Al_2O_3 using HF.[74]

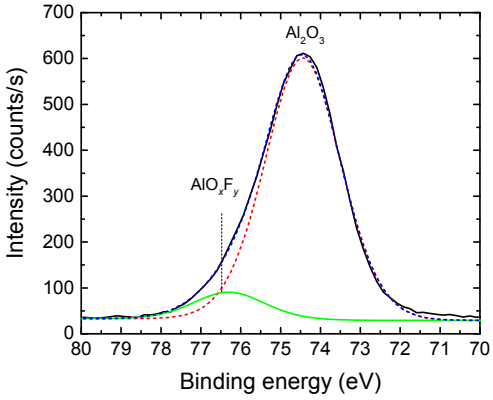

Figure S5.3 Al2p XPS peak for an Al_2O_3 films exposed to 60 s SF_6 plasma, indicating the contribution corresponding to Al_2O_3 and AlO_xF_y. The additional AlO_xF_y peak at a binding energy of approximately 75.6 eV was only observed after SF_6 plasma exposure, which is in line with what was found for fluorination using HF.[74] The position of 75.6 eV lies between the binding energy reported for Al_2O_3 (~74.6 eV) and AlF_3 (~77.5) and is consistent with several reports on AlO_xF_y films.[79–81] The formed surface layer is therefore likely an aluminum oxyfluoride (AlO_xF_y), rather than a AlF_3 layer. Although the exact stoichiometry of the AlO_xF_y remains unknown, a possible reaction for the fluorination by F radicals is $Al_2O_3 + 2F \rightarrow 2\ AlOF + O_2$.

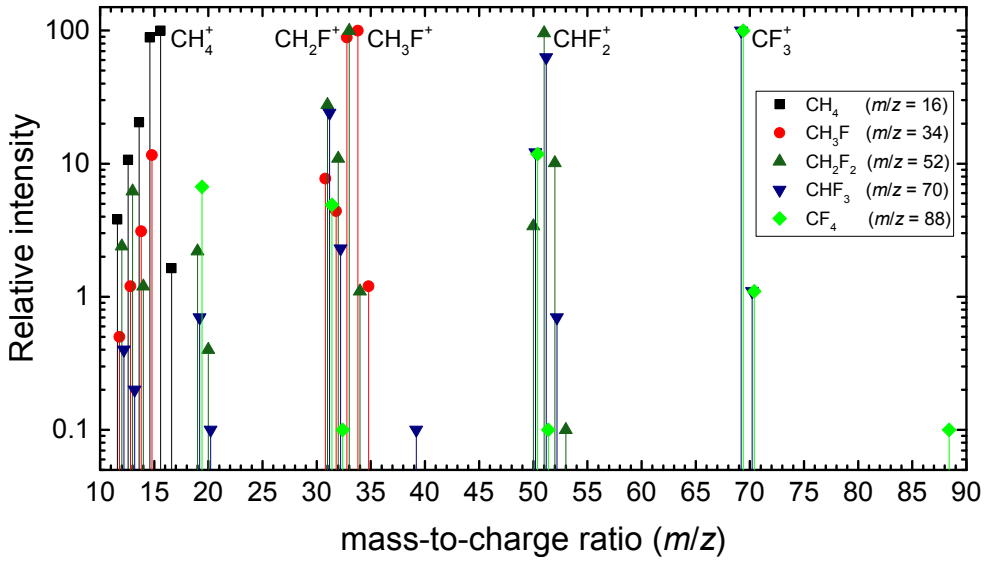

Figure S5.4 QMS cracking patterns for CH_yF_{4-y} ($y \leq 4$) species. Note that a few m/z ratios (e.g. 31, 50, and 69) correspond to different CH_yF_{4-y} species simultaneously (see Table 5.1 of the main text). The spectra were taken from the NIST database.[65]

References

[1] Barrière, A. and Lachter, A., *Appl. Opt.* **1977**, 16(11), 2865–2871.

[2] Siqueiros, J. M., Machorro, R., and Regalado, L. E., *Appl. Opt.* **1988**, 27(12), 2549.

[3] Pellicori, S. F. and Colton, E., *Thin Solid Films* **1992**, 209(1), 109–115.

[4] Bridou, F., Cuniot-ponsard, M., Desvignes, J., Richter, M., Kroth, U., and Gottwald, A., *Opt. Commun.* **2010**, 283(7), 1351–1358.

[5] Kedawat, G., Srivastava, S., Jain, V. K., Kumar, P., Kataria, V., Agrawal, Y., *et al.*, *ACS Appl. Mater. Interfaces* **2013**, 5(11), 4872–4877.

[6] Muallem, M., Palatnik, A., Nessim, G. D., and Tischler, Y. R., *ACS Appl. Mater. Interfaces* **2015**, 7(1), 474–481.

[7] Hennessy, J., Balasubramanian, K., Moore, C. S., Jewell, A. D., Nikzad, S., France, K., *et al.*, *J. Astron. Telesc. Instruments, Syst.* **2016**, 2(4), 041206.

[8] Hennessy, J., Jewell, A. D., Balasubramanian, K., and Nikzad, S., *J. Vac. Sci. Technol. A Vacuum, Surfaces, Film.* **2016**, 34(1), 01A120.

[9] Sun, Y. K., Lee, M. J., Yoon, C. S., Hassoun, J., Amine, K., and Scrosati, B., *Adv. Mater.* **2012**, 24(9), 1192–1196.

[10] Ding, F., Xu, W., Choi, D., Wang, W., Li, X., Engelhard, M. H., *et al.*, *J. Mater. Chem.* **2012**, 22(25), 12745.

[11] Park, J. S., Mane, A. U., Elam, J. W., and Croy, J. R., *Chem. Mater.* **2015**, 27(6), 1917–1920.

[12] Jackson, D. H. K., Laskar, M. R., Fang, S., Xu, S., Ellis, R. G., Li, X., *et al.*, *J. Vac. Sci. Technol. A Vacuum, Surfaces, Film.* **2016**, 34(3), 031503.

[13] Zhou, Y., Lee, Y., Sun, H., Wallas, J. M., George, S. M., and Xie, M., *ACS Appl. Mater. Interfaces* **2017**, 9(11), 9614–9619.

[14] Shapira, A., Tiurin, O., Solomatin, N., Auinat, M., Meitav, A., and Ein-Eli, Y., *ACS Appl. Energy Mater.* **2018**, 1(12), 6809–6823.

[15] Mäntymäki, M., Ritala, M., and Leskelä, M., *Coatings* **2018**, 8(8), 277.

[16] Kim, S., Lee, J., Ai, V., Lee, S., Balaji, N., Ahn, S., *et al.*, *Mater. Sci. Eng. B* **2013**, 178(9), 660–664.

[17] Um, H. D., Kim, N., Lee, K., Hwang, I., Seo, J. H., and Seo, K., *Nano Lett.* **2016**, 16(2), 981–987.

[18] Wan, Y., Samundsett, C., Bullock, J., Allen, T., Hettick, M., Yan, D., *et al.*, *ACS Appl. Mater. Interfaces* **2016**, 8(23), 14671–14677.

[19] Javey, A., Ballif, C., Geissbühler, J., Hettick, M., Cuevas, A., De Wolf, S., *et al.*, *Nat. Energy* **2016**, 1(3), 15031.

[20] Zhao, J., Wang, A., Altermatt, P., and Green, M. A., *Appl. Phys. Lett.* **1995**, 66(26), 3636–3638.

[21] Zhang, Y., Liu, R., Lee, S. T., and Sun, B., *Appl. Phys. Lett.* **2014**, 104(8),

083514.
[22] Xu, D., Yu, X., Zuo, L., and Yang, D., *RSC Adv.* **2015**, 5(58), 46480–46484.
[23] Hsu, F. H., Wang, N. F., Tsai, Y. Z., Wu, C. Y., Cheng, Y. S., Chien, M. H., *et al.*, *Thin Solid Films* **2014**, 573, 159–163.
[24] Dumas, L., Quesnel, E., Robic, J.-Y., and Pauleau, Y., *J. Vac. Sci. Technol. A Vacuum, Surfaces, Film.* **2002**, 18(2), 465–469.
[25] Sun, J., Shao, J., Yi, K., and Zhang, W., *Appl. Opt.* **2014**, 53(7), 1298.
[26] Larruquert, J. I. and Keski-Kuha, R. A., *Opt. Commun.* **2003**, 215(1), 93–99.
[27] Lee, C.-C., Liao, B.-H., and Liu, M.-C., *Opt. Express* **2007**, 15(15), 9152.
[28] Pandey, R. K., Kumar, M., Khan, S. A., Kumar, T., Tripathi, A., Avasthi, D. K., *et al.*, *Appl. Surf. Sci.* **2014**, 289, 77–80.
[29] Kennedy, M., Ristau, D., and Niederwald, H. S., *Thin Solid Films* **1998**, 333(1), 191–195.
[30] Dumas, L., Quesnel, E., Pierre, F., and Bertin, F., *J. Vac. Sci. Technol. A Vacuum, Surfaces, Film.* **2002**, 20(1), 102–106.
[31] Stenzel, O., Wilbrandt, S., Du, S., Franke, C., Kaiser, N., Tünnermann, A., *et al.*, *Opt. Mater. Express* **2014**, 4(8), 1696.
[32] Ylilammi, M. and Ranta-aho, T., *J. Electrochem. Soc.* **1994**, 141(5), 1278–1284.
[33] Mäntymäki, M., Hämäläinen, J., Puukilainen, E., Munnik, F., Ritala, M., and Leskelä, M., *Chem. Vap. Depos.* **2013**, 19(4), 111–116.
[34] Mäntymäki, M., Hämäläinen, J., Puukilainen, E., Sajavaara, T., Ritala, M., and Leskelä, M., *Chem. Mater.* **2013**, 25(9), 1656–1663.
[35] Mäntymäki, M., Heikkilä, M. J., Puukilainen, E., Mizohata, K., Marchand, B., Räisänen, J., *et al.*, *Chem. Mater.* **2015**, 27(2), 604–611.
[36] Pilvi, T., Arstila, K., Leskelä, M., and Ritala, M., *Chem. Mater.* **2007**, 19(14), 3387–3392.
[37] Pilvi, T., Ritala, M., Leskelä, M., Bischoff, M., Kaiser, U., and Kaiser, N., *Appl. Opt.* **2008**, 47(13), C271.
[38] Hennessy, J., Jewell, A. D., Greer, F., Lee, M. C., and Nikzad, S., *J. Vac. Sci. Technol. A Vacuum, Surfaces, Film.* **2015**, 33(1), 01A125.
[39] Puurunen, R. L., *J. Appl. Phys.* **2005**, 97(12), 121301.
[40] George, S. M., *Chem. Rev.* **2010**, 110(1), 111–131.
[41] Lee, Y., DuMont, J. W., Cavanagh, A. S., and George, S. M., *J. Phys. Chem. C* **2015**, 119(25), 14185.
[42] Lee, Y., Sun, H., Young, M. J., and George, S. M., *Chem. Mater.* **2016**, 28(7), 2022–2032.
[43] DuMont, J. W. and George, S. M., *J. Chem. Phys.* **2017**, 146(5), 1–10.
[44] Lee, Y., Dumont, J. W., and George, S. M., *Chem. Mater.* **2016**, 28(9), 2994–3003.

[45] George, S. M. and Lee, Y., *ACS Nano* **2016**, 10(5), 4889–4894.
[46] Vos, M. F. J., Knoops, H. C. M., Synowicki, R. A., Kessels, W. M. M., and Mackus, A. J. M., *Appl. Phys. Lett.* **2017**, 111(11), 113105.
[47] Cardinaud, C., *Comptes Rendus Chim.* **2018**, 21(8), 723–739.
[48] D'Agostino, R. and Flamm, D. L., *J. Appl. Phys.* **1981**, 52(1), 162–167.
[49] Mao, M., Wang, Y., and Bogaerts, A., *J. Phys. D. Appl. Phys.* **2011**, 44(43), 435202.
[50] Kokkoris, G., Panagiotopoulos, A., Goodyear, A., Cooke, M., and Gogolides, E., *J. Phys. D. Appl. Phys.* **2009**, 42(5), 055209.
[51] Oh, S.-j., Lee, H.-c., Chung, C.-w., Oh, S.-j., Lee, H.-c., and Chung, C.-w., *Phys. Plasmas* **2017**, 24(1), 013512.
[52] Luo, Y.-R., *Comprehensive Handbook of Chemical Bond Energies*, CRC-Press, Boca Raton, FL, **2007**, ISBN 9780849373664.
[53] Liao, B.-H., Liu, M.-C., and Lee, C.-C., *Appl. Opt.* **2008**, 47(13), C41–5.
[54] Sun, J., Li, X., Zhang, W., Yi, K., and Shao, J., *Appl. Opt.* **2012**, 51(35), 8481–8489.
[55] Heil, S. B. S., van Hemmen, J. L., Hodson, C. J., Singh, N., Klootwijk, J. H., Roozeboom, F., *et al.*, *J. Vac. Sci. Technol. A Vacuum, Surfaces, Film.* **2007**, 25(5), 1357.
[56] Heil, S. B. S., Langereis, E., Roozeboom, F., van de Sanden, M. C. M., and Kessels, W. M. M., *J. Electrochem. Soc.* **2006**, 153(11), G956.
[57] Knoops, H. C. M., de Peuter, K., and Kessels, W. M. M., *Appl. Phys. Lett.* **2015**, 107(1), 014102.
[58] Mameli, A., Merkx, M. J. M., Karasulu, B., Roozeboom, F., Kessels, W. M. M., and Mackus, A. J. M., *ACS Nano* **2017**, 11(9), 9303–9311.
[59] Knoops, H. C. M., Langereis, E., van de Sanden, M. C. M., and Kessels, W. M. M., *J. Vac. Sci. Technol. A Vacuum, Surfaces, Film.* **2012**, 30(1), 01A101.
[60] Dillon, A. C., Ott, A. W., Way, J. D., and George, S. M., *Surf. Sci.* **1995**, 322(1), 230–242.
[61] Frank, M. M., Chabal, Y. J., and Wilk, G. D., *Appl. Phys. Lett.* **2003**, 82(26), 4758–4760.
[62] Langereis, E., Keijmel, J., Van De Sanden, M. C. M., and Kessels, W. M. M., *Appl. Phys. Lett.* **2008**, 92(23), 1–4.
[63] Ayotte, P., Hébert, M., and Marchand, P., *J. Chem. Phys.* **2005**, 123(18), 184501.
[64] Gross, U., Rüdiger, S., Kemnitz, E., Brzezinka, K. W., Mukhopadhyay, S., Bailey, C., *et al.*, *J. Phys. Chem. A* **2007**, 111(26), 5813–5819.
[65] NIST Chemistry WebBook.
[66] Majumdar, A., Behnke, F., Hippler, R., Matyash, K., and Schneider, R., *J. Phys. Chem. A* **2005**, 109(41), 9371–9377.

[67] Sansonetti, J. E. and Martin, W. C., *J. Phys. Chem. Ref. Data* **2005**, 34(4), 1559–2259.
[68] Radovanov, S. B., Tomčik, B., Petrović, Z. L., and Jelenković, B. M., *J. Appl. Phys.* **1990**, 67(1), 97–107.
[69] Gaydon, R. and Pearse, A., *The Identification of Molecular Spectra*, Chapman & Hall, London, **1950**.
[70] Durrant, S. F., Mota, R. P., and Bica De Moraes, M. A., *J. Appl. Phys.* **1992**, 71(1), 448–455.
[71] Labelle, C. B. and Gleason, K. K., *J. Appl. Polym. Sci.* **2001**, 80(11), 2084–2092.
[72] Proshina, O. V., Rakhimova, T. V., Lopaev, D. V., Šamara, V., Baklanov, M. R., and de Marneffe, J.-F., *Plasma Sources Sci. Technol.* **2015**, 24(5), 055006.
[73] Heil, S. B. S., Van Hemmen, J. L., Van De Sanden, M. C. M., and Kessels, W. M. M., *J. Appl. Phys.* **2008**, 103(10).
[74] Cano, A. M., Marquardt, A. E., DuMont, J. W., and George, S. M., *J. Phys. Chem. C* **2019**, 123(16), 10346–10355.
[75] Dekker, J., Kolari, K., and Puurunen, R. L., *J. Vac. Sci. Technol. B* **2006**, 24(5), 2350 – 2355.
[76] Kolari, K., *Microelectron. Eng.* **2008**, 85(5-6), 985–987.
[77] Langereis, E., Heil, S. B. S., Knoops, H. C. M., Keuning, W., van de Sanden, M. C. M., and Kessels, W. M. M., *J. Phys. D. Appl. Phys.* **2009**, 42(7), 073001.
[78] Potts, S. E., Dingemans, G., Lachaud, C., and Kessels, W. M. M., *J. Vac. Sci. Technol. A Vacuum, Surfaces, Film.* **2012**, 30(2), 021505.
[79] Roodenko, K., Halls, M. D., Gogte, Y., Seitz, O., Veyan, J. F., and Chabal, Y. J., *J. Phys. Chem. C* **2011**, 115(43), 21351–21357.
[80] Liao, B.-H., Hsiao, C.-N., and Lee, C.-C., *Opt. Mater. Express* **2016**, 6(5), 1506.
[81] Kim, D. S., Yu, Y. Y., and Char, K., *J. Appl. Phys.* **2004**, 96(4), 2278–2285.

Atomic Layer Deposition of Cobalt Using H_2-, N_2-, and NH_3-Based Plasmas: On the Role of the Co-reactant

6

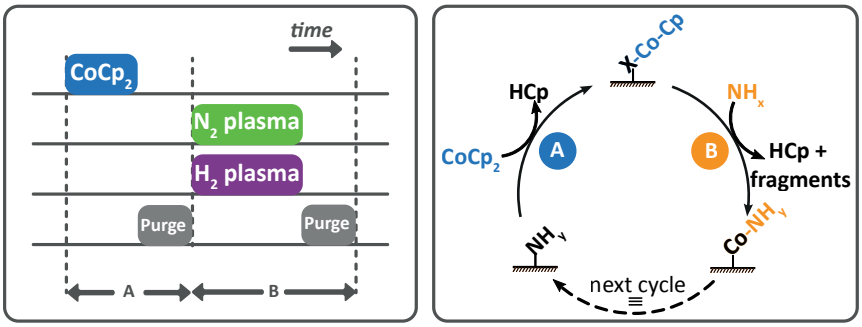

This work investigates the role of the co-reactant for atomic layer deposition of cobalt (Co) films using cobaltocene ($CoCp_2$) as the precursor. Three different processes were compared: an AB-process using NH_3 plasma, an AB-process using H_2/N_2 plasma, and an ABC-process using subsequent N_2 and H_2 plasmas. A connection was made between the plasma composition and film properties, thereby gaining an understanding of the role of the various plasma species. For NH_3 plasma, H_2 and N_2 were identified as the main species apart from the expected NH_3, while for the H_2/N_2 plasma also NH_3 was detected. Moreover, HCp was observed as a reaction product in the precursor and co-reactant sub-cycles. Both AB-processes showed self-limiting half-reactions and yielded similar material properties, i.e. high purity and low resistivity. For the AB-process with H_2/N_2, the resistivity and impurity content depended on the H_2/N_2 mixing ratio, which was linked to the production of NH_3 molecules and related radicals. The ABC-process resulted in high-resistivity and low-purity films, attributed to the lack of $NH_{x,\ x\leq 3}$ species during the co-reactant exposures. The obtained insights are summarized in a reaction scheme where $CoCp_2$ chemisorbs in the precursor sub-cycle, and NH_x species eliminate the remaining Cp in the consecutive sub-cycle.

Published as: M.F.J. Vos, G. van Straaten, W.M.M. Kessels and A.J.M. Mackus, *J. Phys. Chem. C* **122**, 39 (2018).

6.1 Introduction

Atomic layer deposition (ALD) is a thin film deposition technique which relies on the cycle-wise alternation of precursor and co-reactant doses. The self-limiting nature of the surface reactions during ALD generally allows for good uniformity on large-area substrates and excellent conformality on 3D-structures.[1] Although the precursor that is used for an ALD process generally receives considerable attention, the choice of the co-reactant is equally important, since it can greatly affect the properties of the deposited material as well as the technological and industrial feasibility of the process. For ALD of metals, a wide range of co-reactants has been explored, with gases or plasmas of O_2, H_2 and NH_3 being the most common choices.[1–4] In addition, less common chemicals like hydrazine (N_2H_4), silane (SiH_4), disilane (Si_2H_6), formic acid (CH_2O_2) and tertiary butyl hydrazine ($C_4H_{12}N_2$) have been used.[2,5–8] Moreover, certain ALD processes make use of what can be referred to as an advanced ALD cycle, in which either two or more co-reactants are dosed simultaneously, or after each other in an ABC-type manner. For instance, mixed H_2/N_2 plasmas have been used for ALD of a variety of materials.[9–12] Furthermore, Hämäläinen *et al.* deposited Ir, Pd, Rh and Pt at low temperatures (120 °C - 200 °C) using consecutive O_3 and H_2 exposures, and similar ABC-type cycles were later reported for the ALD of Ru (at 150 °C) using subsequent O_2 and H_2 doses and for Pt (at room temperature), using subsequent O_2 and H_2 plasmas.[13–16]

H_2-, N_2-, and NH_3-based plasmas (e.g. plasmas using NH_3, H_2, N_2, or H_2/N_2 mixtures as source gases) have previously been used as co-reactants for ALD of a wide range of metals and metal nitrides. See Table 6.1 for an overview of selected metals and metal nitrides which have been deposited using a NH_3 plasma or a mixed H_2/N_2 plasma as co-reactant. For instance, Kim *et al.* found that for ALD of Ir using Ir(EtCp)COD ((ethylcyclopentadienyl)(1,5-cyclooctadiene)Iridium), NH_3 plasma yielded a lower surface roughness in comparison to when using O_2 gas as the co-reactant.[17] Furthermore, Ten Eyck *et al.* employed a H_2/N_2 plasma for ALD of Pd on a polymer substrate, and claimed that a H_2/N_2 plasma leads to formation of reactive NH_2 groups on the polymer, needed for chemisorption of the $Pd(hfac)_2$ (palladium (II) hexafluoroacetylacetonate) precursor.[10] Moreover, the use of NH_3 plasmas instead of H_2 plasmas for ALD of Ru, Ag and Ni resulted in higher GPC and lower resistivity values.[18–20] The choice for the co-reactant is generally less straightforward for ALD of Co, Ni and Cu, as compared to noble metals, since their reduction potential is lower which makes impurity incorporation more probable.[4] For this reason H_2-, N_2-, or NH_3-based plasmas can be preferred over the O-containing co-reactants commonly used for noble metal ALD. How-

ever, for certain elements the use of N_2, NH_3 or H_2/N_2 plasmas and mixtures thereof can also result in a metal nitride film (e.g. AlN, TiN and TaN).[9,21–24] In general, deposition of a metal nitride becomes more likely for metals with a low reduction potential, as is illustrated in Table 6.1 Al, Ta and Ti have reduction potentials between -0.6 V and -1.7 V, while for Co, Ni and noble metals it is -0.26 V or higher.[25] Consequently, the use of for instance a mixed H_2/N_2 plasma leads to deposition of AlN on one hand, and metallic Co on the other hand.[26]

Table 6.1 List of selected metals and metal nitrides which have been deposited using NH_3 plasma and/or H_2/N_2 plasma as co-reactant. The third column indicates whether the use of NH_3 and/or H_2/N_2 plasma resulted in a metal or metal nitride film. In addition the reduction potential E^0 of the corresponding element is listed.[25] As the reduction potential decreases, C, O, and N incorporation (and therefore metal nitride deposition) become more likely. In general, the use of a NH_3 or H_2/N_2 plasma yields metal deposition for reduction potentials of $\sim$ -0.3 and above, while for elements below Co a metal nitride film is obtained. Note that W and Mo do not follow the trend based on the reduction potential. W and Mo are however reported to be very prone to nitridation and their nitrides are stable.[27]

Element	Reported co-reactant(s)	Reported state	Reference	E^0 (eV)
Pt	NH_3	metal	72	1.180
Ir	NH_3	metal	17	1.156
Pd	H_2/N_2	metal	10	0.951
Ag	NH_3	metal	19	0.800
Ru	NH_3 & H_2/N_2	metal	12,77	0.455
Ni	NH_3	metal	20	-0.257
Co	NH_3 & H_2/N_2	metal	26,27,29	-0.280
W	NH_3 & H_2/N_2	nitride	78	0.100
Mo	H_2/N_2	nitride	79	-0.200
In	H_2/N_2	nitride	24	-0.338
Ga	NH_3 & H_2/N_2	nitride	23,24	-0.549
Ta	NH_3 & H_2/N_2	nitride	9,21,80	-0.600
Nb	NH_3 & H_2/N_2	nitride	81,82	-1.100
Ti	NH_3 & H_2/N_2	nitride	83,84	-1.163
Hf	H_2/N_2	nitride	85	-1.550
Al	NH_3 & H_2/N_2	nitride	11,23	-1.662

Co is a ferromagnetic transition metal used in for instance magnetoresistive random-access memory (MRAM) and $CoSi_2$ contacts.[40–44] Currently Co mostly receives much attention for applications in interconnect technology, in order to reduce the RC-delay in state-of-the-art devices.[45] Firstly, Co has been suggested as

a viable candidate as liner for Cu interconnects, since Co can be thinner than the conventional Ta liner, which leaves more space for Cu.[46,47] Moreover, Co is also being investigated for replacement of Cu or W in small-dimension interconnects in the front-end-of-line.[48,49] It is therefore valuable to select Co ALD as a model system for studying the influence of the co-reactant. A wide range of precursor and co-reactants have been investigated for ALD of Co, as is shown in Table 6.2. As compared to other precursors, the $CoCp_2$ (bis(cyclopentadienyl)cobalt(II), cobaltocene) precursor has previously given good results, i.e. a low resistivity and high purity, while also being a readily-available and low-cost precursor. Interestingly, ALD of Co using $CoCp_2$ as the precursor can be achieved using different co-reactants. Specifically, the studies of Lee *et al.* and Yoon *et al.* reported growth of high-quality Co films using NH_3 plasma and H_2/N_2 plasma, respectively.[26,30] A direct comparison between the two different processes as well as a connection between the plasma composition and the obtained material properties have not been made so far.

Table 6.2 ALD processes reported in the literature for the deposition of Co, listing deposition temperature T, growth per cycle (GPC) and resistivity ρ.

Precursor	Co-reactant	T (°C)	GPC (Å)	ρ (μΩ·cm)	Ref.
$CoCp_2$	NH_3 plasma	300	0.48	10	27
$CoCp_2$	H_2/N_2 plasma	150-450	0.26-0.65	18	26
$CoCp_2$	NH_3[a]	100 -300	0.37-0.97	-	28
$Co(MeCp)_2$	NH_3 plasma	100 -350	0.4-1.9	31	29
Co(CpAMD)[b]	NH_3 plasma	200 -250	0.5	140	30
$Co_2(CO)_8$	H_2 plasma	75 -110	1.2	-	31
$CpCo(CO)_2$	H_2 plasma	125 -175	1.1	-	32
$Co(AMD)_2$[c]	H_2 plasma	340	0.50	285	33
$Co(AMD)_2$[c]	NH_3 plasma	350	0.26	50	34
^{t}Bu-Allyl$Co(CO)_3$	dimethylhydrazine	140	0.5	-	35
CCTBA[d]	H_2 plasma	125-200	0.8	90	36
Co(DBDB)[e]	Formic acid	170-180	0.95	13[f]	7,37
Co(DBDB)[e]	*tert*-butylamine	170-200	0.98	15[f]	37,38

[a]Hot-wire ALD. [b]Cyclopentadienyl isopropyl acetamidinato-cobalt. [c]Bis(*N,N'*-diisopropylacetamidinato)cobalt(II). [d]Dicobalt hexacarbonyl *tert*butylacetylene. [e]Bis(1,4-di*tert*-butyl-1,3-diazabutadienyl)cobalt(II). [f] Measured on Ru substrate.

In this work, a detailed study of the use of H_2-, N_2-, and NH_3-based plasmas as co-reactants for ALD of Co using $CoCp_2$ as precursor is presented. As is illustrated in Figure 6.1, three ALD processes with different co-reactants were investigated: an AB-type process with NH_3 plasma (referred to as 'AB-NH_3 process', Figure 6.1a), an AB-process with a mixed H_2/N_2 plasma ('AB-H_2/N_2 process', Figure 6.1b) and an ABC-process with subsequent N_2 and H_2 plasmas ('ABC-N_2-H_2 process', Figure 6.1c). As will be shown, the separation of the H_2 and N_2 plasmas in an ABC-type cycle gives insight in the role of $NH_{x,\ x\leq 3}$ species that are present in both the NH_3 plasma and the H_2/N_2 plasma (but not in the N_2 or H_2 plasmas).

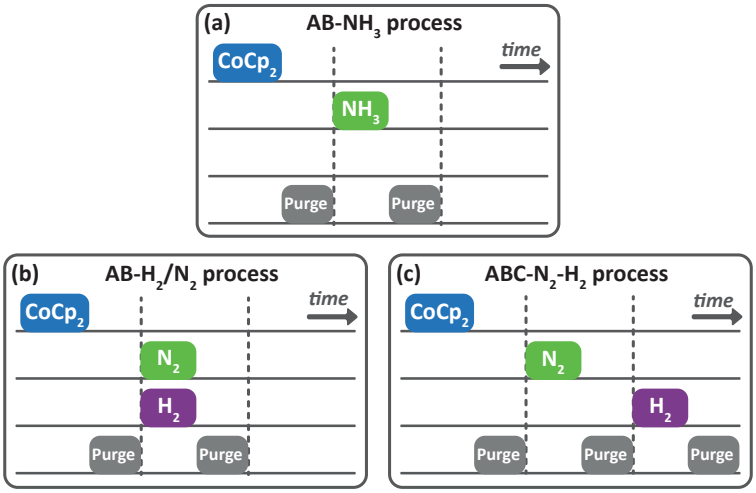

Figure 6.1 Schematic overview of the three Co ALD processes investigated in this study: (a) AB-NH_3, (b) AB-H_2/N_2 and (c) ABC-N_2-H_2 process. The ABC-process uses separate N_2 and H_2 plasmas exposures. Note that each purge step is followed by a pump step (see experimental details Section 6.2.1) which is not shown in the figure for simplicity.

This work is structured as follows. First, the experimental conditions related to the film deposition, the plasma studies and the film analysis are discussed in Section 6.2. In Section 6.3.1, the species present in the NH_3 and H_2/N_2 plasmas are identified and the role of the H_2/N_2 ratio on the plasma composition is investigated. This is followed in Section 6.3.2 by a study on the reaction products released during the plasma exposures of the three different ALD processes. In Section 6.3.3 the obtained material properties are compared. In addition, the effect of the H_2/N_2 ratio and $NH_{x,\ x\leq 3}$ concentration in the plasma on the material properties are addressed. Next, the role of $NH_{x,\ x\leq 3}$ species and a possible reaction mechanism are discussed in Sections 6.4.1 and 6.4.2, respectively. Finally the main conclusions of this work are summarized.

6.2 Experimental Details

6.2.1 ALD reactor and conditions

Co films were deposited in a home-built ALD reactor, as described in previous work.[60] In short, the reactor is equipped with a remote inductively-coupled plasma (ICP) source and a turbo pump reaching a base pressure of $\sim 10^{-6}$ Torr. During all experiments, the temperature of the substrate table was set to 300 °C, while the walls were heated to 100 °C. Prior to all experiments the reactor wall was covered by Co by running at least 200 cycles of the AB-NH_3 process. The $CoCp_2$ precursor (98%, Sigma-Aldrich) was contained in a stainless steel bubbler. The bubbler and the dosing line were heated to 80 °C and 120 °C, respectively, as was previously found to be appropriate for deposition of CoO_x in the same reactor.[61] The ALD recipe consisted of precursor dosing for 6 s in the first sub-cycle, using Ar as a carrier gas, which resulted in a chamber pressure of approximately 15 mTorr. Subsequently, the reactor was purged with Ar for 3 s and pumped down for 6 s. All plasma exposures were performed at a power of 100 W for 11 s and were followed by a purge and a pump step of 1 s and 11 s, respectively. The precursor dosing and plasma exposure times were based on saturation studies as shown in the Supporting Information (S.I.), Figure S6.1, while the purge and pump times were determined to be long enough to reach a sufficiently low chamber pressure (< 0.1 mTorr) before starting the next sub-cycle. The NH_3, N_2 and H_2 plasmas were started after flowing the source gas into the reactor for 3 s. For the AB-H_2/N_2 process, the N_2 flow was started 2 s before the H_2 flow, and subsequently after 5 s, the H_2/N_2 plasma was ignited. This was done to stabilize the gas flows and minimize overpressures.

The pressure used for the NH_3 plasma was 1.5 mTorr. For the standard H_2/N_2 plasma the N_2 and H_2 pressures were separately set to 1.5 mTorr and 15 mTorr, respectively. Due to the addition of the N_2 to the H_2 gas, the pumping speed increases (as compared to only H_2), leading to a lower total pressure of approximately 13 mTorr for the H_2/N_2 mixture. Moreover, the actual $H_2/(H_2+N_2)$ mixing ratio is approximately ~ 0.77 (for the H_2 and N_2 pressures of 1.5 mTorr and 15 mTorr, respectively), due to the shorter residence time of H_2 as compared to N_2 (see also Section 6.3.1). The results for different $H_2/(H_2+N_2)$ ratios in Section 6.3.3 and Section 6.4.1 were obtained by varying the partial pressures of H_2 and N_2, while keeping the total pressure of the mixture constant at 13 mTorr. For the ABC-N_2-H_2 process, a pressure of 7.5 mTorr was used for both the N_2 and the H_2 plasmas, and both plasma exposures were 11 s long.

To determine the effect of the $H_2/(H_2+N_2)$ ratio on the NH_3 production in Section 6.3.1 a constant pressure of 75 mTorr was used for the gas mixture. This pressure was higher than the 'standard' 13 mTorr to allow for more accurate variation of the gas flows and to enable mixing ratios higher than 80 vol.%. For a pressure of 13 mTorr, it is not possible to keep the pressure constant for mixing ratios higher than ∼80 vol.%, due to the low gas flows used and due to changes in pumping speed upon mixing gas flows.

6.2.2 Plasma studies

Quadrupole mass spectrometry (QMS) measurements were performed using a Pfeiffer Vacuum Prisma QME-200 (mass-to-charge ratio m/z = 1 - 200), attached to the side of the ALD chamber. Measurements were done with the substrate table and reactor walls kept at the standard temperatures of 300 °C and 100 °C, respectively. Note that this means that a considerable part of the QMS signal can be originating from reactions at the reactor walls, since the surface area of the wall is significantly larger than the surface area of the substrate table. It was confirmed that growth also occurs at a deposition temperature of 100 °C, albeit it at a lower GPC (∼0.13 Å as compared to ∼0.29 Å) and with a higher impurity content. Since the aim is to compare the three ALD processes with each other, the temperature difference between the wall and the table is considered to be of minor influence.

For determination of the main species in the NH_3 and H_2/N_2 plasmas, mass scans (i.e. ion current as a function of m/z) for masses 1-30 were used. These mass scans were collected after stabilization of the gas flows and plasma. The $H_2/(H_2+N_2)$ mixing ratios were determined using the QMS ion currents at m/z ratios 2 and 14 (corresponding to H_2^+ and N^+, respectively) from such mass scans. For a complete description of this method see the Supporting Information.

The procedure for time-resolved QMS measurements was similar to the method as previously described by Knoops *et al.*[62] In short, for $m/z \leq 40$, four m/z ratios were measured simultaneously, of which one was always $m/z = 40$. This value corresponds to Ar^+ and is used as reference. For $m/z > 40$, besides $m/z = 40$, only one other m/z ratio was followed per measurement, in order to keep the signal-to-noise ratio optimal while maintaining a reasonable time resolution. Three different cycles were studied using the QMS measurements: a 'normal' (AB- or ABC-type) ALD cycle, a cycle without $CoCp_2$ dosing (but with Ar carrier gas dosing) and a cycle without igniting the plasma(s) (see Figure S6.2). This was done to discern reaction products from species present due to the precursor

dosing, source gas exposure, or plasma ignition. For each type of recipe, ten cycles were performed, and only the signals over the last nine were averaged, assuming the first cycle can deviate due to the recipes performed previously. To further minimize the influence of previous cycles, every set of cycles was preceded by a cleaning step consisting of an O_2 plasma for 90 s followed by a NH_3 plasma for 120 s. Moreover, the purging and gas stabilization times were extended as compared to the standard ALD cycle, in order to separate the effects of pressure overshoots from the reaction products. See Figure S6.3 (S.I.) for a more detailed description and an example of the raw data that is collected using this procedure. Optical emission spectroscopy (OES) was performed using a USB4000 spectrometer from OceanOptics, with a wavelength range of 180 nm - 1100 nm, mounted horizontally to the side of the plasma source.

6.2.3 Film analysis

For characterization of the deposited material, Co films were grown on Si (100) coupons with 450 nm thermal SiO_2. Prior to deposition, the samples were cleaned in situ with an O_2 plasma for 2 minutes. It was found that unloading the samples after the deposition at a table temperature of 300 °C led to significant oxidation of the Co film. Therefore, the substrate table was cooled down to 100 °C after each deposition to minimize the oxidation. Although the effect of the table temperature was not investigated in detail in this study, the GPC and film purity were found to decrease when going to lower sample temperatures, which will be addressed in a follow-up publication. The depositions for generating the saturation curves (Figure S6.1, S.I.) were performed on an ALD-grown Co seed layer to avoid nucleation effects. This Co seed layer was deposited by performing 400 cycles of the standard recipe using NH_3 plasma on a thermal SiO_2 wafer, resulting in a film thickness of approximately 12 nm. Coupons of this seed layer were loaded into the reactor with the table temperature set to 100 °C. After heating the substrate table in vacuum to the standard deposition temperature of 300 °C, the coupons were treated with a NH_3 plasma for 3 min to reduce the surface oxidation.

The ALD growth was monitored in situ by spectroscopic ellipsometry (SE) using a J.A. Woollam, Inc. M2000U ellipsometer.[63] The dielectric function of the deposited films was parameterized using a B-spline model.[64] The Co film microstructure was studied using transmission electron microscopy (TEM) using a JEOL ARM 200F, operated at 200 kV. For the TEM analysis a lamella was prepared using a focused ion beam (FIB) in a FEI Nova600i NanoLab. X-ray photoelectron spectroscopy (XPS) was performed with a Thermo Scientific KA1066 spectrometer, using monochromatic Al Kα X-rays with an energy of 1486.6 eV.

For XPS depth-profiling, sputtering was carried out using Ar^+ ions with an energy of 500 eV. In addition, four-point probe (FPP) resistivity measurements were done using a Keithley 2400 Sourcemeter and Signatron probe.

6.3 Results

6.3.1 Species in NH_3 and H_2/N_2 plasmas

The similarities and differences between the NH_3 plasma and H_2/N_2 plasma were identified by collecting mass spectra in the range m/z = 1-30. As can be seen in Figure 6.2, both plasmas mainly contain H_2 (m/z = 2), N_2 (m/z = 14 and 28) and NH_3 (m/z = 15-17). However, the ratio between these species differs for the two plasmas, with the relative amount of NH_3 being larger for the NH_3 plasma. Mass-to-charge ratios 15 and 16 could correspond to NH_x (x < 3) species formed in the plasma, as well as NH_x species formed by dissociation of NH_3 in the QMS analyzer. However, NH_x ($x < 3$) radicals present in the plasma are likely recombined before being detected in the QMS, meaning the signals for m/z = 15-17 can mainly be attributed to NH_3. Although NH_x ($x < 3$) species cannot directly be detected using the QMS, it can be assumed that they are present in the plasma as a consequence of dissociation of NH_3.[65] See also Table S6.1 (S.I.) for the assignment of species to corresponding mass-to-charge ratios.

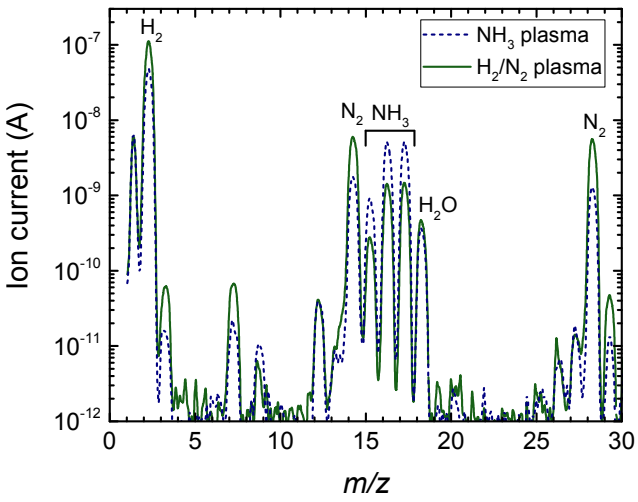

Figure 6.2 Quadrupole mass spectra for a NH_3 plasma and a H_2/N_2 plasma. The main plasma species (H_2, N_2 and NH_3) are indicated in the figure. The NH_3 pressure was 1.5 mTorr, while the H_2/N_2 pressure was 13 mTorr.

By comparing the QMS spectrum for the source gas with the spectrum for the corresponding plasma, it becomes visible which species are formed upon plasma ignition (see Figure S6.5). When a NH_3 plasma is ignited, the signals for m/z ratios 15, 16 and 17 decrease, while the signals at m/z = 2, 7, 14 and 28 increase. These observations indicate that part of the NH_3 is dissociated, leading to formation of both N_2 and H_2. Similarly, in a H_2/N_2 plasma N_2 and H_2 are dissociated upon plasma ignition, followed by the formation of NH_3 (see Figure S6.5b). NH_3 production using a H_2/N_2 plasma occurs mostly at the reactor walls, since a three-body reaction in the gas phase is unlikely for the pressures used in this work.[66,67] The two plasmas were further compared using OES measurements (see Figure S6.6, S.I.).[68] The emission spectra for the NH_3 and H_2/N_2 plasmas were found to be very similar. Moreover, the emission peak at ~336 nm corresponds to the $A^3\Pi \rightarrow X^3\Sigma$ transition of NH and was identified in the spectra for both plasmas (Figure S6.6b, S.I.), corroborating the presence of $NH_{x,\ x<3}$ species.[69,70]

To study the composition of the H_2/N_2 plasma as a function of the mixing ratio between the H_2 and N_2 gasses, QMS spectra where collected for different $H_2/(H_2+N_2)$ ratios. The amount of NH_3 species produced in the plasma was found to depend on the mixing ratio. Figure 6.3 shows the QMS ion currents at m/z ratios 16 and 17 as a function of the $H_2/(H_2+N_2)$ ratio for a constant chamber pressure of 75 mTorr. This pressure is higher than the standard 13 mTorr used for the ALD process, as explained in Section 6.2.1. The m/z ratios 16 and 17 correspond to NH_2^+ and NH_3^+ and their ion currents are a measure for the amount of NH_3 produced in the plasma. Figure 6.3 indicates a maximum in NH_3 production around 60 % - 80 % H_2 in the H_2/N_2 mixture, in agreement with previous work.[62,71] Interestingly, the optimum is found close to the ratio between N and H atoms in the NH_3 molecule (0.75).[71,72] Since the plasma composition depends strongly on the mixing ratio, selecting the $H_2/(H_2+N_2)$ ratio is highly important when using a H_2/N_2 plasmas for ALD, as will also be discussed later. Based on the optimum found in Figure 6.3, a $H_2/(H_2+N_2)$ mixing ratio of ~0.77 was employed for further QMS studies and depositions using the AB-H_2/N_2 process, unless specified otherwise.

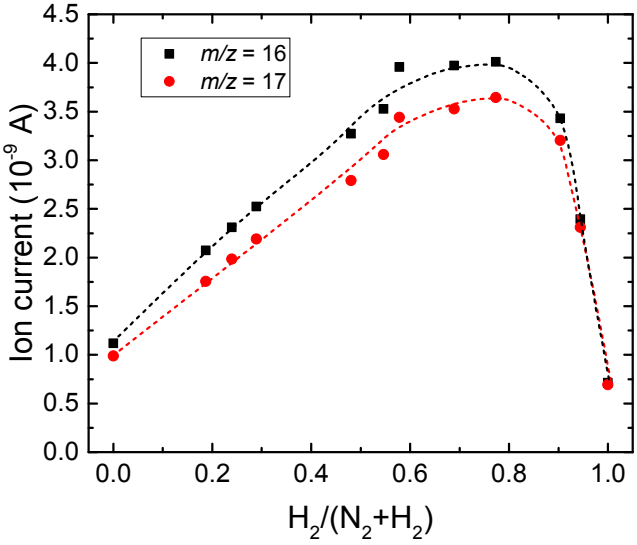

Figure 6.3 QMS ion current at m/z ratio 16 and 17 for H_2/N_2 plasmas as a function of H_2 fraction in the H_2/N_2 mixture. The $H_2/(H_2+N_2)$ mixing ratios on the horizontal axis were determined using the ion currents at m/z ratios 2 and 14, corresponding to H_2^+ and N^+, before igniting the plasma. The total chamber pressure was kept constant at 75 mTorr.

6.3.2 Reaction products during plasma half-cycle

Further insight in the use of NH_3 and H_2/N_2 plasmas was obtained by studying the reaction products formed during the ALD cycles using time-resolved QMS measurements. First, QMS signals were collected for m/z ratios 40 (Ar^+), 59 (Co^+) and 66 (HCp^+) during the precursor sub-cycle (Figure S6.7, S.I.). Based on these results, it can be concluded that HCp ($C_5H_6^+$, $m/z = 66$) is released as a product during the precursor half-reaction. Second, QMS signals were recorded during the co-reactant sub-cycles of the AB-NH_3 process (Figure 6.4a), the AB-H_2/N_2 process (Figure 6.4b) and ABC-N_2-H_2 process (Figure 6.4a). Measurements were done for a normal ALD cycle and for a reference cycle without $CoCp_2$ dosing, using plasma exposures of 11 s (see Figure S6.3, S.I.). Differences between the signals for the two cycles indicate the formation of species as a consequence of the ALD reactions.

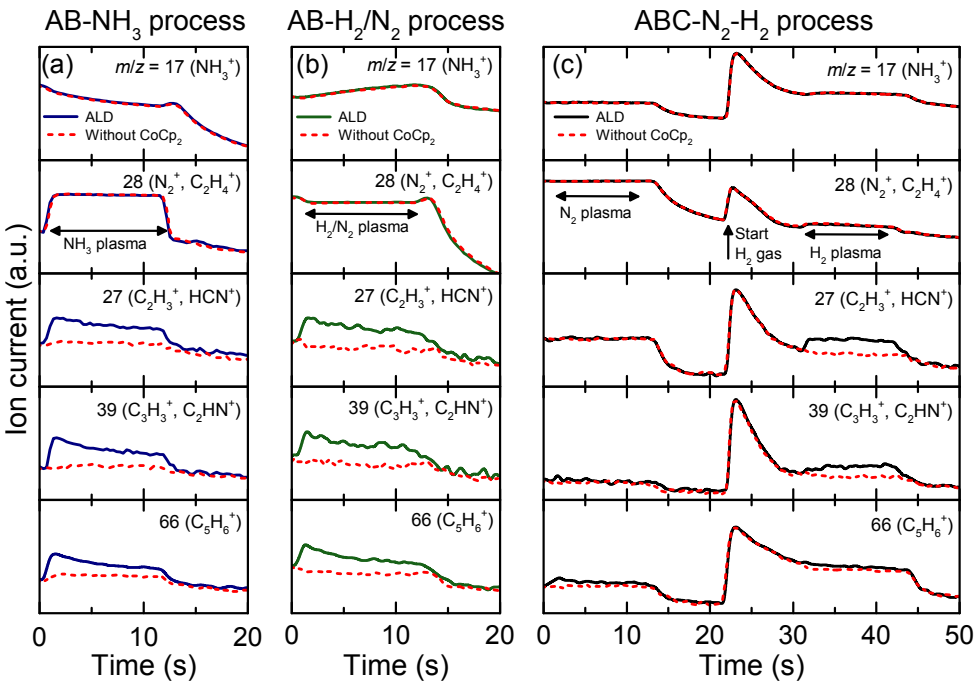

Figure 6.4 Time-resolved QMS signals for m/z ratios 17 (NH_3^+), 28 (N_2^+), 27 ($C_2H_3^+$, HCN^+), 39 ($C_3H_3^+$, HCN^+) and 66 ($C_5H_6^+$), collected during the plasma half-cycle for (a) the AB-NH_3 process, (b) the AB-H_2/N_2 process and (c) the ABC-N_2-H_2 process. A normal ALD cycle and a reference cycle without $CoCp_2$ precursor dosing were measured, with plasma ignition for 11 s during both cycles (indicated with an arrow in the panels for $m/z = 28$). The $H_2/(H_2+N_2)$ mixing ratio of the H_2/N_2 plasma was ~0.77.

Figure 6.4a shows results collected during the plasma sub-cycle of the AB-NH_3 process. The signals for m/z ratios 17 and 28 are very similar for the ALD cycle and the corresponding reference cycle and are related to the main plasma species, namely NH_3 and N_2. The increase in ion current for $m/z = 28$ and decrease for $m/z = 17$ after plasma ignition correspond to the formation of N_2 ($m/z = 28$), which is a consequence of the dissociation of NH_3 ($m/z = 17$). The current for $m/z = 17$ demonstrates a transient behavior, as NH_3 is a 'sticky' molecule and the NH_3 flow does not stabilize within the time of the exposure.[73] Meanwhile, the initial rise in ion currents (at ~0 s) for m/z ratios 27, 39 and 66 upon plasma ignition for the (normal) ALD cycle can be attributed to the release of reaction products (see Table S6.1, S.I.). This rise is not observed for the reference cycle without $CoCp_2$ dosing. The increase for $m/z = 66$, assigned to HCp^+ ($C_5H_6^+$), upon plasma ignition indicates the elimination of the Cp ring from the surface. A similar increase in ion current was observed for $m/z = 65$ ($C_5H_5^+$, data not

shown). The detection of HCp^+ reveals that some of the Cp ligands are still present on the surface after the $CoCp_2$ sub-cycle. Mass-to-charge ratio 27 corresponds to $C_2H_3^+$ or HCN^+ and $m/z = 39$ to $C_3H_3^+$ or C_2HN^+. The presence of, for example, HCN and C_2HN might be caused by reaction of C_xH_y and NH_x species in the plasma. The detection of $C_2H_3^+$ and C_3H3^+ can be explained by dissociative ionization of HCp in the QMS (see the cracking pattern in Figure S6.4) and/or by formation of C_2H_4 and C_3H_4 in the plasma due to dissociation of HCp. Such production channels can unfortunately not be distinguished using the current experimental setup.

The QMS results for the AB-H_2/N_2 process are shown in Figure 6.4b. The ion currents for m/z ratios 17 and 28 behave very similar for the ALD cycle and the reference cycle, and indicate the formation of NH_3 ($m/z = 17$) and consumption of N_2 ($m/z = 28$) in the H_2/N_2 plasma. These findings are in line with the QMS measurements discussed in Section 6.3.1 (and as shown in Figure S6.5). Note that the signal for $m/z = 17$ continues to increase during the plasma exposure, due to the 'sticky' nature of NH_3 and/or ongoing stabilization of the NH_3 production.[73] However, the current for $m/z = 17$ starts to drop after the plasma exposure, accompanied by a small increase in the signal for N_2, indicating that no more N_2 is being consumed. The ion currents for m/z ratios 27, 39 and 66 for the ALD cycle increase when the plasma is started (at $t \approx 0$s), similar to the data shown in Figure 6.4a. This increase can be explained by the release of reaction products, as was discussed for the AB-NH_3 process.

To examine the role of the NH_x species in the plasma in the reaction mechanism, the H_2/N_2 plasma was replaced by separated N_2 and H_2 plasma steps, in an ABC-type cycle (see Figure 6.1). The results for the ABC-N_2-H_2 process in Figure 6.4c show that no NH_3 was present during the N_2 exposure, as can be expected. Moreover, upon ignition of the N_2 plasma (at $t \approx 0$ s), a minimal amount of HCp^+ ($m/z = 66$) is detected (revealed by the small difference with the reference cycle), which is much smaller than for the AB-NH_3 and AB-H_2/N_2 processes. Upon ignition of the subsequent H_2 plasma, a rise in ion currents for both m/z = 17 and 28 (at $t \approx 32$ s, observed for the ALD cycle and also for the reference cycle) indicates that NH_3 and N_2 are released. However, the amounts are almost negligible, and are limited by the amount of nitrogen containing species adsorbed to the substrate and reactor wall after the N_2 plasma exposure. The H_2 plasma mostly leads to the detection of $C_2H_3^+/HCN^+$ ($m/z = 27$) and $C_3H_3^+/C_2HN^+$ ($m/z = 39$) species, and no significant amount of HCp^+. The limited amount of HCp^+ detected during both plasma exposures indicates that the Cp ring is not eliminated as a whole, but rather dissociated due to interaction with the plasmas.

Comparison of the results for the three different ALD processes gives insight in the similarities and differences in reaction mechanisms. Except for the differences in plasma species (m/z = 17 and 28), the results in Figure 6.4 (a) and (b) show very similar reaction products for the AB-NH_3 and the AB-H_2/N_2 processes. These analogies between the two AB-processes suggest a similar reaction pathway, where Cp ligands are eliminated from the surface during both the precursor and plasma sub-cycle. QMS measurements for the ABC-N_2-H_2 process show significant differences in terms of plasma species and reaction products (see Figure 6.4c), as compared to the AB-processes, suggesting a different reaction pathway.

6.3.3 Film properties

Before characterization of the material properties, the ALD behavior of the two AB-processes was studied by determining the GPC as a function of the $CoCp_2$ dosing and the plasma exposure times. As can be seen in Figure S6.1, both the precursor and co-reactant sub-cycles demonstrated self-limiting behavior for the NH_3 plasma as well as for the H_2/N_2 plasma processes. Moreover, the saturation curves for the two processes look very similar, in line with the finding that the two AB-processes show similarities in terms of plasma composition and reaction pathways as discussed in Sections 6.3.1 and 6.3.2. The GPC saturates to a value of 0.29 $\pm$ 0.02 Å, which is slightly lower than reported by Kim and co-workers (0.48 Å).[26,30]

The material properties for the three different ALD processes were investigated for films deposited using 1000 cycles. A film deposited using the AB-NH_3 process was investigated using transmission electron microscopy (TEM) after preparation of a lamella using a focused ion beam (FIB). The cross-sectional images in Figure 6.5 reveal that the film is polycrystalline and the crystal grains can clearly be observed. The film forms a closed layer of approximately 29 nm thick and has a low roughness. Spectroscopic ellipsometry (SE) modeling yielded a film thickness of $\sim$32 nm. The difference between the thicknesses derived from SE and from TEM is thought to be due to the film roughness, which is not included in the SE modeling.

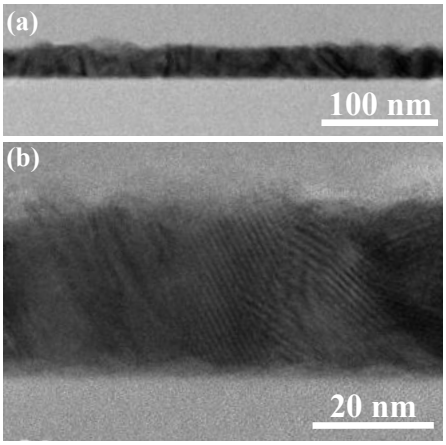

Figure 6.5 (a and b) Cross-sectional transmission electron microscope (TEM) images of a Co film deposited by performing 1000 ALD cycles of the AB-NH_3 process.

Material properties obtained using the different processes are shown in Table 6.3. As can be seen, for both the AB-NH_3 and the AB-H_2/N_2 process the film thickness (determined using spectroscopic ellipsometry, SE) is ~25 nm after 1000 cycles, corresponding to an average GPC of ~0.25 Å. It is noted that the sample prepared for TEM analysis was a different sample than the sample listed in Table 6.3 and the film thickness was slightly higher. The ABC-N_2-H_2 process resulted in an average GPC as high as 0.44 Å. The films deposited using the AB-NH_3 and the AB-H_2/N_2 processes both demonstrate a low resistivity (41 - 42 μΩ cm, as compared to a Co bulk resistivity of 6.24 μΩ cm) and have a similarly low impurity content.[74] The resistivity values obtained for the AB-processes are slightly higher than the best reported value for Co ALD, and lie within the range of values obtained for processes using NH_3 or H_2/N_2 plasma as the co-reactant (10 - 140 μΩ cm, see Table 6.2). This is in contrast to the film deposited using the ABC-N_2-H_2 process, which has a high resistivity (>1000 μΩ cm), likely caused by considerable amounts of impurities found in the film (O, N and C add up to 25 at.%).

Table 6.3 Material properties of Co films for the three different ALD processes as determined from spectroscopic ellipsometry (SE), four-point probe and XPS. 1000 ALD cycles were performed. The impurity contents were determined after sputtering with Ar^+ for 6 min.

ALD process	d (nm)	ρ (μΩ·cm)	[O] (at. %)	[N] (at. %)	[C] (at. %)
AB-NH_3	25	41	0.5 ± 0.3	2.3 ± 0.5	0.6 ± 0.6
AB-H_2/N_2	25	42	1.0 ± 0.4	2.8 ± 0.5	0.7 ± 0.7
ABC-N_2-H_2	44	1×10^3	10.0 ± 0.5	8.4 ± 0.5	7 ± 1

XPS measurements showed that the surface of the Co films is slightly oxidized (Figure S6.8). After Ar+ sputtering, the O contents of the films deposited using both AB-processes (NH_3 and H_2/N_2) are however found to be close to 0 at.%, and metallic Co2p peaks were detected around 780.2 eV.[75] Apart from minimal amounts of O, C and N, no other impurities were detected in the Co films grown the AB-NH_3 and the AB-H_2/N_2 processes. For the film deposited using the ABC-N_2-H_2 process, significant amounts of O, C and N were detected in the bulk of the film, (see the XPS results Figure S6.8 and Figure S6.9). It was found that exchanging the H_2 and N_2 plasma exposures, corresponding to an ABC-type cycle with first the H_2 plasma followed by the N_2 plasma, led to a comparable impurity content of approximately 25 at.% (see Table S6.2, S.I.).

The significant higher GPC and resistivity for the ABC-N_2-H_2 process can be explained by the impurity incorporation, leading to a lower film density and/or a higher surface roughness. The difference between the two AB-processes on one hand and the ABC-N_2-H_2 process on the other hand can most likely be attributed to the absence of NH_x species in the plasmas for the ABC-N_2-H_2 process (see Section 6.3.2), as will also be discussed below.

As described in Section 6.3.1, the amount of NH_3 produced in the H_2/N_2 plasma depends on the ratio between the two source gasses. To study the effect of the NH_3 concentration in the plasma, a set of Co films was deposited for various $H_2/(H_2+N_2)$ ratios, using a constant pressure of 13 mTorr for the gas mixture. The properties of the Co films were studied using spectroscopic ellipsometry (SE), four-point probe (FPP) and XPS and the results are shown in Table 6.4. The thicknesses of the films varied somewhat as a function of H_2 fraction, with higher film thicknesses ($\sim$20 nm) obtained for intermediate ratios of 0.35 and 0.42. The films deposited using low mixing ratios of 0.13 and 0.23 had resistivity values that were too high to be measured ($>10^9$ $\mu\Omega$ cm). For higher mixing ratios, the resistivity of the films decreased with increasing H_2 fraction, which correlates to a significant decrease in O impurity content. In addition to the O content, differences in film structure (e.g. crystallinity, density or porosity) might affect the film resistivity, and further research would be required to obtain a more detailed understanding. The O incorporation is likely due to dissociation of background species (such as H_2O) in the plasma during film growth or, post-deposition oxidation of the films.[76,77] Interestingly, the C and N contents of the films are relatively constant and do not show a clear trend as a function of $H_2/(H_2+N_2)$ ratio. The relation between the $H_2/(H_2+N_2)$ ratio and the material properties will be further discussed in Section 6.4.1.

Table 6.4 Material properties of Co films for the three different ALD processes as determined from spectroscopic ellipsometry (SE), four-point probe and XPS. 1000 ALD cycles were performed. The impurity contents were determined using XPS after sputtering with Ar^+ for 6 min.

$H_2/(H_2+N_2)$	d (nm)	ρ (μΩ·cm)	[O] (at. %)	[N] (at. %)	[C] (at. %)
0.13	17.9	$>10^9$	7.0 ± 0.2	9.5 ± 0.5	4.0 ± 0.9
0.23	19.9	$>10^9$	6.2	9.5	3.8
0.35	20.3	3.6×10^8	5.6	9.3	3.8
0.42	20.3	2.5×10^3	4.2	9.6	3.5
0.52	19.6	1.5×10^3	4.4	8.8	3.8
0.77	17.5	78	0.2	8.4	4.6

6.4 Discussion

6.4.1 Role of NH_x species

The results addressed in Section 6.3 can give insight into the role of different plasma species during Co film growth. Specifically, the data in Table 6.4 show that the impurity content decreases with the H_2 fraction in the H_2/N_2 plasma. Meanwhile, the ion current at $m/z = 17$, indicating NH_3 in the plasma, increased when varying the $H_2/(H_2+N_2)$ ratio up to ~0.77 (see Figure S6.3). This finding is in line with the dependence of the NH_3 content on the mixing ratio as was discussed in Section 6.3.1. In Figure 6.6 the Co concentration of the films is plotted as a function of the ion current for $m/z = 17$. Interestingly, this graph shows a linear trend, suggesting that a higher amount of $NH_{x,\ x\leq3}$ species in the plasma leads to a higher film purity. Note that with a higher NH_3 concentration in the plasma, also the amount of $NH_{x,\ x<3}$ radical species increases, as a consequence of NH_3 dissociation. The increase in Co purity is mostly due to the decline in O content, suggesting that $NH_{x,\ x<3}$ or NH_3 species facilitate the removal of O from the material, or lead to a film which is less prone to post-deposition oxidation. Additional research is required to distinguish between these two possible explanations.

Overall, the findings show that careful consideration is needed when a H_2/N_2 plasma is employed as co-reactant for ALD. Moreover, the dependence on the NH_x concentration explains why H_2 plasmas or N_2 plasmas are not suitable as co-reactants, namely due to the lack of NH_x species. In addition, the fact that

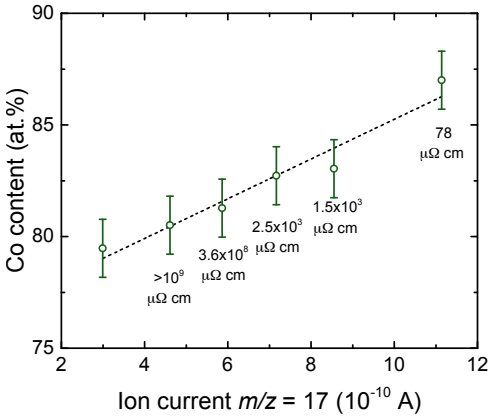

Figure 6.6 Co content from XPS as a function of QMS ion current at $m/z = 17$. The QMS ion current is a measure for the NH_3 production in the H_2/N_2 plasma and was varied by changing the H_2/N_2 mixing ratio of the source gas. The pressure of the H_2/N_2 gas mixture was kept constant at 13 mTorr. The Co content was determined using XPS on films obtained by performing 800 ALD using the various H_2/N_2 mixing ratios. XPS was carried out after sputtering with Ar^+ ions for 3 minutes. The resistivity values of the Co films are indicated in the figure and the dashed line in represents a linear fit through the data. It is noted that the decrease of the film resistivity as a function of NH_x concentration might be related to changes in film structure, aside from the increased film purity.

NH_3 gas cannot be used as co-reactant in a thermal ALD process substantiates the hypothesis that NH_x ($x < 3$) plasma species are necessary. The results thus suggest that $NH_{x,\ x\leq 3}$ species play a crucial role in the Co growth. This is further elaborated on in Section 6.4.2, where a reaction mechanism is proposed. Interestingly, the dependence of the film resistivity on the H_2/N_2 ratio is in agreement with the work of Yoon *et al.* and Hong *et al.* for the deposition of Co and Ru, respectively.[12,26] Both studies observed high resistivity values for high N_2 fractions and suggested that NH_x species in the plasma play an important role in the growth.[12,26] In addition, in the work of Ten Eyck *et al.* the H_2/N_2 ratio was optimized in order to maximize the NH_x generation in the plasma.[10] Finally, ALD processes for Ru, Ni and Ag have been reported to improve when NH_3 plasmas are used instead of H_2 plasmas (in terms of a higher GPC and lower resistivity), which also suggests an important role of NH_x species present in the NH_3 plasmas.[18–20]

6.4.2 Reaction mechanism

The QMS studies addressed in Section 6.3.2 can help to unravel the reaction mechanisms for the ALD growth of Co. Before reviewing the main QMS results, it is relevant to obtain an understanding of the surface groups present on Co after

plasma exposure (i.e. prior to precursor dosing). Although the interaction of a NH_3, H_2, or N_2 plasma with a Co surface has not been studied in detail, the surface science literature on Co gives some insight. For instance, Kizilkaya *et al.* investigated the stability of NH_x groups on Co after NH_3 exposure and found that NH_3 adsorption on Co is followed by decomposition, resulting in NH_x groups remaining on the surface.[78] In addition, Wang *et al.* studied the nitridation of transition-metal surfaces and calculated that Co is not prone to nitridation, although a N-covered surface is stable after formation.[27] Based on these reports it can be expected that NH_x groups are present on the Co film after NH_3 or H_2/N_2 plasma exposure. H adsorbed on the Co surface seems less likely, since H is reported to desorb (as H_2) from Co between temperatures of approximately 300 K - 400 K, which is lower than the sample temperature during ALD (300 °C = 573 K table temperature).[79–81] Notably, the role of N-containing surface species has previously been addressed for ALD of Pt and Ag using N_2 or NH_3 plasmas.[19,28,82] Specifically, N-containing species were proposed to adsorb during the N_2 or NH_3 plasma exposures, and to react with the precursor during the subsequent precursor dose.

In short, the QMS studies in Section 6.3.2 revealed the following. During the precursor and co-reactant sub-cycles HCp (C_5H_6) is released, for both the AB-NH_3 and the AB-H_2/N_2 process. In addition, fragments of the Cp ring (e.g. $C_xH_y^+$ and $C_xH_yN^+$) were detected during the plasma exposure. Furthermore, variation of the H_2/N_2 ratio showed that NH_3 species ($NH_{x,\ x\leq 3}$) play an important role in the growth mechanism. These observations suggest that during the precursor sub-cycle the $CoCp_2$ molecules chemisorb to the surface, and that part of the Cp rings react with H atoms present at the surface, followed by the release of HCp. This is illustrated in step 'A' in Figure 6.7. Considering that chemisorbed H is not stable on a Co surface, it is speculated that NH_y surface groups present after the plasma exposure provide the source of H (NH_y with the subscript y is used to indicate the distinction from NH_x species in the plasma). Additional research such as surface Fourier-transform infrared spectroscopy (FTIR) is required to identify the surface groups to which the precursor binds. Possibly the precursor chemisorbs directly to unoccupied Co surface sites, or to NH_y species after the release of HCp.

In the co-reactant sub-cycle, the Cp ligands remaining after precursor dosing are eliminated by NH_3 radical species from the plasma ($NH_{x,\ x<3}$). This reaction leads to the formation of HCp and C, H and N containing fragments, as illustrated in step 'B' in Figure 6.7. The release of HCp was also observed during the NH_3 plasma exposure in the work of Oh *et al.*[83] Moreover, Shimizu *et al.* and Yuan *et al.* used NH_3 as co-reactant gas for Co and Ni hot-wire ALD using $CoCp_2$ and $NiCp_2$ as precursors, respectively, and claimed that NH_2 gas phase species

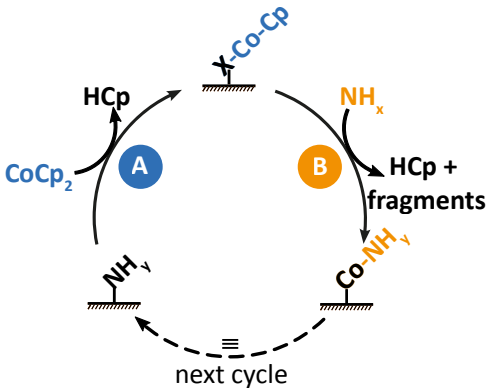

Figure 6.7 Schematic representation of the proposed reaction mechanisms during ALD of Co using NH_3 or H_2/N_2 plasma as the co-reactant. During the precursor sub-cycle ('A'), the $CoCp_2$ binds to the surface, accompanied by the release of HCp. The site to which the $CoCp_2$ chemisorbs is indicated as 'X', since it remains to be identified. In the co-reactant sub-cycle ('B'), the $NH_{x,\ x<3}$ species from the plasma cause the release of HCp and fragments thereof, and lead to the formation of NH_y surface groups. NH_y with the subscript y is used to indicate the distinction from NH_x species in the plasma

formed on the hot-wire are needed for dissociation of the metal-Cp bond.[50,84] In the reaction mechanism shown in Figure 6.7, the $NH_{x,\ x<3}$ species generated in the plasma thus fulfill this role. Furthermore, the $NH_{x,\ x<3}$ species as well as NH_3 lead to formation of NH_y surface groups, which react with the precursor molecules in the next cycle. Although NH_3 can dissociate after adsorption on a clean Co surface, it is believed that $NH_{x,\ x<3}$ plasma species are essential for complete ligand removal. Note that a small amount of N (~2-3 at.%) is present in the Co films deposited using the AB-NH_3 and the AB-H_2/N_2 processes, and that this content is slightly higher (~4.5 at.%) in the (sub)surface region (see Figure S6.9). This corroborates the expectation based on the surface science literature that N containing species (e.g. NH_y) are present and that they are more stable on the surface than in the bulk. However, a remaining question is how the surface NH_y species leave the film, such that they are not incorporated in the film. Since the films contain only a small amount of N, it is speculated that most of the N diffuses out of the surface region, and desorbs in the form of either NH_3 or N_2. Interestingly, an analogy appears to exist between the proposed reaction mechanism and the ALD growth of noble metal using O_2 as the co-reactant. During noble metal ALD, chemisorbed O plays a crucial role in the reaction mechanism, while the stability of noble metal oxides is limited.[85] This is similar to ALD of Co, where NH_x species appear needed for chemisorption of the precursor and removal of the Cp ligands, but are not built into the film.

6.5 Conclusion

The use of H_2-, N_2-, and NH_3-based plasmas as co-reactant for ALD of Co using $CoCp_2$ was investigated. A direct comparison was made between ALD processes with a NH_3 plasma and a combined H_2/N_2 plasma as co-reactant. It was shown that the NH_3 and H_2/N_2 plasmas contain comparable plasma species, including $NH_{x,\ x\leq 3}$, although the relative concentrations are different. Moreover, the reaction products detected during the plasma sub-cycle are very similar, suggesting analogous reaction pathways. Variation of the mixing ratio of H_2 and N_2 in the H_2/N_2 plasma showed that the lowest resistivity is achieved for ratios with the highest $NH_{x,\ x\leq 3}$ concentration. In addition, films deposited using plasmas with a lower $NH_{x,\ x\leq 3}$ concentration contained significant amounts of O impurities. Deposition using an ABC-type cycle with consecutive N_2 and H_2 plasma steps resulted in a Co film with significant amounts of impurities and a high resistivity. These insights indicate that the NH_x species present in both the NH_3 plasma and the H_2/N_2 plasma are necessary for eliminating the precursor ligands and for obtaining high-purity films, which explains why H_2 plasmas or N_2 plasmas are not suitable as co-reactants. Furthermore, based on the QMS results and surface science literature, a reaction mechanism was proposed where $NH_{x,\ x<3}$ play an essential role, leading to the release of HCp in both sub-cycles. Overall the work shows that the plasma composition can strongly affect the obtained material properties and that the co-reactant of a metal ALD process should be carefully selected. Specifically, when using a H_2/N_2 plasma for Co ALD, selecting the $H_2/(H_2+N_2)$ ratio is crucial. Other literature reports further illustrate the importance of choosing a suitable co-reactant and demonstrate that NH_3 or H_2/N_2 plasmas can be preferred over other co-reactants.[17–20,28] This suggests that the findings of this work can be generalized and can also apply to other metal ALD process.

Acknowledgements

The authors gratefully acknowledge J.J.A. Zeebregts, C.A.A. van Helvoirt and C. van Bommel for technical assistance and dr. Harm Knoops and dr. Nick Thissen for fruitful discussion. The authors would also like to thank Dr. M. A. Verheijen for the TEM analysis. Solliance and the Dutch province of Noord-Brabant are acknowledged for funding the TEM facility. This work was financially supported by the Netherlands Organization for Scientific Research (NWO) through the Zwaartekracht program 'Research Centre for Integrated Nanophotonics'.

6.6 Supporting Information

ALD behavior

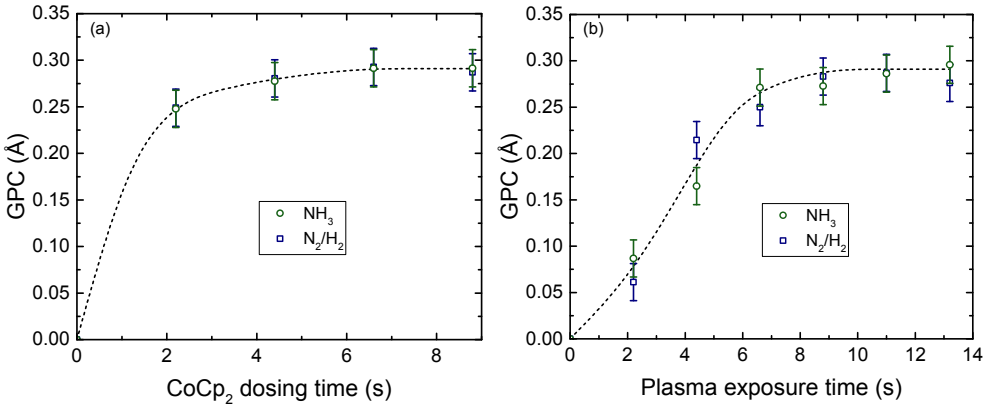

Figure S6.1 Growth per cycle (GPC) as a function of (a) $CoCp_2$ dosing time and (b) plasma exposure time for the AB-NH_3- and the AB-H_2/N_2 processes, plotted in the same graphs. The default $CoCp_2$ dosing time and plasma exposure time were 6 s and 10 s, respectively. The lines serve as guides to the eye. The saturation curves for the two processes look very similar and the GPC in saturation is approximately the same (0.29 $\pm$ 0.02 Å). The precursor dosing time shows saturation after roughly 5 s, and a plasma exposure time of 9 s is needed to reach saturation.

Procedure for time-resolved quadrupole mass spectrometry measurements

To be able to differentiate between signals caused by reaction products from signals caused by species present due to either the precursor dosing, source gasses, or plasma ignition, different types of cycles were used. These three different cycles were: a 'normal' ALD cycle, a cycle without precursor dosing and a cycle without igniting the plasma(s). See Figure S6.2 for schematics of the three different cycles.

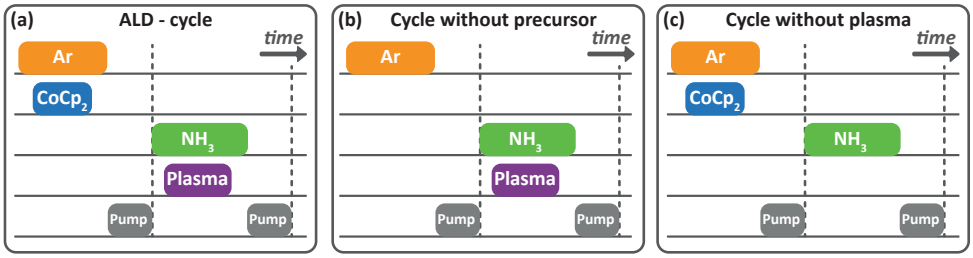

Figure S6.2 Schematic illustrations showing the three different cycles that were used for the QMS studies for the case of the AB-NH_3 process.

The three different sets of cycles were performed sequentially. Figure S6.3 shows an example of the raw data that is collected by this procedure. As can be seen, every set of ten ALD cycles was preceded by plasma cleaning steps or a 'plasma reset'. This plasma reset consisted of a 90 s O_2 plasma (to remove contamination from the reactor wall), a reducing NH_3 plasma for 120 s, and a final pump step of 60 s. For each set of ten cycles, the signal over the last nine was averaged, since the first cycle was typically affected by the plasma reset.

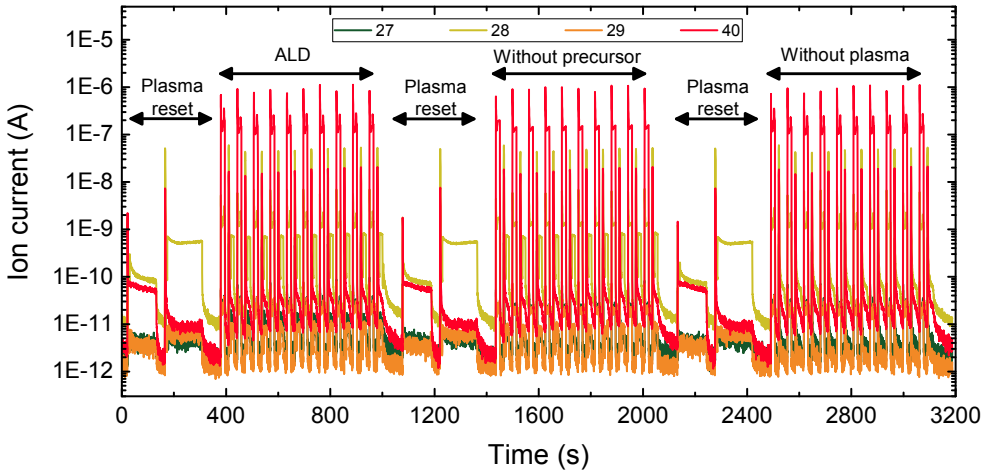

Figure S6.3 Raw QMS data collected for four different m/z ratios (27, 28, 29 and 40). Three different sets of cycles were performed, separated from each other by plasma resets.

QMS cracking patterns

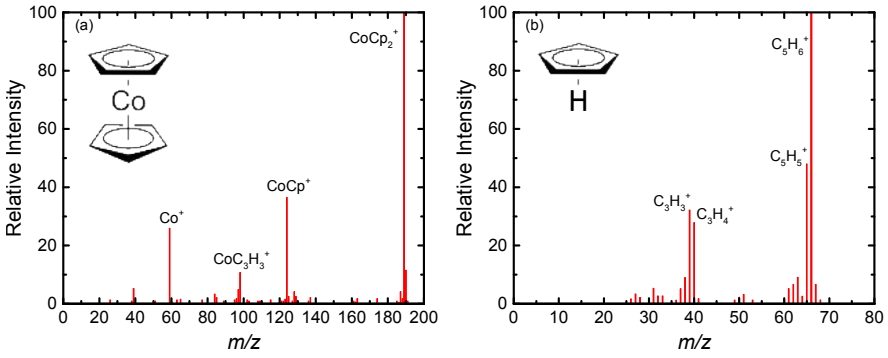

Figure S6.4 QMS cracking patterns for (a) $CoCp_2$ and (b) HCp, both taken from the NIST database. The cracking pattern for $CoCp_2$ is dominated by signals at $m/z = 59$ (Co), 124 (CoCp) and 189 ($CoCp_2$). Signals at 39, 40, 65 and 66 are the main contributions in case of HCp.

Assignment of species to m/z ratios

Table S6.1 *m/z* ratios, their assigned ions and their (main) assigned parent molecules. The assignments are based on cracking patterns taken from the NIST database.

m/z	Assigned ion(s)	Assigned parent species	*m/z*	Assigned ion(s)	Assigned parent species
2	H_2^+	H_2	27	$C_2H_3^+$, HCN^+	C_2H_4, C_5H_6, HCN
12	C^+	HCN	28	N_2^+, $C_2H_4^+$	N_2, C_2H_4
13	CH^+	HCN	39	$C_3H_3^+$, C_2HN^+	C_5H_6, C_3H_4, $Co(C_5H_5)_2$, C_2HN
14	N^+	N_2, NH_3	40	Ar^+, $C_3H_4^+$, $C_2H_2N^+$	Ar, C_3H_4, C_5H_6, C_2H_2N
15	NH^+	NH_3	59	Co^+	$Co(C_5H_5)_2$
16	NH_2^+	NH_3	65	$C_5H_5^+$	C_5H_6, $Co(C_5H_5)_2$
17	NH_3^+	NH_3	66	$C_5H_6^+$	C_5H_6, $Co(C_5H_5)_2$
18	H_2O^+, NH_4^+	H_2O, NH_3	98	$CoC_3H_3^+$	$Co(C_5H_5)_2$
24	C_2^+	C_2H_4, C_5H_6	124	$Co(C_5H_5)_2^+$	$Co(C_5H_5)_2$
25	C_2H^+	C_2H_4, C_5H_6	189	$Co(C_5H_5)_2^+$	$Co(C_5H_5)_2$
26	$C_2H_2^+$, CN^+	C_2H_4, C_5H_6, HCN			

Comparison of NH_3 and H_2/N_2 plasma using QMS and OES

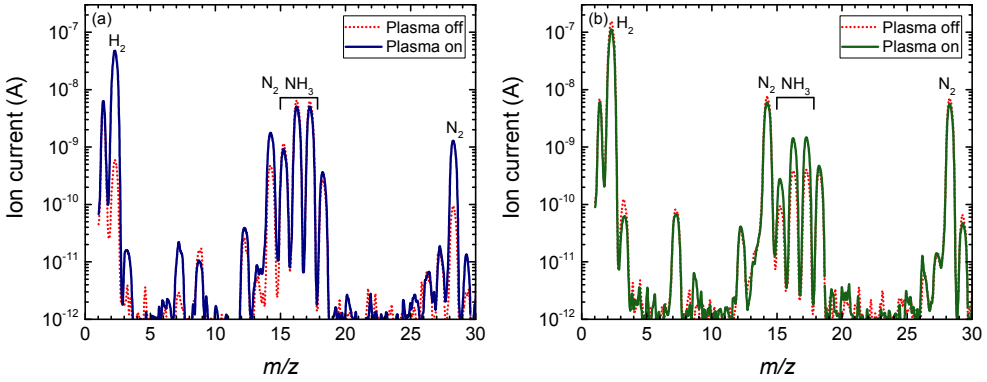

Figure S6.5 QMS mass spectra for (a) NH_3 and (b) H_2/N_2, gas and plasma. The spectra were collected for the source gas only ('plasma off') and after plasma ignition ('plasma on'). Comparison of the two spectra in (a) indicates that part of the NH_3 is dissociated upon plasma ignition, leading to formation of N_2 (m/z = 14 and 28) and H_2 (m/z = 1 and 2). On the contrary, (b) shows that part of the H_2 and N_2 in the H_2/N_2 plasma is consumed, leading to the formation of NH_3, as revealed by the increase in ion current for m/z ratios 15-17.

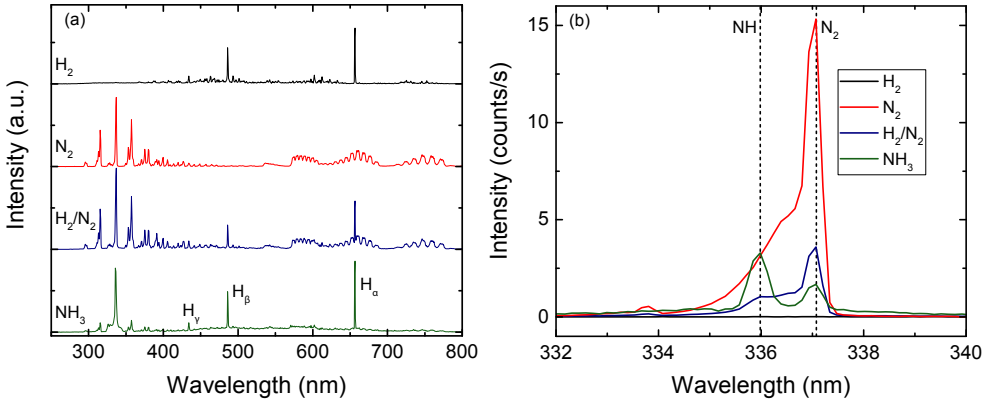

Figure S6.6 Optical emission spectra for H_2, N_2, H_2/N_2 and NH_3 plasmas over the wavelength range of (a) 280 nm - 800 nm and (b) 332 nm - 340 nm. The emission spectra for the NH_3 and H_2/N_2 plasmas are very similar. (a) The spectra have been scaled and offset for clarity. (b) An emission line for excited NH can be seen at 336 nm in the spectra for both plasmas, indicating that $NH_{x,\ x<3}$ radical species are present.

QMS precursor half-cycle

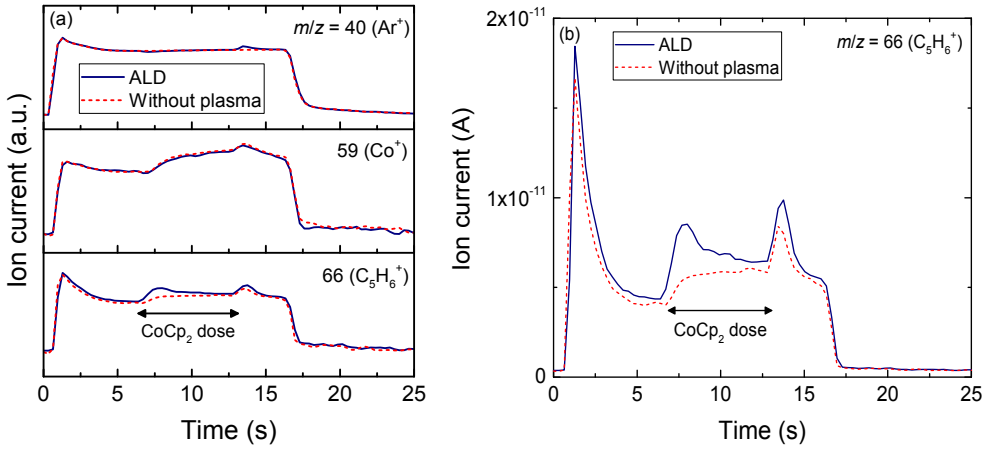

Figure S6.7 (a) Time-resolved QMS signals for m/z ratios 40 (Ar^+), 59 (Co^+) and 66 ($C_5H_6{}^+$), collected during the precursor sub-cycle of the AB-NH_3 process, plotted on a logarithmic vertical scale. (b) The QMS signal for $m/z = 66$, plotted using a linear vertical scale. QMS measurements were done for the normal ALD cycle, and for a reference cycle without igniting the plasma, both using a $CoCp_2$ dose of 6 s. Comparing the two signals gives insight into which species are formed as a consequence of the ALD reactions. Note that the Ar carrier gas is diverted before sending it through the $CoCp_2$ bubbler in order to stabilize the gas flow. This leads to an increase in chamber pressure, which explains the initial increase in ion currents just after $t = 0$. After the Ar starts flowing through the bubbler at around 7 s (indicated with an arrow in the figure), the ion currents for m/z ratios 59 and 66 increase, related to Co^+ and HCp^+ ($C_5H_6{}^+$), respectively. Subsequently changing the Ar gas flow from the bubbler to the purge line at $t = 13$ s leads to a pressure spike, accompanied by a peak in the ion currents. During the 'normal' ALD cycle the increase at $t = 7$ s for $m/z = 66$ is significantly higher than for the reference cycle without plasma exposure (note that the vertical scale is logarithmic in (a)). This difference in ion current suggests that HCp is released when the precursor molecule chemisorbs to the surface. Note that similar QMS measurements for the AB-H_2/N_2 process also revealed the release of HCp during precursor dosing, suggesting a similar reaction mechanism.

X-ray photoelectron spectroscopy

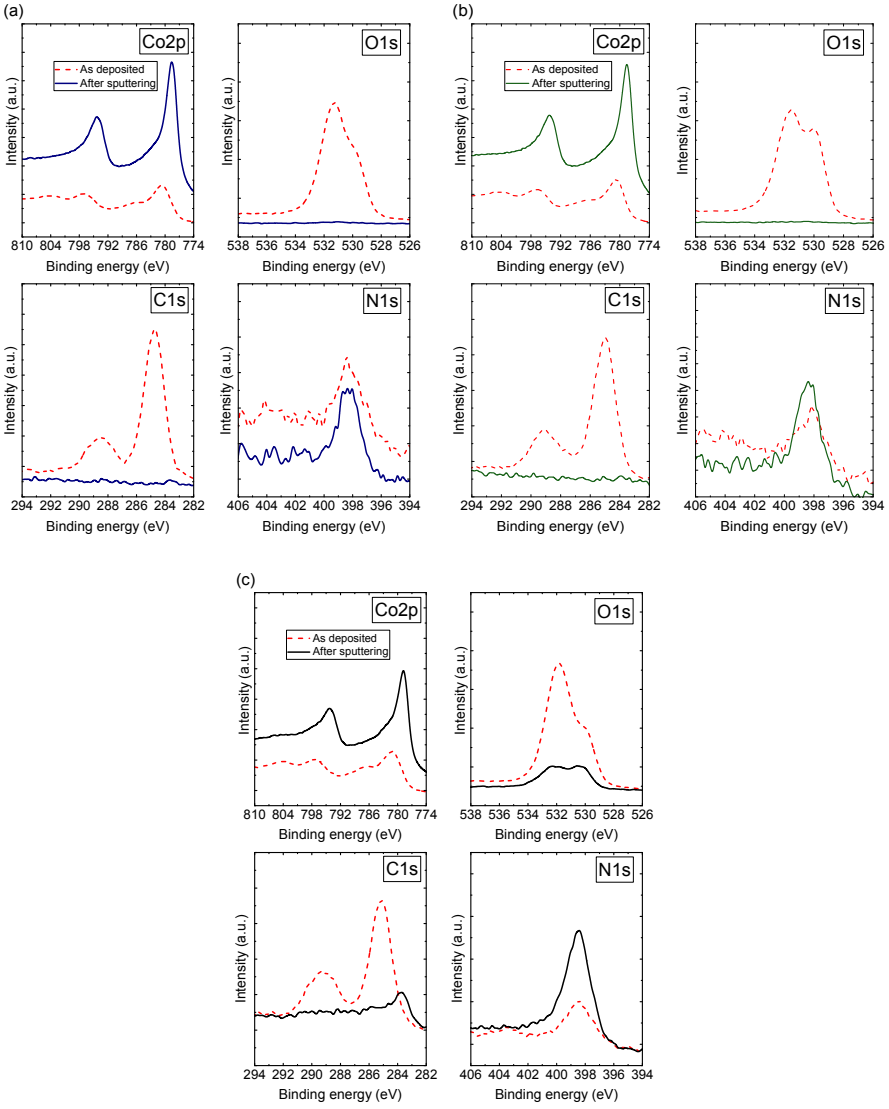

Figure S6.8 XPS spectra for the Co2p, O1s, C1s and N1s peaks for Co films deposited using the (a) AB-NH_3 process, (b) the AB-H_2/N_2 process and (c) the ABC-N_2-H_2 process. 1000 cycles were performed for all samples. 6 minutes Ar^+ sputtering was applied to remove the surface contamination. The films deposited using the AB-NH_3- and AB-H_2/N_2 processes contain small amounts of impurities, while the film deposited using the ABC-N_2-H_2 process is significantly contaminated with O, C and N. The surface of the films is slightly oxidized. However, the metallic Co2p peaks is visible around 780.2 eV after Ar^+ sputtering, for the films deposited using the AB-processes.

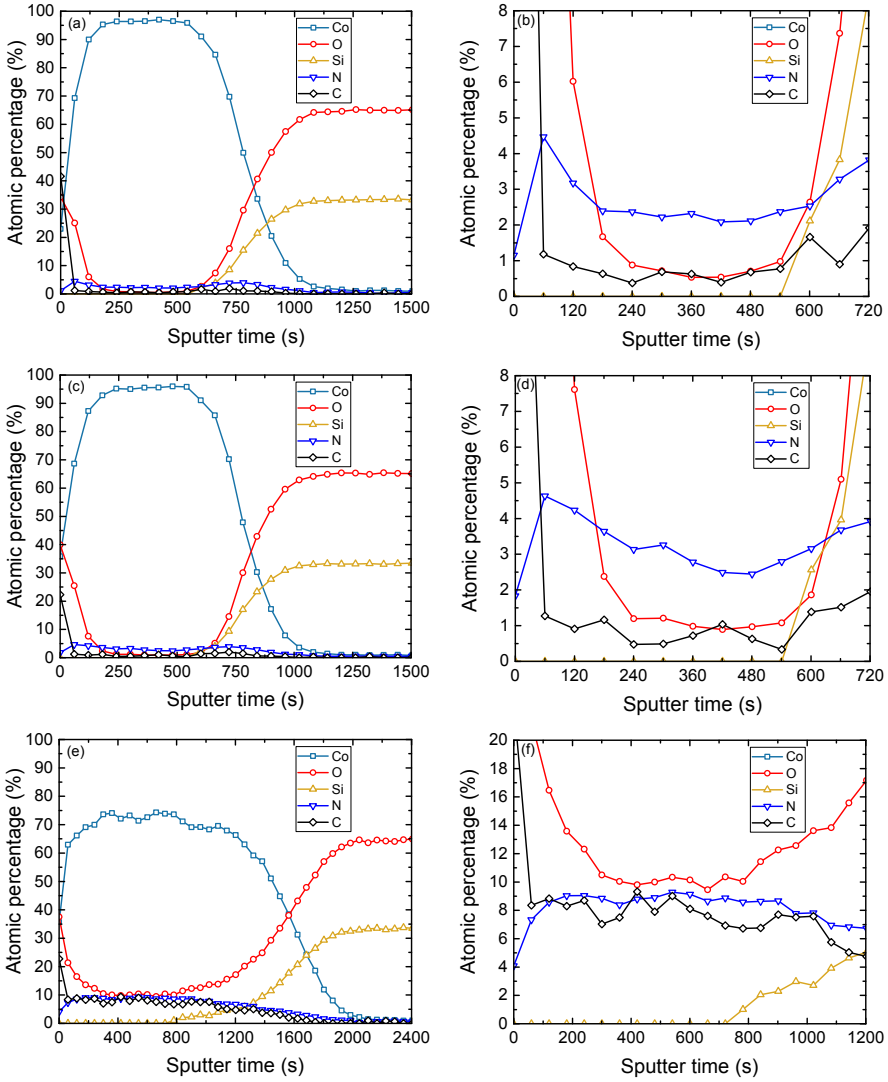

Figure S6.9 XPS depth profiles for Co films deposited using (a, b) the AB-NH_3 process, (c, d) the AB-H_2/N_2 process and (e, f) the ABC-N_2-H_2 process. 1000 cycles were performed for all samples. (b,d,f) show the impurity contents (O, N and C) in more detail. For the AB-NH_3 process and the AB-H_2/N_2 process the N-content is slightly higher in the subsurface region ($\sim$4.5 at.% as compared to $\sim$2.5 at.%), suggesting that N species (e.g. NH_y) are more stable on the surface than in the bulk. Moreover, the trend of the N-content corroborates the out diffusion of N.

Material properties for ABC-processes

Table S6.2 Material properties of Co films for the ABC-processes as determined from SE, four-point probe and XPS. Two different three-step processes were used, an ABC-cycle with the N_2 plasma first, followed by the H_2 plasma and an ABC-cycle with the H_2 plasma first followed by the N_2 plasma. The impurity contents were determined using XPS after sputtering with Ar^+ for 6 min.

ALD process	Cycles	d (nm)	ρ (μΩ·cm)	[O] (at. %)	[N] (at. %)	[C] (at. %)
ABC-N_2-H_2	1000	44	1×10^3	10.0	8.4	7.2
ABC-H_2-N_2	350	28	7×10^3	8.9	8.5	7.8

Ion current as a function of H_2/N_2 mixing ratio

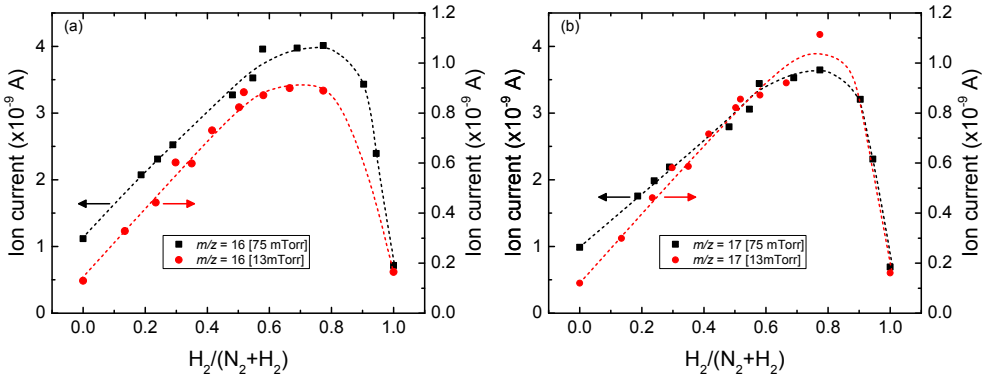

Figure S6.10 QMS ion current at (a) m/z ratio 16 and (b) m/z ratio 17 as a function of H_2 fraction in the H_2/N_2 gas mixture, for a pressure of 13 mTorr and 75 mTorr. The ion currents at m/z ratios 16 and 17 are measures for the NH_3 content in the H_2/N_2 plasma. The lines are guides to the eye. Due to the low gas flows used for a pressure of 13 mTorr, it is not possible to keep the pressure constant for mixing ratios higher than ∼80 vol.%. As mentioned in the main text, adding N_2 gas to the H_2 gas increases the pumping speed, thereby changing the total pressure. This makes obtaining certain mixing ratios for a constant total pressure not straightforward. However, the similarities between the trends for the two different pressures confirm that the optimum in the NH_3 production corresponds to 70 vol.% - 80 vol.% H_2, both at 13 mTorr and 75 mTorr. The data for 75 mTorr is also shown in the main text in Figure 6.3.

References

[1] George, S. M., *Chem. Rev.* **2010**, 110(1), 111–131.

[2] Miikkulainen, V., Leskelä, M., Ritala, M., and Puurunen, R. L., *J. Appl. Phys.* **2013**, 113(2), 021301.

[3] Hämäläinen, J., Ritala, M., and Leskelä, M., *Chem. Mater.* **2014**, 26(1), 786–801.

[4] Bernal Ramos, K., Saly, M. J., and Chabal, Y. J., *Coord. Chem. Rev.* **2013**, 257(23), 3271–3281.

[5] Kalanyan, B., Losego, M. D., Oldham, C. J., and Parsons, G. N., *Chem. Vap. Depos.* **2013**, 19(4), 161–166.

[6] Grubbs, R. K., Steinmetz, N. J., and George, S. M., *J. Vac. Sci. Technol. B Microelectron. Nanom. Struct.* **2004**, 22(4), 1811.

[7] Klesko, J. P., Kerrigan, M. M., and Winter, C. H., *Chem. Mater.* **2016**, 28(3), 700–703.

[8] Golrokhi, Z., Marshall, P. A., Romani, S., Rushworth, S., Chalker, P. R., and Potter, R. J., *Appl. Surf. Sci.* **2017**, 399, 123–131.

[9] Kim, H., Kellock, A. J., and Rossnagel, S. M., *J. Appl. Phys.* **2002**, 92(12), 7080–7085.

[10] Ten Eyck, G. A., Pimanpang, S., Juneja, J. S., Bakhru, H., Lu, T. M., and Wang, G. C., *Chem. Vap. Depos.* **2007**, 13(6), 307–311.

[11] Alevli, M., Ozgit, C., Donmez, I., and Biyikli, N., *J. Cryst. Growth* **2011**, 335(1), 51–57.

[12] Hong, T. E., Mun, K.-y., Choi, S.-k., Park, J.-y., Kim, S.-H., Cheon, T., *et al.*, *Thin Solid Films* **2012**, 520(19), 6100–6105.

[13] Hämäläinen, J., Puukilainen, E., Kemell, M., Costelle, L., Ritala, M., and Leskelä, M., *Chem. Mater.* **2009**, 21(20), 4868–4872.

[14] Hämäläinen, J., Puukilainen, E., Sajavaara, T., Ritala, M., and Leskelä, M., *Thin Solid Films* **2013**, 531, 243–250.

[15] Lu, J. and Elam, J. W., *Chem. Mater.* **2015**, 27(14), 4950–4956.

[16] Mackus, A. J. M., Garcia-Alonso, D., Knoops, H. C. M., Bol, A. A., and Kessels, W. M. M., *Chem. Mater.* **2013**, 25(9), 1769–1774.

[17] Kim, S.-W., Kwon, S.-H., Jeong, S.-J., Park, J.-S., and Kang, S.-W., *Electrochem. Solid-State Lett.* **2008**, 11(11), H303.

[18] Sari, W., Eom, T.-K., Kim, S.-H., and Kim, H., *J. Electrochem. Soc.* **2011**, 158(1), D42–D47.

[19] Minjauw, M. M., Solano, E., Sree, S. P., Asapu, R., Van Daele, M., Ramachandran, R. K., *et al.*, *Chem. Mater.* **2017**, 29(17), 7114–7121.

[20] Lee, H. B. R., Bang, S. H., Kim, W. H., Gu, G. H., Lee, Y. K., Chung, T. M., *et al.*, *Jpn. J. Appl. Phys.* **2010**, 49(5), 05FA11.

[21] Kim, H., Detavenier, C., Van Der Straten, O., Rossnagel, S. M., Kellock, A. J., and Park, D. G., *J. Appl. Phys.* **2005**, 98(1), 014308.
[22] Chung, H.-S., Kwon, J.-D., and Kang, S.-W., *J. Electrochem. Soc.* **2006**, 153(11), C751.
[23] Ozgit-Akgun, C., Goldenberg, E., Okyay, A. K., and Biyikli, N., *J. Mater. Chem. C* **2014**, 2(12), 2123–2136.
[24] Alevli, M. and Gungor, N., *J. Vac. Sci. Technol. A Vacuum, Surfaces, Film.* **2018**, 36(1), 01A110.
[25] Rumble, J., editor, *CRC Handbook of Chemistry and Physics*, CRC Press, Boca Raton, FL, 98th edition, **2017**.
[26] Yoon, J., Lee, H.-B.-R., Kim, D., Cheon, T., Kim, S.-H., and Kim, H., *J. Electrochem. Soc.* **2011**, 158(11), H1179.
[27] Wang, T., Yan, Z., Michel, C., Pera-Titus, M., and Sautet, P., *ACS Catal.* **2018**, 8, 63–68.
[28] Longrie, D., Devloo-Casier, K., Deduytsche, D., Van den Berghe, S., Driesen, K., and Detavernier, C., *Ecs J. Solid State Sci. Technol.* **2012**, 1(6), Q123–Q129.
[29] Xie, Q., Jiang, Y. L., Musschoot, J., Deduytsche, D., Detavernier, C., Van Meirhaeghe, R. L., *et al.*, *Thin Solid Films* **2009**, 517(16), 4689–4693.
[30] Lee, H.-B.-R. and Kim, H., *Electrochem. Solid-State Lett.* **2006**, 9(11), G323.
[31] Park, J., Lee, H. B. R., Kim, D., Yoon, J., Lansalot, C., Gatineau, J., *et al.*, *J. Energ. Chem.* **2013**, 22(3), 403–407.
[32] Sowa, M. J., Yemane, Y., Prinz, F. B., and Provine, J., *J. Vac. Sci. Technol. A Vacuum, Surfaces, Film.* **2016**, 34(5), 051516.
[33] Bertuch, A., Keller, B. D., Ferralis, N., Grossman, J. C., and Sundaram, G., *J. Vac. Sci. Technol. A Vacuum, Surfaces, Film.* **2017**, 35(1), 01B141.
[34] Han, J. H., Kim, H. Y., Lee, S. C., Kim, D. H., Park, B. K., Park, J. S., *et al.*, *Appl. Surf. Sci.* **2016**, 362, 176–181.
[35] Huotari, H., Haukka, S., Matero, R., Rahtu, A., Tois, E., and Tuominen, M., *ECS Trans.* **2006**, 1(10), 131–135.
[36] Sowa, M. J., Yemane, Y., Zhang, J., Palmstrom, J. C., Ju, L., Strandwitz, N. C., *et al.*, *J. Vac. Sci. Technol. A Vacuum, Surfaces, Film.* **2017**, 35(1), 01B143.
[37] Kim, J. Y., Seo, S., Kim, D. Y., Jeon, H., and Kim, Y., *J. Vac. Sci. Technol. A Vacuum, Surfaces, Film.* **2004**, 22(1), 8–12.
[38] Kim, J. Y., Kim, D. Y., Park, H. O., and Jeon, H., *J. Electrochem. Soc.* **2005**, 152(1), G29.
[39] Kim, E.-J. and Kim, D.-H., *Electrochem. Solid-State Lett.* **2006**, 9(8), C123.
[40] Jian-Gang, Z. H., *Proc. IEEE* **2008**, 96(11), 1786–1798.
[41] Nistor, L. E., Rodmacq, B., Auffret, S., and Dieny, B., *Appl. Phys. Lett.* **2009**,

94(1), 1–4.
[42] Li, L., Han, D., Lei, W., Liu, Z., Zhang, F., Mao, X., *et al.*, *J. Appl. Phys.* **2014**, 116(12), 123904.
[43] Hwang, I. Y., Kim, J. H., Oh, S. K., Kang, H. J., and Lee, Y. S., *Surf. Interface Anal.* **2003**, 35(2), 184–187.
[44] Lee, H. B. R., Son, J. Y., and Kim, H., *Appl. Phys. Lett.* **2007**, 90(21), 2005–2008.
[45] Tokei, Z., Ciofi, I., Roussel, P., Debacker, P., Raghavan, P., Van Der Veen, M. H., *et al.*, *2016 IEEE Symp. VLSI Technol.* **2016**, pp. 1–2.
[46] He, M., Zhang, X., Nogami, T., Lin, X., Kelly, J., Kim, H., *et al.* **2013**, 160(12), 3040–3044.
[47] Zhang, X., Cao, L., Ryan, V., Ho, P. S., Taylor, B., Witt, C., *et al.*, *ECS J. Solid State Sci. Technol.* **2015**, 4(1), N3177–N3179.
[48] Mont, F. W., Zhang, X., Wang, W., Kelly, J. J., Standaert, T. E., Quon, R., *et al.*, *IITC 2017 - 2017 IEEE Int. Interconnect Technol. Conf.* **2017**, pp. 7–9.
[49] Bekiaris, N., Wu, Z., Ren, H., Naik, M., Park, J. H., Lee, M., *et al.*, *IITC 2017 - 2017 IEEE Int. Interconnect Technol. Conf.* **2017**, pp. 1–3.
[50] Shimizu, H., Sakoda, K., Momose, T., Koshi, M., and Shimogaki, Y., *J. Vac. Sci. Technol. A Vacuum, Surfaces, Film.* **2012**, 30(1), 01A144.
[51] Kim, J. M., Lee, H. B. R., Lansalot, C., Dussarrat, C., Gatineau, J., and Kim, H., *Jpn. J. Appl. Phys.* **2010**, 49, 05FA10.
[52] Kim, K., Lee, K., Han, S., Jeong, W., and Jeon, H., *J. Electrochem. Soc.* **2007**, 154(3), H177.
[53] Lee, K., Kim, K., Park, T., Jeon, H., Lee, Y., Kim, J., *et al.*, *J. Electrochem. Soc.* **2007**, 154(10), H899.
[54] Lee, H.-B.-R. and Kim, H., *ECS Trans.* **2008**, 16(4), 219–225.
[55] Lee, H.-B.-R., Kim, W.-H., Lee, J. W., Kim, J.-M., Heo, K., Hwang, I. C., *et al.*, *J. Electrochem. Soc.* **2010**, 157(1), D10.
[56] Kwon, J., Saly, M., Halls, M. D., Kanjolia, R. K., and Chabal, Y. J., *Chem. Mater.* **2012**, 24(6), 1025–1030.
[57] Park, J. H., Moon, D. Y., Han, D. S., Kang, Y. J., Shin, S. R., Jeon, H. T., *et al.*, *Surf. Coatings Technol.* **2014**, 259, 98–101.
[58] Kerrigan, M. M., Klesko, J. P., Rupich, S. M., Dezelah, C. L., Kanjolia, R. K., Chabal, Y. J., *et al.*, *J. Chem. Phys.* **2017**, 146(5), 052813.
[59] Kerrigan, M. M., Klesko, J. P., and Winter, C. H., *Chem. Mater.* **2017**, 29(17), 7458–7466.
[60] Heil, S. B. S., Langereis, E., Roozeboom, F., van de Sanden, M. C. M., and Kessels, W. M. M., *J. Electrochem. Soc.* **2006**, 153(11), G956.
[61] Donders, M. E., Knoops, H. C. M., van den Sanden, M., Kessels, W. M. M., and Notten, P. H. L., *J. Electrochem. Soc.* **2011**, 158(4), G92.

[62] Knoops, H. C. M., Langereis, E., van de Sanden, M. C. M., and Kessels, W. M. M., *J. Vac. Sci. Technol. A Vacuum, Surfaces, Film.* **2012**, 30(1), 01A101.
[63] Langereis, E., Heil, S. B. S., Knoops, H. C. M., Keuning, W., van de Sanden, M. C. M., and Kessels, W. M. M., *J. Phys. D. Appl. Phys.* **2009**, 42(7), 073001.
[64] Johs, B. and Hale, J. S., *Phys. Status Solidi Appl. Mater. Sci.* **2008**, 205(4), 715–719.
[65] D'Agostino, R., Cramarossa, F., De Benedictis, S., and Ferraro, G., *Plasma Chem. Plasma Process.* **1981**, 1(1), 19–35.
[66] Van Helden, J. H., Van Den Oever, P. J., Kessels, W. M. M., Van De Sanden, M. C. M., Schram, D. C., and Engeln, R., *J. Phys. Chem. A* **2007**, 111(45), 11460–11472.
[67] Van Helden, J. H., Wagemans, W., Yagci, G., Zijlmans, R. A. B., Schram, D. C., Engeln, R., *et al.*, *J. Appl. Phys.* **2007**, 101(4), 043305.
[68] Mackus, A. J. M., Heil, S. B. S., Langereis, E., Knoops, H. C. M., van de Sanden, M. C. M., and Kessels, W. M. M., *J. Vac. Sci. Technol. A Vacuum, Surfaces, Film.* **2010**, 28(1), 77–87.
[69] Gaydon, R. and Pearse, A., *The Identification of Molecular Spectra*, Chapman & Hall, London, **1950**.
[70] Bazinette, R., Paillol, J., and Massines, F., *Plasma Sources Sci. Technol.* **2015**, 24(5).
[71] Nagai, H., Takashima, S., Hiramatsu, M., Hori, M., and Goto, T., *J. Appl. Phys.* **2002**, 91(5), 2615–2621.
[72] Amorim, J., Baravian, G., and Sultan, G., *Appl. Phys. Lett.* **1996**, 68(14), 1915–1917.
[73] Roscioli, J. R., Zahniser, M. S., Nelson, D. D., Herndon, S. C., and Kolb, C. E., *J. Phys. Chem. A* **2016**, 120(9), 1347–1357.
[74] Dean, J., *Lange's Handbook of Chemistry*, volume 5, McGraw-Hill, New York, 15th editi edition, **1999**, ISBN 0070163847.
[75] Moulder, J. F., Stickle, W. F., Sobol, P. E., and Bomben, K. D., *Handbook of X-ray Photoelectron Spectroscopy*, Perkin-Elmer Corporation, Minnesota, **1992**, ISBN 9780962702624.
[76] Johns, C., Islam, M. S., and Groza, J. R., in Groza, J. R., Shackelford, J. F., Lavernia, E. J., and Powers, M. T., editors, *Mater. Process. Handb.*, chapter 8, CRC Press, ISBN 9780849332166, **2007**.
[77] Nastasi, M., Misra, A., and Mayer, J. W., in Groza, J. R., Shackelford, J. F., Lavernia, E. J., and Powers, M. T., editors, *Mater. Process. Handb.*, chapter 10, CRC Press, **2007**.
[78] Kizilkaya, A. C., Niemantsverdriet, J. W., and Weststrate, C. J., *J. Phys. Chem. C* **2016**, 120(7), 3834–3845.
[79] van Helden, P., van den Berg, J.-A., and Weststrate, C. J., *ACS Catal.* **2012**,

2(6), 1097–1107.
[80] Zowtiak, J. M. and Bartholomew, C. H., *J. Catal.* **1983**, 83(1), 107–120.
[81] Gopalakrishnan, R. and Viswanathan, B., *Surf. Technol.* **1984**, 23(2), 173–177.
[82] Dendooven, J., Ramachandran, R. K., Solano, E., Kurttepeli, M., Geerts, L., Heremans, G., *et al.*, *Nat. Commun.* **2017**, 8(1), 1–12.
[83] Oh, I. K., Kim, H., and Lee, H. B. R., *Curr. Appl. Phys.* **2017**, 17(3), 333–338.
[84] Yuan, G., Shimizu, H., Momose, T., and Shimogaki, Y., *Microelectron. Eng.* **2014**, 120, 230–234.
[85] Mackus, A. J., Leick, N., Baker, L., and Kessels, W. M., *Chem. Mater.* **2012**, 24(10), 1752–1761.

Area-Selective Deposition of Ruthenium by Combining Atomic Layer Deposition and Selective Etching

7

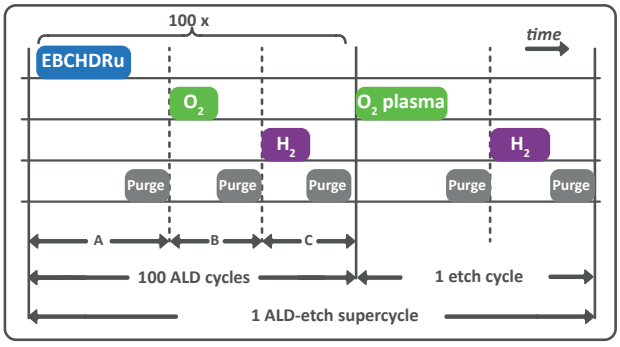

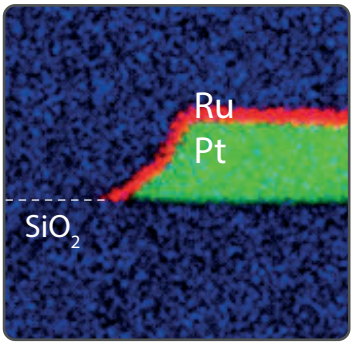

Area-selective atomic layer deposition (ALD) is expected to become a key technology for nanoelectronics with sub-5 nm dimensions. In this work, it is demonstrated that ALD can be combined with selective etching to improve the selectivity of area-selective ALD. For area-selective ALD of Ru on a Pt or Ru surface (metal-on-metal), it is shown that periodic O_2 plasma etching steps can be used to remove unwanted Ru nucleation on the SiO_2 non-growth area. Using this supercycle approach with etch cycles integrated into the Ru ALD process, the area-selective ALD of $\sim$8 nm of Ru was demonstrated onto Pt/SiO_2 patterns, with no detectable material being deposited on the SiO_2.

Published as: M.F.J. Vos, S.N. Chopra, M.A. Verheijen, J.G. Ekerdt, S. Agarwal, W.M.M. Kessels and A.J.M. Mackus, *Chem. Mater.* **31**, 11 (2019).

7.1 Introduction

Current nanopatterning techniques used for integrated circuit fabrication typically rely on a combination of deposition, lithography, and etch steps. Due to alignment issues, nanopatterning is becoming very challenging as device dimensions approach sub-5 nm scales.[1,2] In recent years, area-selective ALD has emerged as an alternative, bottom-up approach to nanomanufacturing.[3,4] By limiting the deposition to specific areas, area-selective ALD enables self-aligned fabrication, and can reduce the number of processing steps during device manufacturing, such as patterning and chemical mechanical polishing. Since ALD operates in a surface-reaction-controlled regime with sequential precursor and co-reactant exposures, separated by purge steps, area-selective ALD is also characterized by growth with precise thickness control and high con-formality.[5,6]

Currently, one of the main challenges for industrial application of area-selective ALD is obtaining a sufficiently high selectivity.[7] The selectivity is generally limited to a few tens of ALD cycles due to eventual nucleation on the area where no deposition is desired ('non-growth area'). Cleaning based on etching has previously been implemented in industrial selective epitaxy processes,[8] which serves as inspiration here for exploring novel combinations of area-selective ALD and selective etching. For example, during the selective epitaxial growth of Si by chemical vapor deposition (CVD), an etchant gas, typically HCl, is added to the CVD gas mixture to remove unwanted nucleation on SiO_2 or Si_3N_4 non-growth areas.[9,10] Due to the cyclewise nature of ALD, it is especially valuable to develop deposition processes that involve an intermittent correction or cleaning step to increase the growth selectivity.

Area-selective ALD of metal-on-metal is of interest for applications in metal interconnects in semiconductor devices. In particular, ALD of Ru is significant, since Ru (bulk resistivity of 7.1 $\mu\Omega$ cm) is considered either as a Cu diffusion barrier, or as a replacement for Cu lines[11–15] Furthermore, Ru is used as an electrode in dynamic random access memory, gate metal in transistors, and seed layer for electroplating.[16–21] Area-selective ALD of Ru on metal seed layers can simplify device processing for these applications. Several processes for area-selective ALD of Ru already exist, and depend on inherent selectivity, area-activation or area-deactivation.[22–26] Here, we demonstrate a method for area-selective ALD of Ru on Pt or Ru (metal-on-metal) with SiO_2 as the non-growth area, which exploits the inherent selectivity between the two different substrate materials.

Our approach to achieve area-selective ALD with high selectivity is based on deposition and cleaning, and consists of periodic selective etch steps integrated

into an ALD process as illustrated in Figure 7.1. The resulting supercycle of ALD and etch steps offers a promising opportunity to improve the growth selectivity of ALD processes. An essential requirement for this approach is that there should be an initial difference in nucleation behavior on the different substrate areas or materials.[27] After a certain number of cycles, nuclei start to form on the non-growth area, and the addition of etch steps can lead to removal of these nuclei. Typically, some material is also removed on the growth area, where deposition is actually desired. However, as long as substantially more material is deposited than etched on the growth area per supercycle, this approach can provide a sufficiently high net growth rate, while improving the overall growth selectivity. By repeating such a supercycle of ALD and etching as many times as required, the desired thickness can be obtained on the growth area.

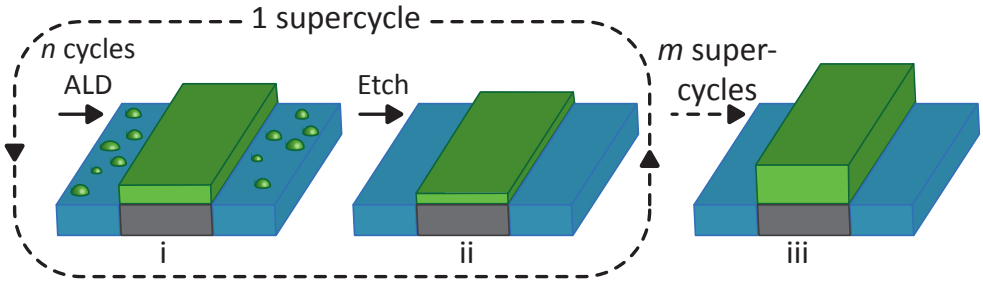

Figure 7.1 Schematic illustration of the concept of combining ALD with periodic etching to achieve area-selective deposition with a high selectivity. (i) When using an ALD process with an (insufficient) inherent selectivity, ALD leads to film growth on the growth area (gray, e.g. Pt, Ru), and island formation on the non-growth area (blue, e.g. SiO_2). (ii) Inclusion of etch steps in a supercycle recipe results in removal of the unwanted deposition on the non-growth area. (iii) By repeating the supercycle, a film with the desired thickness can be obtained selectively on the growth area.

It is important that the following two requirements are met when combining ALD with etching to improve the selectivity of the deposition process: (i) growth-area selectivity, which refers to an initial difference in nucleation behavior (in terms of nucleation delay or growth per cycle) between the growth and non-growth areas; and (ii) etch selectivity, where only the deposited material is etched, with almost no etching of the substrate material or other materials that are present. Several additional aspects are desirable, and can lead to a more ideal area-selective ALD process. First, to retain the merits of ALD, the etching process is preferred to be self-limiting and isotropic. In the case of plasma etching, this means that the ion contribution should be insignificant. The conformal nature of ALD on 3D-structures is especially preserved by combining ALD with isotropic atomic layer etching (ALE).[28] Second, the etch step should have a negligible effect on the

neighboring materials and underlying substrate, for instance in terms of roughening or incorporation of impurities. Furthermore, possible impurities should be easily removed, or at least not inhibit growth on the growth area in the subsequent ALD cycles. Note that having inhibiting species on the non-growth area can actually be beneficial for the selectivity.[27] Third, the ALD and etch processes should be compatible, meaning that they can be performed at similar conditions, such as temperature and pressure. Fourth, ideally the etch rate of the nuclei or islands on the non-growth area is higher than the etch rate of the material on the growth area, such that a high net growth rate on the growth area is obtained. In addition to considering these aspects, both the repetition frequency and the duration of the etch step should be optimized, in order to obtain the highest net growth rate.

Recently, Vallat et al. demonstrated a combination of ALD and selective etching to improve the overall selectivity of area-selective ALD.[27] In an O_2-plasma-enhanced ALD process for Ta_2O_5 that shows an inherent growth selectivity for a TiN surface over Si or SiO_2, NF_3 etching gas was added to the O_2 plasma step during every ninth cycle. The addition of the NF_3 allowed for the removal of Ta_2O_5 on Si and/or SiO_2 non-growth areas such that the area-selective deposition of Ta_2O_5 on TiN could be achieved.[27]

7.2 Experimental details

All deposition and etching experiments were performed using a home-built ALD reactor with an inductively-coupled plasma source operated at a radio-frequency (RF) of 13.56 MHz.[29] The reactor walls and manifold lines were heated to 100 and 105 °C, respectively. After using the reactor for deposition of a different material, the chamber was first conditioned with 500 cycles of Al2O3 ALD followed by 500 cycles of thermal RuO_x ALD (using a 60 s O_2 gas dose at 1 mbar as co-reactant step). This procedure yielded reproducible Ru film growth. All substrates were cleaned after being loaded into the reactor and prior to the deposition using a 60 s O_2 plasma (100 W), followed by a 30 s reducing H_2 gas treatment. Small coupons of single-side polished Si wafers with thermally-grown SiO_2 of ∼430-450 nm and ALD-grown Pt or Ru on SiO_2/Si were used as SiO_2, Pt, and Ru substrates. In addition, a sample consisting of Pt lines on top of ∼450 nm thick thermally-grown SiO_2 was used to characterize the area-selective growth through scanning electron microscopy (SEM) and energy-dispersive X-ray spectroscopy (EDX) elemental mapping. The lines of 1, 2, and 3 µm width were patterned by electron-beam lithography (EBL) using poly(methyl methacrylate) resist, which was followed by evaporation of Pt (∼50 nm thick), and lift-off. See the Supporting Information (S.I.), Figure S7.1, for a more detailed description of

the procedure. In situ spectroscopic ellipsometry (SE) was performed using a J.A. Woollam, Inc. M2000U ellipsometer to monitor the deposition and etching of Ru.[30,31] SE measurements were taken after every 10 ALD cycles and after every etch cycle. Additional details on the SE modeling and other analysis techniques can be found in the Supporting Information.

Ethylbenzenecyclohexadiene Ru(0) (EBCHDRu) (Hansol Chemical, Korea) was used as the Ru precursor, and was heated to 90 °C.[32] Ar was used as a carrier gas, resulting in a chamber pressure of ∼18 mTorr during the precursor dose. Ru films were deposited at 150 °C using a thermal ABC-type ALD process consisting of an EBCHDRu precursor dose (step A), an O_2 gas dose (step B), and H_2 gas dose (step C), with durations of 15, 15, and 5 s, respectively. The additional H_2 pulse in this ABC-type ALD process serves to reduce surface RuO_x, formed during the O_2 gas pulse, and enables growth of metallic Ru at temperatures < 200 °C.[33] The low deposition temperature is essential for obtaining inherent growth selectivity of Ru on Pt or Ru versus SiO_2. The growth per cycle (GPC) on Pt or Ru is higher than on SiO_2 at low temperatures, whereas there is a negligible difference in GPC at temperatures ≥ 200 °C (see discussion Figure 7.2 below). After the precursor step the line and chamber were purged with Ar for 4 s and pumped down for 5 s, while a pump step of 10 s was included after both the O_2 pulse and the H_2 pulse. Note that the experiments were done in a high vacuum system, in which pump steps are sufficient to remove reaction products. Additional details and experimental results for this ALD process are given in the Supporting Information, Figures S7.2 and S7.3.

It is known that exposing Ru to O_3 or to an O_2 plasma, leads to formation of volatile RuO_4.[34,35] Therefore, an O_2 plasma was used to etch the unwanted Ru nucleation occurring on SiO_2. This radical-assisted etching process does not etch SiO_2 under the conditions used in these experiments. The process enables etching with high etch selectivity, which is one of the main requirements for the ALD-etch supercycle approach. Exposing Ru to an O_2 plasma however leads to surface oxidation, and therefore an etch cycle also including a H_2 gas expo-sure was used. The O_2 plasma etching was performed using a RF power of 100 W for 20 or 30 s, while the subsequent H_2 gas dose was 15 s. The H_2 dose was found to be sufficiently long to reduce the film to metallic Ru (see Figure S7.4, S.I.). The O_2 and H_2 pressures were set to 0.02 and 0.2 mbar, respectively, for both the ALD and the etch cycles. The etching of Ru was quasi self-limiting, with the etch rate slowing down after 10 s of O_2 plasma exposure. For instance, the thickness decrease was approximately 0.9 nm for 30 s O_2 plasma, as compared to 1.1 nm for 60 s O_2 plasma. The quasi self-limiting etch behavior is believed to be caused by the formation of a surface oxide, which is more slowly etched than a metallic Ru film.[34,36] The Ru etch process will be investigated more extensively in Chapter 8.

7.3 Results and discussion

Firstly, the ALD of Ru was characterized on Pt and SiO_2 without using etch cycles. All depositions were done at 150 °C, since the difference in GPC on Pt compared to SiO_2 was maximum at this temperature. As shown in the inset of Figure 7.2a, after 400 ALD cycles there is approximately 9 nm of Ru growth on the Pt, compared to 4 nm on the SiO_2. This difference in growth behavior is explained by the catalytic activity of Pt. We have previously reported that the dissociative chemisorption of O_2 and catalytic combustion of the precursor ligands enable the area-selective ALD of Pt and Fe_2O_3 on Pt seed layers.[37,38] For the case of Ru ALD, Pt as well as Ru, also facilitate the dissociation of O_2, and the formed O can subsequently lead to the combustion of the precursor ligands.[39] Since a similar pathway does not occur on the inert SiO_2 surface, this provides the growth selectivity of Ru on Pt-group metals at low deposition temperatures.

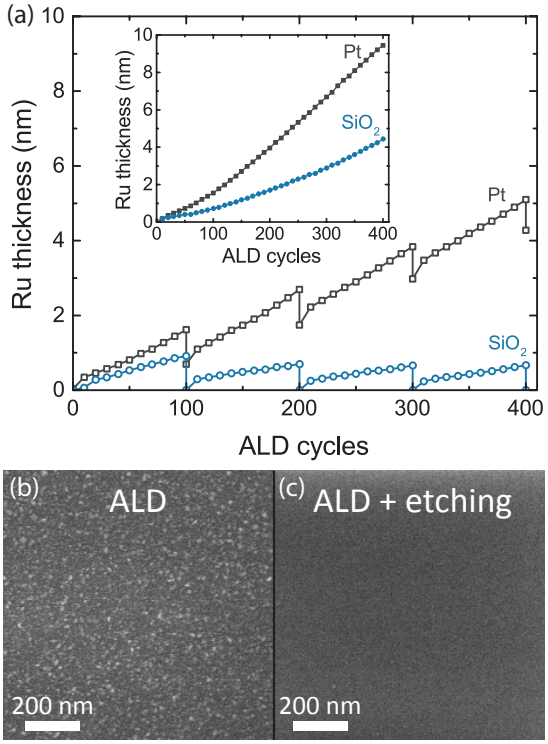

Figure 7.2 (a) Inset: Thickness as a function of ALD cycles for deposition on SiO_2 and Pt without etch cycles. Main figure: Ru film thickness as a function of ALD cycles for growth on SiO_2 and Pt with an intermittent etch cycle after every 100 ALD cycles. (b, c) Top-view SEM images after 400 Ru ALD cycles on SiO_2, (b) without etch cycles, or (c) with an etch cycle after every 100 ALD cycles.

To improve the selectivity of the ALD process, an etch cycle was integrated into the ALD process as illustrated in Figure 7.1. A supercycle recipe was performed in which one etch cycle was included after every 100 ALD cycles, using O_2 plasma and H_2 gas exposure times of 30 s and 15 s, respectively. As can be seen in Figure 7.2a, a recipe consisting of 4 supercycles resulted in a negligible amount of Ru on SiO_2, while the Ru thickness on the Pt substrate was approximately 4.3 nm, as determined from SE. Approximately 1 nm of Ru is removed after each etch cycle, both on the SiO_2 and the Pt. However, since the GPC of Ru on Pt is higher than on SiO_2, the super-cycle recipe results in net film deposition. A slightly enhanced growth is observed on both Pt and SiO_2 for the first ten ALD cycles after each etch cycle, which is attributed to a more reactive surface due to the O_2 plasma exposure and subsequent H_2 gas dose (e.g. higher density of reactive sites). In addition, the growth rate on SiO_2 was found to be slightly higher during the first 100 ALD cycles as compared to each subsequent set of 100 ALD cycles, suggesting that the initial substrate has more sites on which Ru ALD can nucleate than the surface obtained after etching. Note that performing the Ru ALD-etch supercycle on a (blanket) Ru-coated substrate yielded similar results as on Pt, which indicates that the approach can also be employed to achieve area-selective ALD of Ru on a Ru pattern, and possibly also other catalytic materials.

The Ru deposition on SiO_2 was further investigated using SEM. Due to the differences in density, surface topography, and conductivity, Ru islands appear bright in the SEM images, whereas dark regions represent SiO_2.[40] When comparing the SEM images in Figure 7.2b and c, it is seen that the etch cycle using 30 s O_2 plasma after every 100 ALD cycles was sufficient to remove nearly all the Ru islands formed on SiO_2, which corroborates the results of Figure 7.2a. Analysis of the nuclei visible with SEM yields a surface coverage Θ on the non-growth area of 0.0013, which corresponds to a selectivity factor S of 0.997 for a Ru thickness of 4.3 nm on the Pt growth area.[41] Furthermore, XPS measurements in the region corresponding to C1s/Ru3d (294 eV - 276 eV, see Figure S7.5, S.I.) only revealed a small C1s singlet peak, whereas no Ru3d doublet peak was detected. The XPS detection limit for Ru on top of SiO_2 was estimated to be below 0.01 monolayer, or 1.7×10^{13} at./cm^2.[42] Interestingly, the data demonstrates that the sensitivity for Ru nuclei detection is higher for SEM than for XPS.

After demonstrating the principle of the supercycle approach on blanket substrates, deposition was done onto a SiO_2 sub-strate with patterned Pt lines. A supercycle recipe of 800 ALD cycles was performed with an etch cycle after every 100 ALD cycles using an O_2 plasma time of 20 s. An etch time of 20 s was used, since experiments using plasma exposure times between 5 s and 60 s revealed that this was sufficiently long to obtain selectivity. The SEM image in Figure 7.3a, shows a clean SiO_2 surface in between the Pt lines, further demonstrating the selectivity of the approach. In addition, Ru was only detected by EDX on top of the Pt lines (see Figure 7.3b). Furthermore, the cross-sectional TEM image and EDX mapping in Figure 7.4a and Figure 7.4b (of the sample as used for Figure 7.3), reveal that the Ru film on the evaporated Pt ($\sim$50 nm) is approximately 8 nm thick, and conformally coats the Pt. The EDX mapping in Figure 7.4c, collected at the edge of one of the Pt lines, demonstrates that the Ru only covers the Pt, and not the SiO_2 substrate, corroborating that a high selectivity is achieved.

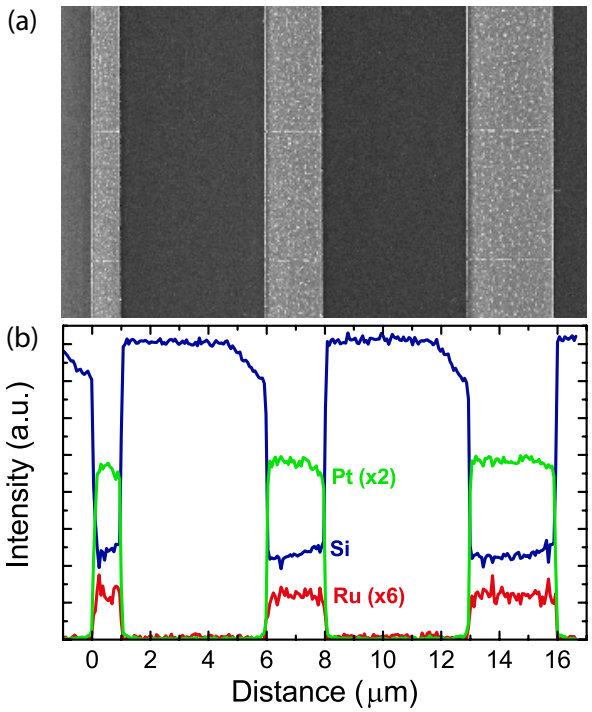

Figure 7.3 (a) SEM image and (b) corresponding EDX line scan of a patterned substrate with alternating lines of Pt (bright) and SiO_2 (dark) after 800 ALD cycles. The etch cycle was performed after every 100 Ru ALD cycles, using an O_2 plasma duration of 20 s. Note that the small white spots present on the Pt lines in (a) originate from resist residue remaining after development and before Pt evaporation. The Ru and Pt signals in (b) were rescaled for clarity.

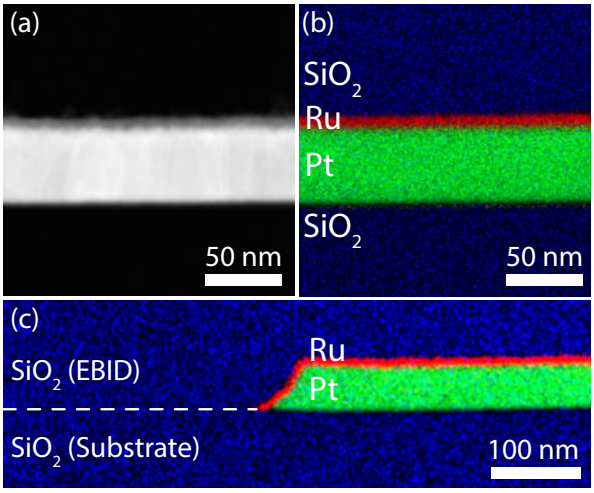

Figure 7.4 (a) Cross-sectional high-angle annular dark field scanning TEM image of a Pt line with approximately 8 nm of Ru. (b) EDX elemental mapping of the corresponding region. (c) EDX elemental mapping at the edge of a Pt line, showing the high selectivity of the Ru ALD-etch supercycle recipe. The SiO_2 layer at the top was deposited by electron-beam induced deposition (EBID) to protect the Pt/Ru structure during TEM-lamella preparation.

The obtained material properties were investigated to further assess the potential of the ALD-etch supercycle approach. XPS measurements revealed a Ru film of high-purity, and only a small O1s peak was detected (corresponding to $<$5 at.% O), which is comparable in intensity as for the ALD only recipe (see Figure S7.6, S.I.). Furthermore, four-point-probe measurements yielded a resistivity of approximately 22 $\mu\Omega$ cm (after correcting for the Pt resistance) for 8 nm of Ru deposited using ALD-etch supercycles.

Comparing the growth on Pt with and without etch cycles in Figure 7.2a, it is clear that the GPC increases with the number of cycles when no etching is performed, while this effect seems to be suppressed by the periodic etch cycles (See also Figure S7.7, S.I.). Note that the GPC is essentially given by the slope of the plot for the thickness versus ALD cycles. The gradual increase in GPC for the normal ALD recipe is attributed to an increase in surface roughness as the film thickness increases, which manifests as an effective increase in the surface area available for growth.[43] We speculate that this increase in GPC is suppressed by the periodic etch cycles, as the radical-assisted O_2 etching leads to smoothing of the Ru film. This smoothing effect can be explained by the fact that Ru regions protruding from the surface are more easily etched by the O_2 plasma than smooth regions of the Ru film. Smoothing of thin films, including Ru, by ALE

has been reported previously, and the O_2 plasma etching process for Ru used in this work can be qualified as quasi-ALE.[44] To confirm this hypothesis, Ru films of approximately 8 nm were analyzed by atomic force microscopy (AFM), yielding root-mean-square roughness values of 1.3 nm and 0.9 nm for films deposited without and with etch cycles, respectively.* The inclusion of the etch cycles thus has the benefit of smoothing the Ru film, in addition to enhancing the selectivity.

7.4 Conclusion

In summary, it was demonstrated that area-selective ALD with high selectivity can be obtained by combining ALD with selective etching. Specifically, a Ru ALD process was combined with etch cycles of O_2 plasma and H_2 gas to remove any unwanted growth on SiO_2. Approximately 8 nm of Ru was deposited on Pt patterns, while both EDX and SEM confirmed that the neighboring SiO_2 was clean. In addition, it was found that inclusion of the etch cycles leads to smoothing of the Ru film, as evidenced by a lower surface roughness than for ALD only. This study provides valuable insight into how area-selective ALD can be combined with selective etching to deposit materials on a surface with high selectivity, while maintaining the ALD-merits of high conformality, and precise thickness control. Finally, the general requirements and guidelines for ALD-etch supercycles discussed in this work can help to extend the approach to other material systems.

Acknowledgements

The authors would like to thank C.A.A. van Helvoirt, J.J.A. Zeebregts, C.O. van Bommel, and J.J.L.M. Meulendijks for their technical assistance. R. Mahlouji and B. Barcones Campo are acknowledged for preparation of the Pt lines on SiO_2, and the TEM lamella, respectively. In addition, the authors thank D.A. Kane for performing the AFM measurements. This work was financially supported by the Netherlands Organization for Scientific Research (NWO) through the Zwaartekracht program 'Research Centre for Integrated Nanophotonics'. In addition, the work of S.N.C. was made possible through the National Science Foundation (NSF) Graduate Research Opportunities Worldwide program, and a NASCENT Whaley fellowship. Solliance and the Dutch province of Noord-Brabant are acknowledged for funding the TEM facility.

* Note that metallic films, including Ru, are typically polycrystalline, whereas the AlF_3 films of Chapter 4 are amorphous. Together with the different substrates (Pt vs Al_2O_3), the difference in crystallinity explains the difference in surface roughness between the Ru films and the AlF_3 films ($\leq$0.2 nm RMS roughness). See also Section 2.3.9.

7.5 Supporting Information

Pt pattern fabrication

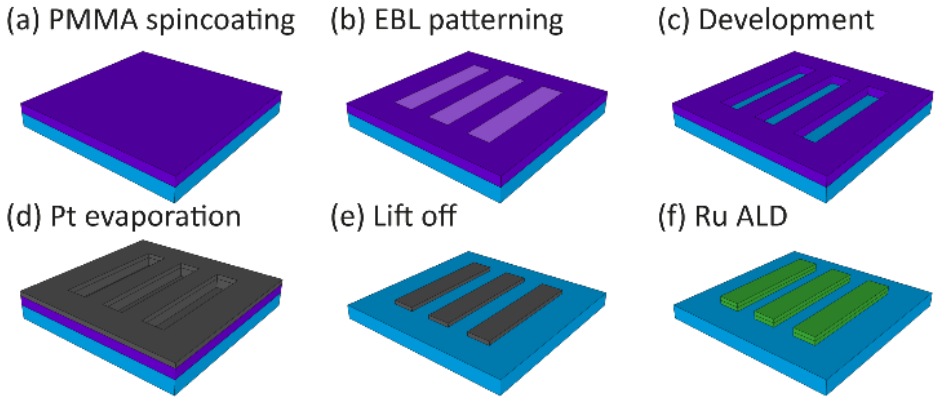

Figure S7.1 Process flow for the fabrication of Pt patterns on top of SiO_2. Poly(methyl methacrylate) (PMMA) was spincoated on ∼450nm SiO_2 , and then locally exposed using electron beam lithography (EBL). The exposed PMMA resist was removed using methyl isobutyl ketone (MIBK), after which∼50nm Pt was evaporated. The Pt on top of the PMMA was removed in a lift-off procedure, followed by the selective Ru ALD on top of the Pt patterns. Note that the sidewalls of the Pt lines are also covered by Ru after ALD.

Ru ALD process

Ru was deposited using an ABC-type ALD cycle, consisting of an EBCHDRu (ethylbenzenecyclohexadieneRu) precursor, an O_2 gas (step B), and H_2 gas (step C) doses. The H_2 dose is included for reduction of the surface after the O_2, and allows for deposition of metallic Ru even at low temperatures. As can be seen in Figure S7.2, dosing times of 15 s (EBCHDRu), 15 s (O_2) and 5 s (H_2) were found to be sufficient to saturate the reactions during the three different sub-cycles. For a deposition temperature of 225 °C, a saturated growth rate (GPC) of ∼0.35Å was found. The temperature dependence of the ALD process is investigated in Chapter 8. Figure S7.3 shows the influence of the O_2 and H_2 dosing times on the film resistivity. As can be seen in the inset of Figure S7.3b, a short H_2 dose of 1 s resulted in a relatively high resistivity of approximately 800 μΩ cm. However, for longer H_2 doses, the resistivity decreased significantly, indicating the H_2 dose allows for deposition of metallic Ru. A more detailed characterization of this ALD process will be published elsewhere.

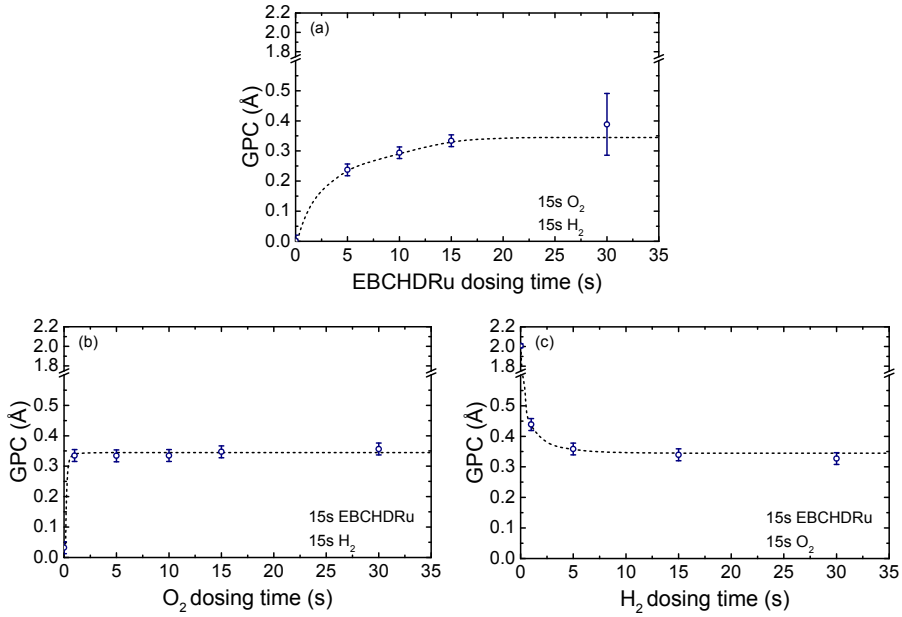

Figure S7.2 Saturation curves for the Ru ABC-type ALD cycle, showing the GPC as a function of (a) EBCHDRu precursor, (b) O_2, and (c) H_2 dosing time. The depositions were performed at a temperature of 225 °C on a Ru seed layer.

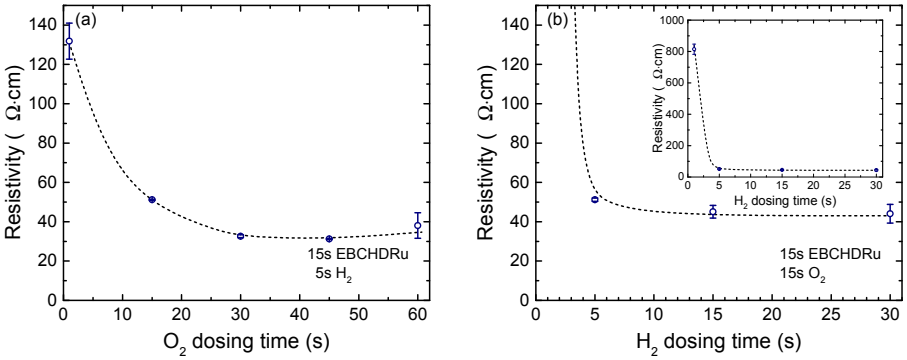

Figure S7.3 Film resistivity as function of (a) O_2 and (b) H_2 dosing time. 500 ALD cycles were performed at 225 °C on SiO_2.

Additional experimental details

In situ spectroscopic ellipsometry (SE) was performed using a J.A. Woollam, Inc. M2000U ellipsometer to monitor the deposition and etching of Ru. The Ru thickness evolution was fit using a B-spline model in the wavelength range of 1.2 to 4.5 eV by first modeling the final in situ measurement, after which the data were dynamically fitted backwards while including the optical parameters in the fit. Scanning electron microscopy (SEM) images were taken using a Zeiss Sigma with a beam voltage of 5 kV. Top-view EDX studies were performed using a FEI Nova NanoLab 600i SEM. Aberration corrected transmission electron microscopy (TEM, JEOL JEM ARM200F) was used for examination of selective Ru film growth. Cross-sectional EDX studies were performed in scanning TEM mode, using the JEM ARM200F, equipped with a 100 mm^2 EDX detector.

X-ray photoelectron spectroscopy

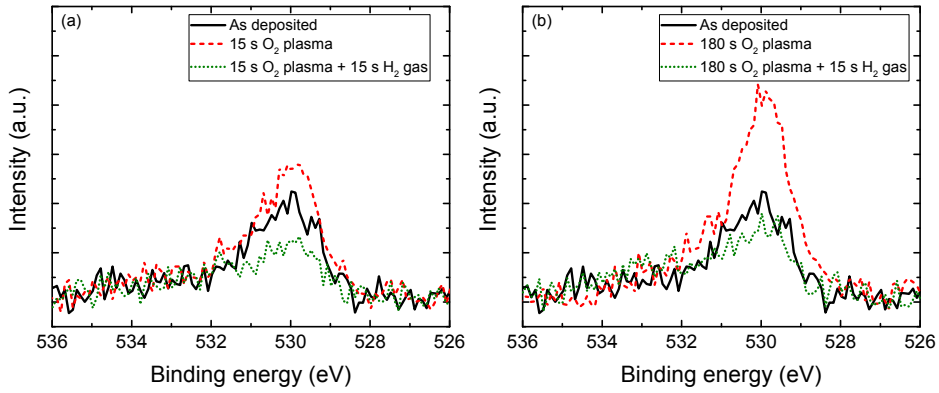

Figure S7.4 (a) XPS spectra for the O1s peak for an as-deposited Ru film, after 15 s of O_2 plasma, and after 15 s of O_2 plasma followed by 15 s of H_2 gas. (b) XPS spectra for the O1s peak for an as-deposited Ru film, after 180 s of O_2 plasma, and after 180 s of O_2 plasma followed by 15 s of H_2 gas. These data suggest that a 15 s H_2 pulse is sufficient to reduce the RuO_x formed during the preceding O_2 plasma exposure step. The Ru film was deposited using ALD only. See Figure S7.6 for XPS data corresponding to a Ru film deposited using the ALD-etch supercycle.

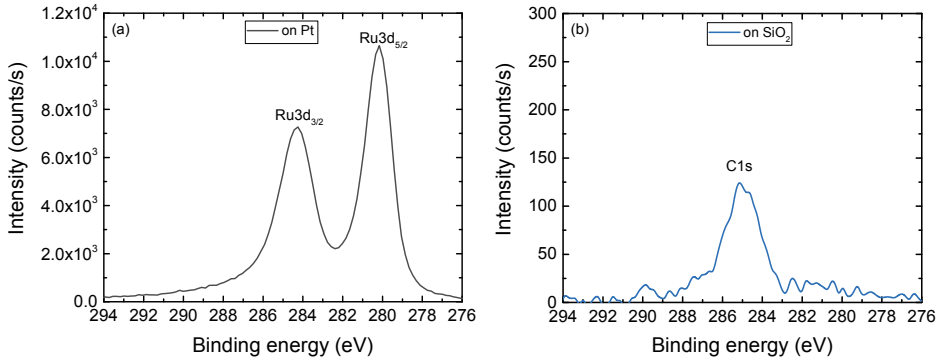

Figure S7.5 XPS spectra for the region corresponding to Ru3d/C1s (294 eV - 276 eV), collected on (a) Pt and (b) SiO_2 after 400 ALD cycles. The etch cycle was performed after every 100 ALD cycles. A clear Ru3d doublet was detected on the Pt substrate. This is in contrast to the SiO_2, for which only a small C1s singlet peak is visible, indicating the absence of a significant amount of Ru. Note the different scales for the vertical axes.

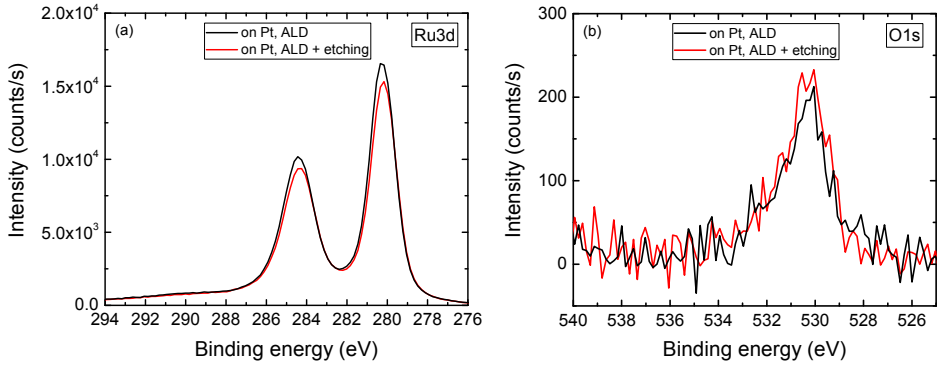

Figure S7.6 XPS spectra for (a) the Ru3d peak and (b) the O1s peak, collected on$\sim$8 nm thick Ru films deposited on Pt without and with etch cycles, by performing 400 and 800 ALD cycles respectively. 30 s Ar^+ sputtering was carried out to remove the surface oxide. The composition of both films was found to be very similar, with an O-content of $<$5 at.%.

Growth on Pt with and without etch cycles

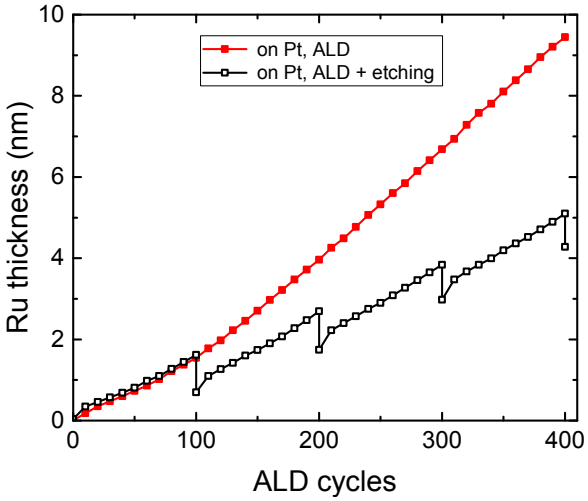

Figure S7.7 Ru film thickness as a function of cycles for deposition on Pt with and without etch cycles. The etch cycle was performed after every 100 ALD cycles. Spectroscopic ellipsometry measurements were done every 10 ALD cycles and after every etch cycle. If no etch cycles are performed, the an enhancement of the growth rate (i.e. the slope of the thickness versus cycles) can be observed around 100 ALD cycles. The etch cycle seems to suppress this enhancement, which is believed to be related to smoothing of the film surface, as was discussed Section 7.3. Note that this is the same data as shown in Figure 7.2, plotted differently for comparison.

References

[1] Schuegraf, K., Abraham, M. C., Brand, A., Naik, M., and Thakur, R., *IEEE J. Electron Devices Soc.* **2013**, 1(3), 66–75.

[2] Thoms, S., Macintyre, D. S., Docherty, K. E., and Weaver, J. M. R., *Microelectron. Eng.* **2014**, 123, 9–12.

[3] Fang, M. and Ho, J. C., *ACS Nano* **2015**, 9(9), 8651–8654.

[4] Mackus, A. J. M., Bol, A. A., and Kessels, W. M. M., *Nanoscale* **2014**, 6(2011), 10941–10960.

[5] Leskelä, M. and Ritala, M., *Thin Solid Films* **2002**, 409(1), 138–146.

[6] George, S. M., *Chem. Rev.* **2010**, 110(1), 111–131.

[7] Mackus, A. J. M., Merkx, M. J. M., and Kessels, W. M. M., *Chem. Mater.* **2019**, 31(1), 2–12.

[8] Jastrzebski, L., *J. Cryst. Growth* **1983**, 63, 493–526.

[9] Rai-Choudhury, P. and Schroder, D. K., *J. Electrochem. Soc.* **1971**, 118(1), 107–110.

[10] Goulding, M. R., *Mater. Sci. Eng. B* **1993**, 17(1-3), 47–67.

[11] Dean, J., *Lange's Handbook of Chemistry*, volume 5, McGraw-Hill, New York, 15th editi edition, **1999**, ISBN 0070163847.

[12] Henderson, L. B. and Ekerdt, J. G., *Thin Solid Films* **2009**, 517(5), 1645–1649.

[13] Arunagiri, T. N., Zhang, Y., Chyan, O., El-Bouanani, M., Kim, M. J., Chen, K. H., *et al.*, *Appl. Phys. Lett.* **2005**, 86(8), 1–3.

[14] Tokei, Z., Ciofi, I., Roussel, P., Debacker, P., Raghavan, P., Van Der Veen, M. H., *et al.*, *2016 IEEE Symp. VLSI Technol.* **2016**, pp. 1–2.

[15] Wen, L. G., Roussel, P., Pedreira, O. V., Briggs, B., Groven, B., Dutta, S., *et al.*, *ACS Appl. Mater. Interfaces* **2016**, 8(39), 26119–26125.

[16] Kim, S. K., Kim, W. D., Kim, K. M., Hwang, C. S., and Jeong, J., *Appl. Phys. Lett.* **2004**, 85(18), 4112–4114.

[17] Kwon, O. J., Cha, S. H., and Kim, J. J., *J. Electrochem. Soc.* **2004**, 151(2), C127–132.

[18] Schaekers, M., Capon, B., Detavernier, C., and Blasco, N., *ECS Trans.* **2010**, 33(2), 135–144.

[19] Suh, Y.-S., Lazar, H., Chen, B., Lee, J.-H., and Misra, V., *J. Electrochem. Soc.* **2005**, 152(9), F138.

[20] Waechtler, T., Ding, S. F., Hofmann, L., Mothes, R., Xie, Q., Oswald, S., *et al.*, *Microelectron. Eng.* **2011**, 88(5), 684–689.

[21] Yeo, S., Choi, S. H., Park, J. Y., Kim, S. H., Cheon, T., Lim, B. Y., *et al.*, *Thin Solid Films* **2013**, 546, 2–8.

[22] Färm, E., Lindroos, S., Ritala, M., and Leskelä, M., *Chem. Mater.* **2012**, 24(2), 275–278.

[23] Zyulkov, I., Krishtab, M., De Gendt, S., and Armini, S., *ACS Appl. Mater. Interfaces* **2017**, 9(36), 31031–31041.

[24] Park, J. Y., Yeo, S., Cheon, T., Kim, S. H., Kim, M. K., Kim, H., *et al.*, *J. Alloys Compd.* **2014**, 610, 529–539.
[25] Junige, M., Löffler, M., Geidel, M., Albert, M., Bartha, J. W., Zschech, E., *et al.*, *Nanotechnology* **2017**, 28(39), 395301.
[26] Minjauw, M. M., Rijckaert, H., Driessche, I. V., Detavernier, C., and Dendooven, J., *Chem. Mater.* **2019**, 31(5), 1491–1499.
[27] Vallat, R., Gassilloud, R., Eychenne, B., and Vallée, C., *J. Vac. Sci. Technol. A* **2017**, 35(1), 01B104.
[28] Lee, Y., Huffman, C., and George, S. M., *Chem. Mater.* **2016**, 28(21), 7657–7665.
[29] Heil, S. B. S., Langereis, E., Roozeboom, F., van de Sanden, M. C. M., and Kessels, W. M. M., *J. Electrochem. Soc.* **2006**, 153(11), G956.
[30] Langereis, E., Heil, S. B. S., Knoops, H. C. M., Keuning, W., van de Sanden, M. C. M., and Kessels, W. M. M., *J. Phys. D. Appl. Phys.* **2009**, 42(7), 073001.
[31] Leick, N., Weber, J. W., Mackus, A. J. M., Weber, M. J., van de Sanden, M. C. M., and Kessels, W. M. M., *J. Phys. D. Appl. Phys.* **2016**, 49(26), 269601.
[32] Hong, T. E., Choi, S.-H., Yeo, S., Park, J.-Y., Kim, S.-H., Cheon, T., *et al.*, *ECS J. Solid State Sci. Technol.* **2012**, 2(3), P47–P53.
[33] Lu, J. and Elam, J. W., *Chem. Mater.* **2015**, 27(14), 4950–4956.
[34] Nakahara, M., Tsunekawa, S., Watanabe, K., Arai, T., Yunogami, T., and Kuroki, K., *J. Vac. Sci. Technol. B Microelectron. Nanom. Struct.* **2001**, 19(2001), 2133.
[35] Hsu, C. C., Coburn, J. W., and Graves, D. B., *J. Vac. Sci. Technol. A Vacuum, Surfaces, Film.* **2006**, 24(1), 1–8.
[36] Saito, S. and Kuramasu, K., *Jpn. J. Appl. Phys.* **1992**, 31(1), 135–138.
[37] Mackus, A., Thissen, N. F. W., Mulders, J. L., Trompenaars, P. H. F., Verheijen, M. A., Bol, A. A., *et al.*, *J. Phys. Chem. C* **2013**, 117(20), 10788–10798.
[38] Singh, J. A., Thissen, N. F., Kim, W. H., Johnson, H., Kessels, W. M., Bol, A. A., *et al.*, *Chem. Mater.* **2018**, 30(3), 663–670.
[39] Leick, N., Agarwal, S., Mackus, A. J. M., Potts, S. E., and Kessels, W. M. M., *J. Phys. Chem. C* **2013**, 117(41), 21320–21330.
[40] Cazaux, J., *J. Electron Microsc. (Tokyo).* **2012**, 61(5), 261–284.
[41] Parsons, G. N., *J. Vac. Sci. Technol. A* **2019**, 37(2), 020911.
[42] Shard, A. G., *Surf. Interface Anal.* **2014**, 46(3), 175–185.
[43] Nilsen, O., Karlsen, O. B., Kjekshus, A., and Fjellvåg, H., *Thin Solid Films* **2007**, 515(11), 4550–4558.
[44] Kanarik, K. J., Tan, S., and Gottscho, R. A., *J. Phys. Chem. Lett.* **2018**, 9(16), 4814–4821.

Atomic Layer Deposition and Etching of Ruthenium for Area-Selective Deposition: Temperature and Supercycle Optimization

8

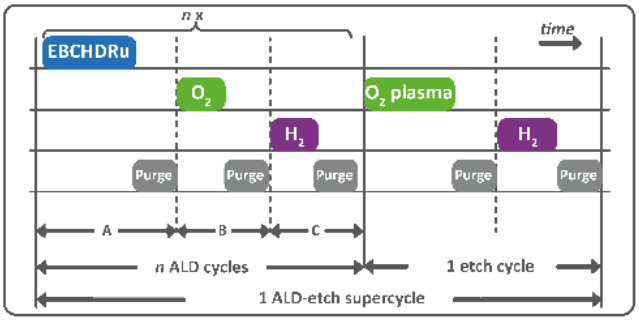

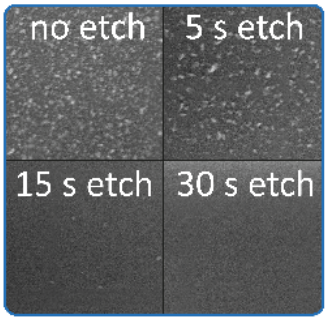

For sub-5 nm technology nodes, the fabrication of semiconductor devices is anticipated to involve the use of area-selective atomic layer deposition (ALD). While area-selective ALD has been reported for a variety of materials, most approaches yield a limited selectivity, due to growth initiation on defects or impurities on the non-growth area. Recently, we demonstrated that Ru ALD can be combined with selective etching to achieve area-selective ALD of metal-on-metal with high selectivity. Cycles consisting of an O_2 plasma and an H_2 gas dose were integrated in an ALD-etch supercycle recipe to remove unwanted nucleation on the SiO_2 non-growth area, while obtaining deposition on the Pt or Ru growth area. This work reports on the optimization of the ALD-etch supercycle in terms of selectivity and net deposition. By performing depositions between 100 °C and 200 °C on SiO_2, Al_2O_3, Pt, and Ru, it was determined that a substrate temperature of 150 °C offered some selectivity, which served as the starting point for achieving area-selective deposition using ALD-etch supercycles. The material deposited on the SiO_2 non-growth area was quantified using various analytical techniques, demonstrating that the selectivity improves for longer O_2 plasma etch times. Furthermore, the Ru thickness decrease per etch cycle and the net Ru deposition on Pt after 4 supercycles were determined as a function of O_2 plasma time. Based on these results, general principles for the optimization of ALD-etch supercycles are discussed. Overall this work illustrates how ALD and etch processes can be selected to simultaneously obtain a high selectivity and a high net deposition.

M.F.J. Vos, S.N. Chopra, J.G. Ekerdt, S. Agarwal, W.M.M. Kessels and A.J.M. Mackus, in preparation for submission to *ACS Appl. Mater. Interfaces*.

8.1 Introduction

As integrated circuit manufacturing is moving towards sub-5 nm technology nodes, there is an ongoing effort to develop alternative fabrication techniques that can meet the increasingly demanding patterning requirements.[1] Traditionally, semiconductor devices are fabricated by repetition of deposition, lithography and etch steps.[2] This top-down approach, while highly sophisticated, becomes challenging to use for next generation devices due to misalignment of device features.[3,4] Bottom-up fabrication methods that are characterized by deposition of material only where needed, can possibly solve alignment issues by making some lithography-based patterning steps obsolete.[5] For this reason, area-selective deposition is regarded as an alternative, bottom-up approach to device fabrication. The industry has been employing area-selective chemical vapor deposition (CVD) processes, including selective epitaxy of Si and SiGe and selective capping of Cu interconnects by Co.[6,7] In recent years, with the wide-scale implementation of atomic layer deposition (ALD) in semiconductor manufacturing, especially area-selective ALD has emerged as a promising method for area-selective deposition.[8,9] ALD is a vapor-phase thin film deposition technique based on cycles consisting of sequential precursor and co-reactant exposures that are separated by purge steps. The technique relies on self-limiting surface reactions, allowing for deposition with precise thickness control, good uniformity and high conformality, which gives area-selective ALD several advantages in comparison to area-selective CVD.[10–14]

Although several methods have been developed to achieve area-selective ALD, the selective growth can typically only be retained for a limited number of ALD cycles. Nucleation caused by defects or impurities on the non-growth area leads to growth after an initial inhibition period, resulting in loss of selectivity.[9] Industrial application of area-selective ALD requires high selectivity for thicknesses on the growth area of up to $/sim$10 nm, which is often not possible.[59] To achieve a sufficiently high selectivity, it will be necessary to employ methods that involve an intermittent correction or cleaning step to remove nucleation from the non-growth area during the deposition process.[9]

Interestingly, the use of cleaning steps has already been reported around fifty years ago for area-selective epitaxy of Si.[15,16] By adding an etchant gas such as HCl to the Si source gas, unwanted Si nucleation on SiO_2 or Si_3N_4 is removed, resulting in area-selective CVD of Si on Si areas.[15–17] Methods that improve the selectivity of ALD by correcting for deposition on the non-growth area have only recently been considered in the ALD community. Hashemi *et al.* proposed a lift-off strategy for the area-selective ALD of Al_2O_3 films on SiO_2 in the presence of Cu.[18] ALD on Cu areas was deactivated using a self-assembled monolayer (SAM),

but some dielectric deposition still occurred on the SAM layer. Post-deposition etching of the SAM layer using acetic acid resulted in removal of any Al_2O_3 that was deposited on the Cu/SAM, thereby leading to an improvement of the selectivity. In case more deposition occurs on the non-growth area, it is necessary to integrate etch steps *during* the deposition process, as was demonstrated by Vallat *et al.*[19,20] After a number of ALD cycles for Ta_2O_5 or TiO_2, an O_2/NF_3 plasma etch step was used to remove nuclei from Si and SiO_2 non-growth areas, and to simultaneously inhibit growth in subsequent ALD cycles by forming unreactive Si-F surface groups. By performing multiple of these ALD-etch supercycles, the area-selective deposition of Ta_2O_5 and TiO_2 on TiN was achieved. More recently, Song *et al.* demonstrated area-selective ALD of TiO_2 on SiO_2 in the presence of H-terminated Si as the non-growth area by integrating atomic layer etching (ALE) cycles in ALD-ALE supercycles.[21] The ALE cycles consisting of WF_6 and BCl_3 doses resulted in removal of TiO_2 deposited on the H-terminated Si non-growth area, which enabled selective deposition of up to $\sim$ 12 nm TiO_2 on SiO_2.[21]

The method of combining deposition and etching is highly promising, since it allows for significant improvement of the selectivity that can be achieved. Although the etch step typically also results in removal of deposited material from the growth area (where deposition is actually desired) the ALD-etch supercycle can be repeated as often as required in order to obtain the target thickness on the growth area. Nevertheless, considerably more material should be deposited than etched during one supercycle, such that the method provides a sufficiently high *net* growth rate. It is noted that *'growth-area selectivity'* and *'etch selectivity'* are the two main parameters which are important for the approach.[22] 'Growth-area selectivity' refers to preferential deposition of a material on the growth area, while the non-growth area is left blank. 'Etch selectivity' refers to preferential removal of a material with respect to a mask, underlying material or other materials present in a device. For example, O_3 etches Ru and photoresist with high selectivity towards the Ru (i.e. Ru is etched faster).

Recently, we extended the approach based on ALD-etch supercycles to area-selective ALD of metal-on-metal, in this case Ru on Pt or Ru.[22] Ru has a low bulk resistivity of 7.1 $\mu\Omega$ cm and its oxide, RuO_2, also exhibits a low resistivity as compared to other metal oxides.[34,35] Area-selective ALD of Ru is relevant for industrial applications, since Ru is investigated for use in metal interconnects, either as a diffusion barrier for Cu (which demonstrates a low solubility in Ru), or as the conducting wire material itself.[23–27] Ru also has applications as an electrode in dynamic random access memory (DRAM), gate metal in transistors, and seed layer for electroplating.[28–33]

Although area-selective ALD is in an early stage of development, there are several reports on area-selective ALD of Ru. For example, Minjauw *et al.* recently reported on the thermal ALD process using RuO_4 and H_2, which demonstrates inherent selectivity and allows for deposition on H-terminated Si in the presence of SiO_2 as non-growth area.[36] Park *et al.* patterned octadecyltrichlorosilane (OTS) self-assembled monolayers (SAMs) to block Ru ALD, in order to obtain Ru lines on SiO_2 and HfO_2 surfaces.[37] In addition, Ru was selectively deposited on SiCN by Zyulkov *et al.*, while inhibiting growth on amorphous C (a-C) by using an H_2 plasma treatment prior to ALD.[38] The H_2 plasma exposure results in formation of CH_3 surface groups on a-C, which are not reactive towards the (ethylbenzyl)(1-ethyl-1,4-cyclohexadienyl)Ru precursor (EBECHRu). Färm *et al.* achieved the area-selective ALD of Ru by patterning a seed layer of $RuCl_3$ using microcontact printing.[39] This $RuCl_3$ seed layer was oxidized to RuO_x, which was successfully used to activate subsequent Ru ALD growth at 250 °C. Finally, ALD of Ru on Pt was demonstrated by Junige *et al.*, where the Pt was locally deposited on the SiO_2 substrate using electron-beam induced deposition (EBID).[40]

In our previous work, a thermal Ru ALD cycle was combined with a selective etch cycle to remove Ru deposited on the SiO_2 non-growth area. The ALD-etch supercycle allowed for area-selective deposition of Ru on Pt and Ru, while obtaining a clean SiO_2 surface.[22] Whereas Pt was primarily used to achieve elemental contrast when employing chemical analysis techniques (e.g. X-ray photoelectron spectroscopy and energy-dispersive X-ray spectroscopy), the area-selective ALD of Ru on Ru is more relevant for industrial applications. The thermal Ru ALD process shows considerable growth on catalytic Pt and Ru at low deposition temperatures, and less growth on dielectric SiO_2 (and Al_2O_3). This difference in growth behavior served as the starting point for the development of the area-selective deposition process, and was explained by the fact that the Pt and Ru substrates facilitate the catalytic dissociation of O_2.[22,41,42] The O formed on Pt or Ru can subsequently participate in the combustion of the Ru precursor ligands, whereas SiO_2 does not demonstrate catalytic activity for this reaction.[41,42] To improve the selectivity of the Ru ALD process, Ru nuclei formed on defects on the SiO_2 non-growth area were removed using an etch cycle which is based on an O_2 plasma exposure, leading to formation of volatile RuO_4. An H_2 gas dose was added after the O_2 plasma to reduce the formed surface RuO_x to metallic Ru. This etch process results in removal of only Ru and not Pt or SiO_2, and is therefore selective.[43,44]

In this work, a more detailed study of the ALD and etch processes for Ru is provided in the context of area-selective deposition. Specifically, the temperature dependence of the thermal Ru ALD process, the O_2 plasma etching process and their effect on the net deposition of Ru on Pt are investigated. To assess the selectivity as a function of O_2 plasma etch time, the deposition on the SiO_2 non-growth area is characterized using various techniques. The O_2 plasma etch time and the etch frequency were varied, such that a clean SiO_2 non-growth area is maintained, while maximizing the deposition on the growth area (i.e. high net growth rate). Based on the insights obtained from these experiments, general principles are extensively discussed to provide guidelines for the design and optimization ALD-etch cycles for area-selective deposition.

This chapter is structured as follows. First, the experimental conditions concerning the ALD and etching of Ru, as well as the characterization of the deposited films are described in Section 8.2. This is followed in Section 8.3 by the experimental results. In Section 8.3.1 the results on the effect of the deposition temperature on the ALD growth are presented. Section 8.3.2 then addresses the optimization of the ALD-etch supercycle; both the net deposition on Pt and the selectivity are evaluated as a function of O_2 plasma time. Section 8.4 provides a general discussion on how a high selectivity and a high net deposition can simultaneously be obtained when using ALD-etch supercycles. Finally, the main conclusions are presented in Section 8.5.

8.2 Experimental details

8.2.1 Thermal atomic layer deposition and plasma etching of Ru

Ru films were deposited using the thermal ABC-type ALD process described in Section 7.5. The ABC-type cycle is illustrated in Figure 8.1a, and consists of a 15-s ethylbenzenecyclohexadiene Ru(0) (EBCHDRu) precursor dose ('A'), a 15-s O_2 gas dose ('B'), and a 5-s H_2 gas dose ('C'). The Ru growth using the ABC-type ALD process was examined on SiO_2, Al_2O_3, Ru and Pt at temperatures between 100 °C and 200 °C. Due to the addition of a reducing H_2 dose to the cycle, the ABC-type process results in deposition of metallic Ru at temperatures below 200 °C.[45,46]

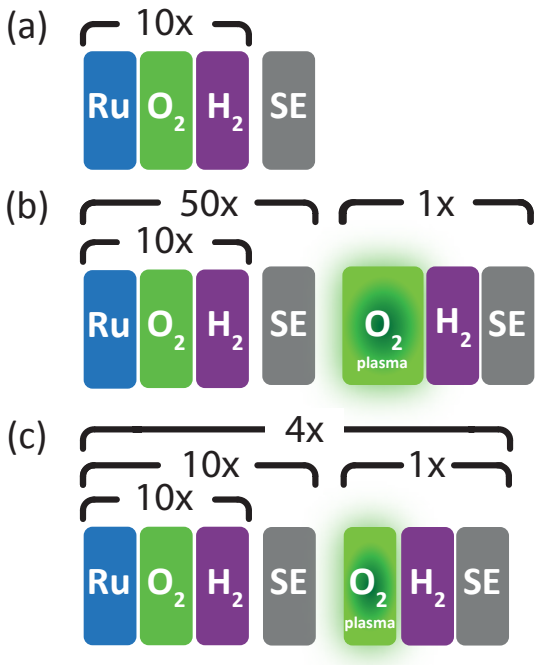

Figure 8.1 Different types of recipes used in this study: (a) the 'standard' thermal Ru ALD recipe, consisting of EBCHDRu precursor, O_2 gas, and H_2 gas doses, (b) an ALD recipe followed by a post-deposition etch cycle consisting of an O_2 plasma and an H_2 gas dose, and (c) a supercycle recipe with the same etch cycle included after every 100 thermal Ru ALD cycles. A spectroscopic ellipsometry (SE) measurement was always performed after every 10 ALD cycles and after every etch cycle.

The unwanted Ru present on the non-growth area was etched using an O_2 plasma. The etching of Ru occurs through the formation of volatile RuO_4, as is illustrated in Figure 8.2. The Ru film on the growth area is also exposed to this O_2 plasma, and some material is therefore also removed from the growth area. Furthermore, the Ru surface region is simultaneously oxidized. For this reason, every O_2 plasma etch step is followed by a reducing H_2 gas exposure. These exposures together form the etch cycle which is implemented either as a post-deposition etch step (i.e. after the complete deposition, see Figure 8.1b), or after a number of Ru ALD cycles during the recipe in a supercycle fashion (see Figure 8.1c).

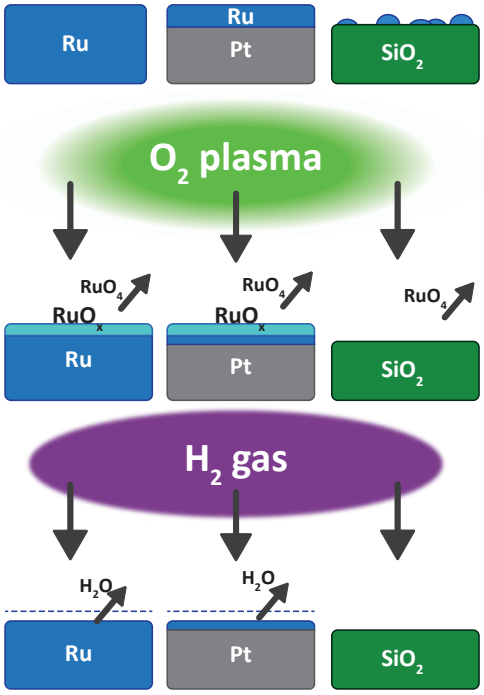

Figure 8.2 Schematic illustration of the etch cycle used to remove unwanted nucleation on the SiO_2 surface. Exposing the surfaces to an O_2 plasma leads to the formation of volatile RuO_4. After the O_2 plasma exposure, the Ru on the Ru or Pt growth area is slightly oxidized, and the subsequent H_2 gas exposure results in reduction of the surface. The O_2 plasma does not etch the SiO_2 or Pt substrates, hence the etching step is selective.

8.2.2 ALD reactor and conditions

Ru film deposition and etching was performed using a home-built ALD reactor.[47] The EBCHDRu precursor (Hansol Chemical, Korea) was contained in a stainless steel canister heated to 90 °C and Ar was used as a carrier gas. To avoid condensation of the precursor, the dosing line and the walls of the reactor were heated to 105 °C and 100 °C, respectively. Prior to Ru metal deposition, the reactor chamber was conditioned with 500 thermal ALD cycles of Al_2O_3 followed by 500 thermal ALD cycles of RuO_x. For the RuO_x process, a 15-s EBCHDRu dose and a 60-s O_2 gas dose (at 0.75 Torr) were used.

Ru growth was investigated on Ru, Pt, SiO_2, Al_2O_3, Co and TiN substrates. Wafer pieces with the corresponding materials were loaded in the reactor simultaneously. Single-side polished Si wafers with a thermal oxide of ∼430-450 nm were used as the SiO_2 substrates. The Pt film (∼15 nm) was deposited by performing

360 ALD cycles at 300 °C on thermal SiO_2, using an ABC-type cycle consisting of (methylcyclopentadienyl)trimethylplatinum ($MeCpPtMe_3$) precursor, O_2 plasma and H_2 plasma exposures.[48] The Al_2O_3 film (∼20 nm) was deposited with TMA ($Al(CH_3)_3$) and O_2 plasma using 150 thermal ALD cycles at a temperature of 200 °C. The Co sample (∼25 nm) was prepared by performing 1000 ALD cycles at 450 °C using $CoCp_2$ and an NH_3 plasma.[49] For the TiN substrate (∼13 nm), 450 cycles were carried out at 200 °C using $Ti(NMe_2)_4$ (TDMAT) and an Ar/H_2 plasma.[50] Substrates used for ALD only (without etching, Figure 8.3) received an H_2 gas pretreatment for 30 s. Substrates used for ALD-etch supercycles were cleaned using an O_2 plasma (100 W) for 1 minute, followed by a 30 s reducing H_2 gas treatment, in order to minimize effects related to surface contamination. The O_2 and H_2 pressures were set to 15 mTorr and 150 mTorr, respectively, during all experiments. A more detailed characterization of this ALD process will be published elsewhere.[51] The O_2 plasma etching step was performed using a power of 100 W, and different O_2 plasma exposure times of 5 s, 15 s, 30 s and 60 s were investigated. The O_2 plasma exposure was followed by an H_2 gas dose of 15 s, which was previously found to be sufficiently long to reduce the surface back to metallic Ru after oxidation occurred during the O_2 plasma exposure.[22]

8.2.3 Sample characterization

In situ spectroscopic ellipsometry (SE) data were collected using a J.A. Woollam, Inc. M2000U ellipsometer to monitor the deposition and etching of Ru. The data were fit using a B-spline model in the wavelength range of 1.2 eV to 4.5 eV.[52,53] Depositions on SiO_2 were modeled by first defining the thickness and dielectric function of the SiO_2 substrate using a wavelength point-to-point exact numerical inversion of the experimental data.[52] For deposition of Ru on Pt, a B-spline model was used to fit the optical response and thickness of the Pt substrate. The Ru thickness evolution was fit by first modeling the last *in situ* measurement. Subsequently, this fit was used as input for the first-to-last measurement, and this procedure was then repeated for all preceding measurements (i.e. dynamically fit backwards in time), while including the optical parameters in the fit.[53] The final Ru thicknesses on SiO_2, Al_2O_3, and Pt at each deposition temperature was determined using *ex situ* SE measurements taken at angles of 60°, 70°, and 80° with a J.A. Woollam, Inc. M2000D ellipsometer (1.2 eV - 6.5 eV). Since Ru growth starts out as island growth on SiO_2 and Al_2O_3, the thickness determined from SE can be regarded as an *apparent thickness*. X-ray photoelectron spectroscopy (XPS) was used to quantify the deposited Ru on the various substrates, and was carried out with a Thermo Scientific KA1066 spectrometer, using monochromatic Al Kα X-rays with an energy of 1486.6 eV. The quantification was done using the

Ru3p peak instead of the Ru3d peak, since the Ru3d and C1s XPS peak regions overlap. Although the sensitivity for the Ru3p peak is slightly lower, detection of Ru in the presence of C is more accurate using the Ru3p peak, especially for low Ru coverages on SiO_2 and Al_2O_3.[54] Scanning electron microscopy (SEM) images were taken using a Zeiss Sigma with a beam voltage of 5 kV, which allowed for identification of Ru nuclei due to the differences in density and conductivity between Ru and SiO_2.[55]

8.3 Results

8.3.1 Temperature optimization

To investigate whether the deposition temperature could be tuned to obtain selectivity, Ru ALD on SiO_2, Al_2O_3 and Pt substrates was investigated at different temperatures between 100 °C and 200 °C using *ex situ* SE and XPS. Figure 8.3 shows the final thickness and the Ru3p XPS peak area after performing 400 ALD cycles as a function of deposition temperature. For 200 °C, the amount of Ru deposition was approximately the same on all substrates, with thickness values around 9 nm, and similar Ru3p peak areas. As the deposition temperature was decreased, a difference in the Ru deposition on Pt versus SiO_2 and Al_2O_3 was observed. For a temperature of 150 °C, the amount of Ru on Pt is significantly higher than on SiO_2 and Al_2O_3. As can be seen in Figure 8.3a, 8.4 nm of Ru was deposited on Pt, as compared to 2.7 nm and 0.5 nm on SiO_2 and Al_2O_3, respectively. In addition, Figure 8.3b shows a much higher Ru peak area for the Pt substrate, as for SiO_2 and Al_2O_3. Further decreasing the temperature resulted in considerably less growth on the Pt substrate (3 nm for 125 °C and 0.7 nm for 100 °C), and negligible deposition on both SiO_2 and Al_2O_3. For the depositions at temperatures of 100 °C and 125 °C, no clear Ru was detected on SiO_2 and Al_2O_3 using both SE and XPS (see the Supporting Information, S.I., Figure S8.1 for the XPS spectra).

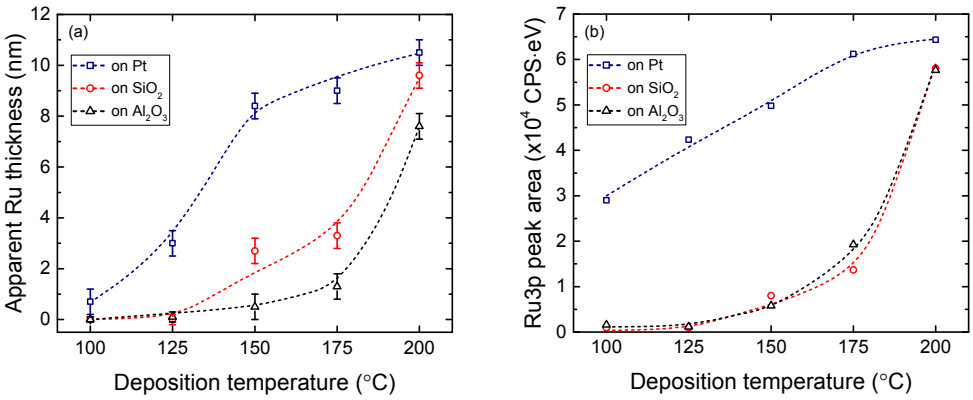

Figure 8.3 (a) Apparent Ru thickness from spectroscopic ellipsometry (SE) and (b) Ru3p XPS peak area (in counts per second·eV) as a function of deposition temperature after 400 ALD cycles, on Pt, SiO_2, and Al_2O_3 substrates. The lines serve as guides to the eye.

Based on the results of Figure 8.3, 150 °C was selected as the optimum deposition temperature to achieve area-selective deposition of Ru onto Pt, since the difference in thickness between Pt and SiO_2/Al_2O_3 is maximum at this temperature, and further decreasing the deposition temperature would lead to an impractically low growth rate on the Pt substrate. In addition, the growth of Ru on Co and TiN was investigated at 150 °C. XPS analysis showed that only limited growth occurred on Co and TiN, comparable to the growth on SiO_2 and Al_2O_3 (see Figure S8.2, S.I.). Furthermore, SE analysis revealed that Ru ALD also showed immediate growth on a Ru substrate. These findings corroborate that the catalytic activity of Ru and Pt is leading to more growth of Ru on these substrates than on SiO_2, Al_2O_3, Co and TiN. After selecting 150 °C as the optimum temperature, the material deposited on SiO_2 was studied in more detail using SEM (see Figure S8.3, S.I.). The SEM images reveal that Ru islands are present on the SiO_2, which motivates the combination of this ALD process with etching.

8.3.2 Supercycle optimization

Prior to studying the ALD-etch supercycle approach, a post-deposition O_2 plasma treatment was investigated as a potential alternative to improve the selectivity of the area-selective ALD process at 150 °C. 500 Ru ALD cycles were performed at 150 °C, followed by a post-deposition etch cycle consisting of 3 minute O_2 plasma exposure and 30 s H_2 gas (see Figure 8.1b). It was found that while the O_2 plasma etch step removed some Ru islands from the SiO_2, a significant number of islands remained on the surface (see Figure S8.3, S.I.), which was corroborated by SE analysis. Since it can be expected that small Ru nuclei are more easily etched

than large Ru islands, it is beneficial to perform etch steps earlier on during the ALD process instead of post-deposition. More importantly, the cyclic nature of ALD is highly suitable for implementation of correction steps during the deposition process.

An etch cycle was incorporated into a supercycle recipe as illustrated in Figure 8.1c. The supercycle recipe consisted of 400 ALD cycles and the etch cycle of O_2 plasma and H_2 gas steps was included after every 100 ALD cycles. As shown in Figure 8.4, without including etch cycles there was approximately 4 nm of Ru growth on the SiO_2 layer (Figure 8.4a), as compared to ∼9 nm on the Pt substrate (Figure 8.4b). The thickness on SiO_2 was slightly higher than in Figure 8.3a, due to a different pretreatment prior to ALD. Adding an etch cycle with 5 s O_2 plasma exposure after every 100 ALD cycles results in etching of approximately 1 nm of Ru from SiO_2 in each supercycle. Nevertheless, an apparent thickness of about 2 nm was measured on the SiO_2 surface after 4 supercycles. For a supercycle recipe using 15 s O_2 plasma exposures, there was no detectable Ru on the SiO_2 substrate and net deposition of ∼ 5 nm on the Pt substrate. Prolonging the O_2 plasma exposure to 30 s and 60 s produced similar results: no Ru was detected on SiO_2 using SE, while the Ru thicknesses on the Pt substrate were approximately 4 nm and 2.4 nm, respectively. These results suggest that a plasma duration of between 5 s and 15 s is optimal, since it results in minimal to no deposition on SiO_2, while there is net Ru growth on Pt of ∼5-6 nm.

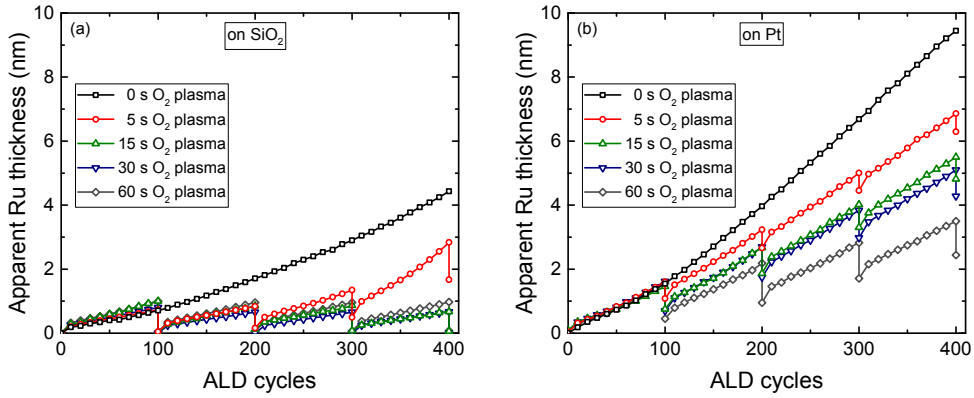

Figure 8.4 Apparent thickness as a function of ALD cycles for growth on (a) SiO_2 and (b) Pt using deposition-etch supercycles with different O_2 plasma etch times of 0, 5, 15, 30 and 60 s. In total four ALD-etch supercycles were performed, with an etch cycle after every 100 ALD cycles. SE measurements were done every 10 ALD cycles and after every etch cycle. The deposition temperature was 150 °C.

When investigating the Ru thickness on SiO_2 as a function of ALD cycles in more detail (Figure 8.4a), several observations can be made. A slight variation in the growth per cycle (GPC, i.e. the local slope of the graph) appears to exist for the different depositions using varying O_2 plasma times (e.g. the GPC for 60 s is higher than for 30 s). This variation can be explained by deviations in the sample temperature, together with the strong dependence of the growth on the temperature (Figure 8.3). In addition, it can be seen that the first 10 ALD cycles after each etch cycle lead to more Ru deposition on both SiO_2 and Pt than the subsequent 90 cycles. This enhanced deposition is attributed to the surface modification during the O_2 plasma and H_2 gas steps, causing a higher reactivity of the surface with the precursor in the following 10 ALD cycles. The data also show that the decrease in Ru film thickness on Pt per etch cycle depends on the O_2 plasma duration, as will be addressed later (see Figure 8.7). Moreover, it is observed that the GPC increases with the number of cycles when no etch cycles were performed (especially around 100 ALD cycles). In Chapter 7, it is discussed that the enhancement of the GPC as a function of the number of ALD cycles is possibly caused by an increase of the surface roughness, which can result in an effective increase in the surface area available for precursor adsorption.[22,56] This enhancement of the GPC is likely suppressed by the etch cycles. The etching can lead to smoothing of the Ru film, since regions protruding from the surface are more easily etched than smooth regions of the film.[22,57,58]

To evaluate the obtained selectivity as a function of O_2 plasma time, the Ru surface coverage on SiO_2 was determined using SEM. Figure 8.5 shows SEM images collected after performing 4 supercycles on SiO_2 with O_2 plasma times between 0 s and 60 s. In addition, Table 8.1 lists the corresponding surface coverage Θ, density of nuclei n, selectivity S, and net Ru thickness on Pt. For this analysis, the selectivity was defined as $S = (\Theta_{Pt} - \Theta)/(\Theta_{Pt} + \Theta)$.[59] Note that a higher value for the selectivity does not necessarily indicate an improvement, as the obtained net growth on Pt should also be taken into account.[59]

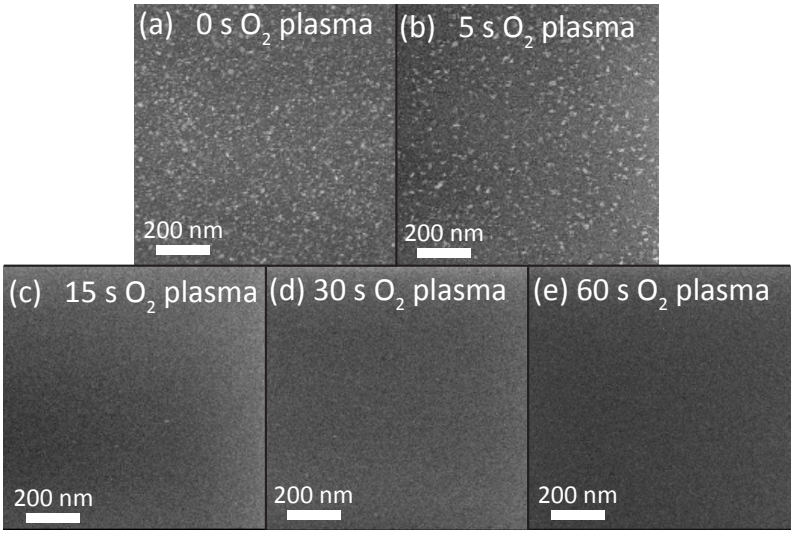

Figure 8.5 Top-view SEM images after 4 Ru ALD-etch supercycles on SiO_2 with an etch cycle after every 100 ALD cycles. O_2 plasma times between 0 s and 60 s were investigated.

Figure 8.5a shows that the SiO_2 surface was almost fully covered with Ru nuclei when no etch cycles are performed. Analysis of the nuclei yields a surface coverage Θ of 0.7, which corresponds to a selectivity of 0.18.[59] A supercycle recipe with an O_2 plasma duration of 5 s resulted in less Ru nuclei (see Figure 8.5b), but the nuclei still account for a coverage of 0.13 and the obtained selectivity is 0.77 (Table 8.1). For O_2 plasma times of 15 s and 30 s, nearly all Ru nuclei were removed, and the selectivity increased to 0.988 and 0.997, respectively. At the same time, the film thickness on the Pt substrate decreased to 4.8 nm and 4.3 nm. Finally, Figure 8.5e shows that a practically clean SiO_2 surface was obtained using an O_2 plasma time of 60 s, corresponding to a selectivity of 0.9996. Nevertheless, the thickness on Pt was only 2.4 nm, and additional ALD-etch supercycles would be required to obtain a thicker Ru film on the growth area. The selectivity and the final thickness on Pt are also plotted as function of O_2 plasma time in Figure 8.7. Note that also XPS was employed to investigate the Ru deposited on SiO_2, which yielded similar results (see Figure S8.4, S.I.).

Table 8.1 Surface coverage Θ and number density of nuclei n of Ru on the SiO_2 non-growth area, selectivity S and Ru thickness on the Pt growth area (d_{Pt}) after 4 supercycles using an O_2 plasma time between 0 s and 60 s. The selectivity was calculated using $S = (\Theta_{Pt} - \Theta)/(\Theta_{Pt} + \Theta)$, where Θ_{Pt} was 1 (representing a closed film) for all samples.[59,60] No nuclei density is listed for 0 s, since the nuclei cannot be distinguished from each other.

O_2 plasma time (s)	Coverage θ	n ($\times 10^{-3}$ nm^{-2})	Selectivity S	d_{Pt} (nm)
0	0.7 ± 0.1	-	0.18 ± 0.07	9.4 ± 0.2
5	0.13 ± 0.05	1.1 ± 0.1	0.78 ± 0.08	6.3
15	0.006 ± 0.002	0.11 ± 0.03	0.988 ± 0.004	4.8
30	0.0013 ± 0.0005	0.03 ± 0.01	0.997 ± 0.001	4.3
60	0.0002 ± 0.0001	0.003 ± 0.001	0.9996 ± 0.0002	2.4

In order to obtain the maximum net deposition, both the O_2 plasma etch duration and the etch frequency should be optimized (i.e. the ratio of ALD and etch cycles. Figure 8.6a shows that 4 supercycles with an O_2 plasma of 5 s after every 100 ALD cycles resulted in almost 2 nm deposition on the SiO_2 non-growth area. In contrast, no Ru was detected using SE on SiO_2 for the same O_2 plasma exposure of 5 s after every 50 ALD cycles (see Figure 8.6b). Note that also no Ru deposition on SiO_2 was detected when using supercycles with an O_2 plasma duration of 15 s after every 100 ALD cycles (see Figure 8.6c). On Pt, the final Ru thickness was approximately 1 nm lower when using a 5 s O_2 plasma after every 50 ALD cycles as compared to when using a 15 s O_2 plasma after every 100 ALD cycles. Upon close examination of Figure 8.6b and c, it can be seen that the growth rate on Pt (i.e. the slope of the thickness versus ALD cycles) was slightly lower for 5 s O_2 plasma after every 50 ALD cycles than for 15 s every 100 ALD cycles. For instance, between 360 and 400 ALD cycles, the average growth rates were ~0.17 Å/cycle and ~0.20 Å/cycle, respectively. The lower growth rate for etching after every 50 ALD cycles is likely due to the smoothing effect and corresponding reduced precursor adsorption. The smoothing effect is believed to be more pronounced when the etch cycle is included after 50 cycles because the etch step is performed more often as compared to etching after 100 ALD cycles. The combination of the lower average GPC and the additional etching results in a lower final thickness on Pt for 5 s O_2 plasma after every 50 ALD cycles. This finding suggests that performing the etch cycle after more ALD cycles, but using a longer O_2 plasma time, is beneficial in terms of net deposition, as will be elaborated on in Section 8.4.

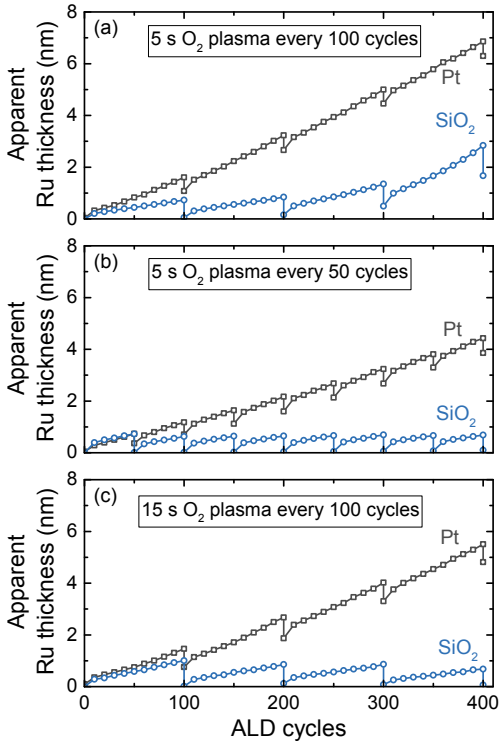

Figure 8.6 Apparent Ru thickness as a function of ALD cycles on SiO_2 and Pt. The employed ALD-etch supercycle recipes contained etch cycles with an O_2 plasma for (a) 5 s after every 100 ALD cycles, (b) 5 s after every 50 ALD cycles, and (c) 15 s after every 100 cycles.

Insight into the etch behavior was obtained by evaluating the Ru thickness decrease on Pt as a function of O_2 plasma exposure time based on the data shown in Figure 8.4b. As can be seen in Figure 8.7b, the amount of Ru removed from the Pt growth area depends on the duration of the O_2 plasma etch step. This indicates that the etching by the O_2 plasma exposure is not a self-limiting reaction. The etch per cycle is however not linearly increasing, and slows down as a function of O_2 plasma exposure time, i.e. the etch rate (in nm/s) is higher at the start of the O_2 plasma. As the film gets more oxidized the etching appears to become more difficult. This quasi self-limiting etch behavior suggests that the etching of a RuO_2 film is less favorable than etching of metallic Ru, in line with the literature.[43,61] Etching of metallic Ru has been performed using both O_3 gas and an O_2 plasma, and is believed to be driven by radicals.[43,44,62] This is in contrast to etching of RuO_2, which requires energetic ions from an O_2 plasma and is mostly reported using reactive-ion etching (RIE).[61–64]

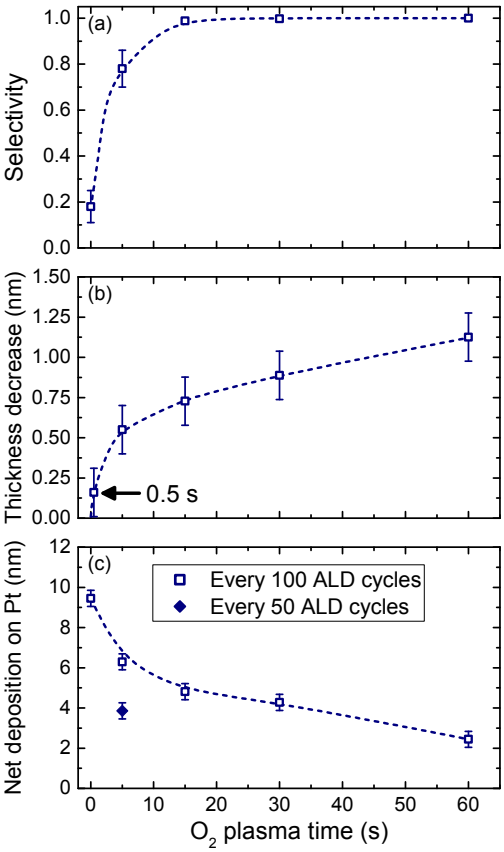

Figure 8.7 (a) The selectivity, (b) the average Ru thickness decrease on the Pt growth area per etch cycle, and (c) the net deposition on the Pt growth area after 4 supercycles, with an etch cycle performed after every 50 or 100 ALD cycles. The etch process demonstrates quasi self-limiting behavior. The reported thickness decrease in (b) is the decrease after the complete etch cycle, i.e. after the H_2 gas dose. Note that an additional experiment was performed to determine the thickness decrease for 0.5 s of O_2 plasma (corresponding data not shown in Figure 8.4).

The dependence of the etch rate on the etch time implies that both the O_2 plasma duration and the frequency should be optimized such that no material is deposited on SiO_2, while obtaining a maximum thickness on the Pt substrate (see Section 8.4). This also becomes evident from Figure 8.7c, where the net deposition (after 400 ALD cycles) is plotted as a function of the O_2 plasma time. Due to the fact that the etch per cycle does not saturate, the net deposition continues to decrease for longer plasma times. However, because the etch behavior is quasi self-limiting, the data point for an O_2 plasma etch of 5 s after every 50 ALD cycles (40 s etching in total), shows a lower net deposition ($\sim$3.9 nm) than the

data point for 15 s after every 100 ALD cycles (60 s etching in total, ~4.8 nm). This observation indicates that the etch frequency has a larger effect on the net deposition than the etch duration.

8.4 Discussion

The results presented in Section 8.3.2 demonstrate that ALD-etch supercycles offer an interesting opportunity to improve the selectivity of area-selective ALD processes. However, the implementation of etch cycles results in a decrease of the deposition on the growth area, meaning that generally a trade-off should be made between selectivity and net deposition. As was discussed in the introduction, ALD-etch supercycles have previously been reported for area-selective deposition of Ta_2O_5 and TiO_2.[19–21] Vallat *et al.* used the nucleation delay of Ta_2O_5 and TiO_2 growth on Si and SiO_2 as a starting point for the development of ALD-etch supercycles, while in the work of Song *et al.* the initially low growth rate of TiO_2 deposition on H-terminated Si was exploited.[19–21] Although both studies demonstrated a high selectivity with ALD-etch supercycles, it remains to be determined which supercycle ratios yield the optimal results in terms of selectivity and net deposition.

For the Ru ALD-etch supercycles studied in this work, it was found that the selectivity S increased with the O_2 plasma time, while the net Ru deposition on the Pt growth area decreased (see Figure 8.7). The data in Table 8.1 suggest that a supercycle using an etch cycle with 30 s O_2 plasma after 100 ALD cycles is close to the optimal ALD-etch supercycle configuration, obtaining a selectivity of 0.997 and a net deposition of 4.3 nm of Ru on Pt. However, further investigation is also required in this case, in order to verify whether this is the optimum, or whether performing the etch cycle after slightly more ALD cycles would increase the obtained thickness (see text related to Figure 8.6). Since the optimum configuration has not been determined so far for the different ALD-etch supercycles reported here and in the literature, it is relevant to discuss some guidelines for the optimization of ALD-etch supercycles. Several observations made for the Ru ALD and etch processes in Section 8.3, and Figure 8.4 in particular, are important for such a discussion:

- At a deposition temperature of 150°C, the Ru growth starts immediately on both the Pt growth area and on the SiO_2 non-growth area, but the growth rate on SiO_2 is lower than on Pt.
- The etch cycle results in removal of Ru from the SiO_2 non-growth area as well as from the Pt growth area. However, close inspection of Figure 8.4 demonstrates

that the etch rate on SiO_2 is higher than on Ru. For example, for an O_2 plasma time of 5 s, the Ru thickness decrease is around 1 nm on the SiO_2 non-growth area, as compared to ∼0.5 nm on Pt.

- On both SiO_2 and Pt, the growth rate depends on the number of performed ALD cycles, due to the change in Ru surface coverage on the SiO_2 substrate (i.e. Ru growth on SiO_2 differs from Ru growth on a closed Ru film), or development of the surface roughness, respectively.

In general, the development of an ALD-etch supercycle should aim at two aspects: (i) minimizing the deposition on the non-growth area, and (ii) maximizing the net deposition on the growth area. Typically, a competition exists between those two aspects. In Section 8.1 it was discussed that growth-area selectivity is required for the ALD-etch supercycle approach to work, which means that growth should occur preferentially on the growth area. We can thus define different growth rates (i.e. growth per cycle, GPC) for growth on the growth area (GPC_G) and on the non-growth area (GPC_{NG}). Note that for now constant GPC values are assumed. When aiming for perfect selectivity ($S = 1$), the net deposition on the non-growth area after performing N supercycles should be equal to zero:

$$D_{net,NG} = \alpha N\ GPC_{NG} - \beta N\ EPC\ =\ 0, \tag{8.1}$$

where α and β are the number of deposition and etch cycles in one supercycle, respectively, and EPC is the etch per cycle. For simplicity, it is assumed here as a starting point that the etch rate is the same for material on the growth area as for the non-growth area. The requirement that there should be no net deposition on the non-growth area (Equation 8.1) determines the cycle ratio κ, which is the ratio between the number of deposition and etch cycles in one supercycle:

$$\kappa = \frac{\alpha}{\beta} = \frac{EPC}{GPC_{NG}}. \tag{8.2}$$

The deposition on the growth area can be calculated using:

$$D_{net,G} = \alpha N\ GPC_G - \beta N\ EPC. \tag{8.3}$$

The following relation for the net deposition on the growth area can be derived by combining Equations 8.2 and 8.3:

$$D_{net,G} = \alpha N\left[GPC_G - GPC_{NG}\right]. \tag{8.4}$$

Equation 8.4 represents the simple etch-back strategy for which the amount of material removed from the growth area equals the amount of material that needs to

be removed from the non-growth area to obtain perfect selectivity. For this case, it is evident that the growth rate on the non-growth area GPC_{NG} should be as low as possible to maximize the net deposition on the growth area. This is schematically elucidated in Figure 8.8 for two different values of GPC_{NG}. Comparison of the plots in Figure 8.8a and b illustrates that a lower value for GPC_{NG} yields a higher net deposition on the growth area G_G, since less etch cycles are needed.

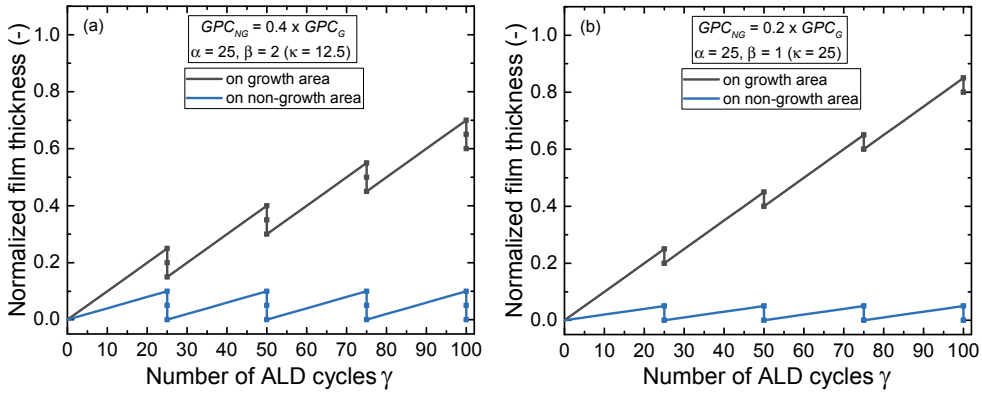

Figure 8.8 Calculated film thickness as a function of ALD cycles for ALD-etch supercycles assuming a growth rate on the non-growth area GPC_{NG} which is (a) 0.4 times and (b) 0.2 times GPC_G. A lower value for GPC_{NG} can allow for a higher net deposition on the growth area, because less etching is necessary. Note that the cycle ratio κ is the ratio between ALD cycles α and etch cycles β.

So far it was assumed that material from the non-growth area is removed at the same rate as from the growth area (see Equation 8.4). However, as was briefly mentioned above for the case of Ru, material on the non-growth area is likely to be etched faster than on the growth area. Approximately twice the amount of Ru was removed from SiO_2 as from Pt during the etch cycle when using a 5-s O_2 plasma exposure (see Figure 8.4). Such a difference in etch behavior can for example be due to differences in morphology. If we define EPC_G and EPC_{NG} for the etching of material from the growth area and the non-growth area, respectively, the following equation holds:

$$D_{net,G} = \alpha N \left[GPC_G - GPC_{NG} \frac{EPC_G}{EPC_{NG}} \right]. \tag{8.5}$$

Equation 8.5 illustrates which strategies can be taken to maximize the net deposition on the growth area. First of all, the most straightforward strategy is to reduce the growth rate on the non-growth area as much as possible. In addition, it can be seen that it is beneficial to aim for a higher etch rate on the non-growth area, i.e. a low value for the ratio between the etch rates EPC_G/EPC_{NG}. From

Equation 8.5 it also becomes evident that selectivity can even be achieved in case the growth rates on the growth and non growth area are the same, but there is a significant difference in etch rates instead. A difference in etch rate can for example be obtained if the surface morphology of material on the non-growth area deviates from the morphology of material on the growth area. Interestingly, the concept of a higher etch rate for nuclei as compared to films is already exploited in practice for selective epitaxial growth of Si.[65] For the Ru ALD-etch supercycles, the data also suggest that a difference in etch rates exists, which can likely be explained by different surface morphologies. Due to a large contrast in surface energy between Ru and SiO_2, the Ru nucleation on SiO_2 starts out as island growth (Volmer-Weber growth),[66,67] while the surface energies for Ru and Pt are more similar.[68,69] A higher etch rate for Ru nuclei is in line with the observed smoothing effect, as it indicates that areas protruding from the surface (including nuclei or islands) are etched faster than the bulk of the film.

To illustrate the concept of different etch rates, Figure 8.9a shows an example where $EPC_{NG} = 2 \times EPC_G$. By comparing Figure 8.9a to Figure 8.8a, it can be seen that a higher etch rate for material on the non-growth area indeed allows for a higher net deposition. Note that except for the etch rate, the same values are used for Figure 8.9a and Figure 8.8a.

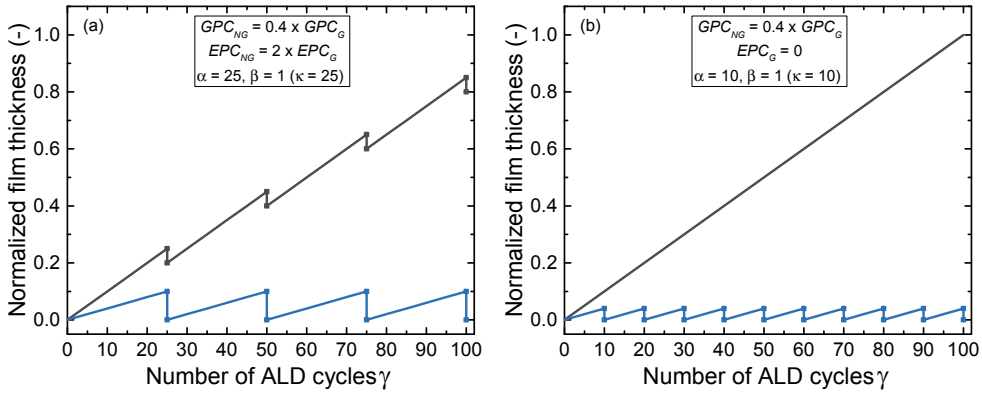

Figure 8.9 Calculated film thickness as a function of ALD cycles assuming a growth rate on the non-growth area GPC_{NG} which is 0.4 times GPC_G, (a) for $EPC_{NG} = 2 \times EPC_G$, and (b) for the ideal situation where $EPC_G = 0$. Note that a different etch chemistry, or different etch conditions might be required to obtain the situation depicted in (b), meaning that the etch process for (b) is not necessarily the same as in (a).

Although the situation depicted in Figure 8.9a represents an improvement as compared to Figure 8.8a, in the ideal case only nuclei on the non-growth are affected by the etch cycles. This potential strategy is illustrated in Figure 8.9b, and

offers a very interesting method to circumvent the trade-off between high selectivity and high net deposition. It is important to realize that the etch rate of nuclei on the non-growth area EPC_{NG} likely depends on the nuclei size, as it can be expected that small nuclei are more easily removed than bigger nuclei or particles. Because the nuclei size typically increases with the number of performed ALD cycles (γ), the etch rate can also depend on the number of performed ALD cycles, i.e. $EPC_{NG} = f(\gamma)$. Furthermore, as was already discussed, the growth rates in Equation 8.5 can also change as a function of the number of ALD cycles γ (e.g. when there is a nucleation delay).[66,67] In the most likely case, GPC_{NG} increases with the number of ALD cycles, while EPC_{NG} decreases as a function of γ. The number of ALD cycles performed prior to the etch cycle ($=\alpha$) therefore affects the amount of etching that is required. The situation where material on the growth area is not removed can thus hypothetically be approached when small nuclei or individual atoms are present on the non growth area, and only a mild etch step is sufficient to remove those. Finally it is noted that if the material on the growth area is not (or very slightly) etched during the etch cycle, an etch process can be employed that does not exhibit self-limiting surface reactions, since the uniformity and conformality of the film on the growth area are not (significantly) affected by the etch process.

An aspect which has not been addressed so far in this discussion is the time-dependence of the etch rates (i.e. $EPC = f(t)$). As was shown in Figure 8.7a, the Ru etch process shows a quasi self-limiting behavior, and the etch rate slows down with time. In general, the etch rate can also be constant as a function of time (meaning that the thickness decreases linearly with time), or the etch process can demonstrate self-limiting behavior (in case of an ALE process). For a linear etch behavior, doubling the etch time would result in double the amount of material removed. For ALE, the etch time would not affect the amount of material etched (as long as saturation is assured). For an ALE process, the number of etch cycles is thus the only parameter which can be used to change the amount of material removed. However, for quasi self-limiting etching it becomes more complicated (see Figure 8.7b). In this case, doubling the etch time, results in less than twice the amount of removed material. For the Ru ALD-etch supercycles, it was found that an O_2 plasma time of 15 s resulted in etching of 0.73 nm of Ru, while 30 s leads to a decrease of 0.89 nm. Finally, effects of the etch cycles on the GPC, such as smoothing and enhanced surface reactivity, also play a role in the optimization.[21] Because of these effects, the obtained net deposition is typically more complicated than just the sum of the deposition and etch components of the individual processes.

The discussion above, and Equation 8.5 in particular, help to clarify which information is required to fully optimize an ALD-etch supercycle. Logically, the growth rate on the growth area should be known when developing an ALD process. In addition, it should be investigated how the growth rate changes on the non-growth area as a function of ALD cycles (e.g. whether there is a nucleation delay). Generally, these are aspects which are studied when developing an area-selective ALD process. However, from the presented analysis, we learn that the nuclei size on the non-growth area as a function of cycles (related to GPC_{NG}), and the dependence of the etch rate on the nuclei size (related to EPC_{NG}) should be studied as input for optimization of the supercycle recipe. This is also the case for the Ru ALD-etch supercycles, as limited information is currently available on the size development of Ru nuclei when using the EBCHDRu precursor. By analyzing the nuclei size as function of ALD cycles using for example transmission electron microscopy (TEM), more insight can be obtained.[70] Finally, it is important to know how the ALD and etch cycles influence each other, e.g. whether there is an growth or etch delay (or enhancement) when switching from one to the other.

8.5 Conclusion

In this work, a thermal ALD process and a plasma-based etch process for Ru were characterized and combined in order to obtain area-selective deposition. At a deposition temperature of 150 °C, the Ru ALD process showed the largest difference in growth behavior between the Pt/Ru growth areas and the SiO_2/Al_2O_3 non-growth areas. However, the selectivity of the thermal Ru ALD process was limited and some Ru island growth occurred on the SiO_2 non-growth area. A significant improvement of the selectivity was achieved by integrating an etch cycle consisting of an O_2 plasma exposure and an H_2 gas dose in an ALD-etch supercycle, because it resulted in the removal of Ru nuclei from the SiO_2 non-growth area. The selectivity of the process was shown to increase with the O_2 plasma exposure time, although the net deposition on the Pt growth area decreased significantly. This observation illustrates the trade-off between selectivity and net deposition which generally has to be made when employing ALD-etch supercycles. Based on an extensive discussion, it was argued that this trade-off can be circumvented by identifying conditions for which the etch rate of material on the non-growth area is much higher than on the growth area. From this analysis it therefore followed that future research should focus on the investigation of the etch rate on the non-growth area as a function of performed ALD cycles.

Acknowledgements

The authors would like to thank C.A.A. van Helvoirt, J.J.A. Zeebregts, C.O. van Bommel, and J.J.L.M. Meulendijks for their technical assistance. This work was financially supported by the Netherlands Organization for Scientific Research (NWO) through the Zwaartekracht program 'Research Centre for Integrated Nanophotonics'. In addition, the work of S.N.C. was made possible through the National Science Foundation (NSF) Graduate Research Opportunities Worldwide program, and a NASCENT Whaley fellowship.

8.6 Supporting Information

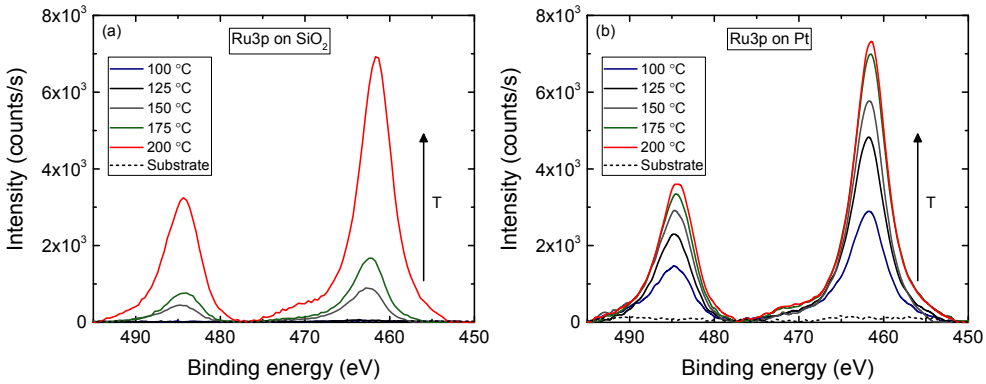

Figure S8.1 XPS spectra for the Ru3p peak after performing 400 ALD cycles on (a) SiO_2 and (b) Pt at temperatures between 100 °C and 200 °C. Almost no deposition is observed on SiO_2 for temperatures below 150 °C, while Ru is clearly present on Pt even for 100 °C.

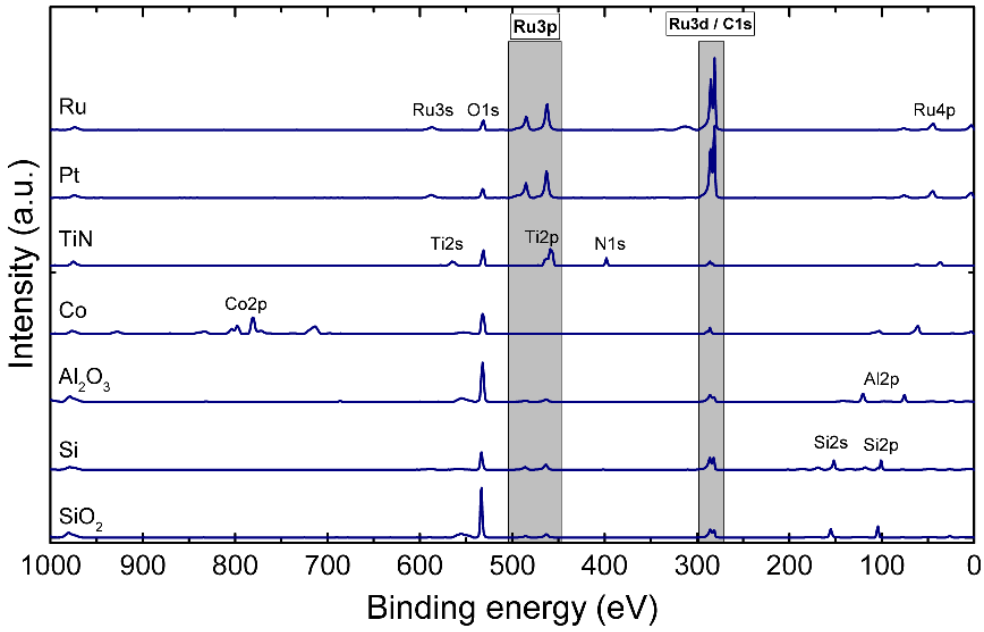

Figure S8.2 XPS survey spectra collected after 400 cycles Ru ALD at a deposition temperature of 150 °C, on Ru, Pt, TiN, Co, Al_2O_3, Si, and SiO_2 substrates. Significant growth is observed on the Ru and the Pt surfaces, while minimal Ru is deposited on the other substrates. These results suggest that the catalytic activity of the Pt and Ru leads to enhanced nucleation.

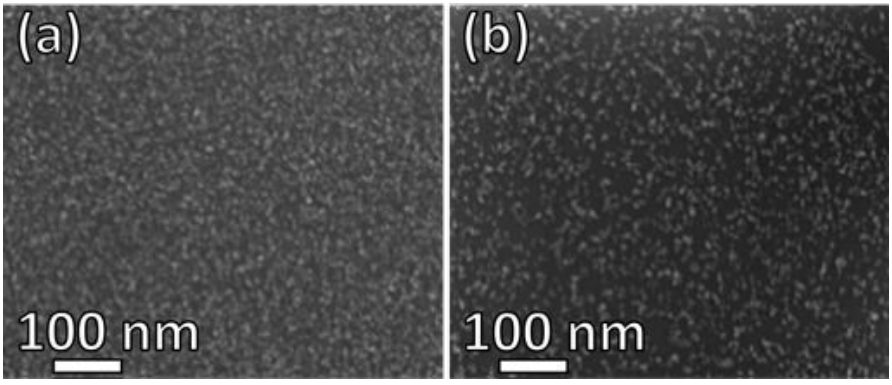

Figure S8.3 Top-view SEM images after (a) 500 cycles of Ru ALD at 150 °C and (b) 500 cycles Ru ALD at 150 °C followed by a post-deposition etch cycle using a 3 minute O_2 plasma and a 30 s H_2 gas dose. The substrate was SiO_2.

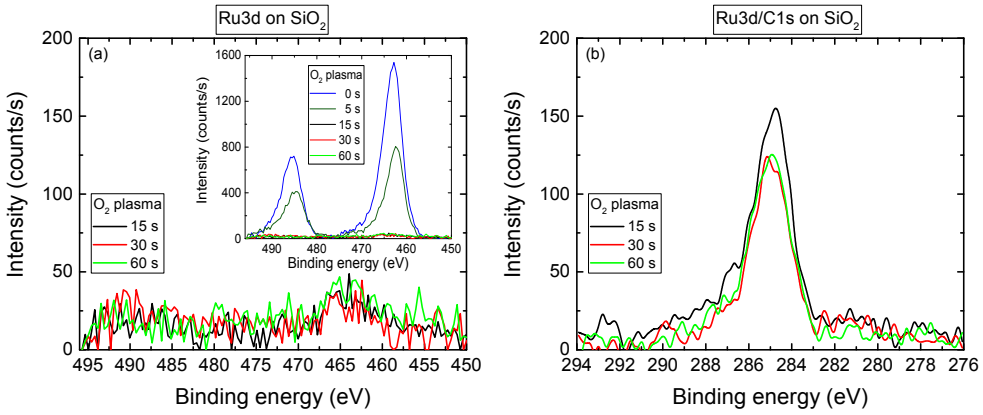

Figure S8.4 XPS spectra collected on SiO_2 for (a) the Ru3p peak and (b) the Ru3d/C1s peaks after performing 4 supercycles with an etch cycle after every 100 ALD cycles, using O_2 plasma times of 15 s, 30 s and 60 s. The inset of (a) also shows data for O_2 plasma times of 0 s and 5 s using a different vertical scale. While clear Ru peaks are observed when no etching is performed, or when a 5 s plasma is used, the Ru coverage on the SiO_2 is close to the XPS sensitivity limit for an O_2 plasma time of 15 s or longer. Note that the singlet peak in (b) at approximately 285 eV is corresponding to C1s. This data corroborates the SEM data in Figure 8.5, which showed that an O_2 plasma etch time of 15 s or longer is sufficient to remove most of the Ru nucleation from SiO_2.

References

[1] Schuegraf, K., Abraham, M. C., Brand, A., Naik, M., and Thakur, R., *IEEE J. Electron Devices Soc.* **2013**, 1(3), 66–75.
[2] Thoms, S., Macintyre, D. S., Docherty, K. E., and Weaver, J. M. R., *Microelectron. Eng.* **2014**, 123, 9–12.
[3] Mulkens, J., Hanna, M., Wei, H., Vaenkatesan, V., Megens, H., and Slotboom, D., *Proc. SPIE 9422, Extrem. Ultrav. Lithogr. VI* **2015**, 9422(March 2015), 94221Q.
[4] Mulkens, J., Hanna, M., Slachter, B., Tel, W., Kubis, M., Maslow, M., *et al.*, *Proc. SPIE 10145, Metrol. Insp. Process Control Microlithogr. XXXI* **2017**, 10145(March 2017), 1014505.
[5] Clark, R., Tapily, K., Yu, K. H., Hakamata, T., Consiglio, S., O'Meara, D., *et al.*, *APL Mater.* **2018**, 6(5), 058203.
[6] Radamson, H. H. and Kolahdouz, M., *J. Mater. Sci. Mater. Electron.* **2015**, 26(7), 4584–4603.
[7] Yang, C. C., Flaitz, P., Wang, P. C., Chen, F., and Edelstein, D., *IEEE Electron Device Lett.* **2010**, 31(7), 728–730.
[8] Fang, M. and Ho, J. C., *ACS Nano* **2015**, 9(9), 8651–8654.
[9] Mackus, A. J. M., Merkx, M. J. M., and Kessels, W. M. M., *Chem. Mater.* **2019**, 31(1), 2–12.
[10] Leskelä, M. and Ritala, M., *Thin Solid Films* **2002**, 409(1), 138–146.
[11] George, S. M., *Chem. Rev.* **2010**, 110(1), 111–131.
[12] Mackus, A. J. M., Dielissen, S. A. F., Mulders, J. J. L., and Kessels, W. M. M., *Nanoscale* **2012**, 4(15), 4477–4480.
[13] Methaapanon, R., Geyer, S. M., Lee, H.-B.-R., and Bent, S. F., *J. Mater. Chem.* **2012**, 22(48), 25154.
[14] Mackus, A. J. M., Bol, A. A., and Kessels, W. M. M., *Nanoscale* **2014**, 6(2011), 10941–10960.
[15] Joyce, B. and Baldrey, J., *Nature* **1962**, 195(4840), 485–486.
[16] Rai-Choudhury, P. and Schroder, D. K., *J. Electrochem. Soc.* **1971**, 118(1), 107–110.
[17] Goulding, M. R., *Mater. Sci. Eng. B* **1993**, 17(1-3), 47–67.
[18] Hashemi, F. M. S., Prasittichai, C., and Bent, S. F., *ACS Nano* **2015**, 9(9), 8710–8717.
[19] Vallat, R., Gassilloud, R., Eychenne, B., and Vallée, C., *J. Vac. Sci. Technol. A* **2017**, 35(1), 01B104.
[20] Vallat, R., Gassilloud, R., Salicio, O., El Hajjam, K., Molas, G., Pelissier, B., *et al.*, *J. Vac. Sci. Technol. A* **2019**, 37(2), 020918.
[21] Song, S. K., Saare, H., and Parsons, G. N., *Chem. Mater.* **2019**, 31(13), 4793–

4804.
[22] Vos, M. F. J., Chopra, S. N., Verheijen, M. A., Ekerdt, J. G., Agarwal, S., Kessels, W. M. M., *et al.*, *Chem. Mater.* **2019**, 31(11), 3878–3882.
[23] Tamboli, D., Osso, O., McEvoy, T., Vega, L., Rao, M., and Banerjee, G., *ECS Trans.* **2010**, 33(10), 181–187.
[24] Henderson, L. B. and Ekerdt, J. G., *Thin Solid Films* **2009**, 517(5), 1645–1649.
[25] Arunagiri, T. N., Zhang, Y., Chyan, O., El-Bouanani, M., Kim, M. J., Chen, K. H., *et al.*, *Appl. Phys. Lett.* **2005**, 86(8), 1–3.
[26] Tokei, Z., Ciofi, I., Roussel, P., Debacker, P., Raghavan, P., Van Der Veen, M. H., *et al.*, *2016 IEEE Symp. VLSI Technol.* **2016**, pp. 1–2.
[27] Wen, L. G., Roussel, P., Pedreira, O. V., Briggs, B., Groven, B., Dutta, S., *et al.*, *ACS Appl. Mater. Interfaces* **2016**, 8(39), 26119–26125.
[28] Kim, S. K., Kim, W. D., Kim, K. M., Hwang, C. S., and Jeong, J., *Appl. Phys. Lett.* **2004**, 85(18), 4112–4114.
[29] Kwon, O.-K., Kwon, S.-H., Park, H.-S., and Kang, S.-W., *J. Electrochem. Soc.* **2004**, 151(12), C753–C756.
[30] Schaekers, M., Capon, B., Detavernier, C., and Blasco, N., *ECS Trans.* **2010**, 33(2), 135–144.
[31] Suh, Y.-S., Lazar, H., Chen, B., Lee, J.-H., and Misra, V., *J. Electrochem. Soc.* **2005**, 152(9), F138.
[32] Waechtler, T., Ding, S. F., Hofmann, L., Mothes, R., Xie, Q., Oswald, S., *et al.*, *Microelectron. Eng.* **2011**, 88(5), 684–689.
[33] Yeo, S., Choi, S. H., Park, J. Y., Kim, S. H., Cheon, T., Lim, B. Y., *et al.*, *Thin Solid Films* **2013**, 546, 2–8.
[34] Dean, J., *Lange's Handbook of Chemistry*, volume 5, McGraw-Hill, New York, 15th editi edition, **1999**, ISBN 0070163847.
[35] Ryden, W., Lawson, A., and Sartain, C., *Phys. Rev. B* **1970**, 1(4), 1494–1500.
[36] Minjauw, M. M., Rijckaert, H., Driessche, I. V., Detavernier, C., and Dendooven, J., *Chem. Mater.* **2019**, 31(5), 1491–1499.
[37] Park, K. J., Doub, J. M., Gougousi, T., and Parsons, G. N., *Appl. Phys. Lett.* **2005**, 86(5), 1–3.
[38] Zyulkov, I., Krishtab, M., De Gendt, S., and Armini, S., *ACS Appl. Mater. Interfaces* **2017**, 9(36), 31031–31041.
[39] Färm, E., Lindroos, S., Ritala, M., and Leskelä, M., *Chem. Mater.* **2012**, 24(2), 275–278.
[40] Junige, M., Löffler, M., Geidel, M., Albert, M., Bartha, J. W., Zschech, E., *et al.*, *Nanotechnology* **2017**, 28(39), 395301.
[41] Mackus, A. J. M., Thissen, N. F. W., Mulders, J. J. L., Trompenaars, P. H. F., Verheijen, M. A., Bol, A. A., *et al.*, *J. Phys. Chem. C* **2013**, 117(20), 10788–10798.

[42] Leick, N., Agarwal, S., Mackus, A. J. M., Potts, S. E., and Kessels, W. M. M., *J. Phys. Chem. C* **2013**, 117(41), 21320–21330.
[43] Nakahara, M., Tsunekawa, S., Watanabe, K., Arai, T., Yunogami, T., and Kuroki, K., *J. Vac. Sci. Technol. B Microelectron. Nanom. Struct.* **2001**, 19(2001), 2133.
[44] Hsu, C. C., Coburn, J. W., and Graves, D. B., *J. Vac. Sci. Technol. A Vacuum, Surfaces, Film.* **2006**, 24(1), 1.
[45] Hämäläinen, J., Puukilainen, E., Sajavaara, T., Ritala, M., and Leskelä, M., *Thin Solid Films* **2013**, 531, 243–250.
[46] Hämäläinen, J., Ritala, M., and Leskelä, M., *Chem. Mater.* **2014**, 26(1), 786–801.
[47] Heil, S. B. S., Langereis, E., Roozeboom, F., van de Sanden, M. C. M., and Kessels, W. M. M., *J. Electrochem. Soc.* **2006**, 153(11), G956.
[48] Mackus, A. J. M., Garcia-Alonso, D., Knoops, H. C. M., Bol, A. A., and Kessels, W. M. M., *Chem. Mater.* **2013**, 25(9), 1769–1774.
[49] Vos, M. F., Van Straaten, G., Kessels, W. M., and Mackus, A. J., *J. Phys. Chem. C* **2018**, 122(39), 22519–22529.
[50] Faraz, T., Knoops, H. C. M., Verheijen, M. A., Van Helvoirt, C. A. A., Karwal, S., Sharma, A., *et al.*, *ACS Appl. Mater. Interfaces* **2018**, 10(15), 13158–13180.
[51] Chopra, S. N., Vos, M. F., Verheijen, M. A., Ekerdt, J. G., Kessels, W. M. M., and Mackus, A. J. M., *Prep.* **2017**.
[52] Langereis, E., Heil, S. B. S., Knoops, H. C. M., Keuning, W., van de Sanden, M. C. M., and Kessels, W. M. M., *J. Phys. D. Appl. Phys.* **2009**, 42(7), 073001.
[53] Leick, N., Weber, J. W., Mackus, A. J. M., Weber, M. J., van de Sanden, M. C. M., and Kessels, W. M. M., *J. Phys. D. Appl. Phys.* **2016**, 49(26), 269601.
[54] Moulder, J. F., Stickle, W. F., Sobol, P. E., and Bomben, K. D., *Handbook of X-ray Photoelectron Spectroscopy*, Perkin-Elmer Corporation, Minnesota, **1992**, ISBN 9780962702624.
[55] Cazaux, J., *J. Electron Microsc. (Tokyo).* **2012**, 61(5), 261–284.
[56] Nilsen, O., Karlsen, O. B., Kjekshus, A., and Fjellvåg, H., *Thin Solid Films* **2007**, 515(11), 4550–4558.
[57] Kanarik, K. J., Tan, S., and Gottscho, R. A., *J. Phys. Chem. Lett.* **2018**, 9(16), 4814–4821.
[58] Fang, C., Cao, Y., Wu, D., and Li, A., *Prog. Nat. Sci. Mater. Int.* **2018**, 28(6), 667–675.
[59] Parsons, G. N., *J. Vac. Sci. Technol. A* **2019**, 37(2), 020911.
[60] Gladfelter, W. L., *Chem. Mater.* **1993**, 5(10), 1372–1388.
[61] Saito, S. and Kuramasu, K., *Jpn. J. Appl. Phys.* **1992**, 31(1), 135–138.
[62] Pan, W. and Desu, S., *Phys. Status Solidi* **1997**, 161, 201–215.
[63] Lee, E.-j., Kim, J.-w., and Lee, W.-j., *Jpn. J. Appl. Phys.* **1998**, 37, 2634–2641.

[64] Pan, W., *J. Vac. Sci. Technol. B Microelectron. Nanom. Struct.* **1994**, 12(6), 3208.
[65] Jastrzebski, L., *J. Electrochem. Soc.* **1983**, 130(7), 1571–1579.
[66] Puurunen, R. L. and Vandervorst, W., *J. Appl. Phys.* **2004**, 96(12), 7686.
[67] Puurunen, R. L., *Chem. Vap. Depos.* **2004**, 10(3), 159–170.
[68] Soethoudt, J., Grillo, F., Marques, E. A., van Ommen, J. R., Tomczak, Y., Nyns, L., *et al.*, *Adv. Mater. Interfaces* **2018**, 5(24), 1–11.
[69] Yim, S. S., Lee, D. J., Kim, K. S., Kim, S. H., Yoon, T. S., and Kim, K. B., *J. Appl. Phys.* **2008**, 103(11), 113509.
[70] Mackus, A. J., Weber, M. J., Thissen, N. F., Garcia-Alonso, D., Vervuurt, R. H., Assali, S., *et al.*, *Nanotechnology* **2015**, 27(3), 34001.

Conclusions and outlook

9

Atomic layer deposition (ALD) is an essential technique for the fabrication of integrated circuits for electronics and is expected to also play an important role for future integrated photonics. The shrinking of device dimensions, the increasing complexity of devices, and the growing number of materials being employed, together call for improvements of the ALD technology. This dissertation reports on the development of several advanced ALD processes, as well as the understanding of the underlying principles and growth mechanisms. The development of new processes is key for the extension of the ALD toolbox and will therefore help to broaden the application areas of ALD. More specifically, the following conclusions can be drawn from the work:

- Novel co-reactants and advanced ALD cycles provide an important opportunity for the development of ALD processes that allow for growth of new materials by ALD, as well as a wider range of process parameters (e.g. deposition temperature). As was discussed in Chapter 3, advanced ALD cycles are based on more than just one precursor and one co-reactant dose. Clever design of an advanced ALD cycles can offer a solution in case it is not possible to fulfill all fundamental roles required for ALD growth using a standard AB-type cycle. In addition, advanced ALD cycles allow for area-selective deposition and the growth of multiconstituent materials. Several processes based on the use of a novel co-reactant or an advanced cycle were studied in this work, and the understanding of the ALD growth mechanisms of these processes will help to develop processes for other materials based on similar strategies.

- The choice of the co-reactant is of great significance for an ALD process, although the precursor selection generally receives more attention in the literature. This especially holds for materials which are challenging to deposit with ALD (e.g. metals), since they are prone to impurity incorporation during deposition. Notably, the co-reactant not only affects the obtained material properties, but also the industrial feasibility of the process (e.g. in terms of safety or costs) and

which processing conditions are allowed. The ALD processes for AlF_3 (using SF_6 plasma) and for Co (using H_2/N_2 and NH_3 plasmas) studied in this thesis corroborate that co-reactant selection is crucial.

- SF_6 plasma is a suitable co-reactant for ALD of metal fluorides. Due to the high concentration of very reactive F radicals, an SF_6 plasma allows for high-purity fluoride films with low S-concentrations. Compared to previously used co-reactants for metal fluorides, it offers the benefits that it is readily available, and easy to handle. The deposited AlF_3 films that were discussed in Chapter 4 demonstrated properties in line with the literature reports on AlF_3 films deposited using other techniques. Notably, vacuum UV spectroscopic ellipsometry (VUV-SE) measurements showed that the deposited AlF_3 films are highly transparent (extinction coefficient k $<10^{-4}$ above 300 nm) and have a low refractive index n ($\sim$1.35 at 633 nm).

- The studies on the reaction mechanism of AlF_3 ALD (Chapter 5) revealed that $Al(CH_3)_3$ can react with AlF_3 as well as HF surface species, resulting in $AlF_x(CH_3)_{3-x}$ surface species. The F radicals in the SF_6 plasma were found to be responsible for the fluorination of the surface and for ligand removal, which is accompanied by formation of CH_yF_{4-y} (hydrofluorocarbons) as reaction products. The obtained insights suggest that an SF_6 plasma can be combined as co-reactant with various metal organic precursors based on carbohydrate ligands to achieve ALD of other metal fluorides. Furthermore, the transition from AlF_3 growth to Al_2O_3 etching observed at high temperatures, was explained by the temperature-dependent desorption of $AlF_x(CH_3)_{3-x}$ surface species, and indicates that an SF_6 plasma can also be used for atomic layer etching (ALE).

- ALD of Co was investigated using H_2- and N_2-based plasmas as co-reactants, and it was found that obtaining high-purity films relies on the presence of $NH_{x,\ x\leq3}$ species in the plasma (Chapter 6). The reaction pathways for the AB-processes using NH_3 and H_2/N_2 plasma where found to be similar, with $NH_{x,\ x\leq3}$ species leading to elimination of the precursor ligands. However, when employing a H_2/N_2 plasma as co-reactant, the $H_2/(H_2 + N_2)$ mixing ratio is crucial for obtaining Co films with a low impurity concentration and low resistivity, since the mixing ratio affects the concentration of $NH_{x,\ x\leq3}$ species in the plasma. Based on the experimental results and insights from the surface science literature, a reaction mechanism was proposed where NH_y species on the surface serve as the reactive site for precursor adsorption. The understanding obtained on the use of H_2- and N_2-based plasmas as co-reactants can be extended to ALD of other transition metal films.

- The combination of ALD and etching processes can allow for area-selective deposition with a high selectivity. This was demonstrated by selectively depositing Ru on top of Pt, while obtaining a clean SiO_2 non-growth area, using intermittent etch cycles integrated in an ALD-etch supercycle. The etch cycle consisted of an O_2 plasma exposure followed by a H_2 gas dose, and allowed for removal of Ru nuclei from the SiO_2 non-growth area. In Chapter 7 it was discussed that several guidelines need to be taken into account when designing an area-selective deposition process based on alternating deposition and etching cycles. Not only should the ALD and etch processes of choice demonstrate growth-area and etch selectivity, respectively, they should also have a minimal impact on surrounding materials and have to be mutually compatible (e.g. in terms of deposition temperature and pressure).

- When employing ALD-etch supercycles, careful optimization of the number of ALD and etch cycles in one supercycle is essential to obtain a high selectivity while maximizing the net deposition on the growth area (Chapter 8). For this optimization, it is especially important to investigate the etch rate of material on the non-growth area as a function of ALD cycles. The work also showed that a complimentary set of diagnostics (e.g. XPS, top-view SEM and cross-sectional TEM) is required to assess the selectivity of such area-selective ALD processes. Finally, the obtained understanding will help to develop more area-selective processes based deposition and etching, which is relevant for the transition towards 'atomic scale processing' that is taking place in the semiconductor industry.[1]

Additional research can be performed in various directions to improve the studied advanced ALD processes and to deepen the understanding. Based on the work presented in this thesis, the following recommendations for further research can be given:

- Deposition of metal fluorides other than AlF_3 can be investigated to further demonstrate the potential of SF_6 plasma as co-reactant. In Chapter 5, it is stated that SF_6 plasma can likely be combined with other metal organic precursors to grow a range of metal fluorides. Research in this direction is currently ongoing within the PMP group for the growth of LiF and $LiAl_xF_y$ films, which are relevant for applications in solid-state batteries. The process for $LiAl_xF_y$ is based on a supercycle consisting of the cycle for AlF_3, developed in this work, and a novel cycle for LiF. Moreover, other F-based plasmas such as NF_3 plasma can alternatively be studied as co-reactants. Similar to SF_6 plasmas, these plasmas are widely available in both research and industry.

- Inspired on the development of the AlF_3 process, the ALE process for Al_2O_3 using TMA and SF_6 plasma as reactants can be developed. Currently, most available ALE processes are isotropic thermal processes, or anisotropic plasma-based processes. Since the fluorination of metal oxides using SF_6 plasma is believed to be driven by the (non-directional) F radicals in the plasma, ALE using SF_6 plasma can likely allow for isotropic plasma-based ALE, which is an unexplored category of ALE processes. Initial ALE experiments suggested that anomalously high TMA doses of up to 1 s are needed to reach saturation, whereas for ALD TMA doses are typically in the order of tens of ms. Potentially, tuning of the plasma parameters (e.g. pressure, composition or power) or the sample temperature can result in a more practical ALE process. Combination of this ALE process with ALD in ALD-ALE supercycles could allow for area-selective deposition of Al_2O_3.

- The surface reactions taking place during Co ALD can be studied using surface sensitive techniques such as (reflectance) infrared spectroscopy. The studies on Co ALD suggest that the $CoCp_2$ precursor reacts with NH_y surface species. Although surface science literature has given some insight, the exact reactive surface site has not been identified. Additional experiments could also confirm if the NH_x species in the plasma facilitate the dissociation of the metal-Cp bond, as was speculated in Chapter 6. Furthermore, research on the use of H_2/N_2 and NH_3 plasmas for growth of other transition metal films, as well as metal nitride films would broaden the understanding. Literature reports have demonstrated improved nucleation behavior and growth rates when using a NH_3 plasma or H_2/N_2 plasma, suggesting that their use can be beneficial as compared to other co-reactants.

- ALD-etch supercycles for material systems other than Ru/Pt with SiO_2 as non-growth area can be developed in order to extend the toolbox of area-selective ALD. So far area-selective ALD of a few metal oxides (TiO_2 and Ta_2O_5) and one metal (Ru, this work) has been demonstrated using the ALD-etch approach. For other potential candidate systems, ALD processes with initial growth-area selectivity can be identified, and combined with etching processes demonstrating self-limiting reactions. For instance, ALD processes for HfO_2, Cu and W have been reported that demonstrate growth area-selectivity on various substrates, and ALE processes exist for those materials.[2–7] From an industrial perspective, it is mostly relevant to investigate conducting materials including Cu, Ru, Co and W, as well as insulators such as Al_2O_3 and SiO_2.

- In order to develop ALD-etch supercycles that simultaneously allow for a high selectivity and a high net deposition, situations should be identified were a significant difference exist between the etch rates of material on the growth area and the non-growth area. Ideally only the nuclei on the non-growth area are etched, while the film on the growth area is left intact. Such a situation can potentially be obtained by varying the etch duration and the processing conditions during the etch process, in combination with different surface morphologies on the growth area and the non-growth area. It would be insightful to characterize the etch rate of nuclei as a function of their size in comparison to the etch rate of planar films. Since the nuclei size depends on the number of ALD cycles, this characterization helps to determine when the etch cycle should be performed (i.e. the etch frequency). Transmission electron microscopy (TEM) could be used to measure the nuclei size as a function of ALD cycles, as well as the corresponding etch rates. For the Ru ALD-etch supercycles, these kind of experiments are currently in preparation, such that the process can be optimized further. Finally, in case the ideal situation is approached where only material on the non-growth area is etched, the employed etch process does not need to be an ALE process, since the uniformity and conformality on the growth area are not affected by the etch cycles.

References

[1] Lee, H.-B.-R., *Chem. Mater.* **2019**, 31(5), 1471–1472.
[2] Park, S. D., Lim, W. S., Park, B. J., Lee, H. C., Bae, J. W., and Yeom, G. Y., *Electrochem. Solid-State Lett.* **2008**, 11(4), H71 – H73.
[3] Tao, Q., Jursich, G., and Takoudis, C., *Appl. Phys. Lett.* **2010**, 96(19).
[4] Mohimi, E., Chu, X. I., Trinh, B. B., Babar, S., Girolami, G. S., and Abelson, J. R., *ECS J. Solid State Sci. Technol.* **2018**, 7(9), P491–P495.
[5] Jiang, X., Wang, H., Qi, J., and Willis, B. G., *J. Vac. Sci. Technol. A Vacuum, Surfaces, Film.* **2014**, 32(4), 041513.
[6] Xie, W., Lemaire, P. C., and Parsons, G. N., *ACS Appl. Mater. Interfaces* **2018**, 10(10), 9147–9154.
[7] Klaus, J. W., Ferro, S. J., and George, S. M., *Thin Solid Films* **2000**, 360(1-2), 145–153.

Summary

In electronic integrated circuits (ICs), the downscaling of device dimensions is requiring the integration of new materials, while the downscaling is simultaneously leading to challenges with respect to pattern alignment during fabrication. Furthermore, driven by the transition towards a data-based society, electronics on ICs will in the near future be closely coupled with integrated photonics, which also promotes the introduction of novel materials and processing techniques. Together, these developments demand cutting-edge methods to grow ultrathin films in a controllable and preferably bottom-up manner.

A technology which is playing a significant role in the aforementioned developments is atomic layer deposition (ALD). This deposition technique relies on the cyclic dosing of precursor ('A') and co-reactant ('B') chemicals. It allows for the growth of ultrathin films with a high uniformity on large-area substrates, and excellent conformality on 3D structures, while having a very precise thickness control. In this dissertation, *advanced* cycles beyond traditional AB-type cycles and ALD processes employing novel co-reactants are investigated for growth of AlF_3, Co and Ru. Ultimately, the obtained insights help to extend the ALD toolbox, in terms of the number of materials that can be deposited by ALD, as well as the possible applications of ALD. Examples of advanced ALD processes are ABC-type cycles, and supercycle recipes comprised of two ALD cycles. Advanced ALD processes can for instance be employed for area-selective ALD, which enables bottom-up fabrication, and helps to eliminate pattern alignment issues. Novel co-reactants can enable deposition of new materials by ALD, as well as extension of process parameters (e.g. deposition temperature).

For growth of AlF_3 an ALD process was developed using SF_6 plasma as a novel co-reactant. AlF_3 and other metal fluorides typically have a low refractive index and wide band gap, and due to these optical properties, they find widespread application in both optics and photonics. The AlF_3 films grown using $Al(CH_3)_3$ (TMA) and SF_6 plasma were found to be of high-purity, and demonstrated material properties in line with the expectations for AlF_3. Insights on surface species and formed reaction products were obtained to determine the reaction mechanisms, in which F radicals from the plasma fluorinate the surface and elimiate CH_3 surface groups. These insights on the reaction mechanisms contribute to extending the use of SF_6 plasma to ALD of other metal fluorides.

To understand ALD of Co, the influence of the co-reactant was investigated by employing different advanced ALD cycles. Co as well as Ru are currently being considered for the replacement of Cu in small-dimension interconnects in ICs, due to their superior conductivities at dimensions relevant for the 5-nm technology node and beyond. Co was deposited using $CoCp_2$ as the precursor and using different co-reactants, namely an NH_3 plasma, a mixed H_2/N_2 plasma and consecutive H_2 and N_2 plasmas in an ABC-type cycle. The reaction mechanisms enabling Co growth were investigated using quadrupole mass spectrometry, and it was found that NH_x radicals present in both the NH_3 and the H_2/N_2 plasma are essential for obtaining high-purity Co films.

An ABC-type ALD cycle consisting of subsequent doses of ethylbenzene-cyclohexadiene Ru precursor (EBCHDRu), O_2 gas and H_2 gas was used to grow high-quality Ru films at low deposition temperatures. Area-selective deposition of Ru on top of metal patterns on SiO_2 was achieved by combining the Ru ALD cycle with an etch cycle in a supercycle recipe, demonstrating that advanced ALD cycles provide a promising route to achieve area-selective ALD. Based on the insights obtained from developing the process for area-selective deposition of Ru, it was argued that ALD-etch supercycles should be optimized in terms of selectivity and net deposition. This optimization typically requires the evaluation of the growth rates and etch rates on both the growth and non-growth area as a function of ALD cycles. Finally, a general model was described for ALD-etch supercycles, which revealed that a high selectivity and a high net deposition can simultaneously be obtained for situations where the etch rate of material on the growth area is negligible in comparison to the non-growth area.

To conclude, ALD processes employing novel co-reactants and advanced cycles were studied with the aim to expand the capabilities of the ALD technology. In particular, ALD processes for AlF_3, Co, and Ru were developed and investigated in detail. In addition to an extensive characterization of the deposited materials, the underlying principles and mechanisms of growth were elucidated, which is highly relevant for development of other advanced ALD processes, and key to the extension of the ALD toolbox.

Contributions of the author

This thesis was proof read by A.J.M. Mackus and W.M.M. Kessels, and improved with the help of their comments. All experiments and data analysis were performed by M.F.J. Vos, except for the following:

- TEM images were taken by M.A. Verheijen. In addition, M.A. Verheijen performed the EDX measurements displayed in Figure 7.4.
- SE measurements for the uniformity maps on 200-mm wafers in Figure 4.2 were done by A. Kurek at Oxford Instruments.
- VUV-SE measurements for Figure 4.4 and Figure S4.6 were performed by R.A. Synowicki from J.A. Woollam Co., Inc.
- XRD for Figure S4.5 was performed by C. van Helvoirt.
- RBS measurements for Chapter 4 and Chapter 6 were done by W. Arnold Bik (Acctec B.V.).
- XPS data and SEM images for Figure S7.4 and Figure S8.3 were collected by S.N. Chopra.
- AFM measurements in Chapter 4 and Chapter 7 were done by M. Aghaee and D.A. Kane, respectively.

List of publications

Peer-reviewed publications

- **Reaction Mechanisms during Atomic Layer Deposition of Aluminum Fluoride using $Al(CH_3)_3$ and SF_6 Plasma [Chapter 5]**
  M.F.J. Vos, H.C.M. Knoops, W.M.M. Kessels and A.J.M. Mackus, in preparation (2019).

- **Isotropic Atomic Layer Etching of Al_2O_3 using $Al(CH_3)_3$ and SF_6 Plasma**
  N.J. Chittock, M.F.J. Vos, W.M.M. Kessels and A.J.M. Mackus, in preparation (2019).

- **Growth, Nucleation, and Material Properties of Ru Films Deposited Using an ABC-Type Atomic Layer Deposition Process**
  S.N. Chopra, M.F.J. Vos, M.A. Verheijen, J.G. Ekerdt, W.M.M. Kessels and A.J.M. Mackus, in preparation (2019).

- **Atomic Layer Deposition and Selective Etching of Ru for Area-Selective Deposition: Temperature and Supercycle Optimization [Chapter 8]**
  M.F.J. Vos, S.N. Chopra, M.A. Verheijen, J.G. Ekerdt, S. Agarwal, W.M.M. Kessels and A.J.M. Mackus, in preparation (2019).

- **Area-Selective Deposition of Ruthenium by Combining Atomic Layer Deposition and Selective Etching [Chapter 7]**
  M.F.J. Vos, S.N. Chopra, M.A. Verheijen, J.G. Ekerdt, S. Agarwal, W.M.M. Kessels and A.J.M. Mackus, Chemistry of Materials 31, 11 (2019).

- **Atomic Layer Deposition of Cobalt Using H_2-, N_2-, and NH_3-Based Plasmas: On the Role of the Co-reactant [Chapter 6]**
  M.F.J. Vos, G. van Straaten, W.M.M. Kessels and A.J.M. Mackus, Journal of Physical Chemistry C 122, 39 (2018).

- **Atomic Layer Deposition of Aluminum Fluoride using $Al(CH_3)_3$ and SF_6 Plasma [Chapter 4]**
  M.F.J. Vos, H.C.M. Knoops, R.A. Synowicki, W.M.M. Kessels and A.J.M. Mackus, Applied Physics Letters 111, 113105 (2017).

- **Atomic Layer Deposition of Molybdenum Oxide from $(N^tBu)_2(NMe_2)_2$-Mo and O_2 Plasma**
  M.F.J. Vos, B. Macco, N.F.W. Thissen, A.A. Bol and W.M.M. Kessels, Journal of Vacuum Science and Technology A 34, 01A103 (2015).

- **Low-temperature Atomic Layer Deposition of MoO_x for Silicon Heterojunction Solar Cells**
  B. Macco, M.F.J. Vos, N.F.W. Thissen, A.A. Bol and W.M.M. Kessels, Physica Status Solidi - Rapid Research Letters 9, 7 (2015).

Popular publications

- **Atomic Layer Deposition Process Development**
  M.F.J. Vos, A.J.M. Mackus, W.M.M. Kessels, Atomic Limits Blog, February 2019.

- **Een Nieuw Atoomlaagdepositie Proces voor Efficiëntere Zonnecellen**
  M.F.J. Vos, B. Macco, W.M.M. Kessels, Nevac Blad 54(1), 8, 2016.

Acknowledgments

Here we are. The part of a PhD thesis that is read by most people, but which is written with slightly less precision as the rest. The last four years have been an interesting journey where I got the chance to develop myself further and where I learned a lot about myself. Although one can feel very alone during a PhD, I have been lucky to receive a lot of support from people around me, and I could not have finished this thesis without their help.

First of all I would like to thank my co-promotor, **Adrie**, for all the support and feedback. I appreciate that you took over the daily supervision after you rejoined our group in early 2016. You always made time to discuss new data and give the needed feedback on drafts. After I had a slightly slow start on the Co project, you helped me to push for the highest achievable and I think that together we have achieved some valuable results. I also wish to thank my promotor, **Erwin**, for offering me the opportunity to do my PhD, and for all the guidance throughout my time in the PMP-group. You're positive criticism always helped me to improve my work and go for *the extra mile*. I also want to express my recognition for the way you run the PMP-group.

Big respect also for our technicians, who assisted me with experiments and who kept all the equipment running. I always enjoyed working with all of you, and I am happy I learned also on a more technical level rather than on a scientific level from you. **Janneke**, thank you for making arrangements when needed and for keeping us safe. **Caspar**, it never bothered you to think with me whenever there were issues in the lab. Thank you also for your great humor (*not*). **Cristian**, I appreciate you for all your help and for just for being a cheerful guy in general. **Joris**, thank you for always being willing to help me directly when something popped up and for showing me some insights on the ALDi reactors. (Your music in the lab and the way you tighten bolts was slightly less appreciated though...)

Jeanne and **Lianne**, thank you for all your help with administrative stuff. **Marcel**, our TEM guy, thanks for all the great images. I enjoyed our casual conversations during group outings and other occasions. **Sumit**, your help with the two Ru papers is greatly appreciated, as is also the nice dinner party we had in your house in Colorado.

Morteza, I can always rely on you. Our vivid discussions about important and less important aspects of our lives are mostly entertaining, but sometimes even insightful. **Sulphurman**, a.k.a. Saravana, you never fail to make me laugh (sometimes unintentionally), but you are also there when it comes to serious business. Thank you also for being my tour guide in India. **Shanky**, although we sometimes have opposing views, I've always appreciated your opinion on both scientific and non-scientific topics, and it was great to be sitting in the same office together. Guys, I will cherish our times at parties (including the cake incidents); It seems those days are behind us...

Dibya, thank you for always being cheerful and funny, and for allowing me to teach you some Dutch words. **Bart**, although we stopped working together after I finished my master project; it was partly you who gave me the know-how to get started with my PhD. **Bart**, **old Nick**, **Rene**, **Bas** & **The Harm**: Thank you for all the fun times at conferences and holidays. I am also grateful to The Harm for many fruitful discussions and his political opinions on everything. **Vincent**, thank you for your interest in my work and suggestions during conversations. **Sonali**, it was a pleasure to have you around in the lab, and I am happy I could continue our work after you finished your PhD. **David**, I appreciate your help with AFM measurements. **Reyhaneh**, thank you for fabricating the Pt patterns. **Gerben**, your expertise helped to improve our Co paper. **Marc**, I was lucky to have you around during the final experiments of my PhD on the ALDi. **Petro**, although your visit to our group was very short, it was certainly a fun time, and I appreciate the conversations we had afterwards. **Mahdi**, thank you for always asking how I am doing. **Hairui** & **new Nick**, thank you for our collaboration during the last few months, and good luck with the rest of your projects.

My gratitude also goes out to the rest of my office mates: **Norah**, **Karsten**, **Jimmy**, **Valerio**, **Farzad**, **Willem-Jan** and **Mark**. In addition I would like to acknowledge several former members from the PMP group that I was lucky to work with. **Akhil**, thanks for always being friendly and supportive. **Leo**, your presence in the group was greatly entertaining. I also thank **Tahsin**, **Fiona**, **other Bart**, **Alfredo**, **Valerio Zardetto**, **Jeroen**, **Jan-Willem**, and all the present and former members of the PMP group that I am forgetting, for our collaborations and interaction.

I've been lucky to also be surrounded by great people outside of the work environment, which helped me to forget about the struggles of a PhD student. To my *Spanish* family here in Eindhoven; living with you guys has been an unforgettable experience, and made my PhD life a bit more bearable. **Imanol**, thank you for

being a dear friend and for listening to my complaints while cooking together. **Aida**, the matriarch of the family, thank you for bringing joy to every occasion. It is impressive to see how you take care of the people around you. **Elena**, thank you for always being interested in my PhD. I'm happy you and Jeroen are back in Eindhoven. **Jeroen**, thank you for your great humor, and the butter chicken. Also a big shout out to the new members of la familia: Julen & Maya. **Marina**, although it was only a few months, it was great to have you in the house. Havensingel people: **Lucas**, **Alba**, **Aylim**, **Dimitri**, **Mikel**, **Andrea**, **Alvaro**, **Alberto**, **Ion**, **Nico**, **Sonya**, **Bea**, **Jose**, **Chris**, and **many others**; you often make me feel like I'm on holiday in my own city and I always enjoy our lunches, barbecues, parties and trips together. Dimitris, thank you for the challenging but relaxing bike rides.

Karin, I appreciate our friendship, and thank you for the interest and support. I'm also happy our phone calls could serve as a distraction during your long commutes. I also want to thank the 'old friends' from *'t Karwlus*; **Dennis**, **Quoc**, **Thijs**, & **Sebastiaan**. I think it is great that we still hang out regularly. This brings me to the other 'old friends': **Niels**, **Joeri**, **Bart**, **Natalja**, **Coen**, **Rogier**, **Robert**, **Thomas**, **Frans**, **Robin**, **Diederik** & **Bram**. Most of us have spread out over the country or are too busy with grown-up life, but whenever we meet it is always a pleasure. I am happy for the encouragement I still get from you.

Pap, **Mam**, ik wil jullie ontzettend bedanken voor alle steun die jullie me hebben gegeven. Jullie staan altijd voor ons klaar en niets is daarin te veel. **Vincent**, broeder en vriend, bedankt voor je interesse en luisterend oor, alsook voor de bezoekjes aan De Burger. Wat mij betreft krijgen onze trips naar Berlijn en Madrid spoedig een vervolg.

Finalmente, a la mia **Ragaza**. Forse possiamo dire che siamo il risultato pùi sorprendente da quattro anni di ricerca. I nostri viaggi in Italia e in altre parti del globo mi hanno aiutato a trovare la pace di cui avevo bisogno. Lo so che non era sempre facile, ma mi sei sempre stato vicino. Grazie per tutto. Tu non puzzi.

Curriculum Vitae

8 September 1990	Born in Eindhoven, The Netherlands
2003 - 2009	Diploma Voorbereidend Wetenschappelijk Onderwijs, Carolus Borromeus College, Helmond, The Netherlands
2009 - 2013	Bachelor of Science Degree in Applied Physics, Eindhoven University of Technology, Eindhoven, The Netherlands
2013 - 2015	Master of Science Degree in Applied Physics, Eindhoven University of Technology, Eindhoven, The Netherlands
	Three months research internship in the Plasma Research Laboratory at the Australian National University, Canberra, Australia
2015 - 2019	PhD Project in the group Plasma and Materials Processing, Department of Applied Physics, Eindhoven University of Technology, Eindhoven, The Netherlands
	NEVAC (*Dutch Vacuum Society*) Prize for "best article related to vacuum technology" (April 2016).
	Best Student Paper Award at the 19th International Conference on Atomic Layer Deposition in Bellevue, WA, USA (July 2019).